LUT
Lappeenranta
University of Technology

Yogini Patel

COMPUTATIONAL MODELLING OF NON-EQUILIBRIUM CONDENSING STEAM FLOWS IN LOW-PRESSURE STEAM TURBINES

Thesis for the degree of Doctor of Science (Technology) to be presented with due permission for public examination and criticism in the Auditorium 2310 at Lappeenranta University of Technology, Lappeenranta, Finland on the 7th of July, 2016, at noon.

Acta Universitatis
Lappeenrantaensis 705

Supervisor	Associate Professor Teemu Turunen-Saaresti LUT School of Energy Systems Lappeenranta University of Technology Finland
Reviewers	Professor Tekn. Dr. Damian Vogt Institute of Thermal Turbomachinery and Machinery Laboratory University of Stuttgart Germany
	Doctor Grant Ingram School of Engineering and Computing Sciences Durham University UK
Opponent	Professor Tekn. Dr. Damian Vogt Institute of Thermal Turbomachinery and Machinery Laboratory University of Stuttgart Germany

ISBN 978-952-265-975-0
ISBN 978-952-265-976-7 (PDF)
ISSN-L 1456-4491
ISSN 1456-4491
Lappeenrannan teknillinen yliopisto
Yliopistopaino 2016

Abstract

Yogini Patel
Computational modelling of non-equilibrium condensing steam flows in low-pressure steam turbines
Lappeenranta 2016
162 pages
Acta Universitatis Lappeenrantaensis 705
Diss. Lappeenranta University of Technology
ISBN 978-952-265-975-0, ISBN 978-952-265-976-7 (PDF), ISSN-L 1456-4491, ISSN 1456-4491

The steam turbines play a significant role in global power generation. Especially, research on low pressure (LP) steam turbine stages is of special importance for steam turbine manufactures, vendors, power plant owners and the scientific community due to their lower efficiency than the high pressure steam turbine stages. Because of condensation, the last stages of LP turbine experience irreversible thermodynamic losses, aerodynamic losses and erosion in turbine blades. Additionally, an LP steam turbine requires maintenance due to moisture generation, and therefore, it is also affecting on the turbine reliability. Therefore, the design of energy efficient LP steam turbines requires a comprehensive analysis of condensation phenomena and corresponding losses occurring in the steam turbine either by experiments or with numerical simulations. The aim of the present work is to apply computational fluid dynamics (CFD) to enhance the existing knowledge and understanding of condensing steam flows and loss mechanisms that occur due to the irreversible heat and mass transfer during the condensation process in an LP steam turbine.

Throughout this work, two commercial CFD codes were used to model non-equilibrium condensing steam flows. The Eulerian-Eulerian approach was utilised in which the mixture of vapour and liquid phases was solved by Reynolds-averaged Navier-Stokes equations. The nucleation process was modelled with the classical nucleation theory, and two different droplet growth models were used to predict the droplet growth rate. The flow turbulence was solved by employing the standard k-ε and the shear stress transport k-ω turbulence models. Further, both models were modified and implemented in the CFD codes. The thermodynamic properties of vapour and liquid phases were evaluated with real gas models.

In this thesis, various topics, namely the influence of real gas properties, turbulence modelling, unsteadiness and the blade trailing edge shape on wet-steam flows, are studied with different convergent-divergent nozzles, turbine stator cascade and 3D turbine stator-rotor stage. The simulated results of this study were evaluated and discussed together with the available experimental data in the literature. The grid independence study revealed that an adequate grid size is required to capture correct trends of condensation phenomena in LP turbine flows. The study shows that accurate real gas properties are important for the precise modelling of non-equilibrium condensing steam flows. The turbulence modelling revealed that the flow expansion and subsequently the rate of formation of liquid droplet nuclei and its growth process were affected by the turbulence modelling. The losses were rather sensitive to turbulence modelling as well. Based on the presented results, it could be observed that the correct computational prediction of wet-steam flows in the LP turbine requires the turbulence to be modelled accurately. The trailing edge shape of the LP turbine blades influenced the liquid droplet formulation, distribution and sizes, and loss generation. The study shows that the semicircular trailing edge shape predicted the smallest droplet sizes. The square trailing edge shape estimated greater losses. The analysis of steady and unsteady calculations of wet-steam flow exhibited that in unsteady simulations, the interaction of wakes in the rotor blade row affected the flow field. The flow unsteadiness influenced the nucleation and droplet growth processes due to the fluctuation in the Wilson point.

Keywords: CFD, condensation, steam, two-phase flow, low-pressure steam turbine, loss coefficient, turbulence modelling, real gas, blade trailing edge, unsteadiness

Acknowledgements

This work was carried out at the Lappeenranta University of Technology, Finland in the Laboratory of Fluid Dynamics from November 2010 to May 2016. The research conducted in this study was funded by the Finnish Graduate School in Computational Fluid Dynamics and the Academy of Finland.

Firstly I would like to express my sincere gratitude to my supervisor, Associate Professor Teemu Turunen-Saaresti, for all the guidance and support he provided during this research.

I am grateful to Professor Tekn. Dr. Damian Vogt and Doctor Grant Ingram for reviewing and evaluating the thesis. Their insightful comments and suggestions helped a lot to improve the thesis.

I would like to thank my colleague, Gitesh Patel for all his support throughout this work and feedback during the writing process. I also want to thank Professor Jari Backman, Associate Professor Aki Grönman and all of my colleagues and friends at the Laboratory of Fluid Dynamics for their friendly talks and interesting discussions specially during coffee breaks. Especially I wish to thank Ali Afzalifar and Alireza Ameli for having fun and too much laugh during Seoul trip. I wish to thank Dr Markku Nikku, Ville Rintala and Dr Heikki Suikkanen for their support during the usage of the LUT cluster. I would also like to thank CSC-IT Center for Science Ltd., Finland for allowing to use their cluster.

The journey of this work was very tough. A special thanks goes to my dear friends-cum-family Heta Jurvanen and Tomppa Jurvanen for their constant motivation and support during stressful and difficult moments. I can't forget all the chats and wonderful moments which I shared with you.

Finally, this work would not have been possible without the unconditional love, constant support and motivation of my parents, Natvarbhai and Kantaben Patel. Thank you so much for everything you have done for me and for all the encouragement you have given me. This thesis is dedicated to the memory of my mom, who passed away in 2013. Mom, I miss you so much but I know you are continually watching and protecting me from heaven. Dad, I never forget our every single day talk about my study and everyday life which helped me a lot to reduce my stress level. I am also thankful to my brother, Alpesh Patel, and sister-in-law, Deepali Patel, for their constant love and support. I also thank my wonderful niece, Aastha, and nephew, Naksh for always making me smile. I am extending my sincere gratitude to my grandparents for their kind blessings. They passed away during this research work. Again, I owe thanks to a special person, Gitesh for his continued and unfailing love, support, encouragement and patience.

Yogini Patel
June 2016
Lappeenranta, Finland

To my parents

Contents

Abstract

Acknowledgments

Contents

List of publications 11

Contribution of the author in the publications 13

Nomenclature 15

1 Introduction 19
- 1.1 Background . . . 19
- 1.2 Objective of the study . . . 24
- 1.3 Outline of the thesis . . . 25

2 Literature review of homogeneous condensation 27
- 2.1 Experimental studies . . . 27
- 2.2 Theoretical studies . . . 30
  - 2.2.1 Nucleation theory . . . 30
  - 2.2.2 Droplet growth theory . . . 31
  - 2.2.3 Theoretical developments . . . 32
- 2.3 Numerical studies . . . 34

3 Physical models 37
- 3.1 Governing equations of ANSYS FLUENT . . . 37
- 3.2 Governing equations of ANSYS CFX . . . 38
- 3.3 Nucleation and droplet growth model . . . 39
- 3.4 Real gas properties . . . 41
- 3.5 Turbulence modelling . . . 43
  - 3.5.1 The standard k-ε turbulence model . . . 45
  - 3.5.2 The SST k-ω turbulence model . . . 47
  - 3.5.3 Near-wall treatment . . . 48
- 3.6 Grid convergence index . . . 51

4 CFD calculation models 53
- 4.1 Geometrical details of selected calculation models and grid generation. . . 53
  - 4.1.1 CD nozzle cases . . . 53
    - 4.1.1.1 Moore nozzles . . . 53
    - 4.1.1.2 Moses and Stein nozzle . . . 54
    - 4.1.1.3 Barschdorff nozzle . . . 55
  - 4.1.2 2D turbine cascade . . . 57

4.1.2.1 White stator cascade 57
4.1.3 3D turbine stage 59
4.2 Details of the CFD simulation set-up 62
4.2.1 ANSYS FLUENT solver settings 62
4.2.2 ANSYS CFX solver settings 63

5 Results and discussions **67**
5.1 Influence of real gas modelling on condensing steam flows 67
5.2 Influence of turbulence modelling on 2D condensing steam flows 72
5.2.1 Results of nozzles 72
5.2.1.1 Effect of turbulence level on condensation 72
5.2.1.2 Effect of turbulence model modification 74
5.2.1.2.1 The standard k-ε turbulence model 74
5.2.2 Results of the turbine cascade 81
5.2.2.1 Grid independence study 81
5.2.2.2 Performance of various turbulence models 83
5.2.2.3 Effect of turbulence model modification 86
5.2.2.3.1 The standard k-ε turbulence model 86
5.2.2.3.2 The SST k-ω turbulence model 91
5.2.2.4 Loss analysis 96
5.3 Influence of trailing edge geometry on condensing steam flows 101
5.3.1 Effect on condensation properties 101
5.3.2 Loss analysis 107
5.4 Influence of unsteadiness on condensing steam flows 110
5.5 Influence of turbulence modelling on 3D condensing steam flows 125
5.5.1 Effect on flow properties 126
5.5.2 Effect of turbulence level on condensation 137
5.5.3 Loss analysis 141

6 Conclusions **145**

7 Future suggestions **149**

References **151**

List of publications

This thesis is based on the following publications. The rights have been granted by the publishers to include the material in the thesis. Additional results outside the following works are presented in the thesis.

I Patel, Y., Patel, G., and Turunen-Saaresti, T. (2013). The effect of turbulence and real gas models on the two phase spontaneously condensing flows in nozzle. *In: Proceedings of ASME Turbo Expo 2013: Turbine Technical Conference and Exposition*. Vol. 5B, pp. 1-8, San Antonio, Texas, USA.

II Patel, Y., Turunen-Saaresti, T., Patel, G., and Grönman, A. (2014). Numerical investigation of turbulence modelling on condensing steam flows in turbine cascade. *In: Proceedings of ASME Turbo Expo 2014: Turbine Technical Conference and Exposition*. Vol. 1B, pp. 1-14, Düsseldorf, Germany.

III Patel, Y., Patel G., and Turunen-Saaresti, T. (2015). Influence of turbulence modelling on non-equilibrium condensing flows in nozzle and turbine cascade. *International Journal of Heat and Mass Transfer*. Vol. 88, pp. 165-180.

IV Patel, G., Patel, Y., and Turunen-Saaresti, T. (2015). Influence of trailing edge geometry on the condensing steam flow in low-pressure steam turbine. *In: Proceedings of ASME Turbo Expo 2015: Turbine Technical Conference and Exposition*. Vol. 8, pp. 1-11, Montreal, Canada.

V Patel, Y., Patel, G., and Turunen-Saaresti, T. (2016). Influence of turbulence modelling to condensing steam flow in the 3D low-pressure steam turbine stage. *In: Proceedings of ASME Turbo Expo 2016: Turbomachinery Technical Conference and Exposition*. pp. 1-11, Seoul, South Korea.

Contribution of the author in the publications

The author's contribution to the publications I-V is discussed below.

Publication I

The author planned this paper. The author was responsible for the implementation of modified models into the CFD code and performed all of the numerical simulations and corresponding post-processing. The author wrote the paper, taking into account the comments by the co-authors.

Publication II

The author was responsible for the planning, model implementation, CFD simulations and data analysis. The author wrote this paper together with the co-author, taking into account the comments by the co-authors.

Publication III

The author was in charge of the preparation of the paper and conducting all the numerical simulations. The author was responsible for the implementation of the model into CFD solver. The paper was post-processed, written and revised with the help of Giteshkumar Patel, M.Sc.

Publication IV

The author contributed grid generation, CFD simulations and corresponding model implementation, and provided comments to the corresponding author.

Publication V

The author was responsible for the planning of the paper. The author was responsible for the CFD model design and grid generation in it. The author conducted all of the numerical simulations. The paper was post-processed and written by the author with Giteshkumar Patel, M.Sc. The author revised the paper.

Nomenclature

Latin alphabet

A_m	area of the mth cell	–
A, B, C	virial coefficients	–
C_p	specific heat at constant pressure	$\mathrm{J\,kg^{-1}\,K^{-1}}$
C_v	specific heat at constant volume	$\mathrm{J\,kg^{-1}\,K^{-1}}$
e_a	relative error	–
e_{ext}	extrapolated relative error	–
f_u	droplet response coefficient	–
G_k	production of k	$\mathrm{kg\,m^{-1}\,s^{-3}}$
h	specific enthalpy	$\mathrm{J\,kg^{-1}}$
h_{lv}	specific enthalpy of evaporation	$\mathrm{J\,kg^{-1}}$
H	total enthalpy	$\mathrm{J\,kg^{-1}}$
I	nucleation rate	$\mathrm{m^{-3}\,s^{-1}}$
k	turbulent kinetic energy	$\mathrm{m^2\,s^{-2}}$
K_b	Boltzmann's constant	–
Kn	Knudsen number	–
K_t	thermal conductivity	$\mathrm{W\,m^{-1}\,K^{-1}}$
l_g	mean free path of vapour molecules	m
m^*	mass of stable nucleus	kg
M	liquid mass	kg
M_m	mass of water molecular	kg
N	total number of cells	–
P	pressure	Pa
P_{sat}	saturation pressure	Pa
q_c	condensation coefficient	–
r	radius	m
$\bar{r}$	average radius	m
r_*	critical radius	m
R	gas constant	$\mathrm{J\,kg^{-1}\,K^{-1}}$
Re_λ	Reynolds number	–
s	entropy	$\mathrm{J\,kg^{-1}\,K^{-1}}$
S	supersaturation	–
S_1, S_l	mass source term	$\mathrm{kg\,m^{-2}\,s^{-1}}$
S_2, $S_{F,m}$	momentum source term	$\mathrm{kg\,m^{-2}\,s^{-2}}$
S_3, S_{e1}, S_{e2}	energy source term	$\mathrm{W\,m^{-3}}$
S_c	condensation shock	–
S_k	turbulence kinetic energy source term	$\mathrm{kg\,m^{-1}\,s^{-3}}$
S_p	pressure side shock	–
S_s	suction side shock	–

S_ε	turbulence dissipation rate source term	$\mathrm{kg\,m^{-1}\,s^{-4}}$
t	time	s
T	temperature	K
T_L	lagrangian integral timescale	s
T_s	saturation temperature	K
u	velocity component	$\mathrm{m\,s^{-1}}$
$u^{'}$	fluctuating velocity component	$\mathrm{m\,s^{-1}}$
y	normal distance from the wall	m
y^+	non-dimensional wall distance	–

Greek alphabet

α	phase volume fraction	–
β	liquid phase mass fraction	–
γ	specific heat ratio	–
Γ	mass generation rate	$\mathrm{kg\,m^{-3}\,s^{-1}}$
Γ_E	thermal diffusion coefficient	$\mathrm{W\,m^{-1}\,K^{-1}}$
ε	turbulence dissipation rate	$\mathrm{m^2\,s^{-3}}$
ζ	Markov energy loss coefficient	–
η	number of liquid droplets per unit volume	$\mathrm{m^{-3}}$
θ	non-isothermal correction factor	–
μ	dynamic viscosity	$\mathrm{Pa\,s}$
μ_t	turbulent viscosity	$\mathrm{kg\,m^{-1}\,s^{-1}}$
ρ	density	$\mathrm{kg\,m^{-3}}$
σ	liquid surface tension	$\mathrm{N\,m^{-1}}$
σ_k, σ_ε	turbulent Prandtl numbers	–
τ	viscous stress tensor	Pa
τ_p	droplet response time	s
τ_T	Taylor time microscale	s
τ_w	wall stress tensor	Pa
υ_τ	friction velocity	$\mathrm{m\,s^{-1}}$
χ	turbulence intensity	–
ω	specific dissipation rate	$\mathrm{s^{-1}}$

Subscript

$0, 1, 2$	total, inlet, outlet condition of domain
d	droplet
i, j	cartesian tensor notation, grid index
l	liquid phase
m	mixture

s	saturation
t	turbulence
v	vapour phase
x	cartesian coordinate

Abbreviations

2D	two-dimensional
3D	three-dimensional
AMG	algebraic multigrid
CD	convergent-divergent
CFD	computational fluid dynamics
CTE	conic trailing edge
EOS	equation of state
EWT	enhanced wall treatment
FAS	full-approximation storage
GCI	grid convergence index
HP	high pressure
IP	intermediate pressure
LP	low pressure
LRN	low-Reynolds number
MS $k-\varepsilon$	modified standard k-ε
MSST $k-\omega$	modified SST k-ω
RANS	Reynolds-averaged Navier-Stokes
RMS	root-mean-square
RNG	re-normalisation group
RTE	semicircular trailing edge
SST	shear-stress transport
STE	square trailing edge
SWF	standard wall functions

1 Introduction

1.1 Background

Steam turbines play a crucial role in the power generation cycle. Worldwide, the current power generation systems that utilise steam turbines produce more than 60% of the global supply of electricity. Due to industrialisation, population increment and globalisation, the energy consumption of the world is forecasted to rise by about 34% to 2040 (IEA, 2015). Therefore, the advancement and practical realisation of technologies appropriate to improve the overall efficiency of steam turbines for power production should be encouraged to meet the global electricity demand while regulating and decreasing worldwide greenhouse gas emissions.

It is a fact that the efficiency of power plant predominantly depends on the efficiency of energy conversion (from thermal energy to mechanical energy) in the steam turbines. Generally, steam turbines in large power plant contain three separate stages (i) high pressure (HP), (ii) intermediate pressure (IP) and (iii) low pressure (LP). Figure 1.1 (a) displays a schematic of typical steam flow path in a multistage steam turbine cycle. The steam leaving from the HP stage is reheated in boiler to attain its original temperature and pressure level is considerably decreased. After that the reheated steam is conveyed to the IP stage and to the LP stage. The real LP steam turbine photograph is shown in Figure 1.1 (b). The temperature of the superheated vapour in the last stages of the LP turbine decreases due to rapid expansion, and it condensates shortly as the expansion line crosses the saturation line. Due to expansion process, the superheated steam initially subcools and subsequently droplet nuclei are formed which leads to a mixture of saturated vapour and tiny water droplets. The mixture of these two phases is commonly referred to as wet-steam.

Traditionally, the effect of condensation in steam flow has been studied using convergent-divergent (CD) nozzles because of the simplicity of the essentially one-dimensional flow within them. A typical homogeneous condensation (in the absence of foreign particles or ions) process occurring in a supersonic nozzle is displayed in Figure 1.2. The expansion line is also illustrated in an h-s diagram. As shown in Figure 1.2, dry superheated steam enters the nozzle at point (1). Steam expands from the nozzle inlet to the throat at point (2), where it attains the sonic condition. As steam travels from the nozzle throat downstream, the expansion line crosses the saturation line at point (3) and steam becomes subcooled or supersaturated. Further steam expands, the process of nucleation starts at point (4) which forms a very large number of tiny droplets. The steam state in the region between point (3) and point (4) is referred as meta-stable state. Subsequently, the nucleation rate of steam continues to grow up to the limiting supersaturation and reaches point (5). The nucleation terminates effectively, and accordingly, the number of liquid droplets in the flow remains constant. The region from point (4) to point (5) is called the nucleation zone. The nucleation process ends at the point of maximum subcooling which is called the Wilson Point (i.e. point (5)). Onwards from point (5), the liquid droplets start

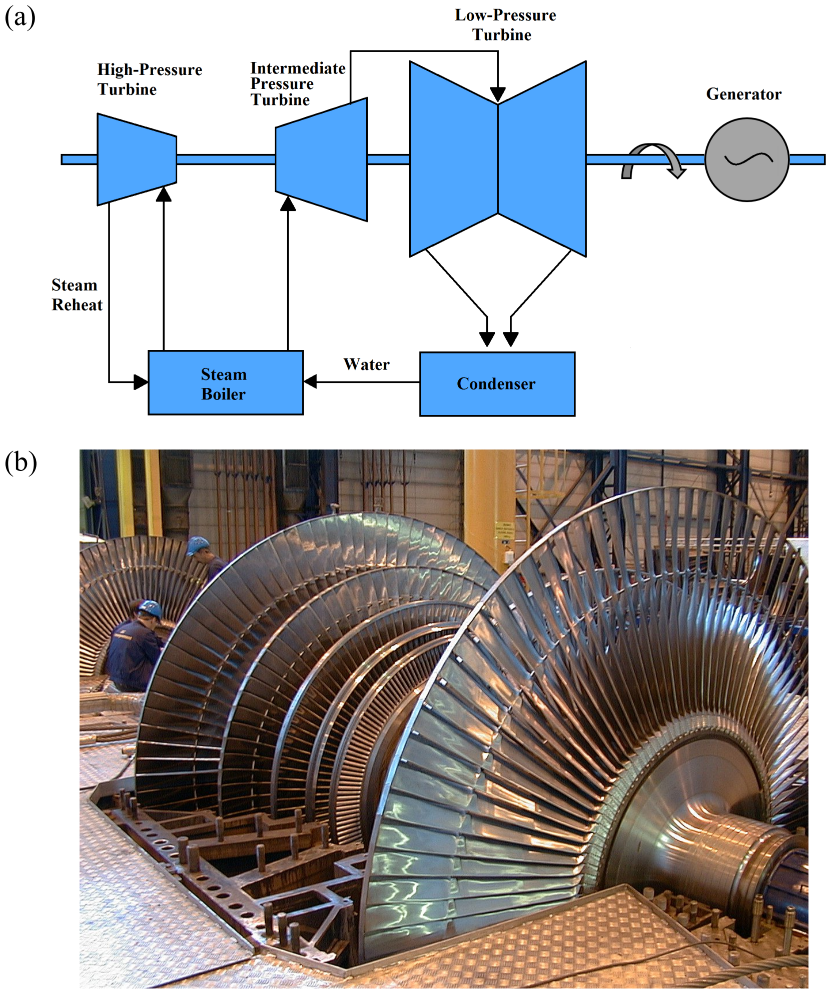
(a)
Low-Pressure Turbine
High-Pressure Turbine
Intermediate Pressure Turbine
Generator
Steam Reheat
Steam Boiler
Water
Condenser
(b)

Figure 1.1: (a) The schematic of a typical steam flow path in a multistage steam turbine cycle and (b) the photograph of LP steam turbine with the permission of Fortum Power and Heat Oy.

to grow. Eventually, the latent heat which is released via droplets due to condensation is conducted back to the vapour phase. In addition, the heat transfer rate is significant in the rapid condensation zone. Due to released latent heat, the supersonic flow decelerates and the pressure increases and is accompanied by a corresponding rise in enthalpy and entropy. The pressure rise is also known as 'condensation shock' (i.e. point (6)). After point (6), further flow expands up to point (7) and the steam almost attains thermodynamic equilibrium in which the temperatures of both phases are close to the saturation level (Buckley, 2003).

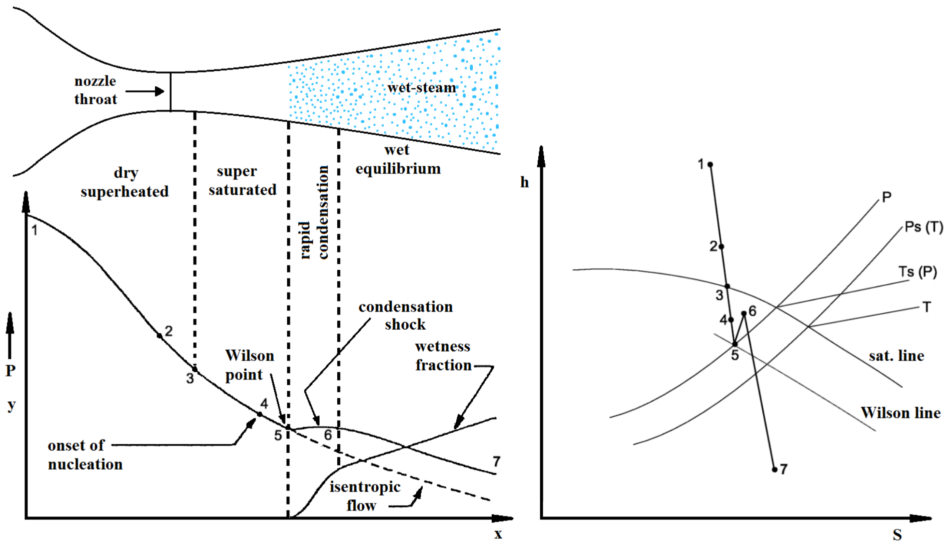
nozzle throat
wet-steam
dry superheated
super saturated
rapid condensation
wet equilibrium
P
y
1
2
3
4
5
6
7
Wilson point
onset of nucleation
condensation shock
wetness fraction
isentropic flow
x
h
1
2
3
4
5
6
7
P
Ps (T)
Ts (P)
T
sat. line
Wilson line
s

Figure 1.2: Homogeneous condensation in supersonic nozzles (Guha, 1995).

For LP turbine stages, a formulation of wetness and the associated expansion process are displayed in Figure 1.3 with an h-s diagram. The released latent heat during the condensation process is conveyed back to the vapour phase which increases the flow entropy. The notable increment in entropy is illustrated in an h-s diagram after droplet formation (Figure 1.3). Further downstream, the droplets grow. Eventually, the droplets deposit on the stator blade surfaces. Thereafter, the deposited droplets form into liquid films. These films convey toward the blade trailing edges due to drag effect. The droplet deposition and water films are indicated in blue in Figure 1.3. Subsequently, the water film breaks up at the blade trailing edge and coarse water droplets are created. These large water droplets having low absolute velocities impinge on the leading edges of succeeding blades with high relative velocities and negative incident. Due to these impacts, the blade leading edges break and erode. Furthermore, the water deposition on the rotor blade in the LP turbine is subject to vigorous centrifugal forces. Consequently, the accurate analysis of condensation phenomena is essential in order to acquire information about finer droplets sizes, droplet deposition and subsequently the erosion effect.

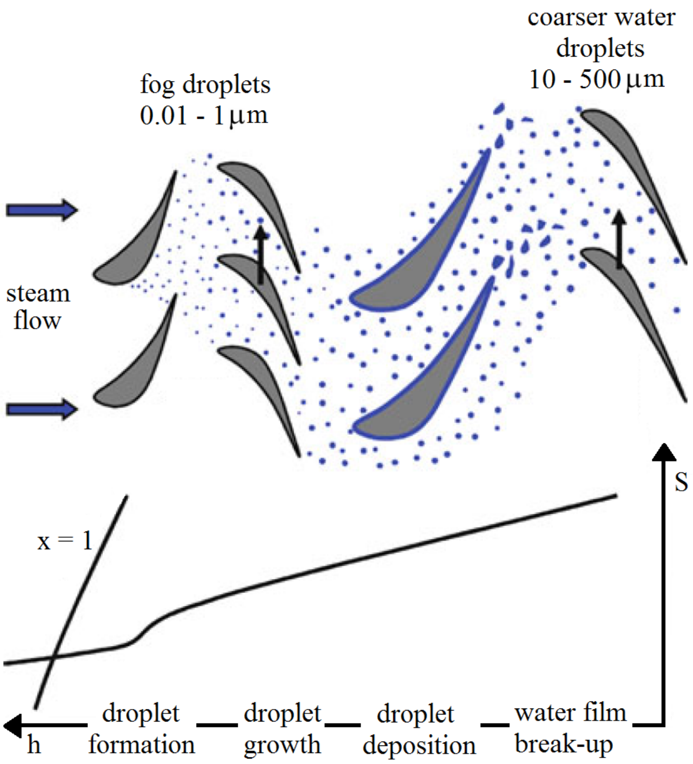

Figure 1.3: Wetness formation in LP turbine stages and the corresponding expansion line (Starzmann et al., 2013a).

The row of last-stage blades in the LP section is a key element of the turbine's design because it determines the machine's overall performance and dimensions. At least the last couple of stages of the LP turbine operate in the two-phase region which produces much more than 10% of the total output. However, the last stages of LP turbines are susceptible to additional losses due to the existence of a second phase. The losses in the LP turbine are displayed in Figure 1.4. The existence of liquid phase in turbine introduces irreversible thermodynamic losses (produce due to heat transfer in fluid/induced by non-equilibrium conditions and phase changes), aerodynamic losses (occurring due to fluid and solid surfaces interactions), and mechanical losses or erosion. From Figure 1.4, it can be seen that about one fourth of the total losses occur due to condensation in the LP turbine.

Additionally, irreversible thermodynamic losses are important to the LP stage efficiency. The correspondence between the wetness percentage in steam and turbine efficiency is often estimated using Baumann's rule, which provides that with every additional percentage of wetness, the turbine efficiency is decreased by approximately 1% (Baumann,

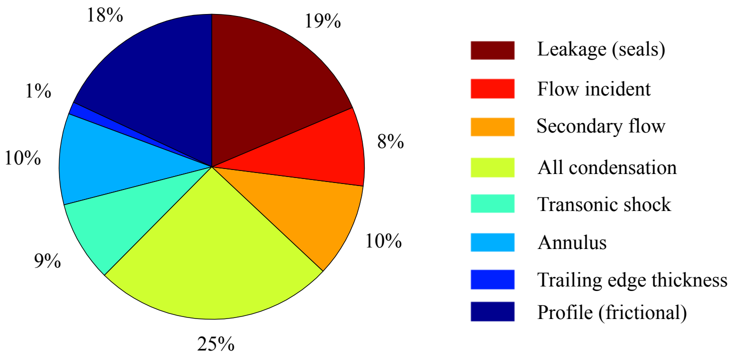

Figure 1.4: Distribution of losses in a typical LP turbine (Jonas, 1995).

1921). The Baumann rule can be expressed as follows:

$$\eta_{st} = \eta_{st,dry}(1 - 0.5\alpha\beta), \tag{1.1}$$

where, η_{st} is the steam turbine efficiency, $\eta_{st,dry}$ is the steam turbine efficiency with superheated steam, and β is the liquid mass-fraction. The constant α is an empirical coefficient known as the Baumann factor. Various experiments carried out on different types of turbines suggested that the value of α lies in the range of 0.4 to 2 (Moore and Sieverding, 1976).

In conventional power plants, the typical exhaust wetness levels in the last few stages of the LP turbine can be around 12%. In contrast, in pressurized water reactor nuclear plants, wetness problems are also experienced in the high-pressure stages, and exhaust wetness may reach as high as 18%. Current research on LP turbine stages is of special importance due to their relatively lower efficiency, frequent maintenance and low reliability. It is a fact that a marginal improvement in the LP turbine performance would produce notable economic benefits. Thus, it is crucial for scientists, utility owners and manufacturers of steam turbines and power plants to understand and to analyse the condensation process that occurs in the LP turbine. Therefore, a detailed analysis of condensing steam flow, either by experiments or with numerical simulations, has great importance. Since the early 1990s, many researchers have conducted comprehensive studies of condensing steam flow experimentally, theoretically and numerically. However, the experimental facilities for wet-steam flows are globally very scarce. Additionally, the accurate measurement of some key parameters (e.g. droplet size and distribution, wetness fraction, etc.) of these flows is very challenging. Therefore, a numerical study of the condensing steam flows is a feasible option. Nevertheless, the detailed experiments of wet-steam flows are important for the validation of numerical models. Moreover, due to enormous advancements in computational power and numerical techniques to fully solve 3D Navier-Stokes equations of flow phenomena, computational fluid dynamics (CFD) modelling of wet-steam flow is very popular among researchers. Therefore, in this thesis, numerical modelling has been chosen to simulate condensing steam flow in CD nozzles, stator cascade and 3D stator-rotor stage. Further, this work also focuses on the analysis of losses that occur due to the irreversible heat and mass transfer during the condensation process.

1.2 Objective of the study

With the tremendous role played by steam turbines in the power generation cycle, it is essential to understand the flow field of condensing steam flow in a steam turbine in order to design an energy efficient turbine. In LP turbines, usually more than 90% of the total liquid mass is in the form of fog (diameter in the range of 0.05 to 2.0 µm) while the rest is concentrated in the form of coarser droplets (diameter in the range of 20 to 200 µm) (Guha, 1998). The presence of the liquid phase in LP turbines introduces thermodynamic and aerodynamic losses as well as erosion in rotating and stationary parts. Therefore, the objective of this work is to conduct a proper analysis of condensing steam flow and the loss mechanism involved in it by utilising commercial CFD codes.

Furthermore, for the precise modelling of the non-equilibrium flow of LP turbines, subcooled thermodynamic properties of vapour are crucial because the nucleation and droplet growth rate are quite sensitive to such properties. Therefore, the dominance of real gas properties in the process of spontaneous condensation is studied.

The flow structures of turbine flows are complex and involve a variety of interesting flow phenomena, for example flow transition from laminar to turbulent, flow separation, secondary flow mixing and rotor-stator interaction, and turbulence is involved in all of these phenomena. Turbulence plays a vital role in transport mechanism of mass, momentum and energy either in main flow regions or in boundary layers on the solid surface walls, particularly in the possible deposition of condensed liquid droplets. Thus, it is essential to model turbulence accurately in condensing steam flow because the ignorance of turbulence modelling to condensing steam flow calculation may induce an incorrect estimation of the key phenomena and erroneous losses. Therefore, in this work the influence of turbulence modelling on condensing steam flow is presented.

The arrangements of stator and rotor blade rows in an LP turbine causes a strong 3D unsteady flow phenomenon. Further, the wakes coming from upstream blade rows and the potential fields of blade rows introduce unsteadiness in the flow. Therefore, the inherent unsteadiness in an LP turbine flow would have some influence on the non-equilibrium condensation. The effect of unsteadiness present in 3D steam condensing flow in an LP turbine has been analysed.

The condensing process in an LP turbine is very sensitive to the variation of the local flow field as well as to the boundary conditions. Moreover, the LP blade profiles including the shape and thickness may have some impact on the condensing phenomena in the LP turbine. For example, the pressure fields within the blade passage are very sensitive to the shape and size of the blade trailing edge (TE). As the liquid phase generation greatly relies on the local rate of change of the pressure fields, it could be assumed that the TE shapes would have an active role in the nucleation and droplet growth process and also other important parameters of condensing steam flow in LP turbines. This work studies the influence of the TE shape on condensing steam flow in the stationary cascade of turbine blades.

In this work, the process of spontaneously condensing steam flows in CD nozzles, stator cascade and 3D stator-rotor stage is modelled using the Eulerian-Eulerian approach of the ANSYS CFD codes (ANSYS FLUENT and ANSYS CFX). In both CFD codes, the mixture of vapour and liquid phases is governed by Reynolds-averaged Navier-Stokes (RANS) equations. The condensation phenomena are modelled on the basis of the classical nucleation theory. The objectives of this study are the following:

- To analyse the significance of computational grid resolution in condensing steam flows.
- To examine the sensitivity of real gas properties to steam condensing flows.
- To investigate the influence of turbulence and its modelling, and to provide new models to take the effect of turbulence into account in wet-steam flows with 2D CD nozzles, turbine cascade and 3D stator-rotor stage.
- To study the influence of blade TE geometry on wet-steam flows.
- To illustrate the effect of unsteadiness in wet-steam flows.
- To extract information about losses which occur due to irreversible heat and mass transfer processes.

1.3 Outline of the thesis

The present work is organized into seven chapters. The content of the individual chapters is briefly the following.

Chapter 1 describes the importance of understanding steam condensing flow phenomena and loss mechanisms during condensation processes within steam turbines. The objectives of this work are listed. The thesis structure is discussed. Chapter 2 contains the literature review and summarises previous efforts by other researchers involving the condensation process. Past and present steam condensing flow measurements are briefly described from various perspectives. The theoretical development and numerical modelling of steam condensing flow is also summarised.

Chapter 3 contains detailed information of physical models utilised for condensing steam flow simulations. The chapter describes the phase-coupling PDEs based on the Eulerian-Eulerian approach to CFD code. Also, calculations of real gas properties, nucleation and droplet growth models are discussed. Chapter 3 also includes detailed descriptions of the turbulence models employed.

Geometrical details of the selected CFD calculation models and grid generation in them are discussed comprehensively in chapter 4. Moreover, the corresponding experimental test cases are also described briefly and the simulation set-ups are reported. Chapter 5 describes the numerical results of this work and discusses the effects of real gas modelling and turbulence modelling on condensing steam flow. Also the influence of the trailing edge geometry on condensing steam flows is presented in the chapter. The later part of the chapter describes the effect of unsteadiness and turbulence modelling on wet-steam flow in the 3D stator-rotor stage.

The conclusions drawn from the present work are listed in chapter 6. The final chapter discusses the suggestions and future prospects related to condensing steam flow modelling.

2 Literature review of homogeneous condensation

Homogeneous and heterogeneous condensation (containing chemical impurities of both insoluble or/and soluble) in nozzles and steam turbines have been widely studied experimentally, theoretically and numerically over several decades. Nevertheless, the proper analysis and understanding of wet-steam flow phenomena and losses (irreversible thermodynamic losses, aerodynamic losses and mechanical losses or erosion) resulting from wetness are currently of great importance. The role of heterogeneous condensation is relatively small compared to the homogeneous condensation in LP turbine flows (Gerber, 2002). Moreover, the available knowledge of heterogeneous condensation modelling is very scant (Bakhtar and Heaton, 2005; Starzmann et al., 2011). Therefore, heterogeneous condensation is not considered in this study. This chapter presents a comprehensive literature review focusing only on the homogeneous condensation of steam. The experimental and computational investigation of wet-steam flows in nozzles and in steam turbines conducted previously are discussed. Moreover, the fundamental physics of phase transition and theoretical methods for the modelling of non-equilibrium condensing flow presented by researchers/scientists are summarized.

2.1 Experimental studies

The first experiment of homogeneous nucleation was conducted in the late 1800s by Helmholtz (1887), who noticed that a saturated steam jet expanding from the orifice into the atmosphere remained clear for some distance and then quickly converted to foggy. A decade later, Wilson (1897) performed cloud chamber experiments in which he utilised the fact that ions facilitate the initiation of condensation. In his experiments, the expansion chamber contained moist and dusty air. He noticed a very small expansion yielded a dense fog when the chamber was dust-free and without fogs then little expansion was resulted. Wilson (1897) discovered that without dust particles, cloud condensation could be produced if the supersaturation ratio exceeded certain limits.

The first experimental study of condensation of vapour in a CD nozzle was conducted by Stodola (1915). In his study he found that the condensation was delayed and appeared in the supersonic part of the nozzle. Subsequently in the same year, Callender (1915) studied the effect of supersaturation in a nozzle, and he estimated the size of droplets which was produced on nucleation of the vapour using the Kelvin-Helmhotlz equation. Later on, Martin (1918) evaluated the limiting supersaturation ratios with the assumption of constant droplet sizes for all conditions, and he presented the outcomes in the Mollier diagram which is known as the Wilson line. Before the mid 1900s, several experimental studies were conducted for condensing steam flows in nozzles e.g. by Rettaliata (1936), Yellott and Holland (1937), Binnie and Woods (1938) and Binnie and Green (1943). These works were dedicated to enhance the information of the Wilson line and limiting supersaturation ratio.

Afterwards, some works focused on the development of optical techniques to measure wet-steam flow properties. Gyarmathy and Meyer (1965) and Gyarmathy and Lesch (1969) were the first who utilised the light scattering technique (which is based on measuring the intensity of the scattered light within small angles distributed in a conical shape along the principal light beam) for inferring droplet radii. Following these works, Moses and Stein (1978) performed experiments with the Laval nozzle considering a variety of starting conditions. In their work, the homogeneous nucleation and the growth of the liquid phase were documented both with the static pressure and the laser light scattering measurements. In addition to these works, they established the Wilson line of steam and were the first to provide information on the average size of the fog droplets formed by nucleation. A point at which homogeneous condensation occurs is called the Wilson point and various Wilson point corresponding to a given expansion rate are joined on the Mollier chart with line is called the Wilson line (Gyarmathy, 1962). Also Moore et al. (1973) conducted measurements of the pressure distribution in nozzles by varying the throat height and divergence angle, utilising the light scattering data to deduce droplet sizes.

Subsequently, comprehensive experiments of condensing flow in nozzles have been organized by numerous researchers, for example Barschdorff (1971), who performed experiments on the pressure distribution in arc nozzle flows. After that, Bakhtar et al. (1975) investigated nucleation phenomena in high-pressure steam flow. Later on, Skillings et al. (1987) presented an experimental investigation on the condensing steam flow in the nozzle, and an aerodynamic shock wave was established in the flow in the divergent part of the nozzle. Significant experimental and theoretical studies were carried out by Bakhtar and Zidi (1989, 1990) by limiting supersaturation in high-pressure steam with three nozzles considering nominal rates of expansion of 3000, 5000 and 10000 per second. In their investigation, they covered the inlet stagnation pressures in the range of 25-35 bar. Moreover, Gyarmathy (2005) conducted detailed experiments with Laval nozzles designed for various expansion rates and the inlet stagnation states, emphasising the Wilson line and the fog structure in high-pressure saturated/subcooled steam flow. Recently, Dykas et al. (2015) conducted experiments on non-equilibrium spontaneous condensation in transonic steam flow in an arc Laval nozzle, providing static pressure measurements and the Schlieren pictures of the flow field.

Earlier experimental investigations have generally utilised the characteristics of typical 1D nozzle profiles. However, these nozzle measurements were unable to provide sufficient information on wet-steam flow to fix empirically the unknown parameters of the theoretical models. Moreover, these 1D nozzle flows are not illustrative of the phenomena which appear in real steam turbines. Since the real flow behaviour in steam turbines is considerably more complex, subsequent experimental studies were dedicated to the 2D flow in turbine blade cascades.

Walters (1973) developed an advanced technique based on light extinction for measuring the wetness and droplet size in a steam turbine. In this technique, when a light beam transmits through the wet-steam flow, the transmitted light intensity is reduced because of scattering and absorption by the flow particle (i.e. water droplet). When a flow particle passes through the light beam, a certain amount of light is to be cut off, and a pulse (light signal reduction) will result. Walters and Skingley (1979) described an optical probe that obtained the fog droplet size and wetness fraction of flows in full size LP steam turbines. Later on, Bakhtar et al. (1995a,b) conducted a series of experiments of condensing steam flow in a rotor-tip cascade and provided validation data for blade static pressure distributions, droplet size, thermodynamic loss, and efficiency over a range of expansion ratios and inlet supercooling levels. White et al. (1996) conducted extensive experiments on non-equilibrium condensing steam flow in a stationary cascade of turbine blades operating transonically. They obtained a large set of measurement data in different test conditions for various parameters, including the blade surface static pressure distribution, wetness fraction, droplet size, normalised entropy, cascade loss coefficients and Schlieren photographs. More recently, Yousif et al. (2013) performed experiments on non-equilibrium spontaneous condensation in transonic steam flow in an LP steam turbine cascade, studying the effect of exit pressure variation on the two-phase flow of saturated vapor and fine water droplets. Subsequently, Dykas et al. (2015) organised experiments with steam condensing flow in the linear blade cascade in which the blade geometry corresponded to the last stage stator of a 200 MW steam turbine. They observed that the presence of the coarse water droplets behind the shock wave is probably caused by the water film separation on the blade suction side.

Along with 2D test cases, wet-steam flows with 3D steam turbines have been studied experimentally by many researchers. However, very few works have been published on 3D LP turbine experiments. Wróblewski et al. (2009a) performed experiments on 3D flows through the last two stages of the LP part of a 360 MW turbine. They measured distributions of pressure, temperature, the velocity flow angle in the inter-row gaps, and water droplet concentration and sizes. Later, Yamamoto et al. (2010) investigated the 3D two-stage stator-rotor cascade flow of an LP steam turbine model in dry-steam and wet-steam conditions. They measured the total and static pressures, and yaw angles of flow velocity vectors at the outlet of the first-stage rotor, second-stage stator, and second-stage rotor. Further, Cai et al. (2009, 2010a,b) conducted experiments of wet-steam flow in a 300 MW direct air-cooling steam turbine and obtained results on wetness, the size distribution of fine droplets, the yaw angle, the pitch angle, the Mach number, and velocity at different back pressures.

Eberle et al. (2013), Schatz and Eberle (2013) and Schatz et al. (2014) performed experiments on a three-stage model steam turbine which was scaled down to study the complex steam flow through the last stages of LP steam turbines. The scaling ratio of the last-stage blading of the test rig to the last-stage blade of the power plant was 1:4.2. They provided the measurements for the wetness and droplet size spectrum in last stage of the turbine using a light extinction method and analysed the effect of temperature variation on the droplet size and wetness fraction in an LP model steam turbine.

2.2 Theoretical studies

Along with experimental studies of condensing flows, extensive theoretical work has been performed. The theory development of spontaneous condensation of steam can be divided typically into two parts: (i) nucleation (which deals the formation of critically sized molecular clusters), and (ii) droplet growth (which is associated with the condensation of steam on formerly generated nuclei).

2.2.1 Nucleation theory

At the beginning of the nineteenth century, Laplace (1806) was the first who laid a foundation for the classical theory of nucleation by deriving the condition for the mechanical equilibrium of a surface separating two phases. Later on, Thomson (1870) (subsequently lord Kelvin) used the result of Laplace and derived the first theoretical expression recognising the existence of supersaturation in steam. He showed that the saturation vapour pressure over a curved surface of a liquid was higher than the saturation vapour pressure over a flat surface of the same liquid. Further, Helmholtz (1886) and Gibbs (1888) derived fundamental equations which govern the equilibrium of thermodynamic systems. Kelvin's equation was later coupled with these relationships, now widely known as the Kelvin-Helmholtz or Gibbs-Thomson equation defining the critical droplet radius for given vapour conditions.

The first step toward understanding the kinetics of phase change was taken by Gibbs (1906), who suggested that the stability of the existing phase can be measured by finding out what is needed to form a nucleus of the new phase within it. Following this work, Volmer and Weber (1926) instigated the development of nucleation theory and recognised that the metastability is related to the kinetics of the transition. They derived an expression for the nucleation rate by taking into account the rate of molecular collisions with the droplet surface and assuming that the probability of formation of nuclei was closely related to the formation energy of the nuclei. Subsequently, Farkas (1927) described the kinetic mechanism of supersaturated vapours and obtained an expression for the steady state nucleation rate. Based on this kinetic theory, many other investigators, such as Becker and Doring (1935), Zeldovich (1942) and Frenkel (1946), have contributed to the development of this theory, and the final outcome of their efforts is now known as 'the classical nucleation theory'. Steady state nucleation is unfeasible if the time taken to reach the steady state is not small compared to the characteristic time for the nucleation process. This issue was resolved by various researchers, such as Zeldovich (1942), Kantrowitz (1951), Courtney (1961), and Kaschiev (1969). A highly recommended explanation concentrating on the underlying physics of this theory is given by McDonald (1962, 1963).

However, the classical nucleation theory has some uncertainties, for example the usage of bulk liquid properties (like the surface tension and condensation coefficient) to illustrate tiny molecular clusters. To avoid these uncertainties, Bijl (1938), Band (1939), Frenkel

(1946), Reiss (1970), Dunning (1969) and Ford (1997) developed a statistical mechanical approach to nucleation theory which focused on the partition functions of clusters and how the concentrations of clusters were distributed based on cluster size. Several improvements to the basic classical nucleation theory were suggested. Some of the improvements were made to eliminate the theoretical inconsistencies of the classical theory, for example, the non-zero formation energy of a single vapour molecule (Girshick and Chiu (1990), Courtney (1961) and Blander and Katz (1972)). Another motivation for improvements was to incorporate physical phenomena which were ignored in the classical theory, like the contribution of the translational and rotational degrees of freedom to the free energy of the condensation clusters (Lothe and Pound (1962)). Resulting from the addition of these free energy terms in the expression of the liquid-drop model, nucleation rates were 10^{17} times greater than those predicted by classical theory. Often the improved theories estimated the nucleation rates well for some substances and conditions, but failed in other cases, just like the original classical theory. The classical theory is derived with the assumption of isothermal conditions. Therefore, some work has been performed on energy transfer in nucleation process. For example Kantrowitz (1951) noted that the droplet temperature did not remain constant during nucleation and derived a non-isothermal correction to the isothermal theory of nucleation. He obtained a correction factor which gives nucleation rates a factor of 90 below those of the liquid-drop model for typical conditions within an LP steam turbine. The classical nucleation theory is commonly used to model the condensation phenomena in LP steam turbines. Therefore, in the present work, the rate of nucleation of the homogeneous condensation has been simulated using the classical nucleation theory of McDonald (1962) with the non-isothermal correction factor of Kantrowitz (1951).

2.2.2 Droplet growth theory

The classical nucleation theory only defines the quantity of liquid droplets at a location in the vapour phase. During the nucleation process, the embryos are formed and grow in supercooled vapour by exchanging mass (vapour molecules) and energy (latent heat) with the vapour phase (Guha, 1995). Therefore, the process of droplet growth where liquid droplets gain molecules and become larger, is also very essential for wet-steam flow analysis. The growth rate of liquid droplets in the steam condensation process was first analysed by Hertz (1882) and Knudsen (1915). The growth process due to the wide range of the radii of the droplets depends on the Knudsen number Kn, which is a parameter to define different regimes of the droplet growth. The Knudsen number can be defined as $Kn = l_g/2r$, which is the ratio of the mean free path of vapour molecules to the droplet diameter. For large Knudsen numbers ($Kn > 1$), the free molecular regime, the growth is determined by kinetic theory. On the other hand, for small Knudsen numbers ($Kn < 1$), the continuum regime, the droplet growth is controlled by diffusion. During the growth process, the droplet diameter approaches and then exceeds the mean free path, $Kn = 1$, which is called the transition regime.

The droplet growth model has been provided by some researchers. For example, Gyarmathy

(1963) derived the growth rate for spherical droplets by heat conduction in which the droplet temperature was combined with a semi-empirical heat transfer coefficient. Further, Hill (1966) developed a growth law based on the kinetic theory by considering the droplet growth rate to be the difference between the impingement rate of the vapour molecules onto the surface of the droplet and the evaporation rate of the droplets. Subsequently, many other investigators, such as Wegener (1966), Konorski (1966), Bakhtar and Yousif (1974), Puzyrewski (1969), contributed to the development of droplet growth equations. Later on, Gyarmathy's droplet growth model was modified by Young (1982), who introduced the Prandtl number and additional calibration factors. He modeled steam condensation in supersonic nozzles in order to demonstrate the importance of the accuracy of the droplet growth theory in non-equilibrium condensing flow and obtained good agreement with experimental data of a low pressure nozzle using the modified droplet growth model. Later, Gyarmathy (1982) and Young (1993) developed a droplet growth model based on the flux matching method. In this method, the system is divided into three regions: a liquid phase and a continuum gas phase separated by a Knudsen layer having a width of the order of the mean free path of the molecules.

Along with the droplet growth model, the appropriate values of the condensation coefficient q_c (corresponding to the fraction of molecules impinging on the droplet that are incorporated into the droplet) and the evaporation coefficient q_e (the ratio of the actual evaporation rate to the theoretical evaporation rate in droplet growth theory) have been subject to debate. Many authors, for example Rideal (1925), Mozurkewich (1986), Beloded et al. (1989), Hagen et al. (1989), Marek and Straub (2001), Morita et al. (2004), and Tsuruta and Nagayama (2004), have suggested the value of q_c to range from 0.001 to 1. More details about the value of this coefficient are presented by Pathak et al. (2013). The values of q_c and q_e are generally taken as unity in order to simplify the analysis even though there is no satisfactory theoretical or experimental evidence which could suggest the values are true for non-equilibrium conditions (Young, 1982).

2.2.3 Theoretical developments

The first successful attempt to combine the nucleation and droplet growth theories with conservation equations for compressible flow was made by Oswatitsch (1942). He performed a step-by-step calculation of the pressure distribution in a nozzle with condensation, and his theoretical results were in good agreement with the measurements of Yellot (1934) and Binnie and Woods (1938). After Oswatitsch's work, other investigators such as Hill et al. (1963), Gyarmathy and Meyer (1965), Campbell and Bakhtar (1970) and Filippov et al. (1973) refined this theoretical treatment and compared it with measurements of CD nozzles in order to prove the correctness of their refinements to the theory.

The nucleation rate is very sensitive to the value of surface tension for small water clusters. Therefore, some works were also dedicated to analyse the influence of surface tension on nucleation phenomena. For example, theoretical works by Oriani and Sundquist (1963), Kirkwood and Buff (1949), Campbell and Bakhtar (1970) and Plummer and Hale (1972) investigated the correct value of the surface tension. The original theoretical method treated the vapour as a perfect gas, and thus, it was valid for comparatively low pressure. In order to increase agreement with experiments, Young (1973) and Bakhtar et al. (1975) counted the second virial coefficient in the equation of state for steam to enlarge the range of the theoretical development. Subsequently, Piran (1975) and Bakhtar and Piran (1979) investigated the equation of state for steam and proposed that the equation of state of Vukalovich (1958) with five virial coefficients was the most suitable for extrapolation into the meta-stable state of steam. Later on, Young (1988, 1992) described the equation of state for superheated and two-phase property calculations for a wide range of applications, and he presented the accuracy of the developed real gas models with large-scale equations.

Gyarmathy (1962) was the first, who performed the theoretical study of two-phase flow in a steam turbine. He demonstrated that the location of the Wilson point in a steam turbine and the resulting properties of the condensed fog depended primarily on the local pressure level and the expansion rate. After the successful development of a one-dimensional two-phase flow theory, some researchers conducted studies to develop the theoretical treatment in two dimensions. For example, Bakhtar and Tochai (1980) established a two-dimensional model for the two-phase flow of steam in a turbine cascade. This model was based on an inviscid time-marching scheme of Denton (1975) coupled with two-phase flow equations including nucleation and droplet growth theories. Bakhtar and Tochai (1980) observed important differences between nucleating and dry steam flows across the channel and at the trailing edge of the turbine cascade. Further, Moheban and Young (1984) have developed a treatment for two-phase flow calculation using an improved version of time-marching scheme of Denton (1983).

During the condensation process, the latent heat release causes such a strong compressive wave that a steady state operating position cannot be found. Therefore, in the late 1900s, some theoretical studies have been performed on unsteady phenomena due to heat addition in compressible flows. Barschdorff and Filippov (1970) investigated the pressure and density data, calculated shock positions in the nozzle, and derived simplified formula for calculating the frequency of oscillation in one-dimensional unsteady flows with condensation. Guha and Young (1991, 1994) developed an unsteady time-marching technique for any flow regime of wet-steam flows. They predicted frequencies of the unsteady oscillation of nozzle flows and studied the effect of temperature fluctuations on the homogeneous nucleation and growth of water droplets in multistage steam turbines. Subsequently, unsteady oscillating condensing flows have been examined by Schnerr (1989) and Winkler and Schnerr (2001).

Some studies have been reported on stationary shock wave stability for example by Blythe and Shih (1976), who established an asymptotic predictive method to describe the condensation phenomena in nozzle flows. Later on, this method was modified by Delale et al. (1993a,b), who provided a detailed structure of the condensation zones for both subcritical and supercritical flows in a nozzle. Young and Guha (1991) and Guha (1994) have discussed the structure of shock waves in vapour-droplet flows. Further, Delale et al. (2001) have investigated the stability limit of stationary normal shock waves in supercritical nozzle flows with homogeneous condensation.

There has also been progress in the development of theoretical studies and the extension of treatments for 2D non-equilibrium two-phase flows to 3D fields. Yeoh and Young (1984) developed a streamline curvature technique to determine the quasi 3D through-flow solution of steam. They investigated the non-equilibrium flow in the primary nucleating stage of an LP turbine and conducted a complete analysis of a six-stage turbine. In the late 1990s, a fully three-dimensional, viscous time-marching two-phase treatment along with nucleation and droplet growth equations was developed by Kosolapov and Liberson (1997), Gerber and Knill (1999) and Liberson and McCloskey (1999).

2.3 Numerical studies

A vast amount of literature exists on the topic of numerical modelling of condensing steam flows. However, this section mentions only some selected works. During the past several decades, extensive numerical studies have been carried out by many researchers on various aspects of steam condensing flow utilising different approaches in which the vapour phase has always been solved by the Eulerian method while the liquid phase has been treated either by the Lagrangian or the Eulerian method. Originally, wet-steam flows were modelled numerically with 1D flow in CD nozzles, as in the works of Barschdorff (1971) and Moore et al. (1973). Since the real flow behaviour in steam turbines is highly complex, subsequent studies have been dedicated to 2D flows in turbine cascades. For example, Bakhtar and Tochai (1980), Young (1992), White and Young (1993), and White et al. (1996) employed more advanced numerical models to handle the additional dimension. Moreover, their numerical methods were based on the inviscid time-marching scheme with a Lagrangian tracking module to track the particle motion explicitly.

Presently, the numerical study of condensing steam flows has been extended to 3D with finite-volume/finite-element Navier-Stokes (NS) equations, handling the interaction between the steam and liquid phases using interphase source terms. Gerber (2002) developed a numerical model based on the Eulerian-Lagrangian approach to simulate two-phase wet-steam flows, and the approach was validated with CD nozzle and turbine cascade experiments. In principle, a mixed Eulerian-Lagrangian approach encounters difficulties with particle tracking and is also computationally expensive for the 3D unsteady flow of an LP turbine. Subsequently, some studies have been conducted to develop fully Eulerian methods. For example, Gerber and Kermani (2004) presented an Eulerian-Eulerian method for non-equilibrium condensing steam flows, which was capable of simulating low and high pressure steam turbines. However, the condensation phenomena involve complex droplet spectra of polydispersed liquid droplets which cannot be modelled using an Eulerian-Eulerian method. Therefore, a Moment-based method was also developed for representing polydispersed droplet size distribution. This method was originally introduced by Hill (1966) for the study of steam condensation in nozzles. Some numerical studies, such as those by White and Hounslow (2000), White (2003) and Gerber and Mousavi (2006, 2007), utilised the method of moments and quadrature method of moments for the representation of polydispersed droplet distributions in the condensing steam flow. Due to immense improvement in the computational power of CFD calculations, in recent years some numerical studies have been attempted to model 3D wet-steam flow across LP turbines including multistage blade rows. For example, Yamamoto et al. (2007a), Yamamoto et al. (2007b) and Yamamoto et al. (2010), presented CFD studies of condensing steam flows through multistage stator rotor cascade channels in an LP steam turbine with non-equilibrium and equilibrium condensations. Starzmann et al. (2011) introduced numerical results for wet-steam flow with a three stage LP steam turbine test rig, in which the effect of different theoretical models for nucleation and droplet growth were examined. Further, Starzmann et al. (2013b) also studied the effect of droplet size on the deposition characteristics of the last stage stator blade and the effect of inter-phase friction on the flow field. More recently, Grübel et al. (2014) performed steady state numerical simulations of LP model steam turbine with three different simplified axisymmetric diffuser models, in which the results of part-load, design-load and over-load conditions were discussed.

Some works have also been dedicated to investigating the unsteadiness in condensing steam flows. The introductory numerical study of unsteady non-equilibrium wet-steam flow in a nozzle was performed by Saltanov and Tkalenko (1975), who obtained the characteristics of the oscillation modes. There were followed by Skillings and Jackson (1987), who calculated droplet size distributions in unsteady nucleating steam flows using a mixed Lagrangian/Eulerian time-marching method. White and Young (1993) presented the numerical results of 2D unsteady condensing steam flow in a nozzle using a time-accurate Euler solver for the first time, calculating the pressure distribution, droplet sizes and their oscillation frequency in nozzle flow. Mundinger (1994) presented an improved 2D numerical scheme for unsteady steam flow calculations for circular arc nozzles. The 2D effects in unsteady nozzle flows of water vapour/carrier gas mixtures have since been investigated by Schnerr et al. (1994), Adam (1996) and Schnerr (2005), who all observed different types of self-excited, condensation-induced oscillations which were dependent on the nozzle geometry. Unsteady wet-steam flow in a steam turbine has also been studied by Winkler and Schnerr (2001) and Senoo and White (2006), who predicted oblique shock waves due to condensation. However, in multistage steam turbines, unsteadiness mainly occurs due to the interaction between stator-rotor blade rows. Unsteady CFD simulations have been carried out by, for example, Bakhtar and Heaton (2005), Yamamoto et al. (2010), Miyake et al. (2012), and Starzmann et al. (2012), who presented the influence of stator-rotor interaction on the non-equilibrium wet-steam flow in steam turbines. Chandler et al. (2013) conducted a numerical study of unsteady multistage condensing flows using a five-stage model turbine.

Some numerical works have also been devoted to the development of numerical techniques for solving the condensing steam flow. Senoo and Shikano (2002) developed a third-order upwind total variation diminishing (TVD) scheme based on Roe's approximate Riemann solver for non-equilibrium wet-steam flow. Later on, this modified technique was utilised by Senoo and White (2006, 2012) to simulate inviscid wet-steam flow in a CD nozzle and in an LP steam turbine stator cascade. Halama et al. (2011) and

Halama and Fořt (2012) have implemented modern and less dissipative flux schemes, and predicted the two-phase flow of condensing steam in a nozzle and steam turbine. Some researchers, such as Wróblewski et al. (2009b), Dykas and Wróblewski (2011) and Dykas and Wróblewski (2013), have developed their in-house CFD code for modelling non-equilibrium wet-steam flow.

Despite the numerous studies that have been conducted with the condensing flows both in nozzles and in turbine cascades, only few have dealt with the influence of turbulence modelling on wet-steam flow prediction. For example, White (2000) presented a numerical method based on a simple stream function technique for the prediction of condensing steam flow in a CD nozzle, and analysed the influence of the viscous effect on condensation within compressible boundary layers. In addition, Simpson and White (2005) performed a numerical study with viscous and steady flow conditions in a CD nozzle and observed that the growth of the boundary layer has a significant impact on the predicted pressure distributions and droplet sizes. Avetissian et al. (2005) investigated the influence of the turbulence level and inlet wetness on the process of spontaneous condensation in Laval nozzles, utilising the moment method and the delta approximation method to determine the droplet size spectrum. The effects of flow turbulence and inlet moisture on the steady and unsteady spontaneously condensing transonic flows with flat and round nozzles have since been examined by Avetissian et al. (2008).

3 Physical models

The condensing flows can be referred to as two-phase gas-liquid flows, in which the gaseous or vapour phase is considered as a carrier phase while the condensed liquid droplets are treated as a dispersed phase within the carrier phase. The history of condensing steam flow modelling shows that these flows have been modelled by applying various CFD approaches in which the carrier steam phase is always treated as the continuum and the liquid droplet phase is tackled in different ways. Generally, the CFD approaches can be subdivided into three categories: the Eulerian-Lagrangian approach, the Eulerian-Eulerian approach and the method of moments. In the mixed Eulerian-Lagrangian approach, the conservation equations of mass, momentum, and energy of the carrier vapour phase are solved in an Eulerian frame of reference. The droplet phase is handled in the Lagrangian frame of reference and the trajectories of the individual liquid droplets are followed. Young (1992) and Gerber (2002) have described this approach in detail. On the other hand, in the Eulerian-Eulerian approach which is also known as the two-fluid approach, both phases are treated as interpenetrating continua (Gerber and Kermani, 2004; Dykas and Wróblewski, 2011). In this approach, the droplet distribution is represented in terms of a finite number of droplet sizes. The Eulerian-Eulerian approach does not need to consider fluid paths from one cell to the next, and hence the behaviour of the fluid from the cell from which it has emerged does not need to be known. The moment-based approach (Hill, 1966; White and Hounslow, 2000), accurately models the exchanges of heat and mass between vapour and liquid phases, but involves substantially less computation than discrete spectrum calculations since it models only the first few moments of size distribution. In the moment method, the droplet formation, growth and transport is defined by a finite number of moments of the droplet size distribution.

In this work, the Eulerian-Eulerian approach is used to model the mixture of vapour and liquid phases. This chapter describes the details of the ANSYS FLUENT and ANSYS CFX numerical methods. The governing equations, and nucleation and droplet growth models are presented. Then, the chapter discusses the superheated and subcooled steam in condensation processes modelled by real gas model and the flow turbulence solved by using two-equation turbulence models. Finally, information about near-wall treatment of turbulent flow and the grid convergence index (GCI) method are reported.

3.1 Governing equations of ANSYS FLUENT

In ANSYS FLUENT, the governing equations are solved as a mixture of vapour and liquid phases. The equation for the conservation of mass is expressed as below:

$$\frac{\partial \rho_m}{\partial t} + \frac{\partial}{\partial x_i}(\rho_m u_{iv}) = S_1, \tag{3.1}$$

where, ρ is the density, u is the velocity, and i is the Cartesian tensor notation. The source term S_1 represents the mass transfer due to the condensation process or evaporation on the already existing droplet. The conservation of momentum can be expressed as follows:

$$\frac{\partial}{\partial t}(\rho_m u_{iv}) + \frac{\partial}{\partial x_j}(\rho_m u_{iv} u_{j_v}) = -\frac{\partial P}{\partial x_i} + \frac{\partial \tau_{ij_m}}{\partial x_j} + S_2. \tag{3.2}$$

Here, P is the pressure, τ_{ij} is the stress tensor component, and S_2 is the momentum source term, which includes the momentum exchange between the liquid droplets and the surrounding vapour, and the smaller terms from the gradient of the Reynolds stress tensor. The conservation of energy is written as

$$\frac{\partial}{\partial t}(\rho_m H_m) + \frac{\partial}{\partial x_j}(\rho_m u_{j_v} H_m) = \frac{\partial P}{\partial t} + \frac{\partial}{\partial x_j}\left(\Gamma_E \frac{\partial T_m}{\partial x_j}\right) + \frac{\partial}{\partial x_j}(u_{iv}\tau_{ij_m}) + S_3, \tag{3.3}$$

where H represents the total enthalpy, T indicates the temperature and Γ_E refers to the effective thermal conductivity. The source term S_3 includes the interphase heat transfer. Along with these conservation equations, two additional transport equations for the liquid phase mass-fraction β, and the number of liquid droplets per unit volume η, were calculated and can be expressed as

$$\frac{\partial}{\partial t}(\rho_m \beta) + \frac{\partial}{\partial x_i}(\rho_m u_{iv} \beta) = \Gamma, \tag{3.4}$$

$$\frac{\partial}{\partial t}(\rho_m \eta) + \frac{\partial}{\partial x_i}(\rho_m u_{iv} \eta) = \rho_m \mathrm{I}, \tag{3.5}$$

respectively, where Γ is the mass generation rate per unit volume due to condensation and evaporation, and I is the nucleation rate. However, in the wet-steam model of ANSYS FLUENT, some assumptions have been made. The condensed liquid phase consists of a large number of tiny droplets whose radii are of the order of 1 µm or less. Therefore, it was assumed that the volume of the condensed liquid phase was infinitesimal. Moreover, due to the submicron sizes of condensed liquid droplets, the interactions between droplets were omitted, and the slip velocity between the liquid droplets and the vapour surrounding them was neglected.

3.2 Governing equations of ANSYS CFX

The mass conservation equations for vapour and liquid phases are written as follows, respectively:

$$\frac{\partial}{\partial t}(\rho_v \alpha_v) + \frac{\partial}{\partial x_j}(\rho_v \alpha_v u_{j_v}) = -\sum_{\mathrm{l=1}}^{\mathrm{n}} \mathrm{S_l} - \sum_{\mathrm{l=1}}^{\mathrm{n}} m^* \alpha_v \mathrm{I}, \tag{3.6}$$

$$\frac{\partial}{\partial t}(\rho_l \alpha_l) + \frac{\partial}{\partial x_j}(\rho_l \alpha_l u_{jl}) = \mathrm{S_l} + m^* \alpha_v \mathrm{I}. \tag{3.7}$$

In Eq. (3.6), the mass transfer of all n liquid phases is taken into account, while Eq. (3.7) only considers one of them. Here subscripts v and l represent the vapour and liquid phases, respectively. In both equations, α and source term $\mathrm{S_l}$ indicate the corresponding phase volume fraction and the mass transfer due to condensation or evaporation on an existing liquid droplet, respectively. Meanwhile, I and m^* stand for the nucleation rate and the mass of a nucleated droplet, respectively.

In ANSYS CFX, a separate equation was used to calculate droplet numbers which can be written as below:

$$\frac{\partial}{\partial t}(\rho_l \eta) + \frac{\partial}{\partial x_j}(\rho_l \eta u_{j_l}) = \rho_l \alpha_v \mathrm{I}. \tag{3.8}$$

The momentum equation was solved only for the vapour phase. However, if larger droplets are present in the flow, there exists a velocity difference between vapour and liquid droplets. Under such a condition, separate momentum transport equations are needed. The momentum equation of the vapour phase is based on the RANS equations which can be written as

$$\frac{\partial}{\partial t}(\rho_v \alpha_v u_{i_v}) + \frac{\partial}{\partial x_j}(\rho_v \alpha_v u_{i_v} u_{j_v}) = -\alpha_v \frac{\partial P}{\partial x_i} + \frac{\partial}{\partial x_j}(\alpha_v \tau_{ij_v}) + \mathrm{S_{F,m}}. \tag{3.9}$$

The source term $\mathrm{S_{F,m}}$ contains all of the terms from the gradient of the Reynolds stress tensor and the interfacial momentum transfer terms. The energy conservation equation for the vapour phase is written as

$$\begin{aligned}\frac{\partial}{\partial t}(\rho_v \alpha_v H_v) + \frac{\partial}{\partial x_j}(\rho_v \alpha_v u_{j_v} H_v) = -\alpha_v \frac{\partial P}{\partial t} + \frac{\partial}{\partial x_j}\left(\alpha_v \Gamma_E \frac{\partial T_v}{\partial x_j}\right) \\ + \frac{\partial}{\partial x_j}(\alpha_v u_{i_v} \tau_{ij_v}) + \mathrm{S_{e1}} + \mathrm{S_{e2}}.\end{aligned} \tag{3.10}$$

Here, source terms $\mathrm{S_{e1}}$ and $\mathrm{S_{e2}}$ represent the total viscous stress energy contribution and the contribution to the energy transport owing to the interphase heat transfer, respectively. The mentioned source terms of the conservation equation have been discussed in further detail by Gerber and Kermani (2004).

3.3 Nucleation and droplet growth model

The phase change phenomenon regarding to the condensing steam flow involves two main processes: nucleation and droplet growth. In both CFD codes, the nucleation rate (i.e. the formation of liquid droplet nuclei due to the homogeneous condensation per unit mass of the mixture) was obtained from the classical theory of non-isothermal homogeneous condensation by McDonald (1962). The nucleation rate can be written as below:

$$\mathrm{I} = \frac{q_c}{(1+\theta)} \left(\frac{\rho_v^2}{\rho_l}\right) \sqrt{\frac{2\sigma}{M_m^3 \pi}} e^{-\left(\frac{4\pi r_*^2 \sigma}{3K_b T_v}\right)}. \tag{3.11}$$

Here, q_c is a condensation coefficient which is generally considered as unity, K_b is the Boltzmann constant, M_m is the molecular mass of water, and θ is the non-isothermal correction factor. The formulation of θ has been adopted from Kantrowitz (1951):

$$\theta = \frac{2(\gamma - 1)}{\gamma + 1}\left(\frac{h_{lv}}{RT_v}\right)\left(\frac{h_{lv}}{RT_v} - 0.5\right), \tag{3.12}$$

where γ represents the ratio of specific heat capacities, R displays the gas constant and h_{lv} indicates the specific enthalpy of evaporation at pressure P. Some authors have been included a calibration coefficient in the exponent in the nucleation rate formulation to calibrate the nucleation rate e.g. Grübel et al. (2014). However, in this work, all the simulations have been performed without any calibration factor in the nucleation rate equation.

In the case of ANSYS FLUENT, Γ was obtained from the addition of mass increase due to nucleation and due to the growth/demise of liquid droplets. The expression of Γ was adopted from Ishizaka et al. (1995) and is written as

$$\Gamma = \frac{4}{3}\pi\rho_l \mathrm{I} r_*^3 + 4\pi\rho_l\eta\bar{r}^2\frac{\partial\bar{r}}{\partial t}. \tag{3.13}$$

Here, $\bar{r}$ represents the average radius of the liquid droplet while r_* demonstrates the Kelvin-Helmholtz critical droplet radius. If the radius of the droplet is larger than r_*, the droplet will grow, otherwise the droplet evaporates. The critical droplet radius was estimated from the following expression:

$$r_* = \frac{2\sigma}{\rho_l R T_v ln S}, \tag{3.14}$$

where S is the supersaturation ratio which is defined by the ratio of vapour pressure to the equilibrium saturation pressure as

$$S = \frac{P}{P_{sat}(T_v)}. \tag{3.15}$$

Condensing steam flow involves two mechanisms. The first one is associated with the transfer of mass from the vapour phase to the liquid droplets, and the second one corresponds to the transfer of heat from the generated droplets to the vapour phase in the form of latent heat (Ishizaka et al., 1995). As described previously, after the droplet formation, condensation only happens because of droplet growth. The subcooling of the vapour phase decreases rapidly because of released latent heat during the growth process. Hence, nucleation no longer takes place. The growth rate of a droplet strongly depends on the rate at which heat is conducted away from the droplet (Young, 1982).

In ANSYS FLUENT, the droplet growth rate is determined by the heat transfer conditions surrounding the droplet (Hill, 1966). The equation of the droplet growth model is written as

$$\frac{\partial \bar{r}}{\partial t} = \frac{P}{h_{lv}\rho_l\sqrt{2\pi RT_v}}\frac{\gamma+1}{2\gamma}C_p(T_l - T_v). \tag{3.16}$$

Here, T_l is the droplet temperature, and more details about to the droplet temperature calculation have been presented by Young (1982).

In the case of ANSYS CFX, the droplet growth rate equation of Gyarmathy (1976) is used and can be expressed as

$$\frac{dr}{dt} = \frac{k_v}{r(1+cK_n)} \cdot \frac{(T_l - T_v)}{(h_v - h_l)\rho_l}, \tag{3.17}$$

where K_n is the Knudsen number, c is the constant value, r is the droplet radius, and k_v is the vapour phase thermal conductivity. Gerber and Kermani (2004) have discussed the droplet growth rate in further detail. Further, the temperature of submicron liquid droplets can be estimated from the subcooling of the steam ($\Delta T = T_s(p) - T_v$) using the following expression (Gyarmathy, 1962):

$$T_l = T_s(p) - \Delta T\left(\frac{r^*}{r}\right), \tag{3.18}$$

where, T_s is the saturation temperature.

3.4 Real gas properties

Accurate modelling of condensing steam flow requires the thermodynamic properties of vapour in the superheated region, at the saturated line and in the wet-steam region because nucleation and growth processes in these non-equilibrium condensing steam flows are quite sensitive to the thermodynamic properties. The equation of state (EOS) and the thermodynamic properties for the superheated region were based on the formulations of Young (1988). The equation of state for the vapour phase utilises a virial form with temperature and density as the independent variables and can be written as

$$P_v = \rho_v \mathrm{R} T_v(1 + B\rho_v + C\rho_v^2). \tag{3.19}$$

Here, B and C are the second and third virial coefficients formulated as empirical functions of temperature and are presented as

$$B = a_1\left(1 + \frac{T_v}{\alpha}\right)^{-1} + a_2 e^{\tau}\left(1 - \frac{1}{e^{\tau}}\right)^{5/2}\tau^{-1/2} + a_3\tau, \tag{3.20}$$

$$C = a(\tau - \tau_0)e^{-\alpha\tau} + b. \tag{3.21}$$

In Eq. (3.20), $\tau = \frac{1500}{T_v}$, $\alpha = 10000$, $a_1 = 0.0015$, $a_2 = -0.000942$ and $a_3 = -0.0004882$. In contrast in Eq. (3.21), $\tau = \frac{T_v}{647.286}$, $\tau_0 = 0.8978$, $\alpha = 11.16$, $a = 1.772$ and $b = 1.5\times10^{-6}$.

Moreover, both virial coefficients cover the temperature range approximately from 273 to $1000\,\mathrm{K}$. Young (1988) provides more information on the applicability range and corresponding accuracy of real gas formulations. Furthermore, in ANSYS FLUENT, the formulations of conservation equations were based on the mixture properties of vapour and liquid phases. The mixture properties were estimated from the following correlations:

$$\begin{aligned}
h_m &= h_l\beta + (1-\beta)h_v \\
s_m &= s_l\beta + (1-\beta)s_v \\
C_{p_m} &= C_{p_l}\beta + (1-\beta)C_{p_v} \\
C_{vm} &= C_{vl}\beta + (1-\beta)C_{vv} \\
\mu_m &= \mu_l\beta + (1-\beta)\mu_v \\
Kt_m &= Kt_l\beta + (1-\beta)Kt_v.
\end{aligned} \tag{3.22}$$

Here, h is the specific enthalpy, s is the entropy, C_p is the specific heat at a constant pressure, C_v is the specific heat at a constant volume, μ is the dynamic viscosity and Kt is the thermal conductivity.

To analyse the effect of real gas on steam condensing flow, the local EOS was formulated in this work. The form of the local real gas EOS can be expressed as follows:

$$P_v = RT_v(\rho_v A(T_v) + B(T_v)\rho_v^2). \tag{3.23}$$

Here, A and B represent the first and second virial coefficients, respectively. Their values were obtained from the polynomial function of temperature as follows:

$$A(T_v) = a_0 + a_1T_v + a_2T_v^2, \tag{3.24}$$

$$B(T_v) = b_0 + b_1T_v + b_2T_v^2. \tag{3.25}$$

The coefficients a_i, b_i $(i = 0, 1, 2)$ were approximated employing regression analysis using IAPWS-IF97 formulas. Other thermodynamic properties were estimated from the fourth order polynomial of temperature T and density ρ, as below:

$$\begin{aligned}
\phi_v(T,\rho) = {} & a_1 + a_2T + a_3\rho + a_4T^2 + a_5T\rho + a_6\rho^2 + a_7T^3 + a_8T^2\rho + a_9T\rho^2 \\
& + a_{10}\rho^3 + a_{11}T^4 + a_{12}T^3\rho + a_{13}T^2\rho^2 + a_{14}T\rho^3 + a_{15}\rho^4.
\end{aligned} \tag{3.26}$$

Here, ϕ_v indicates C_{p_v}, C_{vv}, h_v, S_v, μ_v and K_{tv}. In Eq. 3.26, the coefficients a_i $(i = 1, 2, 3, ..., 15)$ were evaluated using multivariable non-linear regression applying the non-linear least square fitting method. The real gas EOS and other formulations of steam properties were applicable in the limited range of pressure (i.e. 1 to $70\,\mathrm{kPa}$) and temperature (i.e. 273.15 to $500\,\mathrm{K}$). The thermodynamic properties approximated with the author's local real gas EOS were compared to IAPWS-IF97, and an error estimation was calculated for each property. The errors in thermodynamic properties compared to the IAPWS-IF97 are presented in Figure 3.1. The figure illustrates that the average errors for the estimated P_v, ρ_v, h_v, Kt_v and μ_v are less than ± 0.03% compared to IAPWS-IF97, while the corresponding errors in C_{p_v}, C_{v_v} and S_v are less than ± 0.5%. The above-mentioned local EOS for real gas and other thermodynamic properties for superheated steam have been implemented by the author into the CFD code via user defined subroutines.

The saturated pressure and temperature were estimated based on the work of Reynolds (1979). At the saturated liquid line, the values of ρ_l and σ_l were acquired from Reynolds (1979) and Young (1982), respectively, while other thermodynamic properties, e.g. C_{p_l}, μ_l and Kt_l at the saturated liquid line, were calculated according to the work of Eckert and Drake (1972).

In ANSYS CFX, the real gas properties were evaluated from the IAPWS-IF97 formulation. The ANSYS CFX works on a lookup table approach which requires the definition of the minimum and maximum values of temperature and pressure, and the maximum number of integration points within the range in question. Based on this, the solver defines a lookup table of all required thermodynamic properties of vapour and water for the specified range of temperatures and pressures that will be encountered in each iteration. More details about the IAPWS-IF97 formulation have been presented by Wagner and Kruse (1998).

3.5 Turbulence modelling

Turbulent flows are characterised by velocity fields which fluctuate rapidly both in space and time. These fluctuations appear on a small scale and at a high frequency, and therefore, direct CFD simulations of these flows require enormous computational power and time. The alternative is to apply a time-averaging and ensemble-averaging on flow equations to neglect small scales. The resulting averaged modified set of equations is computationally less expensive to solve. However, after the averaging process, the averaged governing equations include additional unknown terms of Reynolds stress and fluxes. Therefore, the turbulence models are required to evaluate these additional variables.

In an LP steam turbine, more than 90% of the total mass concentration of the liquid phase consists of a very large number of very fine submicron droplets (Guha, 1995). Therefore, it could be assumed that the droplets have no direct influence on the flow turbulence, and in this work, the direct influence of the condensed liquid droplets on the vapour phase turbulence was not investigated. However, there exist an indirect influence through the velocity field introduced to the turbulence models. The turbulence in the vapour phase influences the dispersion of the liquid droplets. In the present work, Reynolds-averaged two-equation turbulence models were employed for modelling the flow turbulence. Due to the relatively small mass concentrations and sizes of the droplets, the turbulence equations

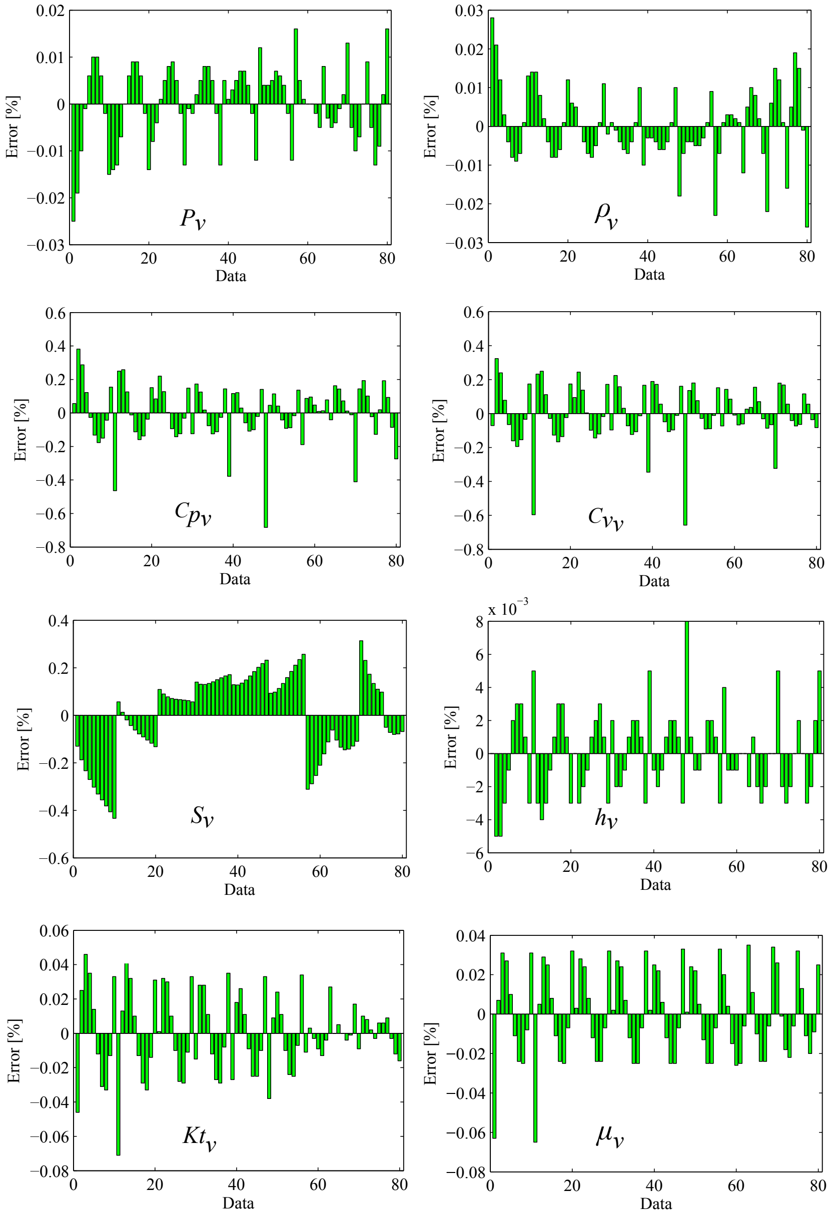

Figure 3.1: Estimated errors of thermodynamic properties based on the IAPWS-IF97.

were solved for the mixture of the vapour and liquid phases. The performance of various turbulence models, namely the Spalart-Allmaras, the standard k-ε, the renormalisation group (RNG) k-ε, the realizable k-ε, the k-ω and the shear stress transport (SST) k-ω

models for wet-steam flow modeling have been studied. The influence of turbulence modelling on condensing steam flow has been assessed. For these purposes, the standard k-ε and the SST k-ω turbulence models have been modified.

3.5.1 The standard k-ε turbulence model

The standard k-ε turbulence model proposed by Launder and Spalding (1974) was utilised in this work. It is a semi-empirical model based on two transport equations for the turbulence kinetic energy k and the dissipation rate ε. The equations of k and ε in ANSYS FLUENT can be written as

$$\begin{aligned}\frac{\partial}{\partial t}(\rho_m k) + \frac{\partial}{\partial x_i}(\rho_m u_{iv} k) = \frac{\partial}{\partial x_j}\left[\left(\mu_m + \frac{\mu_{t_m}}{\sigma_k}\right)\frac{\partial k}{\partial x_j}\right] + G_k + G_b \\ -\rho_m \varepsilon - Y_M + S_k,\end{aligned} \tag{3.27}$$

$$\begin{aligned}\frac{\partial}{\partial t}(\rho_m \varepsilon) + \frac{\partial}{\partial x_i}(\rho_m u_{iv} \varepsilon) = \frac{\partial}{\partial x_j}\left[\left(\mu_m + \frac{\mu_{t_m}}{\sigma_\varepsilon}\right)\frac{\partial \varepsilon}{\partial x_j}\right] + \frac{\varepsilon}{k}(C_{1\varepsilon} G_k - C_{2\varepsilon}\rho_m \varepsilon \\ + C_{1\varepsilon} C_{3\varepsilon} G_b) + S_\varepsilon,\end{aligned} \tag{3.28}$$

where σ_k and σ_ε are the turbulent Prandtl numbers for k and ε, respectively. Here, G_k and G_b represent the production of turbulence kinetic energy due to the mean velocity gradients and buoyancy, respectively. The contribution of the fluctuating dilatation in compressible turbulence to the overall dissipation rate is described by Y_M. S_k and S_ε represent the source terms of turbulent equations. The production term G_k is balanced by the interaction of the Reynolds stresses and mean velocity gradient, and can be represented as

$$G_k = -\rho_m \overline{u'_{iv} u'_{j_v}} \frac{\partial u_{j_v}}{\partial x_i}. \tag{3.29}$$

The turbulent viscosity μ_{t_m} is related to the value of k and ε which can be defined as

$$\mu_{t_m} = \rho_m C_\mu \frac{k^2}{\varepsilon}. \tag{3.30}$$

The model constants were considered as σ_k= 1.0, σ_ε = 1.3, $C_{1\varepsilon}$ = 1.44, $C_{2\varepsilon}$ = 1.92, and C_μ = 0.09 (Launder and Spalding, 1974).

The applicability of the k-ε turbulence model has been proven in various flow phenomena. However, there are still some limitations to its relevance: for example, flows with large velocity gradients, strong contraction or expansion, surface curvature, rotational effects such as swirl or separated flows, and transition. In LP turbine flows, the above-mentioned phenomena are present. Therefore, solving non-equilibrium homogeneous condensing steam flows of an LP turbine may require some modifications to the k-ε turbulence model.

In the present work, the k-ε turbulence model has been modified based on the work of

Avetissian et al. (2005, 2008), in which the modulation of turbulence kinetic energy due to liquid droplets has been introduced through source terms. The effect of liquid droplets in the flow introduces additional turbulent kinetic energy and its dissipation to the flow via the acceleration/deceleration of the droplets. These modifications directly influence on turbulent viscosity and Reynolds stresses. Hence, the momentum and energy transport equations will be affected. Additionally, the turbulent viscosity was modified by means of an expansion procedure for resolving implicit algebraic equations for the Reynolds stress tensor in terms of mean velocity gradients (Speziale, 1987; Gatski and Speziale, 1993). The modified term of turbulent viscosity, including the turbulence production to dissipation ratio, is expressed as

$$\mu_{t_m} = \frac{\rho_m C_\mu}{1 + (G_k/\varepsilon - 1)/C_1} \frac{k^2}{\varepsilon}, \tag{3.31}$$

where C_1 is the Rotta return-to-isentropy approximation of the pressure-strain correlation (Lumley, 1980).

The source term of the transport equation of k represents the addition of turbulent kinetic energy including the effect of liquid mass generation and the droplet response time. The source term S_k in Eq. (3.27) can be expressed as

$$S_k = \frac{4\mathrm{M}}{\tau_p}(1 - f_u)k. \tag{3.32}$$

Here, M is the liquid mass and τ_p is the droplet response time. The response time of a droplet to changes in the flow velocity or flow temperature is important in establishing non-dimensional parameters to characterise the flow, which relates to the time required for a liquid droplet to respond to a change in velocity. The following expression of τ_p was used:

$$\tau_p = \frac{2\bar{r}^2 \rho_l}{9\mu_v}. \tag{3.33}$$

In Eq. (3.32), f_u is the coefficient of the droplet response to fluid velocity fluctuations. The expression of f_u was adopted from Zaichik et al. (2003) and can be written as

$$f_u = \frac{2\left(\frac{\tau_p}{T_L}\right) + \left(\frac{\tau_T}{T_L}\right)^2}{2\left(\frac{\tau_p}{T_L}\right) + 2\left(\frac{\tau_p}{T_L}\right)^2 + \left(\frac{\tau_T}{T_L}\right)^2}, \tag{3.34}$$

where T_L is the Lagrangian integral time microscale of fluctuations of velocity which was calculated from the ratio of turbulent kinetic energy to the dissipation rate. T_L can be defined as below:

$$T_L = C_\mu^{\frac{1}{2}} \frac{k}{\varepsilon}. \tag{3.35}$$

In Eq. (3.34), τ_T is the Taylor time microscale of velocity fluctuations which characterises the time of interaction of particles in small-scale turbulent motion. The definition of τ_T

can be presented as

$$\tau_T = \left(\frac{2Re_\lambda}{15^{\frac{1}{2}}a_0}\right)^{\frac{1}{2}}\left(\frac{\mu_m}{\rho_m\varepsilon}\right)^{\frac{1}{2}}, \tag{3.36}$$

where Re_λ indicates the turbulence Reynolds number based on the Taylor microscale and can be determined as

$$Re_\lambda = \left(\frac{20k^2\rho_m}{3\varepsilon\mu_m}\right)^{\frac{1}{2}}. \tag{3.37}$$

The source term of the ε equation represents the modulation of turbulent dissipation via liquid droplets. The source term S_ε in Eq. (3.28) is presented as below:

$$S_\varepsilon = C_{2\varepsilon}\frac{\varepsilon}{k}S_k. \tag{3.38}$$

The above-mentioned modifications in the standard k-ε turbulence model (from Eqs. 3.31-3.38) were implemented by the author within the CFD code using user defined subroutines.

3.5.2 The SST k-ω turbulence model

The SST k-ω turbulence model was developed by Menter (1994) to effectively blend the robust and accurate formulation of the k-ω model in the boundary-layer region with the free-stream independence of the k-ε model in the free shear layer region. In ANSYS FLUENT, the following governing transport equations for k and its specific rate of dissipation ω were used:

$$\frac{\partial}{\partial t}(\rho_m k) + \frac{\partial}{\partial x_i}(\rho_m u_{i_v} k) = \frac{\partial}{\partial x_j}\left[\left(\mu_m + \frac{\mu_{t_m}}{\sigma_k}\right)\frac{\partial k}{\partial x_j}\right] + \tilde{G_k} - Y_k + S_k, \tag{3.39}$$

$$\frac{\partial}{\partial t}(\rho_m \omega) + \frac{\partial}{\partial x_i}(\rho_m u_{i_v} \omega) = \frac{\partial}{\partial x_j}\left[\left(\mu_m + \frac{\mu_{t_m}}{\sigma_\omega}\right)\frac{\partial \omega}{\partial x_j}\right] + G_\omega - Y_\omega + D_\omega + S_\omega. \tag{3.40}$$

Here, Y_k and Y_ω denote the dissipation of k and ω due to turbulence, respectively and D_ω is the cross-diffusion term. S_k and S_ω represent the source terms, and $\tilde{G_k}$ and G_ω display the generation of turbulence kinetic energy and its specific dissipation rate due to mean velocity gradients, respectively. The production term $\tilde{G_k}$ can be defined as below:

$$\tilde{G_k} = \min(G_k, 10\rho_m\beta^* k\omega), \tag{3.41}$$

where G_k utilises the same expression as described above in Eq. (3.29). Here, β^* indicates the model constant and μ_{t_m} is defined in the SST k-ω turbulence model as

$$\mu_{t_m} = \frac{\rho_m k}{\omega}\frac{1}{max\left[\frac{1}{\alpha^*}, \frac{S_1 F_2}{\alpha_1 \omega}\right]}. \tag{3.42}$$

Here, S_1 is the strain rate magnitude, F_2 is the blending function, α^* is the damping coefficient, and α_1 is the model constant. Additional details concerning to the closure coefficients, model constants, and auxiliary relations can be found in the work of Menter (1994).

In this work, the SST k-ω turbulence model was also modified in the same manner as the k-ε turbulence model. In the SST k-ω turbulence model, the modified turbulent viscosity term was included. Moreover, the source terms for the k and ω equations were included in both of the turbulence equations. The modified definition of μ_{t_m} for the SST k-ω turbulence model can be expressed as

$$\mu_{t_m} = \frac{\rho_m k}{\omega} \frac{1}{max\left[\frac{1}{\alpha^*}\frac{S_1 F_2}{\alpha_1 \omega}\right]} \frac{C_1}{C_1 + \left[\frac{\tilde{G_k}}{\omega \beta^* k} - 1\right]}. \tag{3.43}$$

The expression of modified turbulent viscosity consists of the additional multiplier term, which includes the turbulence production to dissipation ratio and the Rotta constant C_1 as does the modified turbulent viscosity term of k-ε turbulence model.

The source term S_k of the k equation of the modified SST k-ω turbulence model is of the same form as S_k in the modified k-ε turbulence model which is presented in Eq. (3.32). The source term S_ω of the ω equation of the modified SST k-ω turbulence model can be written as

$$S_\omega = C_{2\varepsilon} \omega \beta^* S_k. \tag{3.44}$$

Only the SST k-ω turbulence model and its modified version were utilised in ANSYS CFX. ANSYS CFX uses the same form of the SST k-ω turbulence model as ANSYS FLUENT. Therefore, the transport equations of the k and ω of turbulence model of ANSYS CFX are not listed here. Further details about turbulence models can be found from the ANSYS CFX theory manual (ANSYS Inc., 2014b). The modifications in the SST k-ω turbulence model have been implemented by the author within both the CFD codes using user defined subroutines.

3.5.3 Near-wall treatment

A near-wall region of the flow field is the most challenging and essential part in capturing the accurate flow properties in a numerical investigation. Particularly, the CFD modelling of turbomachinery flows involving the turbulence effect is significantly influenced by the presence of walls, due to the existence of large gradients in the flow variables in the near-wall regions. Further, the viscous effect on the momentum and other scalar transport processes is considerably high near the walls. Hence, an accurate prediction of turbomachinery flows requires a correct representation of the flow in the near-wall regions.

Experiments and mathematical analysis have shown that the turbulent boundary layer region near to the wall surfaces can be subdivided into three layers as shown in Fig. 3.2. In Fig. 3.2, δ presents the turbulent boundary layer thickness and y^+ indicates a non-

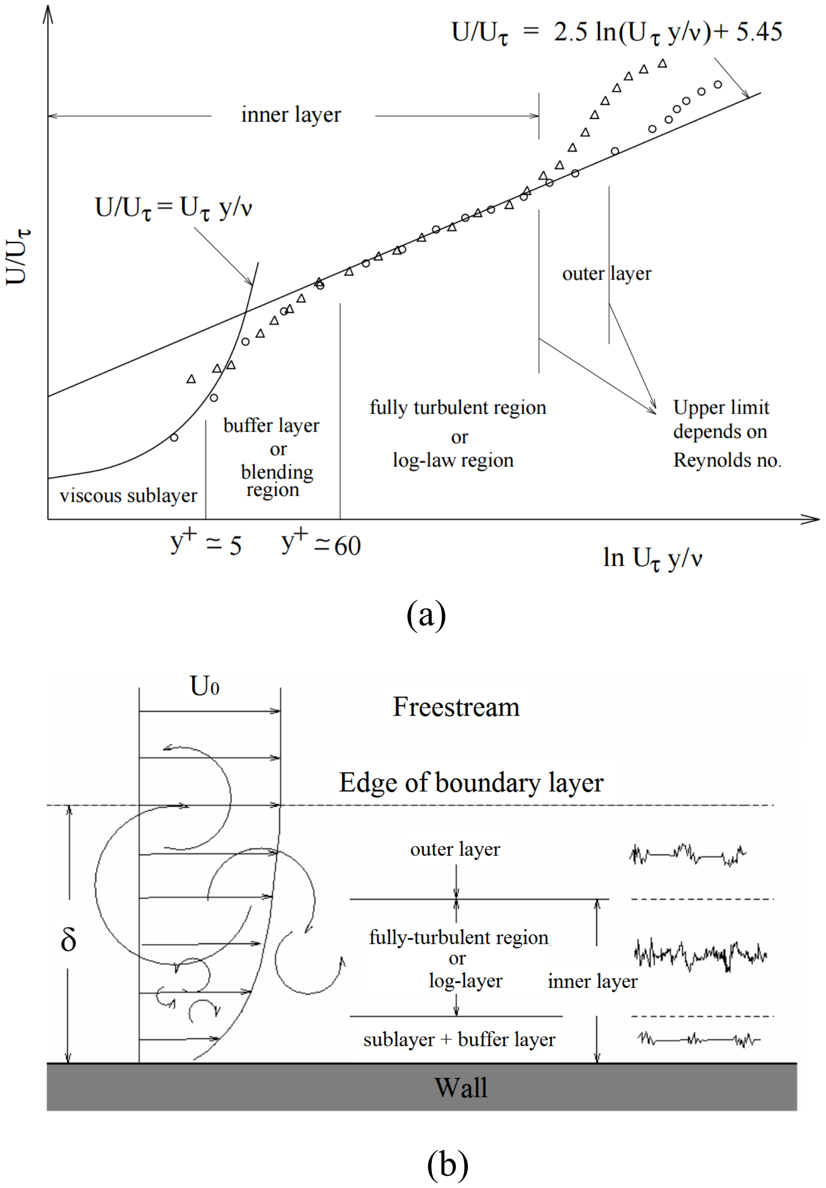
U/U_τ = 2.5 ln(U_τ y/ν)+ 5.45
inner layer
U/U_τ = U_τ y/ν
U/U_τ
outer layer
fully turbulent region
or
log-law region
Upper limit
depends on
Reynolds no.
buffer layer
or
blending
region
viscous sublayer
y+ ≃ 5
y+ ≃ 60
ln U_τ y/ν
(a)
U0
Freestream
Edge of boundary layer
outer layer
δ
fully-turbulent region
or
log-layer
inner layer
sublayer + buffer layer
Wall
(b)

Figure 3.2: Turbulent boundary layer region near to wall surface (Bakker, 2012).

dimensional wall distance, which can be defined as below:

$$y^{+} = \frac{y \upsilon_{\tau} \rho_{m}}{\mu_{m}}, \tag{3.45}$$

where y is the normal distance from the wall, and υ_τ is the friction velocity which can be calculated from the wall shear stress τ_w and the fluid density ρ_m, as below:

$$\upsilon_\tau = \sqrt{\frac{\tau_w}{\rho_m}}. \tag{3.46}$$

The first layer from the wall surface is called the inner layer or sublayer where viscous shear dominates. This layer is more specifically categorised into a viscous sublayer, buffer layer and fully-turbulent region or log-layer. In the inner-most layer, i.e. the viscous sublayer $(0 < y^+ < 5)$, the fluid very close to the wall is dominated by viscous shear in the absence of the turbulent shear stress effects. In this layer, viscosity plays a dominant role in momentum, heat and mass transfer. The fully-turbulent region $(y^+ > 60)$ exists at some distance from the wall and outside the viscous sub-layer, in which turbulence governs the mixing process. Within this inner region, the shear stress is assumed to be constant and equal to the wall shear stress and to vary gradually depending on the distance from the wall. There is a region between the viscous sublayer and the fully-turbulent region called the buffer layer $(5 < y^+ < 60)$, in which the viscous and turbulent effects are of equal importance. The second layer is referred to as an outer layer or defect layer, in which the large scale turbulent eddy shear dominates the flow phenomena.

There are two different approaches to modelling the flow in the near-wall region: a wall functions and a low-Reynolds number (LRN) model. In the wall functions model (semi-empirical approach), the viscous sublayer and buffer layer (viscosity-affected inner region) are not resolved. It is used to bridge the inner region between the wall and the fully turbulent region. The LRN model resolves the viscous sublayer and buffer layer by using a very small mesh near the wall. The values of y^+ close to the lower bound $y^+ = 30$ are most desirable for wall functions, whereas $y^+ \simeq 1$ are most desirable for near-wall modelling.

In ANSYS FLUENT, the simulations were performed by using the standard wall functions (SWF) and the enhanced wall treatment (EWT). Originally, SWF was presented by Launder and Spalding (1974) with the assumption of equilibrium between the production and the dissipation of turbulent kinetic energy. SWF is made of the momentum equation which leads to the law of the wall for the temperature and depends on the dimensionless velocity y^*. EWT blends the linear and logarithmic laws of the wall and provides a smooth transition between the log-law and the viscous sub-layer. However, to resolve the viscous layer, a sufficiently fine mesh is required near the wall boundaries.

In ANSYS CFX simulations, an automatic near-wall treatment was used. This treatment automatically switches from the wall functions approach to the low-Reynolds formulation as the grid is refined.

3.6 Grid convergence index

In CFD, the discretisation error is categorised as an acknowledged error. The discretisation errors refer to variation between the exact solution to the discrete equations on a spatial domain i.e. computational mesh/grid and time, and the exact analytical solution to the Partial Differential Equations (PDEs) of flow governing equations and other models. When a computational mesh is refined to a certain level, the flow solution should become less sensitive to the grid spacing, which can be defined as grid convergence. The percentage of the discretisation error depends on the grid quality. During the grid generation phase, the importance has been given to the appropriate selection of computational grid density and its resolution, aspect ratio, orthogonality, stretching, grid singularities and zonal boundary interfaces. If the grid density in computational domain is not sufficient than it could influence on the prediction of flow structures, such as the boundary layers, the von Karman vortex street, secondary flows, shock intensity and location (Montomoli et al., 2015). However, at preliminary run, it is often difficult to select precise grid density in computational domain. Therefore, the analysis of computational grid influence on numerical solutions should be considered as the first step to CFD simulation. To examine the influence of the grid on numerical solution, Roache (1994, 1997, 1998) and Celik (1993) proposed a methodology. In this dissertation, the errors resulting from the number of grid points are discussed. The influence of grid refinement on the CFD results was studied using the GCI proposed by Celik et al. (2008). The method is based on the Richardson extrapolation technique by Richardson and Gaunt (1927), in which multiple numerical solutions are calculated by adjusting a parameter (grid size) and are used then to extrapolate a more accurate solution. The grid convergence was evaluated using a relative error measure of different flow parameters between the grids as below:

$$e_a^{ij} = \left| \frac{\phi_i - \phi_j}{\phi_j} \right|, \tag{3.47}$$

where ϕ_i and ϕ_j are the selected flow parameters simulated by the *i*th and *j*th grids, respectively. An extrapolated relative error was calculated from the extrapolated value and the flow parameter as follows:

$$e_{ext}^{ij} = \left| \frac{\phi_{ext}^{ij} - \phi_i}{\phi_{ext}^{ij}} \right|, \tag{3.48}$$

where ϕ_{ext}^{ij} indicates the extrapolated value which can be estimated as

$$\phi_{ext}^{ij} = \frac{r_{ij}^p \phi_j - \phi_i}{r_{ij}^p - 1}. \tag{3.49}$$

Here, r indicates the grid refinement factor and p is the order of the discretisation method. The associated r-value has been obtained from the corresponding grid sizes of the selected grids and was calculated as follows:

$$r_{ij} = \left(\frac{h_i}{h_j}\right)^{\frac{1}{2}}, \tag{3.50}$$

where h_i and h_j are the representative grid sizes of the *i*th and *j*th grids, respectively. The representative grid size can be estimated from following expression:

$$h = \frac{1}{N}\sum_{m=1}^{N}(\Delta A_m). \tag{3.51}$$

Here, ΔA_m represents the area of the *m*th cell, and N refers to the total number of cells of the corresponding grid. The GCI provides a uniform measure of convergence for grid refinement studies (Roache, 1994). The GCI value can be achieved as below:

$$GCI^{ij} = F_s \frac{e_a^{ij}}{r^p - 1}, \tag{3.52}$$

where F_s is the safety factor 1.25. The value of the safety factor has been chosen based on the experiences obtained by applying GCI to many situations (Roache, 1994).

4 CFD calculation models

4.1 Geometrical details of selected calculation models and grid generation.

Throughout this work, various CD nozzles have been simulated for different validation purposes. The condensing flow in a transonic stator turbine cascade is simulated in this work as well. Further, the 3D stator-rotor stage of an LP turbine has been modelled: it is not a real LP turbine stage, but the model mimics the flow conditions which occur in a real LP turbine stage. This chapter contains details of the geometry, operating conditions and grid generation in the computational domain of selected cases.

4.1.1 CD nozzle cases

4.1.1.1 Moore nozzles

The experiments of Moore et al. (1973) were based on a series of nozzles. In their measurements, different nozzles were formulated with upper and lower walls between parallel perspex side walls, the nozzle walls being positioned by interchangeable mounting blocks. By employing a range of such blocks, a series of nozzle configurations (nozzles A, B, C, D, and E) were formed. They provided measured results of pressure at the nozzle centreline and the droplet radius at the nozzle centreline near the exit using optical methods. The schematic view of these nozzle configurations is displayed in Figure 4.1. Here, the parameters *b* and *e* indicate the nozzle throat height and the nozzle exit height, respec-

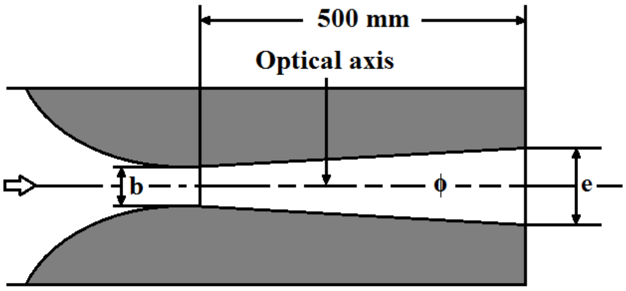

Nozzle	**A**	**B**	**C**	**D**	**E**
b (mm)	**63**	**100**	**120**	**127**	**140**
e (mm)	**114**	**144**	**150**	**148**	**157**

Width of each nozzle is 152 mm

Figure 4.1: The schematic view of the nozzle configurations of the tests of Moore et al. (1973).

tively. However, in the present work only two nozzle configurations have been modelled namely nozzle A and B of Moore et al. (1973).

The computational grid for a nozzle is presented in Figure 4.2. A structural grid was generated in the domain. The grid was refined sufficiently in the throat region. Only half of the computational domain was modelled for the nozzle by applying a symmetric boundary condition at the nozzle axis. For CFD simulations, the operating conditions for the nozzles corresponded to the experiments of Moore et al. (1973). The subsonic flow condition was defined at the inlet employing total pressure and total temperature. Moreover, the flow angle was normal to the nozzle inlet. The outlets of both nozzles were fixed to the supersonic flow condition. At the wall, a no-slip adiabatic wall condition was specified.

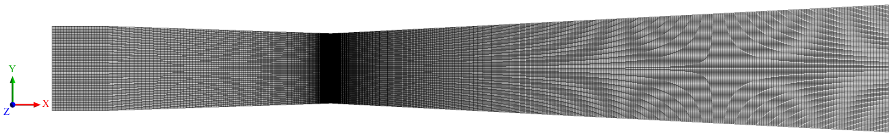

Figure 4.2: The computational mesh of nozzle A of Moore et al. (1973).

To analyse the influence of grid refinement on wet-steam flow, the grid independence study was performed with three grids. Grid refinement was applied throughout the computational domain. The total numbers of nodes in the x- and y-directions corresponding to Grid A, Grid B and Grid C were 474 and 38, 720 and 50, and 755 and 54, respectively. The mean y^+ values of Grid A, Grid B and Grid C were 11, 7 and 5, respectively. Figure 4.2 displays an intermediate grid (Grid B). The details of the grid independence study and corresponding results are discussed in Section 5.1.

4.1.1.2 Moses and Stein nozzle

Moses and Stein (1978) conducted a series of experiments on steam condensation in a Laval nozzle. They organised various tests in which they studied the influence of the initial temperature and pressure variation of steam on the condensation zone. Their nozzle was made of black anodised aluminium having a throat of $1\,\mathrm{cm} \times 1\,\mathrm{cm}$. The profiles of the transonic and supersonic sections of the nozzle were a circular arc of a $68.6\,\mathrm{cm}$ radius, which was coupled smoothly with an arc of a $5.3\,\mathrm{cm}$ radius to form the subsonic entrance. The schematics of the side and top views of the experimental set-up of Moses and Stein (1978) is displayed in Figure 4.3.

The computational domain contains a structural grid, which was more refined in the nozzle throat area (Figure 4.4). The number of cells in the x- and y-directions were 430 and 150, respectively, and the mean y^+ value of the grid was 12. Four test cases were chosen, in which the operating conditions were defined corresponding to the test values. For all of

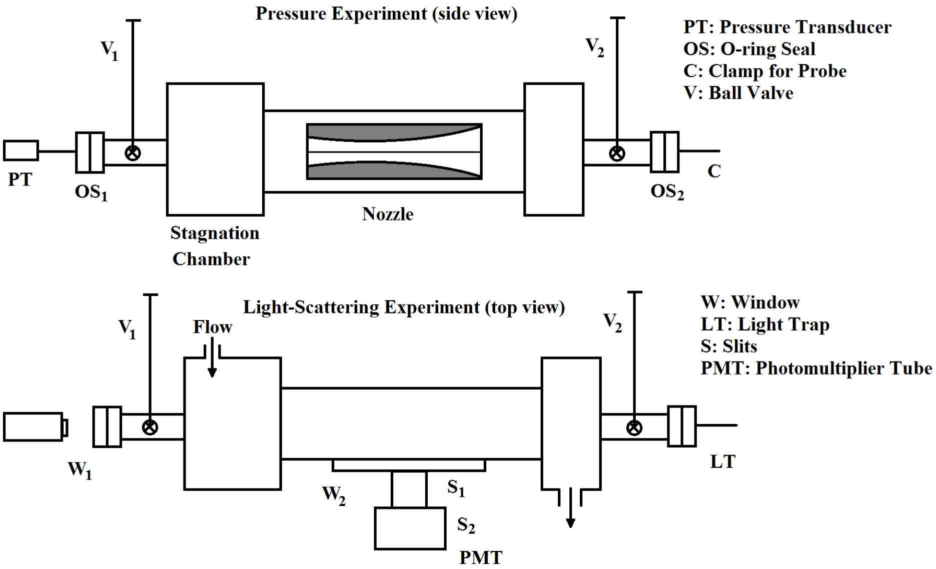
Pressure Experiment (side view)
V_1
V_2
PT: Pressure Transducer
OS: O-ring Seal
C: Clamp for Probe
V: Ball Valve
PT
OS_1
Stagnation Chamber
Nozzle
OS_2
C
Light-Scattering Experiment (top view)
V_1
Flow
V_2
W: Window
LT: Light Trap
S: Slits
PMT: Photomultiplier Tube
W_1
W_2
S_1
S_2
PMT
LT

Figure 4.3: The schematic view of the Moses and Stein (1978) nozzle test configuration.

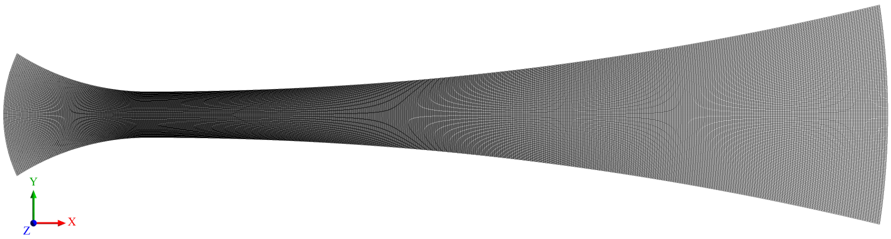

Figure 4.4: The computational mesh of the Moses and Stein (1978) nozzle.

the cases, the outlet boundary condition of the nozzle was considered as a supersonic flow condition. A no-slip adiabatic wall boundary condition was defined at the nozzle walls.

4.1.1.3 Barschdorff nozzle

Barschdorff (1971) performed condensing steam flow experiments with an arc CD nozzle considering various inlet flow temperatures. A sketch of the Barschdorff nozzle is shown in Figure 4.5. In the experiment, the depth of the test section was $50\,\text{mm}$. The nozzle configuration consisted of a wall curvature radius of $584\,\text{mm}$. The throat height was $60\,\text{mm}$. Figure 4.6 displays the computational mesh of the Barschdorff (1971) nozzle, in which the total nodes in the x- and y-directions were 370 and 100, respectively, and the corresponding mean y^+ value was 3.5. In the present work, only one test case was simulated with the Barschdorff nozzle. Boundary conditions corresponding to the experiments of Barschdorff (1971) were applied. The nozzle outlet was fixed with the supersonic condition. An adiabatic no-slip wall boundary was defined at the nozzle walls.

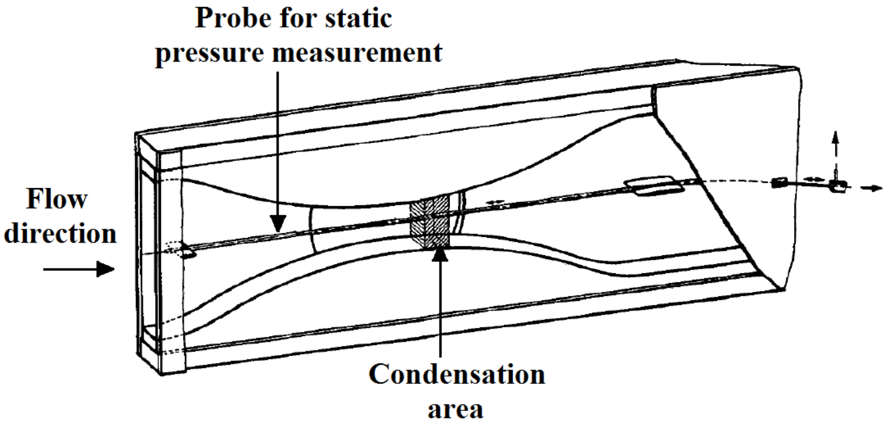
Probe for static pressure measurement
Flow direction
Condensation area

Figure 4.5: The schematic view of the Barschdorff (1971) nozzle configuration.

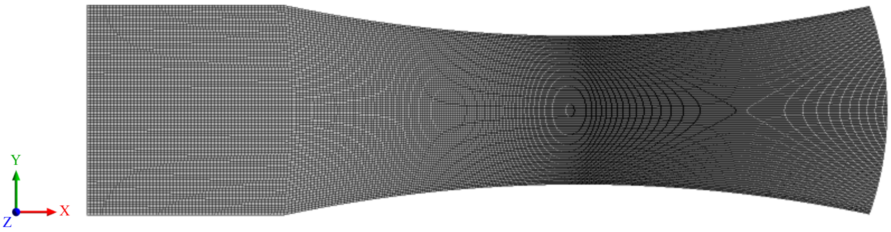

Figure 4.6: The computational mesh of the Barschdorff (1971) nozzle.

4.1.2 2D turbine cascade

4.1.2.1 White stator cascade

White et al. (1996) conducted experiments with the turbine blade profile, which was the planar stator cascade of the fifth stage stator blade from the six-stage LP cylinder of a 660 MW steam turbine. In the cascade, the design exit Mach number was 1.2 and the outlet flow angle was about $71°$. These tests are more associated with the flow in the steam turbine where there is interaction between the aerodynamic effects and the condensation process itself. A schematic view of the test section of White et al. (1996) is shown in Figure 4.7. The depth of the test section was 152 mm, which creates a blade aspect ratio of 1.55. The blade pitch, blade chord and blade stagger angle were 87.59 mm, 137.51 mm and $45.32°$, respectively. Moreover, the inlet flow angle was $0°$. White et al. (1996) performed four different levels of inlet superheat tests which were classified as L (low), M (medium), H (high) and F (very high). Some tests were performed with an inlet moisture

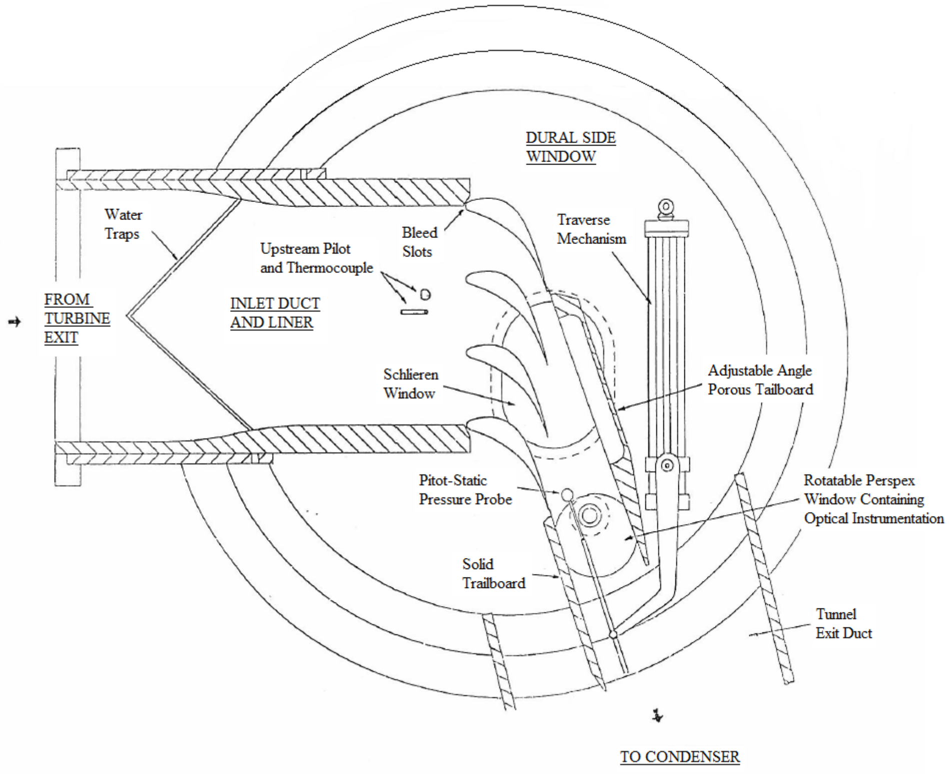
DURAL SIDE WINDOW
Water Traps
Bleed Slots
Traverse Mechanism
Upstream Pilot and Thermocouple
FROM TURBINE EXIT
INLET DUCT AND LINER
Schlieren Window
Adjustable Angle Porous Tailboard
Pitot-Static Pressure Probe
Rotatable Perspex Window Containing Optical Instrumentation
Solid Trailboard
Tunnel Exit Duct
TO CONDENSER

Figure 4.7: The schematic view of the test section of White et al. (1996) for the stator cascade.

of about 1.6% (i.e. W (wet inlet) cases). For all of the tests, the inlet stagnation pressure was maintained at about 0.4 bar.

As shown in Figure 4.7, the experiments of White et al. (1996) originally included four stator vanes, which creates three flow passes in the domain. However, in this work, only two passages of the experimental facility have been assumed, employing a periodic boundary condition in the y-direction. At the inlet and outlet of the domain, the pressure inlet and pressure outlet boundary conditions were specified, respectively. A no-slip adiabatic wall condition was defined at the blade surfaces. A structured and non-uniform grid was generated in the computational domain. Moreover, an O-grid around the blade surfaces was employed, while an H-grid was generated in the remaining computational domain as shown in Figure 4.8. To resolve the boundary layers, a sufficiently fine grid was constructed around the leading and trailing edges of the stator blade.

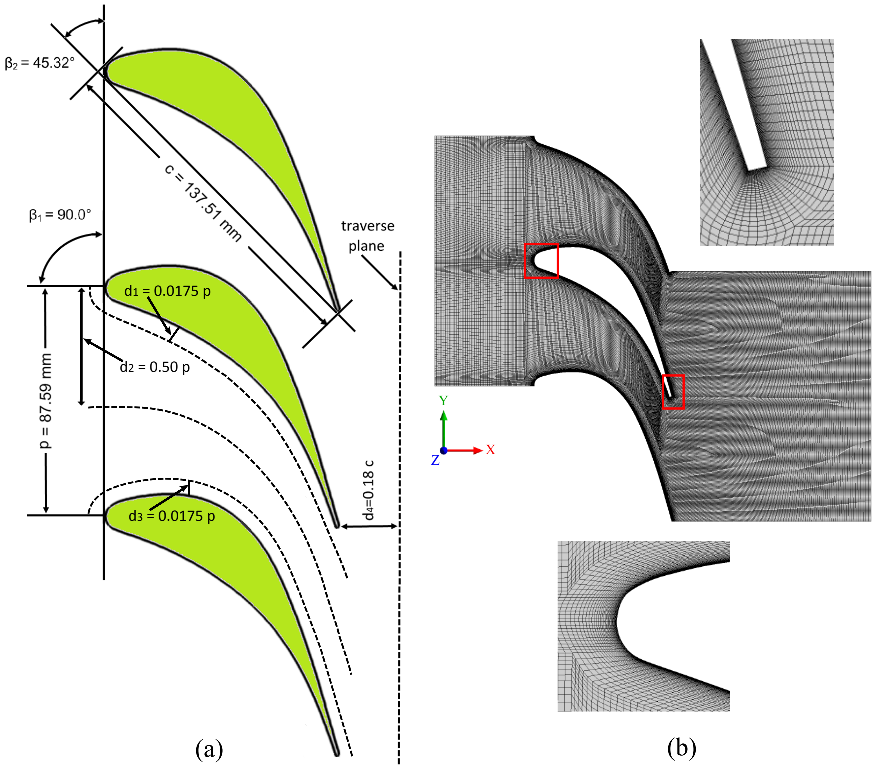

(a) (b)

Figure 4.8: (a) LP turbine stator blade geometry used for the experiments of White et al. (1996). The dotted black lines demonstrate the locations where the CFD data were obtained, and (b) the computational mesh in the domain including the mesh generation around the leading and trailing edges of the stator blade (Grid B).

The grid independence study was performed for the turbine cascade. For this purpose, three different numerical grids were generated and used for comparison, in which the number of grid elements were increased from Grid A (40,970 cells) over Grid B (76,554 cells) to Grid C (103,582 cells). The grid density close to the blade surfaces was refined to achieve a smaller y^+ value and the corresponding mean y^+ values of Grid A, Grid B and Grid C were 0.2, 0.05, and 0.01, respectively. Further, the influence of grid refinement on condensation phenomena was assessed based on the GCI method. The results of the grid independence study and GCI analysis are presented in section 5.2.2.1.

In the present work, five experimental cases entitled L1, L2, L3, W1, and H3 of the test series of White et al. (1996) have been used for different validation and other study purposes. The selected test cases are varied with different exit isentropic Mach numbers and accordingly different total pressure ratios $\mathrm{P_{01}/P_2}$. Here, L1, L2, and L3 are the low inlet superheat tests, whereas H3 is the high inlet superheat test. W1 is performed with inlet wetness.

4.1.3 3D turbine stage

To study the influence of turbulence modelling and unsteadiness on condensing steam flow, a 3D stator-rotor stage was utilised. The used stator vane was the stator cascade of White et al. (1996). However, the utilised rotor blade is not that of a real turbine geometry. It was intended to be representative of 25% of the reaction of the rotor at mid span. The details about the stator-rotor stage design are listed in Table 4.1.

Table 4.1: Details about the stator-rotor stage design.

	Stator	Rotor
Blade height [mm]	76	126.52
Number of blades	30	31
Averaged diameter [mm]	836.42	886.94
Averaged pitch [mm]	87.59	89.88
Rotational angle [°]	12	11.6129

The steam expansion ratio of the design stage is about 4, however, it is comparatively higher than that of the real steam turbine stage. The modelling of whole $360°$ stator-rotor stage requires the huge computational memory and time. Therefore, one option could be considered to model only a single or two passage of each blade row by applying a periodic boundary condition. However, this approximation could be applicable when the pitch ratio between the blade passages is close to the unity. In this work, only a single passage of the stator and the rotor was modelled consisting of $12°$ section of the stator blade passage and approx. $11.6129°$ section of the rotor blade passage employing a periodic boundary condition in the circumferential direction. The modelled pitch ratio at the interface between the stator and rotor was about unity. Figure 4.9(a) presents the schematic of the computational domain of 3D stator-rotor stage. Both blades have a constant profile without twisting in the radial direction. The axial gap between the stator and rotor was assumed to be 40% of the axial chord of the stator. Moreover, the domain was modelled without rotor tip clearance to exclude the influence of tip swirls on the flow. The flow inlet conditions were P_{01} = 40300 Pa, and T_{01} = 354 K which are similar to the inlet flow conditions in the case L1 of White et al. (1996). The domain outlet static pressure was P_2 = 9894 Pa. The boundary condition profiles at spanwise direction at inlet and outlet of the domain are constant. An adiabatic no-slip wall boundary was defined at the blade surfaces and at the hub and shroud surfaces.

In this study, steady state simulations were performed using a mixing plane as an interface between the stator and the rotor domain. In the mixing plane approach, the flow properties at the mixing plane interface were averaged in the circumferential direction at both the stator outlet and the rotor inlet boundaries. The mixing plane averaging between blade passages accounts for time average interaction effects, however, it neglects the transient interaction effects. The unsteady simulations were performed with a sliding mesh. The sliding mesh approach predicts the transient interaction of the flow between the stator and the rotor passage. In this approach, the transient relative motion between the stator and the rotor passage on each side of the general grid interface connection is modelled. The position of interface is updated at each time step, as the relative position of the grids on each side of the interface changes (ANSYS Inc., 2014a).

The computational grid is displayed in Figure 4.9(b). The grid quality/density near solid boundaries is very important for the precise resolution of boundary layers. Therefore, the grid distribution near the solid surfaces was fine enough to achieve a relatively smaller y^+ value. The mean y^+ values for the stator and the rotor blades were 3.5 and 2.5, respectively. To resolve the flow accurately near to the blade surfaces, the O-grid was generated with boundary layer meshing. The grid was more refined around the leading and trailing edges of the stator and rotor blades. Typically, 38 and 51 grid points were distributed along the spanwise direction for stator and rotor blades, respectively. For both blades, the initial wall spacings at the spanwise direction for the first Δs was 0.1 mm at the hub and shroud surfaces. Based on experiences from the conducted grid independence study for a 2D stator cascade case, adequate grid refinement was assumed for the 3D stator-rotor domain. The total number of grid cells of the stator domain was 746660, and the rotor domain contained 2124350 cells. The computational grid included about 2.87 million hexahedral cells. The commercial grid generator Pointwise was employed for all grids in this work.

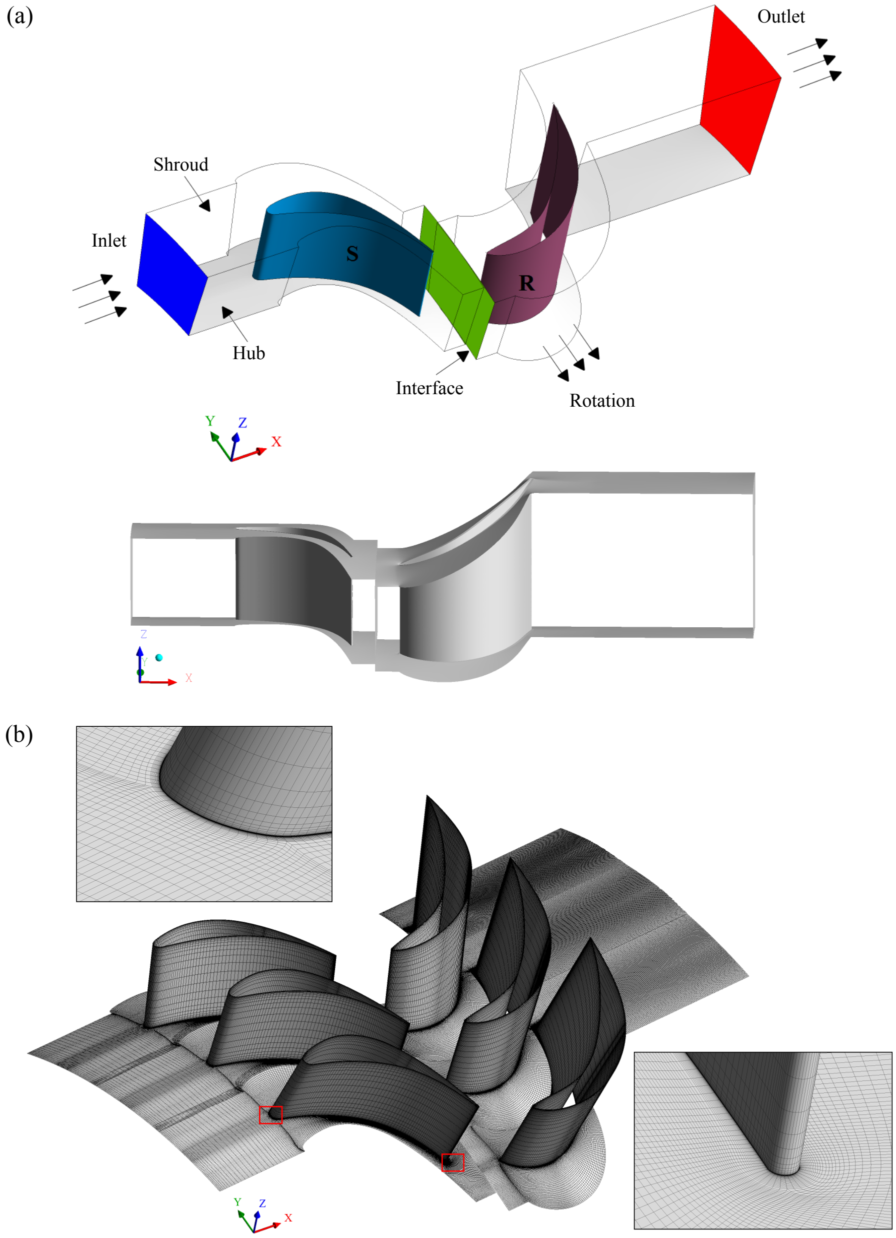
(a)
Outlet
Shroud
Inlet
S
R
Hub
Interface
Rotation
Y
Z
X
Z
X
(b)
Y
Z
X

Figure 4.9: (a) The schematic of the computational domain, (b) computational mesh and the mesh generation around the leading and trailing edges of the stator blade.

4.2 Details of the CFD simulation set-up

All the simulations in this work have been partially performed on an office computer (Intel Xeon, 32 Gb RAM), in the scientific computing cluster (the HP SL230S cluster with 16 nodes, 16 cores/node, mem. 128 Gb/node, 40 Gb/s infiniband) of Lappeenranta University of Technology (LUT) and in the Taito super cluster (the Apollo 6000 XL230a G9 cluster with 407 nodes, 24 cores/node, mem. 256 Gb/node) of the CSC-IT Center for Science Ltd., Finland. Mostly, the calculations of the 2D nozzles and stator cascade were done on the office computer and in the LUT cluster, while all 3D simulations were carried out in the cluster of the CSC-IT Center.

4.2.1 ANSYS FLUENT solver settings

In this work, all of the numerical results of the nozzles and turbine stator cascade obtained with ANSYS FLUENT were performed with steady state RANS equations. Multigrid schemes are well known and extensively used in the CFD community for being the fastest numerical methods for solving CFD problems. These schemes are used to accelerate the convergence of the solver by computing corrections on a series of coarse grid levels. In ANSYS FLUENT, two types of multigrid schemes are available: (i) the algebraic multigrid (AMG), and (ii) the full approximation storage (FAS) methods. AMG is applicable for both pressure-based and density-based implicit solvers, while FAS is used for density-based explicit solvers. The utilised wet-steam model of ANSYS FLUENT was based on the density-based explicit solver; therefore, the FAS multigrid methodology was used.

The algorithm starts with a fluid properties update, in which at first iteration, initialised properties are used. After that, the solver solves the governing equations of mass, momentum and energy simultaneously. These governing equations can be solved either with implicit or with explicit schemes. Then, the turbulence equations and other scalar equations are solved. However, the transport equations for additional scalars are determined segregated from the coupled set, and these transport equations are linearised and solved implicitly. Moreover, if the interphase coupling is included, then the source terms are updated to the corresponding conservation equation of mass. In the subsequent step, the convergence of the solution is checked based on the determined convergence criteria. If the estimated solution fulfills the set limit of convergence criteria, then the solver stops otherwise the solver stats again from the first step using the latest solution. The flowchart of this algorithm is described in Figure 4.10.

The spatial discretisation is very important in order to estimate the accuracy of the converged CFD solution. In ANSYS FLUENT, various options are available for spatial discretisation treatment. In this work, a second order upwind scheme was used for spatial discretisation. However, for constructing an upwind scheme, flux terms are splitted into forward and backward propagating and the appropriate directional differencing is applied to each component. Therefore, the splitting of the flux and its differencing leads to a flux-difference splitting scheme. In this work, the Roe scheme (Roe, 1986) was used to

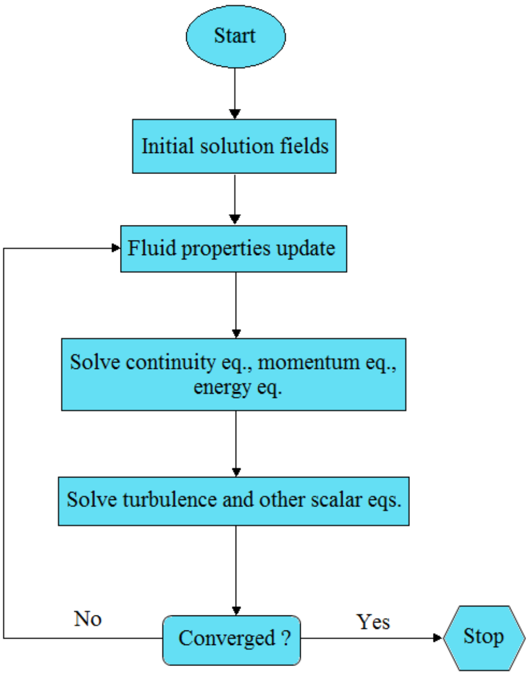
Start
Initial solution fields
Fluid properties update
Solve continuity eq., momentum eq., energy eq.
Solve turbulence and other scalar eqs.
No
Converged ?
Yes
Stop

Figure 4.10: The density-based flow solver algorithm of ANSYS FLUENT.

calculate the convective fluxes. The k-ε models family is applicable to solve flow turbulent far from the wall regions. Therefore, in order to solve flow accurately near the wall regions with k-ε models family, the near-wall treatments are required. All the simulations of CD nozzles have been performed by using the SWF. The 2D stator cascade simulations have been done with EWT to solve boundary layer flow. The Spalart-Allmaras, the k-ω and the SST k-ω models are designed to apply throughout the boundary layer, and therefore, they require sufficiently fine mesh near the wall regions. The results presented in this work were converged to normalised root-mean-square (RMS) residuals of the order of 10^{-4} or lower. It is a fact that the CFD simulations of wet-steam flow are very sensitive, and many factors directly/indirectly influence the convergence of simulations. Therefore, it was necessary to slightly modify the under-relaxation parameters in some cases to converge the simulations. However, the under-relaxation coefficients were modified case dependently, and no specific values suitable for all cases were found.

4.2.2 ANSYS CFX solver settings

The simulations conducted within ANSYS CFX were based on finite-volume discretization. The solution of the RANS equations was based on a coupled solver. The advection flux was treated with a high resolution scheme. Also turbulence models, the volume fraction and energy equations were calculated using high resolution methodology. Steady and unsteady calculations were conducted with ANSYS CFX. For unsteady calculation, fixed time-stepping was used. Figure 4.11 displays the solver algorithm of ANSYS CFX for both steady and unsteady simulations. The algorithm starts with an initial simulation set-up. Step by step it solves hydrodynamic equations, phase volume fractions, the energy balance, flow turbulence and mass fractions. For steady calculations, the solver runs are repeated according to the predefined maximum iterations until a converged solution is achieved. In the case of transient simulations, the CFD code solves the flow governing equations according to specified time steps size. At every time step, a number of iterations are performed before achieving convergence. Once the calculated solution satisfies the determined convergence criteria then solver advances to the succeeding time step. This process continues up to the final time step. For ANSYS CFX simulations, the convergence criteria were met and the normalised RMS residuals were achieved to the order of 10^{-5} or lower.

In this work, the simulations of CD nozzles and 2D steam turbine stator cascade have been performed with ANSYS FLUENT. However, ANSYS CFX is comparatively faster, has good convergence and scaling, and is robust, particularly in 3D turbomachinery flow analysis than ANSYS FLUENT. Due to these advantages, ANSYS CFX was the most suitable option compared to ANSYS FLUENT for 3D stator-rotor stage calculations. Therefore, all the 3D stator-rotor stage simulations have been done by using ANSYS CFX code.

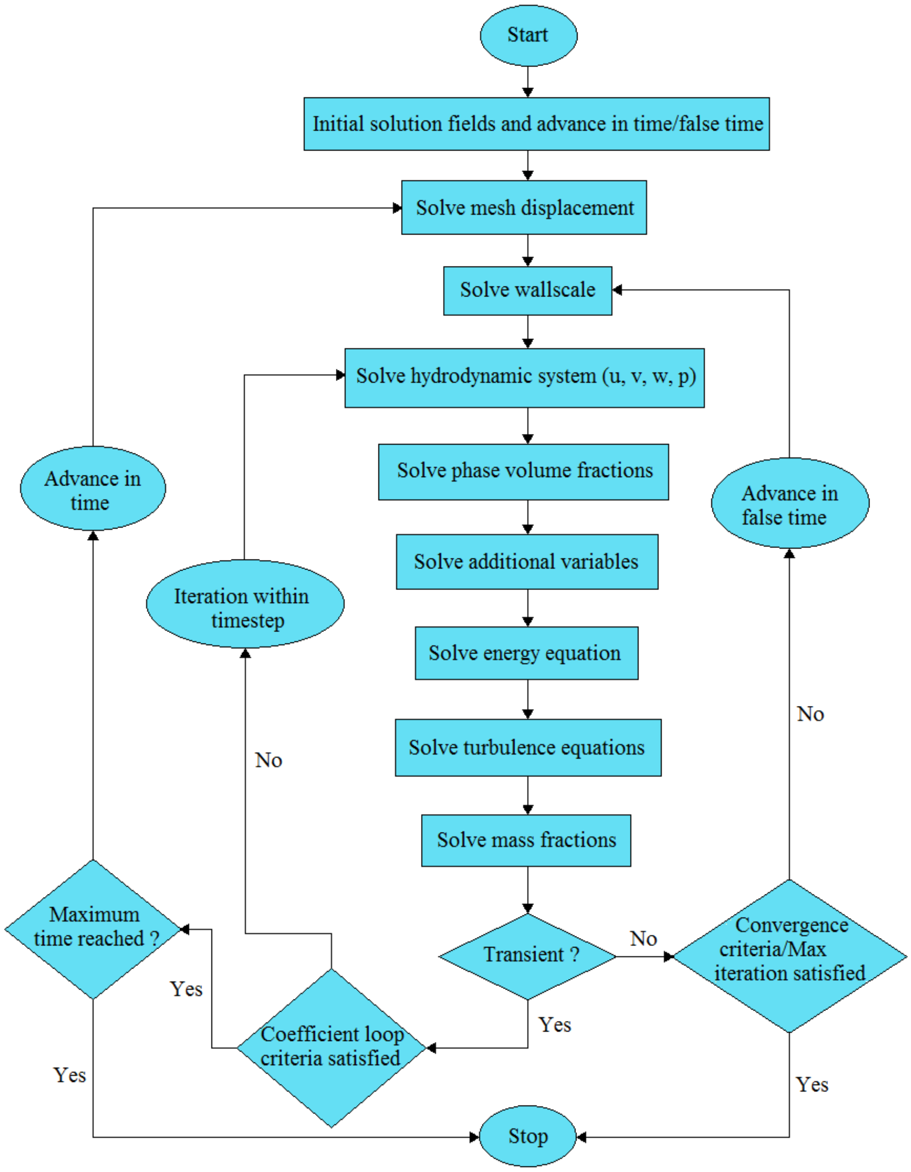
Start
Initial solution fields and advance in time/false time
Solve mesh displacement
Solve wallscale
Solve hydrodynamic system (u, v, w, p)
Solve phase volume fractions
Solve additional variables
Solve energy equation
Solve turbulence equations
Solve mass fractions
Transient ?
Convergence criteria/Max iteration satisfied
Coefficient loop criteria satisfied
Maximum time reached ?
Advance in time
Iteration within timestep
Advance in false time
Stop
Yes
No

Figure 4.11: The flow chart of the solver algorithm of ANSYS CFX.

5 Results and discussions

5.1 Influence of real gas modelling on condensing steam flows

To predict flow expansion accurately, the correct calculation of superheated steam properties is required. Moreover, the nucleation and droplet growth processes are very sensitive to the thermodynamical properties, namely temperature and pressure. Near and below the saturation line, there is a rapid change in the relative concentration of the molecular cluster within steam, which leads to changes in the thermodynamics properties of the steam (Bakhtar and Piran, 1979). Further, the flow in the meta-stable region cannot be modelled accurately using the ideal-gas assumption. Therefore, the accurate prediction of steam expansion close to the saturation line requires a real gas model.

In this work, the influence of real gas modelling on condensing steam flows is studied using ANSYS FLUENT. For this purpose, the author's local EOS (AEOS) for real gas and other steam properties was generated. However, the AEOS is applicable to a limited range of pressure and temperature. The performance of the AEOS has been compared with the EOS of Young (1988) (YEOS). The YEOS is the default selection in the wet-steam model of ANSYS FLUENT. The AEOS was implemented to ANSYS FLUENT with user defined subroutines. The formulations of both EOSs for real gas models are presented in section 3.4.

Firstly, the grid sensitivity analysis are presented in this section. Then, the influence of real gas modelling on non-equilibrium condensing flows in a nozzle is discussed. For this purpose, nozzle A of Moore et al. (1973) is used. At the inlet boundary, P_{01} = $25\,\mathrm{kPa}$ and T_{01} = $354.6\,\mathrm{K}$ were applied. The grid density/resolution in the computational domain should have a significant effect on the results of the numerical simulation up to a certain range. Thus, a grid independence study was conducted. The details about grids are discussed in section 4.1.1.1.

The pressure distribution predicted by various grids is shown in Figure 5.1. It can be observed that some information is missing in Grid A after the nozzle throat. Grid B and Grid C estimated relatively similar distributions of pressure. Further, Figure 5.2 presents the nucleation rate along the nozzle centreline computed with different grids. It can be seen that Grid A estimated a lower peak of the nucleation rate profile than Grid B and Grid C. Therefore, it can be inferred that Grid A is insufficient to capture the small details of the flow. Furthermore, the pressure and wetness fractions along the nozzle centreline obtained by three different grids are discussed in Publication I. The results show that the grid density influenced the pressure distribution. However, the wetness fraction is less sensitive to the grid size in the selected nozzle case. The results depict that the differences of the flow pattern between Grid B and Grid C are negligible. Therefore, Grid B was the optimum selection for further study.

The performance of AEOS for real gas has been assessed with the dry steam flow condition. In Publication I, the calculated pressure distribution and Mach number of dry steam

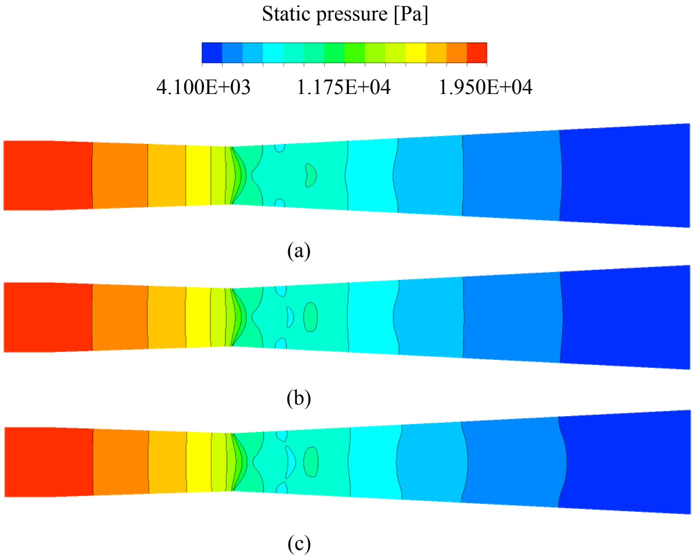

Figure 5.1: Contours of the pressure distribution predicted with (a) Grid A, (b) Grid B, and (c) Grid C.

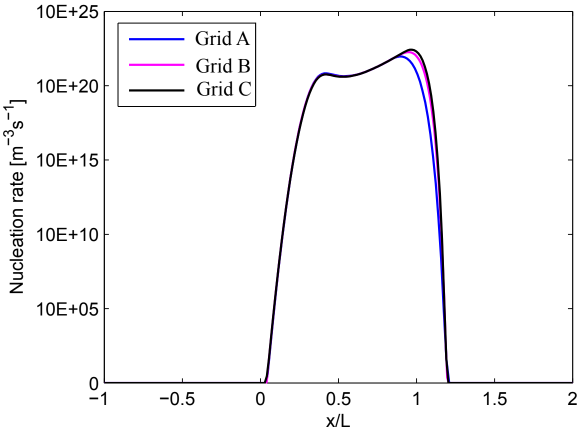

Figure 5.2: Nucleation rate along the nozzle centreline calculated with different grid resolutions.

along the nozzle centreline with the AEOS are compared with the YEOS results. Some variation has been observed in both cases. Subsequently, the AEOS is applied to the condensing steam flow simulations. Condensing steam flow is dry initially. After reaching the Wilson point, liquid droplets are created and a two-phase flow is established. The generated liquid droplet starts to grow rapidly by transferring latent heat in the surrounding subcooled vapour phase. Consequently, the heat addition to the vapour phase from the liquid phase increases the flow temperature and pressure. The increment/rise in pressure is known as the condensation disturbance.

Figure 5.3 displays the contours of pressure distribution estimated by both real gas models. YEOS yields a higher pressure drop than AEOS because of the higher expansion rate. After the throat of the nozzle, the pressure was raised due to a latent heat release from liquid droplets to the vapour phase. The Mach number contours are presented in Figure 5.4. YEOS estimated a shock wave with higher intensity after the throat of the nozzle than AEOS, which is likely due to the higher pressure drop, as can be seen in Figure 5.3. The local speed of sound is increased due to the temperature increment via the latent heat exchange from growing droplets. As a result, the Mach number is decreased in the condensation zone. The Mach number is increased in the divergent part of the nozzle due to the increment in the flow velocity.

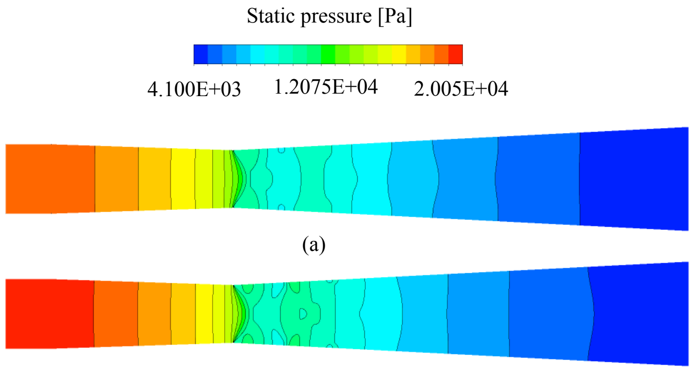

(a)

(b)

Figure 5.3: Contours of the pressure distribution predicted by (a) YEOS and (b) AEOS.

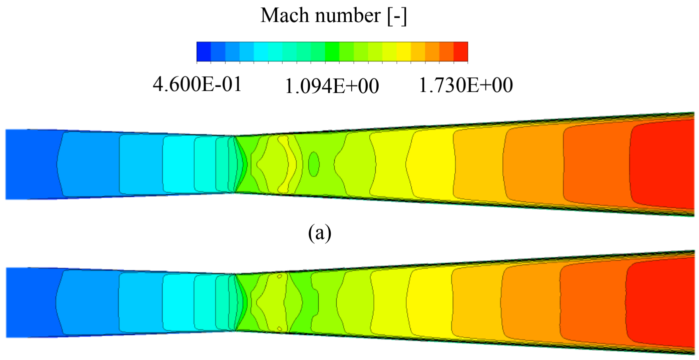

(a)

(b)

Figure 5.4: Contours of the Mach number predicted by (a) YEOS and (b) AEOS.

Further, Figure 5.5 presents a comparison between the predicted results for both real gas models. The precise modelling of non-equilibrium condensing flow is eventually dependent on the accuracy of the nucleation and the droplet growth estimations. As shown in Eq. (3.11), the nucleation rate is expressed as a function of thermodynamic properties and the surface tension.

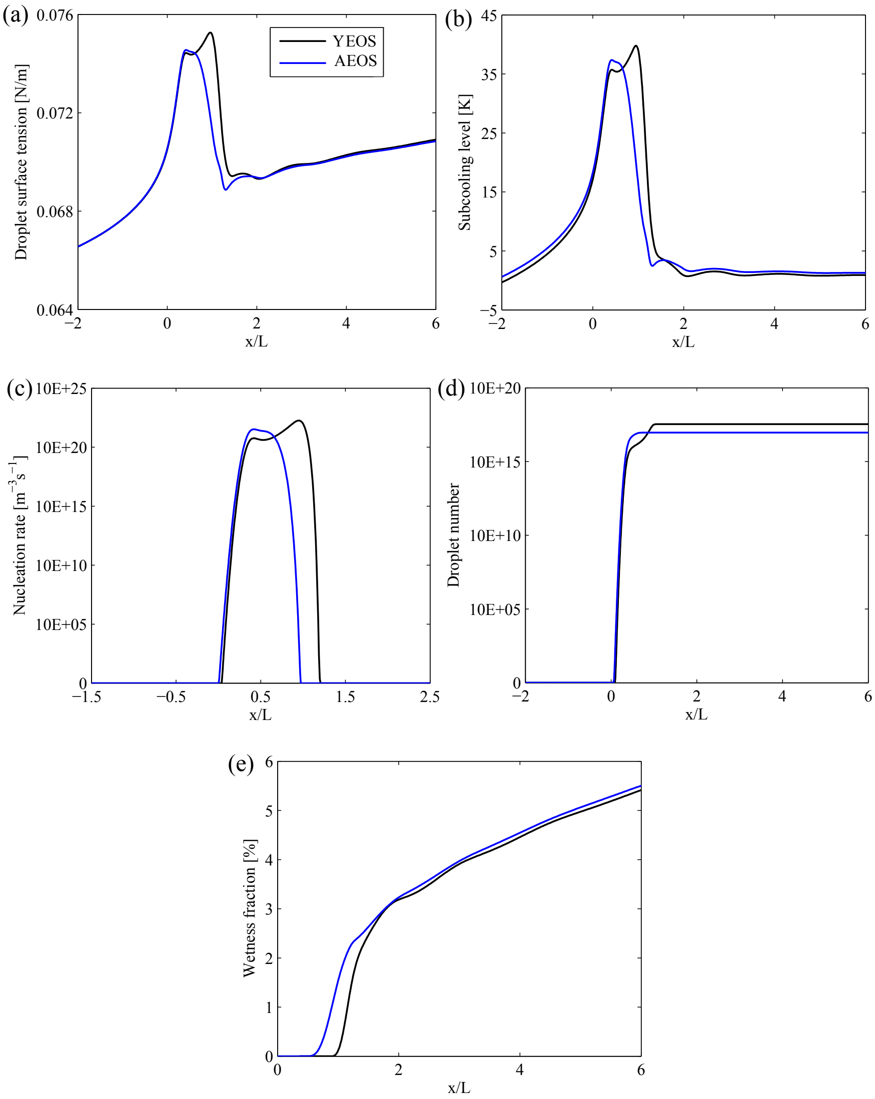

Figure 5.5: Predicted results of the (a) droplet surface tension, (b) subcooling level, (c) nucleation rate, (d) droplet number, and (e) wetness fraction along the nozzle centreline.

The surface tension plays an important role in the nucleation rate. A higher surface tension produces a wider nucleation zone, and as a result it delays the onset of condensation. YEOS yielded a higher value for surface tension compared to AEOS (Figure 5.5(a)). During the expansion of steam, the flow remains dry in a meta-stable equilibrium state before the subcooling becomes high enough to start nucleation. At the Wilson point, the subcooling exceeds its maximum and the highest peak of the nucleation rate appears, and finally, nucleation terminates. It can be noticed that YEOS yielded a higher value for the subcooling level and nucleation rate due to the higher expansion rate. Further, in the case of YEOS, the subcooling and nucleation rate expanded in the downstream of the nozzle compared to the AEOS case (Figure 5.5(b) and (c)). Figure 5.5(d) indicates that YEOS estimated a higher droplet number than AEOS. The increment in the droplet number could be described by the higher nucleation rate. The flow expansion influenced the Wilson point of the flow field, which affected the nucleation rate. Additionally, the wetness fraction in the flow starts to increase after the nucleation reaches the highest peak. Figure 5.5(e) demonstrates that the wetness generation shifts downstream of the nozzle in the case of YEOS because of the wider nucleation region.

The predicted pressure distribution and mean droplet radius along the nozzle centreline for both cases are compared with the experiments of Moore et al. (1973) in Figure 5.6. As discussed before, the flow temperature and pressure increases due to the latent heat releases from the rapidly growing droplets. If the droplet number is higher, it releases more latent heat, which increases the peak of condensation disturbance. Accordingly, in the case of YEOS, the calculated peak of condensation disturbance is higher. The pressure distribution in AEOS was in better agreement with the experiments than that of YEOS. A higher nucleation rate is associated with a lower growth rate, i.e. whenever a large number of tiny liquid droplets nucleate, there will be less growth. In contrast, when lower nucleation happens, the growth rate is predominant and therefore larger liquid droplets are present. Therefore, in the case of YEOS, the average droplet radius is lower compared

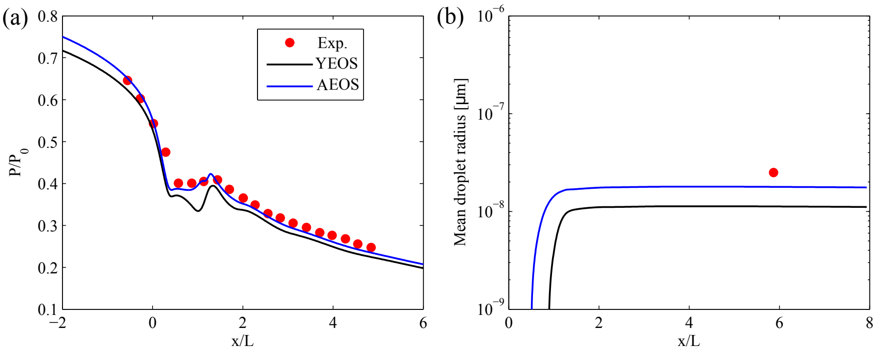

Figure 5.6: Predicted results of (a) the pressure ratio, and (b) the mean droplet radius along the nozzle centreline compared with the nozzle A experiments of Moore et al. (1973).

to the AEOS due to a large number of droplets. Based on the presented results, it can be seen that the estimation of real gas properties plays a vital role in condensing steam flow modelling.

5.2 Influence of turbulence modelling on 2D condensing steam flows

The role of turbulence is crucial in transport phenomena particularly in boundary layers and in the deposition of condensed liquid droplets at surface walls in LP turbine flows. Also, the turbulence may have some direct/indirect influence on shock wave generation under the conditions of subcooled steam flow and on the prediction of absolute losses. Therefore, the influence of turbulence modelling on non-equilibrium condensing flows was studied. For this purpose, various 2D nozzles and turbine cascade have been selected. All simulations presented in this section have been carried out by mean of ANSYS FLUENT. The results are described in this section. Moreover, the effect of the freestream inlet turbulence level at the nozzle and on turbine cascade flows, and the performance of various turbulence models have been demonstrated.

5.2.1 Results of nozzles

5.2.1.1 Effect of turbulence level on condensation

Firstly, the effect of the freestream turbulence intensity on the condensing steam flow was investigated with the Barschdorff (1971) nozzle. The inlet boundary condition was defined as P_{01} = 78390 Pa and T_{01} = 380.55 K. The results with the nozzle were reached with a sufficiently refined grid to obtain a grid independent solution. The flow turbulence intensity has a major effect on the flow field and on the flow transition from the laminar boundary layer to the turbulent boundary layer and its separation. Therefore, the flow turbulence intensity may also have some impact on the condensation process. For this purpose, the numerical simulations were performed considering various freestream inlet turbulence intensities, such as χ = 0.02, 0.05, 0.1, and 0.2 with the standard k-ε turbulence model.

It is clear that the flow intensity is proportional to the turbulent kinetic energy and its dissipation rate. Figure 5.7 presents the predicted distribution of the turbulent viscosity and the turbulent dissipation rate along the nozzle centreline. It can be seen that the higher turbulence intensity increases the turbulent viscosity and turbulent dissipation rate in the flow. Consequently, the increment in viscous dissipation could influence the flow expansion.

Further, Figure 5.8 shows the predicted results with various freestream inlet turbulence intensities along the nozzle centreline. The flow expansion was observed to increase in the case of lower freestream inlet turbulence intensity, as displayed in Figure 5.8(a). Further, the subcooling level, the nucleation rate, and the wetness fraction also were influenced by the flow turbulence intensity. The subcooling level and nucleation rate slightly expanded

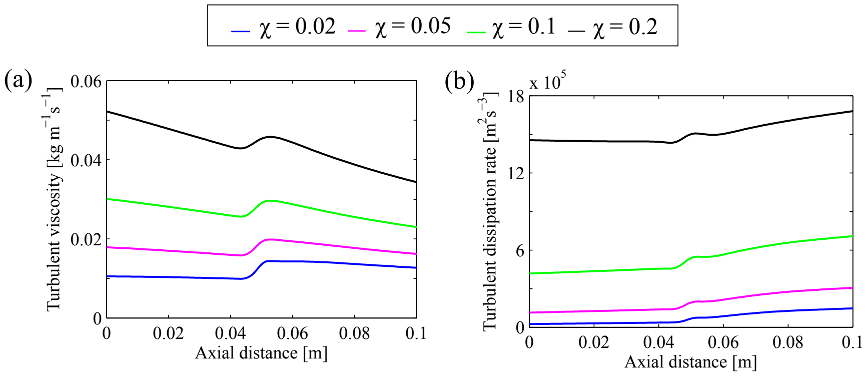

Figure 5.7: Predicted results of (a) the turbulent viscosity, and (b) the turbulent dissipation rate along the nozzle centreline. Here, a 0 m axial distance indicates the nozzle throat.

downstream of the nozzle with higher turbulence intensity due to the lower expansion rate. Subsequently, the wetness fraction decreased with the higher freestream inlet turbulence intensity. Moreover, the droplet number increased, and the mean droplet radius decreased with the lower turbulence intensity (Figures 5.8(e) and (f)). Additionally, the magnitude of the condensation disturbance was also influenced by the freestream turbulence intensity (Figure 5.8(a)). The predicted peak of condensation disturbance was highest when χ = 0.02. This could be explained as follows: the lower inlet freestream turbulence intensity yielded a higher droplet number, which released more latent heat and therefore the flow temperature and pressure raised. Thus, the peak of condensation disturbance grew. Moreover, the significance of the freestream inlet turbulence intensities on the wet-steam flow was studied with nozzle A of Moore et al. (1973) using the modified turbulent viscosity for the k-ε model. More details and results of the effect of the inlet turbulence level on the pressure distribution and turbulence properties along the nozzle centreline are presented in Publication I.

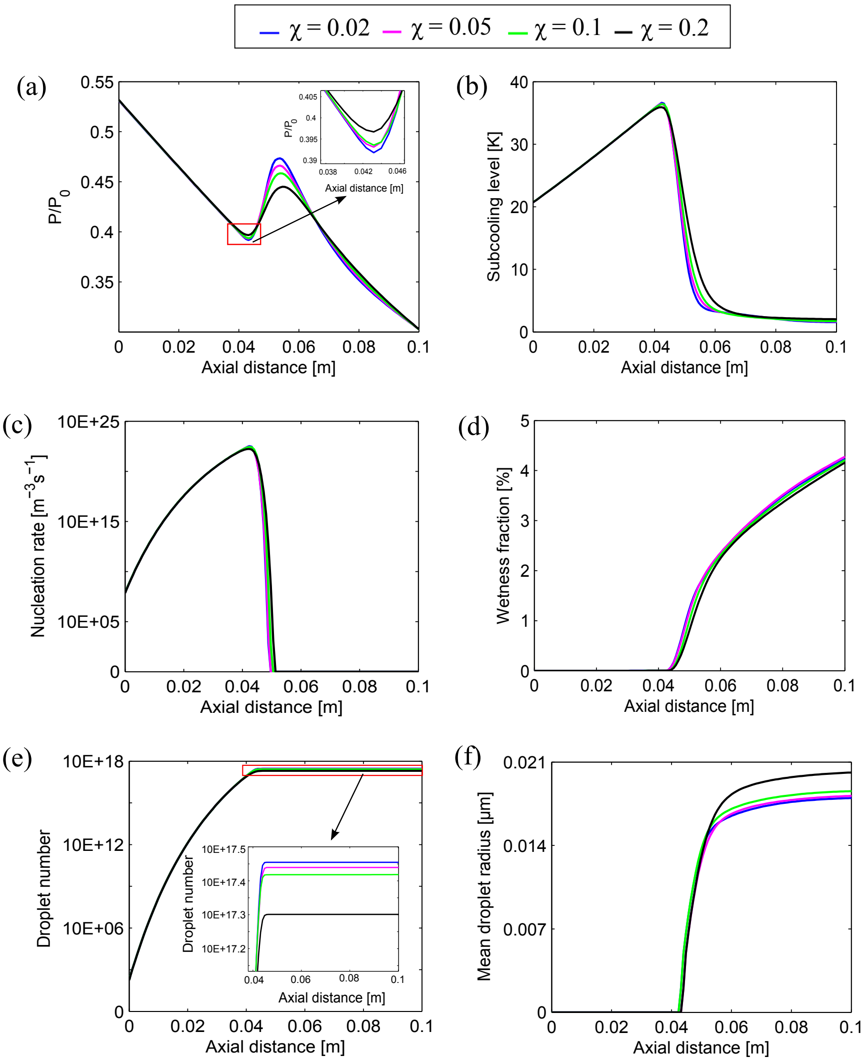

Figure 5.8: Predicted results of the (a) pressure ratio, (b) subcooling level, (c) nucleation rate, (D) wetness fraction, (E) droplet number, and (F) mean droplet radius along the nozzle centreline. Here, a 0 m axial distance indicates the nozzle throat.

5.2.1.2 Effect of turbulence model modification

5.2.1.2.1 The standard k-ε turbulence model

In this work, the turbulence models were modified and their performance was analysed. Firstly, the influence of turbulence modelling was analysed with the modified Sk-ε model.

For this purpose, the Sk-ε model was modified by including the modulation of turbulence kinetic energy due to liquid droplets via source terms (i.e. Eqs. 3.32 and 3.38) and the modified turbulent viscosity term (i.e. Eq. (3.31)). First, this modification on turbulence properties is assessed.

Figures 5.9(a) and (b) present the predicted results of turbulent kinetic energy and its dissipation rate, respectively, with various modifications to the Sk-ε model.

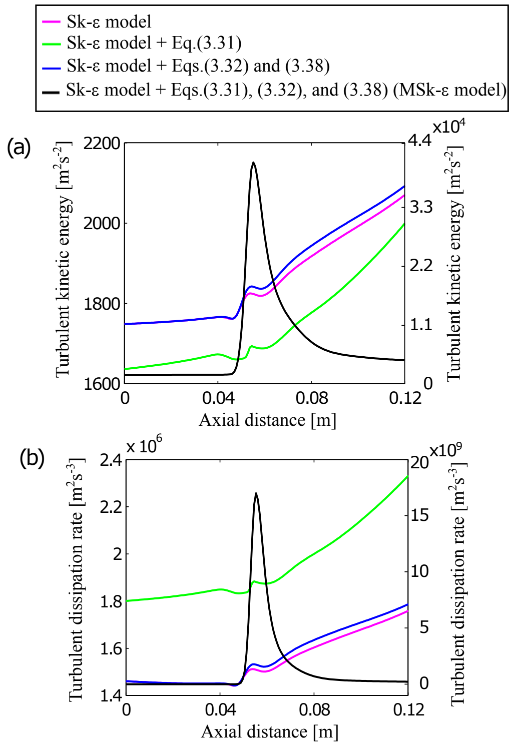

Figure 5.9: Distribution of (a) the turbulent kinetic energy, and (b) the turbulent dissipation rate at the nozzle centreline predicted by the Sk-ε model and other subsequent modifications with it. The right side scales of the y-axis present the MSk-ε model.

Figure 5.9(a) shows that the steep rise in turbulent kinetic energy started around 0.046 m axial distance for all of the models, which indicates the peak location of the nucleation rate. Moreover, the gradual increment in the turbulent kinetic energy appeared at a 0.057 m axial distance for the Sk-ε model, the Sk-ε model + Eq. (3.31) and the Sk-ε model + Eqs. (3.32) and (3.38). This location demonstrates the condensation peak. The subsequent addition of source terms to the Sk-ε model increased the turbulent kinetic and its dissipation rate. This increment took place after the second phase generation. However, the reduction in the turbulent kinetic energy for the Sk-ε model including the modified viscosity term can be explained by the considerably higher dissipation rate, as shown in Figure 5.9(b). The effect of model modification by including both the modified viscosity term and the source terms (i.e. Eqs. (3.31), (3.32) and (3.38)) to the Sk-ε (MSk-ε) turbulence model has been examined as well. The black solid line indicates the predicted trends of the turbulent kinetic energy and its dissipation rate with the MSk-ε turbulence model in Figures 5.9(a) and (b), respectively. It can be observed that the MSk-ε model predicted a notably higher value of the turbulent kinetic energy and its dissipation rate compared to the Sk-ε model and other model modifications, particularly after the throat downstream of the nozzle. The right side y-axis scales in Figures 5.9(a) and (b) apply to the MSk-ε model. The trends of turbulent kinetic energy and its dissipation rate profiles predicted by the MSk-ε model and the Sk-ε model including a modified viscosity term are similar before second phase generation due to the modified viscosity effect. The variation observed before the droplet formation (approx. $0.046\,\mathrm{m}$) in Figure 5.9 is only due to scale differences in the y-axis. The addition of source terms to the turbulence models increased the liquid mass generation rate. Therefore, the Sk-ε model including source terms and the MSk-ε model yielded a higher liquid mass generation rate than the models without source terms. However, the MSk-ε model increased the turbulent kinetic energy and its dissipation rate notably. The significant increment is noted from an axial distance of $0.046\,\mathrm{m}$ to $0.066\,\mathrm{m}$ in both turbulent properties. In this region, the droplet growth rate is higher, and therefore, the liquid mass generation rate increases. Consequently, both turbulent properties are significantly higher in the MSk-ε model. The mass generation rate remains stable/constant due to a lower droplet growth rate after the axial distance of $0.08\,\mathrm{m}$. Therefore, the profiles of turbulent kinetic energy and its dissipation rate in the MSk-ε model are almost constant downstream of the nozzle.

Figure 5.10 compares the estimated profiles of turbulent viscosity and the Reynolds stress by various modifications to the Sk-ε turbulence model. It can be noted that the Sk-ε model including the modified viscosity term and the MSk-ε model predicted a higher turbulent viscosity due to the modified viscosity terms which contain the production to dissipation ratio (Figure 5.10(a)). However, the Sk-ε models with and without source terms yield relatively identical turbulent viscosity distributions. The Reynolds stress was calculated based on the Boussinesq approximation, in which the Reynolds stress is proportional to the turbulent viscosity and the velocity gradients. Figure 5.10(b) shows that the Sk-ε model and the Sk-ε model with source terms estimated a notably higher value of Reynolds stress along the nozzle centreline than the other models. A detailed description of the variation in results related to turbulent viscosity and Reynolds stress are described in Publication III.

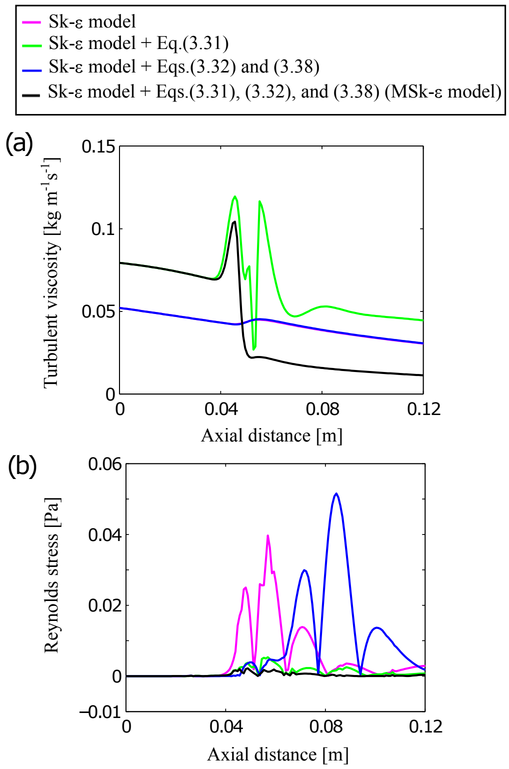

Figure 5.10: Distribution of (a) the turbulent viscosity, and (b) the Reynolds stress along the nozzle centreline predicted by the Sk-ε model and other subsequent modifications with it.

The effect of turbulence modelling on wet-steam flow properties is displayed in Figure 5.11, in which the performance of the inviscid calculation, the Sk-ε and the MSk-ε turbulence models are compared. Also, the predicted pressure distribution along the nozzle centreline is compared with the experimental data of Barschdorff (1971) (Figure 5.11(a)). It is observed that all models were in good agreement with the experiments in regard of pressure distribution. However, the inviscid and the Sk-ε models failed to capture the right location of condensation disturbance. The turbulence modification increased viscous dissipation that influenced the temperature distribution via the energy source, which affected the heat transfer rates. Therefore, the condensation process is extended downstream due to the turbulent viscosity modification and the source term addition to the MSk-ε model. The MSk-ε model estimated the accurate location and magnitude of the pressure rise. The intensity of the condensation disturbance for the inviscid case was almost double compared to the turbulence models due to the higher rate of latent heat released via droplets.

Figures 5.11(b) and (c) show that the MSk-ε model yielded a higher value of the surface tension and the subcooling level than the Sk-ε model. The model modification influenced

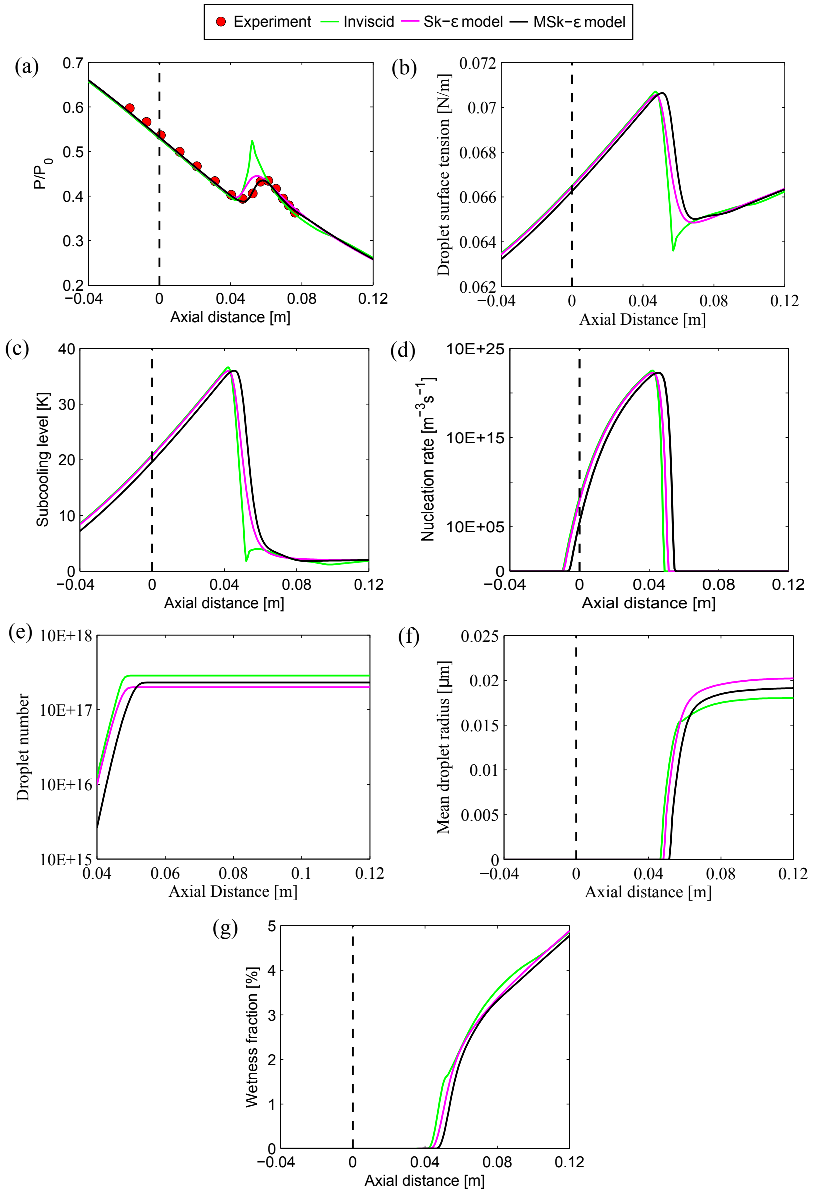

Figure 5.11: Predicted profiles of the (a) pressure ratio, (b) droplet surface tension, (c) subcooling level, (d) nucleation rate, (e) droplet number, (f) mean droplet radius and (g) wetness fraction along the nozzle centreline. The black vertical dashed line at an x=0 axial distance indicates the nozzle throat.

the nucleation rate as well. The nucleation region for the MSk-ε model has shifted downstream of the nozzle because of higher surface tension. The droplet numbers predicted by the inviscid and the MSk-ε models are higher compared to the Sk-ε model as a result of a higher nucleation rate (Figure 5.11(e)). In Figure 5.11(f), it can be observed that the Sk-ε model produced a higher droplet radius than the other models. This increment in the droplet radius resulted from a higher growth rate which generated a lower number of droplets. In the case of MSk-ε, the starting point of wetness generation shifted downstream of the nozzle and predicted a marginally lower wetness fraction than other models (Figure 5.11(g)). Moreover, the consequences of turbulence modelling in terms of the condensing flow in nozzle A of Moore et al. (1973) are presented in Publication I.

The performance of the MSk-ε turbulence model has been examined with various low-pressure nozzles as well. For this purpose, the experimental test cases of nozzles A and B of Moore et al. (1973) and test cases of the Moses and Stein (1978) nozzle were considered. The boundary condition of nozzle A of Moore et al. (1973) is described in detail in section 5.1. In nozzle B of Moore et al. (1973), boundaries P_{01} = $25\,\mathrm{kPa}$ and T_{01} = $358\,\mathrm{K}$ were applied at the inlet corresponding to the experiment. Figures 5.12 and 5.13 compare the predicted results of the MSk-ε turbulence model and the measured data for nozzles A and B of Moore et al. (1973), respectively. It can be seen that the predicted pressure distributions and the location and magnitude of the condensation shock are quite accurate with the experiments for both the nozzles. Furthermore, the agreement between the predicted and the measured mean droplet radius size at the specified exit location is reasonably good.

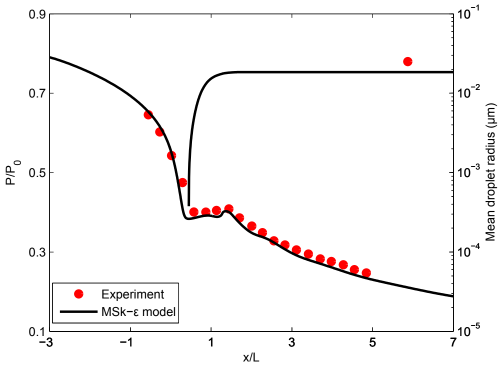

Figure 5.12: Predicted profiles of the (a) pressure ratio and the (b) mean droplet radius along the nozzle centreline compared with the nozzle A experiments of Moore et al. (1973).

For the Moses and Stein (1978) nozzle, two test cases have been chosen. The boundary conditions for the nozzle are P_{01} = 43023 Pa and T_{01} = 366.15 K for case 1, and P_{01} = 41903 Pa and T_{01} = 376.15 K for case 2. Figure 5.14 compares the predicted and the

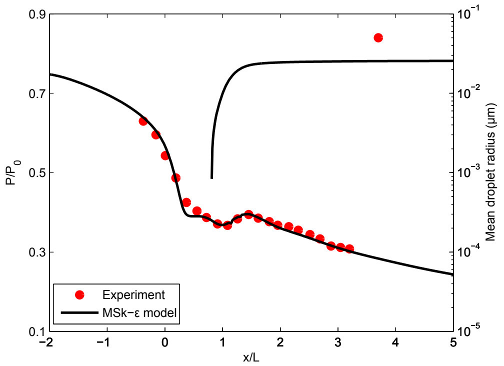

Figure 5.13: Predicted profiles of the (a) pressure ratio and the (b) mean droplet radius along the nozzle centreline compared with the nozzle B experiments of Moore et al. (1973).

measured pressure distribution along the nozzle centreline, in which the numbers 1 and 2 are case numbers. It can be observed that the MSk-ε turbulence model estimated very good agreement with the experiments.

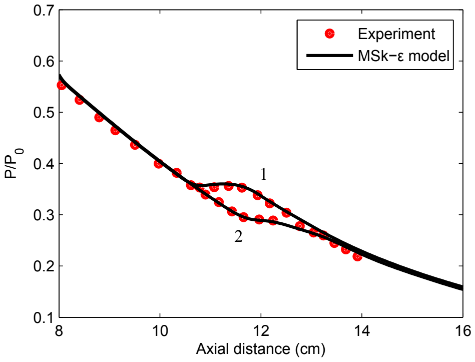

Figure 5.14: Predicted profiles of the pressure ratio along the nozzle centreline compared with the experiments of Moses and Stein (1978). The numbers 1 and 2 represent the test case numbers.

5.2.2 Results of the turbine cascade

The influence of turbulence modelling was investigated with the steam turbine cascade of White et al. (1996). In this study, five experimental cases entailed L1, L2, L3, W1, and H3 of the test series of White et al. (1996) were modelled for distinct validation purposes. Details of the experimental conditions of the selected cases are listed in Table 5.1.

Table 5.1: Experimental conditions for the turbine cascade cases of White et al. (1996).

	Upstream stagnation conditions			Downstream conditions	
Test No.	P_{01} [kPa]	T_{01} [K]	ΔT_{01} [K]	P_2 [kPa]	M_{2s}
L1	40.3	354.0	4.5	16.3	1.24
L2	40.9	354.0	4.0	19.4	1.11
L3	41.7	357.5	7.5	20.6	1.08
W1	41.9	350.0	wet ($\sim$ 1.6%)	17.8	1.20
H3	41.4	376.0	26.0	19.4	1.10

5.2.2.1 Grid independence study

First, the grid independence was studied with the Sk-ε model in order to investigate the influence of grid refinement on the solution. The grids are discussed in detail in section 4.1.2.1. Figure 5.15 presents the wetness fraction predicted with various grids. It is observed that the wetness fraction was influenced by grid refinement. The Grid A was unable to capture as many details of the flow as the other grids. The refined grid was able to resolve the flow with more details and accurately. However, Grid B and Grid C yielded quite similar trends of wetness generation. Further, in Publication III, the average droplet radius contours estimated with different grids are discussed. It can be seen that an adequate grid density is required to properly resolve the flow.

Moreover, the GCI method was used to evaluate the discretisation error measurement. To that end, the average values of the static pressure, velocity, and wetness fraction were extracted for all selected grids in the pitchwise traverse position which was located $50\,\mathrm{mm}$ downstream of the trailing edge. Table 5.2 summarises the grid discretisation errors.

In Table 5.2, Cases A and B indicate the grid refinements from Grid A to Grid B and Grid B to Grid C, respectively. The table shows that the calculated relative error (i.e. e_a) was very small for all parameters. The successive grid refinements (i.e. Case A to Case B) also resulted in the reduction of an extrapolated relative error (i.e. e_{ext}). From the grid refinements, the GCI value was decreased for all three variables. The GCI values indicate that the grid refinement from Grid B to Grid C yielded a negligible discretisation

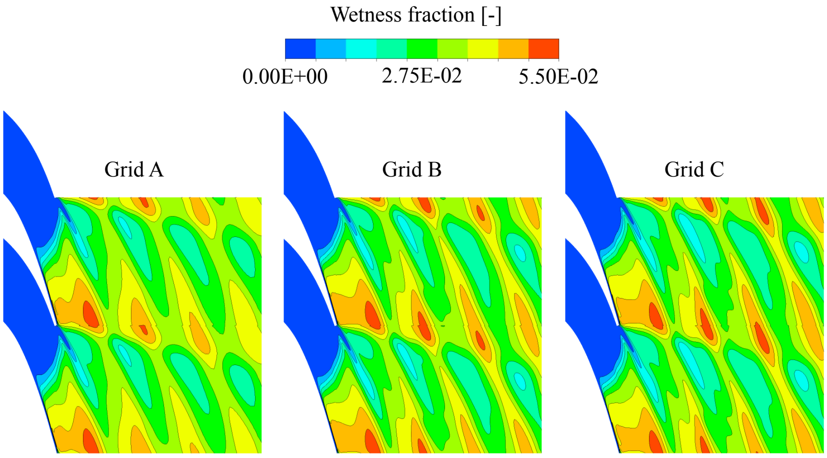

Figure 5.15: Contours of the wetness fraction predicted by the Sk-ε turbulence model with various grid densities.

Table 5.2: Details about the grid discretisation error.

Case	Parameter	e_a (%)	e_{ext} (%)	GCI (%)
Case A	static pressure	0.14	0.25	0.32
	velocity	0.09	0.05	0.06
	wetness fraction	0.18	1.12	1.38
Case B	static pressure	0.05	0.09	0.11
	velocity	0.01	0.01	0.01
	wetness fraction	0.17	1.03	1.30

numerical error. Based on the grid independence study and GCI analysis, an intermediate grid, i.e. Gird B, was selected for further calculations.

5.2.2.2 Performance of various turbulence models

To investigate the performance of turbulence models in wet-steam flows, various turbulence models such as the Spalart-Allmaras, the standard k-ε, the RNG k-ε, the realizable k-ε, the standard k-ω, and the SST k-ω have been used in this work. For this purpose, the low inlet superheat experimental case L1 of White et al. (1996) has been modelled.

Figure 5.16 shows the contours of pressure distribution predicted with various turbulence models. Some variation has been observed in the pressure distribution along the channel particularly in the throat region and downstream of the passage. Moreover, the nucleating and growth processes are rather sensitive to the local pressure distribution and expansion rate. The expansion rate varies in the blade passage, in which it is comparatively low at the entrance but extremely high in the vicinity of the throat. The k-ω and the k-ε models yielded lower flow expansion than other models. However, both the k-ω and the k-ε models failed to capture the condensation disturbance. The results of the pressure distribution around the blade surfaces, nucleation and wetness fraction estimated with all selected turbulence models are compared and discussed in Publication II. The results indicate that the k-ω and the k-ε models predicted a larger nucleation region and subsequently a lower wetness fraction compared to the other models due to lower flow expansion. Other turbulence models yielded relatively similar results.

Further, Figure 5.17 compares the droplet average radius predicted with different turbulence models. The droplet radius distribution is mostly dependent on the total number of droplets formed during the nucleation process. Downstream of the mid-passage, the expansion rate is considerably low, and therefore, the droplet average radius is larger there. However, the flow temperature at blade wakes is higher due to mixing which prevents the droplet growth, and therefore, the droplet average radius is smaller there. Results show that the k-ω and the k-ε models estimated a relatively larger droplet average radius downstream than other models

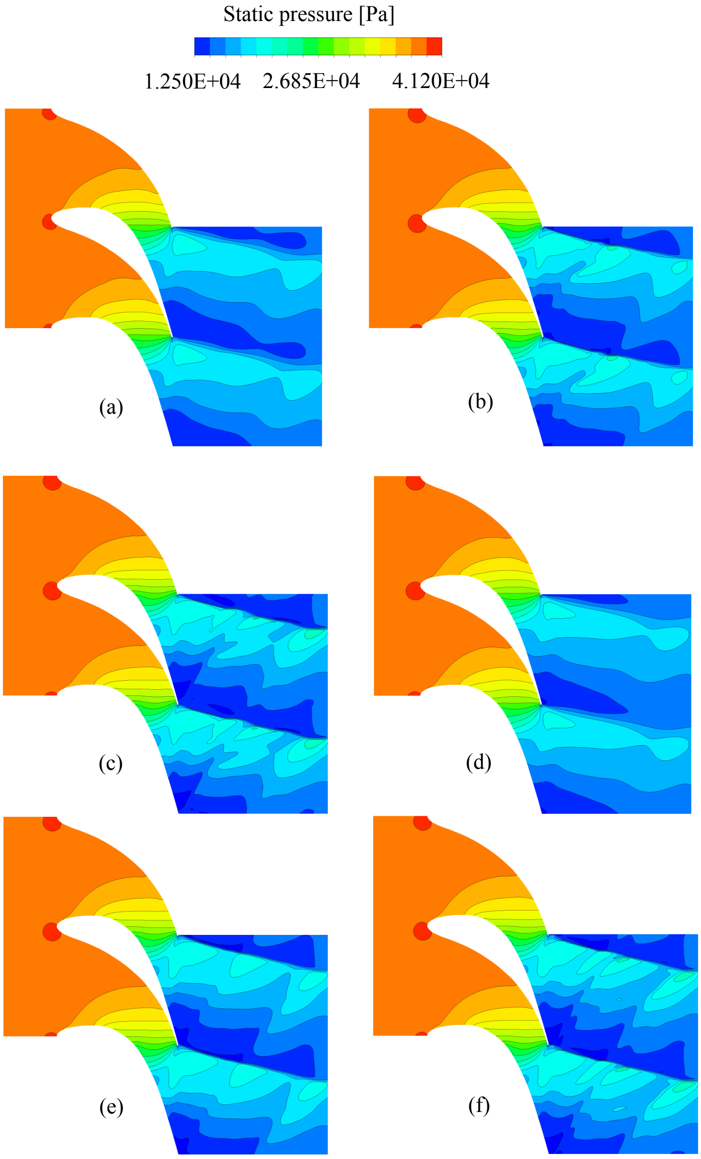

Figure 5.16: Contours of the pressure predicted by (a) the k-ω, (b) the realizable k-ε, (c) the RNG k-ε, (d) the k-ε, (e) the Spalart-Allmaras, and (f) the SST k-ω turbulence models.

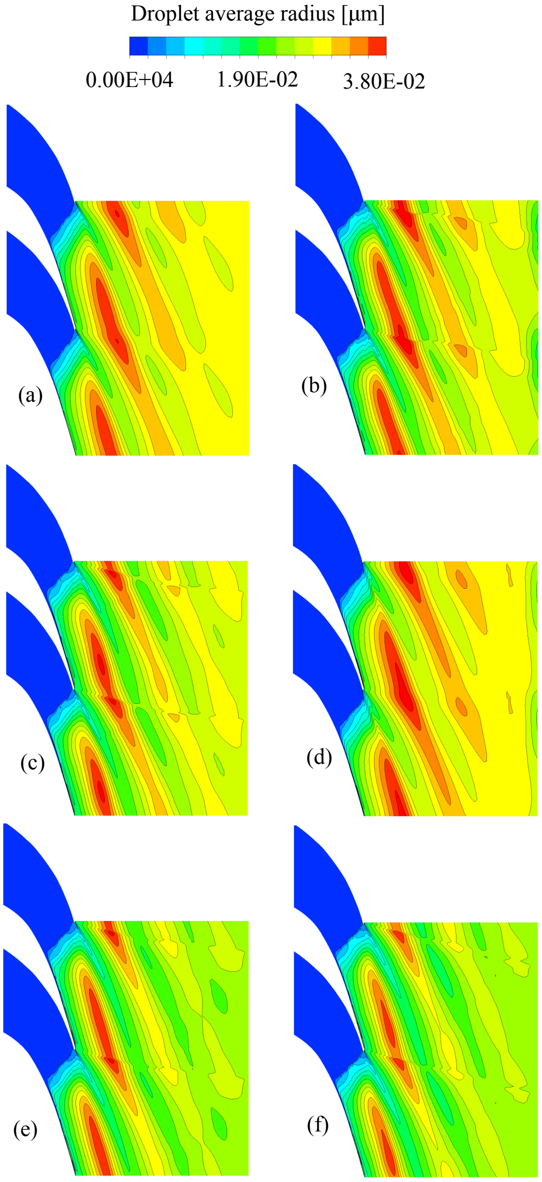

Figure 5.17: Contours of the droplet average radius predicted by (a) the k-ω, (b) the realizable k-ε, (c) the RNG k-ε, (d) the k-ε, (e) the Spalart-Allmaras, and (f) the SST k-ω turbulence models.

5.2.2.3 Effect of turbulence model modification

5.2.2.3.1 The standard k-ε turbulence model

Turbomachinery flows are categorised as wall-bounded flows in which fluid viscosity plays an important role in transport phenomena, particularly near wall surfaces. Also, flow variables vary rapidly within the boundary layer regions. These flows consist of a spectrum of different scales (eddy sizes) in which the largest eddies are of the order of the flow geometry. The large eddies will stretch, be unstable, and subsequently break up into smaller eddies. Further, these small structures experience a similar process and divide into even smaller eddies. This phenomenon continues until a sufficiently short scale is obtained, enabling the fluid viscosity to efficiently dissipate the flow kinetic energy into the internal energy. The above-mentioned process of eddy breakdown from the large scale of injection to the small dissipative scale is called the turbulent cascade process. Thus, it is important to examine the influence of turbulence modelling near the wall surfaces and in the main flow stream.

Figure 5.18 displays the predicted results of turbulent kinetic energy, the turbulent dissipation rate, and turbulent viscosity near the blade surfaces and in the mid-passage. These locations are described in Figure 4.8 in section 4.1.2.1. It is observed that the MSk-ε model predicted a lower value of turbulent kinetic energy compared to the Sk-ε model near the pressure side due to the higher dissipation rate. However, the MSk-ε model estimated a higher turbulent kinetic energy near the suction side, particularly after the second phase generation because of the viscosity modification and the added source terms effects. Further, the turbulent dissipation rate is considerably high for the MSk-ε model near both the pressure and suction surfaces. Therefore, the turbulent viscosity is lower in the MSk-ε model (Figure 5.18 (c)) near wall surfaces compared to the Sk-ε model. The Sk-ε model estimated notably higher values of these turbulent properties at the mid-passage than the MSk-ε model.

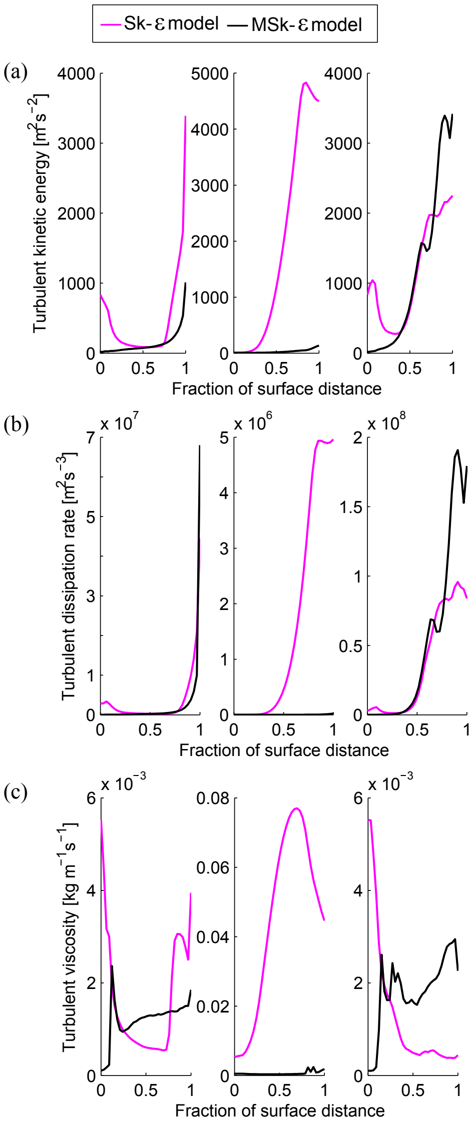

Figure 5.18: Predicted results of the (a) turbulent kinetic energy, (b) turbulent dissipation rate, and (c) turbulent viscosity at near the pressure side (left side), the mid-passage (middle), and near the suction side (right side) for Case L1. Here, 0 and 1 at the x-axis indicate the locations near the leading and trailing edges of the blade, respectively.

Further, Figure 5.19 compares the predicted pressure distribution on the blade surfaces using the Sk-ε and the MSk-ε turbulence models with the experimental data of White et al. (1996). The results of the inviscid calculation are displayed only for the L1 and H3 cases. It can be seen that the inviscid and the turbulence models estimated fairly similar

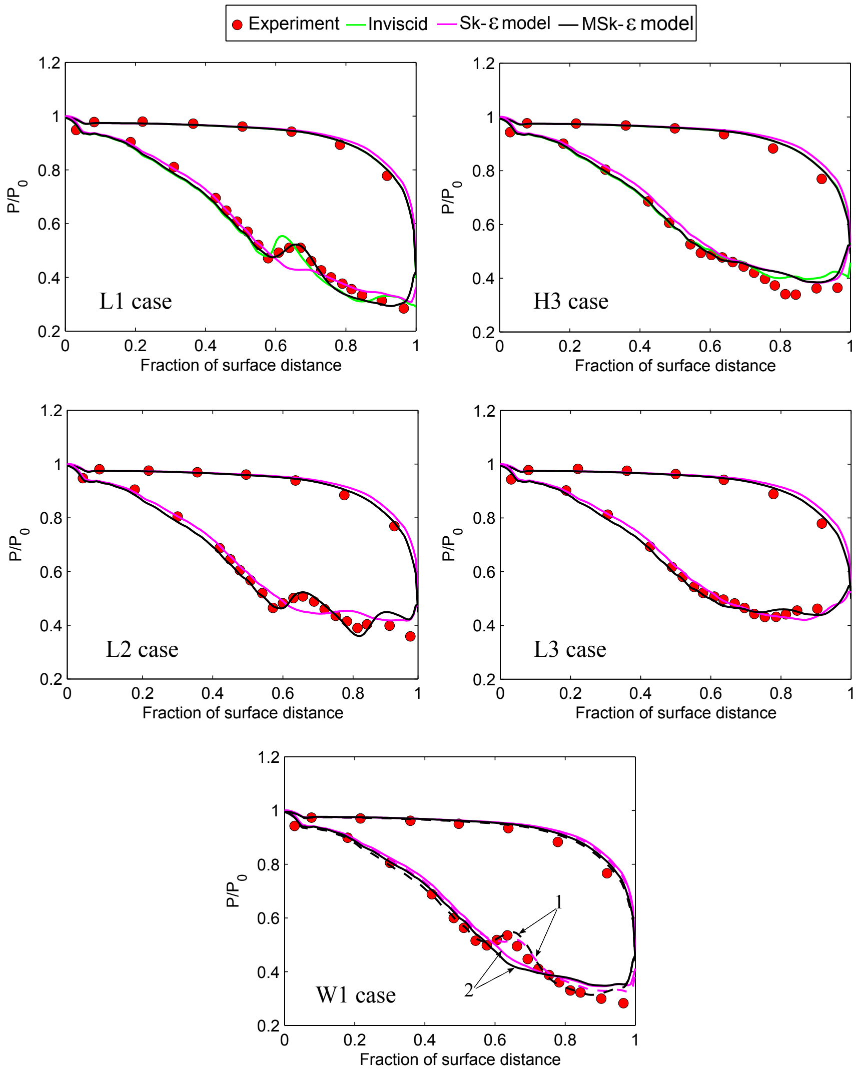

Figure 5.19: Predicted results of blade surface pressure distribution compared with the experimental data of White et al. (1996). In case W1, the numbers 1 and 2 represent the saturated inflow and the wet inflow, respectively.

trends of pressure distribution at the pressure side of the blades for all selected test cases. However, some variation was observed in the suction side pressure distribution. In the case of L1, the inviscid model yielded the correct intensity of the pressure rise, but the location was moved slightly upstream. The Sk-ε model failed to capture the condensation disturbance because the estimated subcooling level in the Sk-ε model is lower than in other models due to smaller flow expansion. As a result, it produced a smaller number of droplets, which directly influenced the amount of latent heat released. The MSk-ε model yielded the correct location and intensity of the condensation disturbance on the suction side. A very good correspondence was observed between the predicted result with the MSk-ε model and the measured data.

In case H3, the inlet superheat was $26\,\mathrm{K}$. Hence, the effect of condensation is absent from the blade surface pressure distributions. In addition, the experimental data displays a second pressure rise close to the blade trailing edge, although this is not observed in the predicted results. This pressure rise is not caused by the condensation phenomenon and it may have appeared due to the reflections from the upper tailboard during measurement (White et al., 1996). The calculated results of pressure distribution of all models are in good agreement with the experiments. However, some discrepancy was noticed between the estimated and the measured results near the suction surface trailing edge. Moreover, the performance of both turbulence models is validated with the other low inlet superheat cases, i.e. L2 and L3 of White et al. (1996). Figure 5.19 shows that the MSk-ε model yielded good results of blade surfaces' pressure distribution for both cases, and agreed well with measured data. The Sk-ε model failed to predict the condensation disturbance for case L2.

The influence of the turbulence model modifications was also investigated with inlet wetness. For this purpose, case W1 of White et al. (1996) was modelled. For the numerical simulations of case W1, the inlet droplet radius ($\approx 0.5\,\mu\mathrm{m}$) and liquid mass fraction ($\approx 1.6\%$) were applied corresponding to the experimental values. Figure 5.19 compares the predicted blade pressure profile of both turbulence models including the wet and saturated inflows with the measured data. It can be observed that both turbulence models failed to predict the pressure rise with the wet inflow condition because the condensation on the primary liquid droplet was high enough to prevent excessive departures from the equilibrium. Therefore, the secondary nucleation was relatively weak and remained up for a longer period. It might also be possible that the utilised values of the inlet wetness fraction and liquid droplet size in the experiments differed marginally from the assumed values (White et al., 1996). In the case of the saturated inflow condition, the MSk-ε model yielded good correspondence with the measurements while the Sk-ε model predicted condensation disturbance with lower strength. In addition, White et al. (1996) provided measured data for the mean droplet radius, static pressure distribution, wetness fraction, and normalised entropy on a traverse plane downstream of the stator for case L1. Therefore, it was also possible to compare the predicted and the experimental results on a traverse plane. The traverse plane is located one quarter of an axial chord length away from the trailing edge. The results of these variables and a detailed discussion are presented in Publication III.

Figure 5.20 shows the Schlieren photograph and the predicted density gradient of case L1 with different models. In the experimental Schlieren photograph of White et al. (1996), the expansion is indicated in red, orange, and yellow, while light blue and green express the small values of the compression. Additionally, the condensation shock, pressure side shock, and suction side shock are labelled $\mathrm{S_c}$, $\mathrm{S_p}$, and $\mathrm{S_s}$, respectively. It can been seen that the inviscid calculation predicted a relatively thinner profile of the $\mathrm{S_s}$ shock due to the absence of viscous dissipation. The MSk-ε model yielded the $\mathrm{S_s}$ shock with a higher intensity than the other models due to the larger entropy generation resulting from the viscous dissipation at the trailing edge. The Sk-ε model failed to estimate the $\mathrm{S_c}$ shock, and the strength of the $\mathrm{S_s}$ shock is weaker than others as well. Generally, the inviscid and the MSk-ε models estimated more accurate shockwave structures than the Sk-ε model, and yielded good agreement with the experiments.

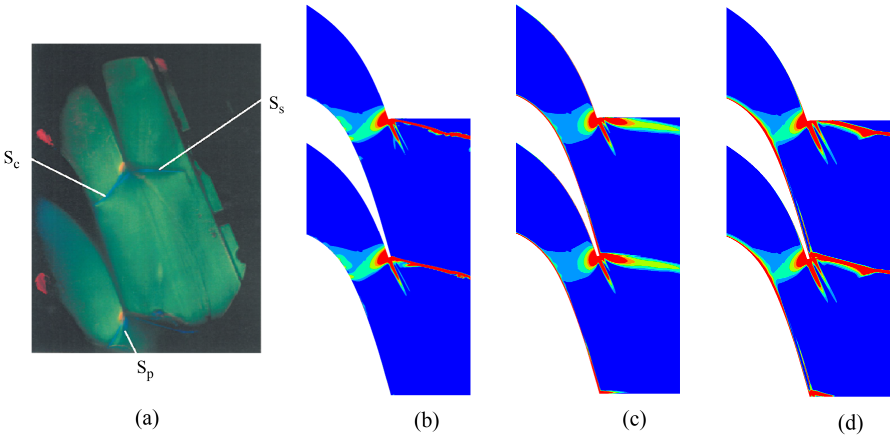

(a) (b) (c) (d)

Figure 5.20: (a) The experimental Schlieren graph of case L1 of White et al. (1996) compared with predicted density gradients of (b) the inviscid calculation, (c) the Sk-ε model, and (d) the MSk-ε model.

Furthermore, the influence of the freestream turbulence intensity on the turbine cascade flow was examined with the values of χ = 0.02, 0.05, and 0.1 with the MSk-ε model. Figure 5.21 presents the contours of the nucleation rate and the wetness fraction estimated with various freestream turbulence intensities using the MSk-ε model. It can be seen that the nucleation zone expanded downstream as the freestream turbulence intensity increased from χ = 0.02 to 0.1. Subsequently, the droplet growth was delayed due to the enlarged nucleation zone. In the case of the wetness fraction, the lower freestream turbulence intensity estimated a relatively higher wetness fraction due to the higher flow expansion rate on the suction side of the blades. Because of the lower flow expansion, the higher freestream turbulence intensity case yielded a smaller number of droplets, which reduced the amount of latent heat released to the vapour phase. Thus, the strength of condensation disturbance declined and its location shifted downstream with the higher freestream turbulence intensity shown in Figure 7 of Publication III.

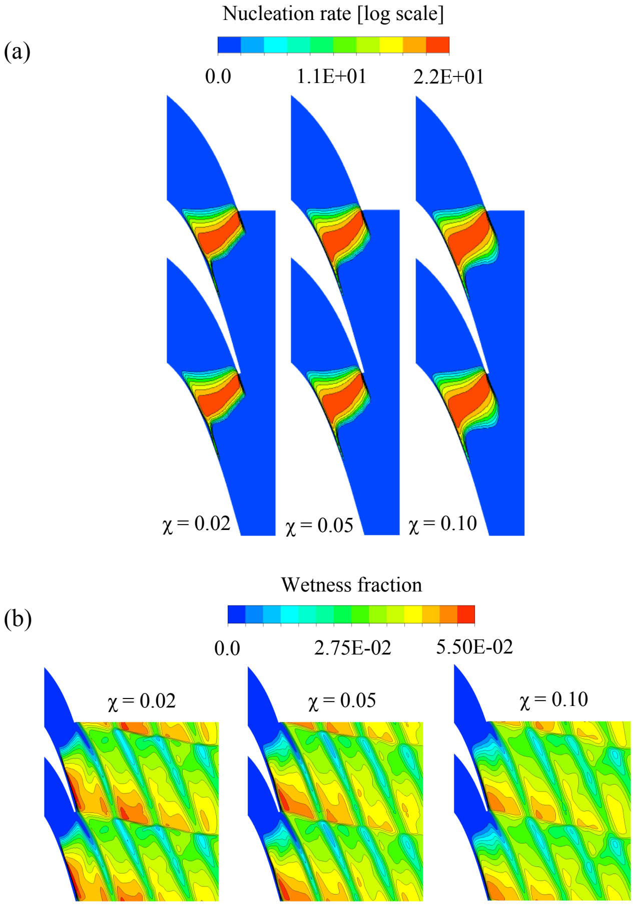

Figure 5.21: Contours of (a) the nucleation rate, and (b) the wetness fraction predicted by the MSk-ε turbulence model with various freestream turbulence intensities.

5.2.2.3.2 The SST k-ω turbulence model

The effect of turbulence modelling on wet-steam flows has been analysed with the modified SST k-ω (MSST k-ω) turbulence model as well. The SST k-ω model was modified in the same manner as the Sk-ε turbulence model. The corresponding modifications in the SST k-ω model is presented in section 3.5.2. In addition, the performance of the MSST k-ω model is compared to the SST k-ω model and discussed in this section.

Figure 5.22 compares the contours of the turbulent viscosity yielded by the SST k-ω and the MSST k-ω turbulence models. It can be seen that the MSST k-ω model predicted a higher value of turbulent viscosity than the SST k-ω model, particularly near the walls and in the wake region of blades. The notable increment in turbulent viscosity for the MSST k-ω model results from the model modification (the source term addition and the viscosity

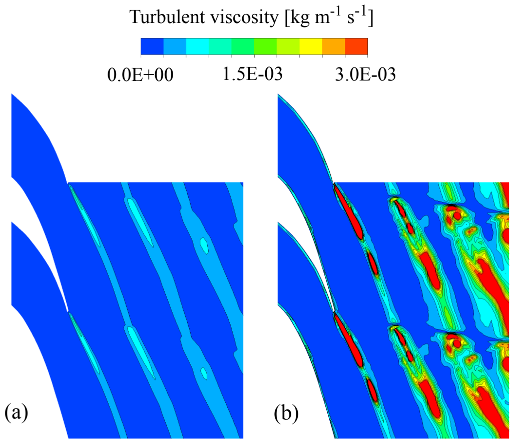

Figure 5.22: Contours of the turbulent viscosity predicted by (a) the SST k-ω and (b) the MSST k-ω turbulence models for the case L1.

modification). Additionally, To shed more light on the effect of turbulence modelling on wet-steam flow, further condensation properties such as the wetness fraction, nucleation rate and droplet radius are predicted near the blade surfaces and in the main flow field using the inviscid calculation and both turbulence models. The related results are described in Publication II. The results indicate that the MSST k-ω model predicted a lower value of the wetness fraction and the nucleation rate near the blade surfaces compared to the other models. The mean droplet radius estimated by the MSST k-ω model is higher than the inviscid and the SST k-ω models.

The contours of nucleation rate, wetness fraction, and droplet average radius estimated by the SST k-ω and the MSST k-ω models are presented in Figure 5.23. It can been seen that the SST k-ω model predicted a higher nucleation rate and its region is larger in the mid passage than that of the MSST k-ω model. However, in the MSST k-ω model, the nucleation region expanded to the wake region of the blade. The MSST k-ω model estimated a higher wetness fraction compered to the SST k-ω model, especially on the suction side of the blade due to a higher expansion rate. Some variation in the prediction of the droplet average radius has been observed between the models. The SST k-ω model calculated a lower droplet average radius than the MSST k-ω model owing to the higher nucleation rate, which estimated a larger number of droplets, preventing droplet growth.

Moreover, the predicted results of the pressure distribution along the blade surface with both the turbulence models and experimental data of White et al. (1996) were compared in selected test cases, and the corresponding results and detailed description are presented in Publication II. Also, the calculated Schlieren profiles were compared with the experimental Schlieren images for the L1 and L3 cases (see Publication II). Based on those results, it was concluded that the MSST k-ω model yielded a more accurate curvature of the shock wave than the other models.

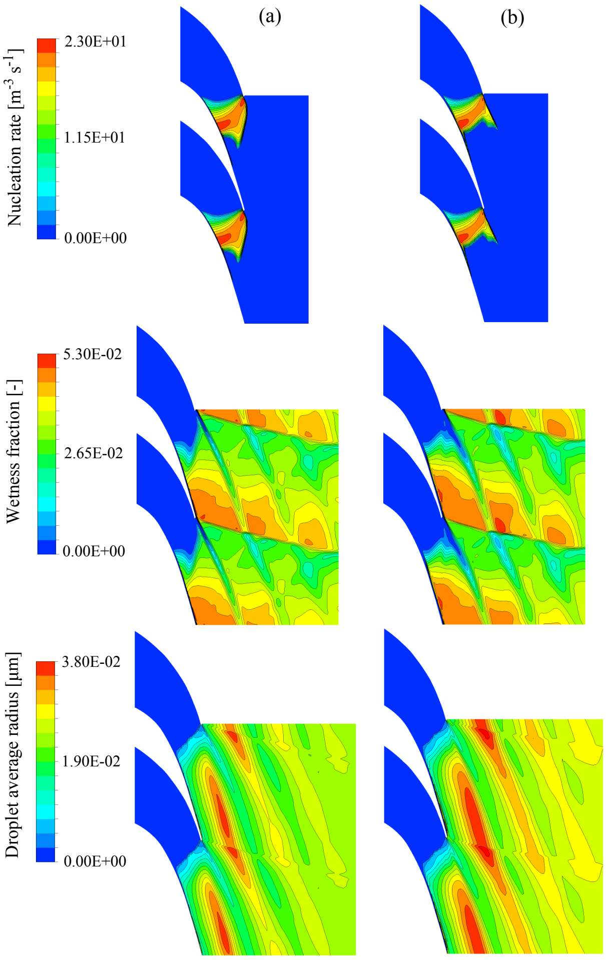

Figure 5.23: Contours of the nucleation rate, the wetness fraction, and the droplet average radius predicted by (a) the SST k-ω and (b) the MSST k-ω turbulence models for the case L1.

Figure 5.24 compares the predicted pitchwise distribution of the mean droplet radius at the traverse position with the experimental data of White et al. (1996). However, the experimental data are available for case L1 and case L3. The droplet radius distribution across the passage mostly depends on the total number of droplets created during the nucleation process which is influenced by the distinct expansion rates along the blade passage, the interaction between trailing edge shock waves and the nucleation zone. It is observed that the mean droplet radius is larger in the mid-pitch region downstream due to the lower expansion rate. Near the blade surfaces, nucleation appears in the rapid expansion region, which results in an enormous number of tiny droplets, and therefore,

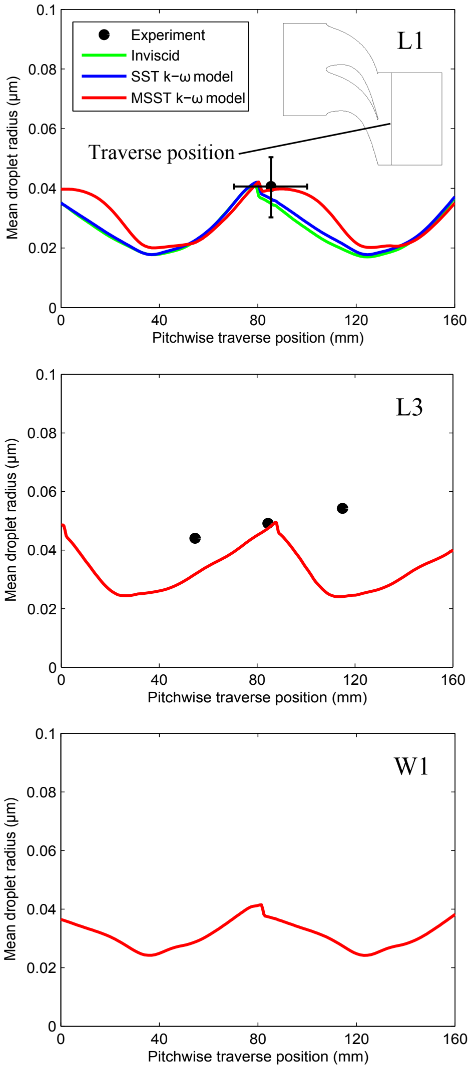

Figure 5.24: Predicted results of the mean droplet radius and comparison with the experimental data of White et al. (1996).

the mean droplet radius is reduced in this region. The MSST k-ω model predicted a higher mean droplet radius than the other models. Further, the results show that the mean droplet radius calculated by the MSST k-ω model agrees well with the measured data for the cases L1 and L3.

The results of the static pressure, wetness fraction, and normalised entropy at the traverse position for both turbulence models and an inviscid case are compared with the experi-

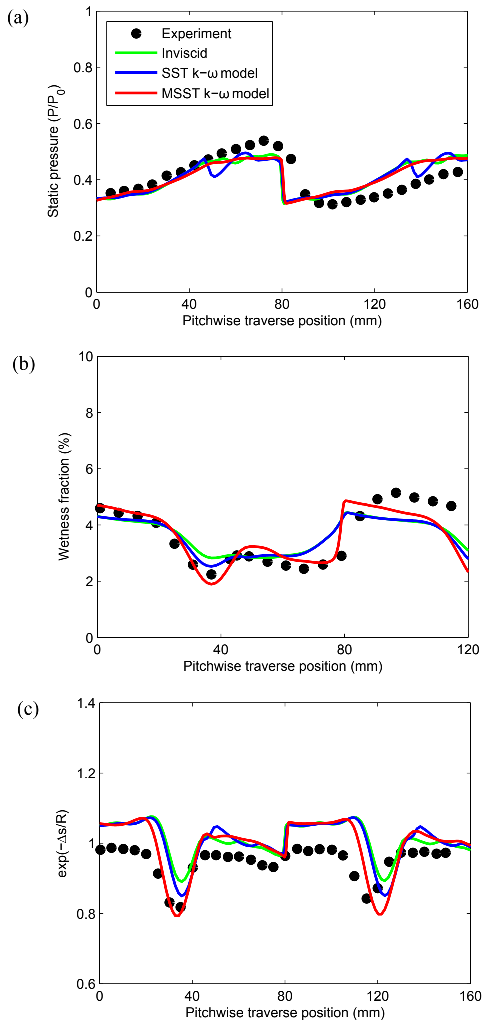

Figure 5.25: Predicted results of the (a) static pressure, (b) wetness fraction, and (c) non-dimensional entropy and comparison with the experimental data of White et al. (1996) for the case L1.

mental data of White et al. (1996) in Figure 5.25. It can be observed that the inviscid and the MSST k-ω models yielded rather similar trends for the static pressure with the measured data. Nevertheless, some variation has been noted in the result of the static pressure for the SST k-ω model. As discussed before, the wetness fraction is relatively low in the wake region of the blade due to the higher the flow temperature. For this reason, the wetness fraction is comparatively low between 35 mm to 45 mm at the traverse position because the trailing edge wake flow passes the traverse plane (Figure 5.25(b)). The MSST k-ω model yielded fairly good agreement with the measured data of the wetness fraction than others. However, some discrepancy has been observed between the predicted and the measured results in the second passage. This could be explained by the fact that the CFD results yielded periodic profiles applying periodic boundary conditions. However, the cascade experiments of White et al. (1996) were conducted with four stator vanes which resulted in three flow passages, and therefore, it could be difficult to achieve periodicity downstream of the flow field. The predicted and measured data of pitchwise variations in a non-dimensional entropy are shown in Figure 5.25(c). The non-dimensional entropy is calculated as $\exp(-\Delta \mathrm{s}/\mathrm{R})$, in which $\Delta \mathrm{s}$ is the increment in a specific entropy above the cascade inlet value. It can be seen that the MSST k-ω model yielded a good trend of entropy distribution with the measured data compared to the inviscid and the SST k-ω models.

5.2.2.4 Loss analysis

The principal aim of turbomachinery designers is to improve the performance of turbomachinery by increasing efficiency. A reduction in the efficiency of turbomachinery translates to loss. The only rational measure of loss in an adiabatic machine is entropy generation (Denton, 1993). The entropy generation in turbomachinery flows is generally addressed via three main processes: (i) viscous friction either in boundary layers or in free shear layers, (ii) heat transfer across temperature variations, and (iii) non-equilibrium processes in very rapid expansions or in shock waves (Denton, 1993). The local entropy generation rates are considerably high in the regions of steep velocity gradients such as blade wakes, edges of separated regions, and vortices, in which the shearing rates are notably high. Further, in these regions, the flow turbulence is the leading phenomenon governing heat, mass, and momentum transfer processes. Therefore, the accurate prediction of entropy generation requires the precise modelling of turbulence in turbomachinery flows. Therefore, in this work, the influence of turbulence modelling on the loss mechanism in the condensing steam flow has been studied.

Figure 5.26 compares the predicted contours of entropy generation by the inviscid calculation and the Sk-ε and MSk-ε models for the case L1 of White et al. (1996). Results show that due to the absence of the boundary layer effect, the entropy generation by the inviscid model was relatively weaker compared to the turbulence models. In both turbulence models, the maximum entropy is generated at the suction surface after the throat and near the trailing edge of the blade. The MSk-ε model predicted higher entropy generation than the Sk-ε model particularly in the blade wake region owing to higher viscous dissipation.

Further, White et al. (1996) provided information about losses that occur due to the irreversible heat and mass transfer during the condensation process. Therefore, the Markov energy loss coefficient based on the entropy increase was calculated in this work. The Markov energy loss coefficient can be defined as

$$\zeta = \frac{T_2 . \Delta s}{0.5 u_2^2}, \tag{5.1}$$

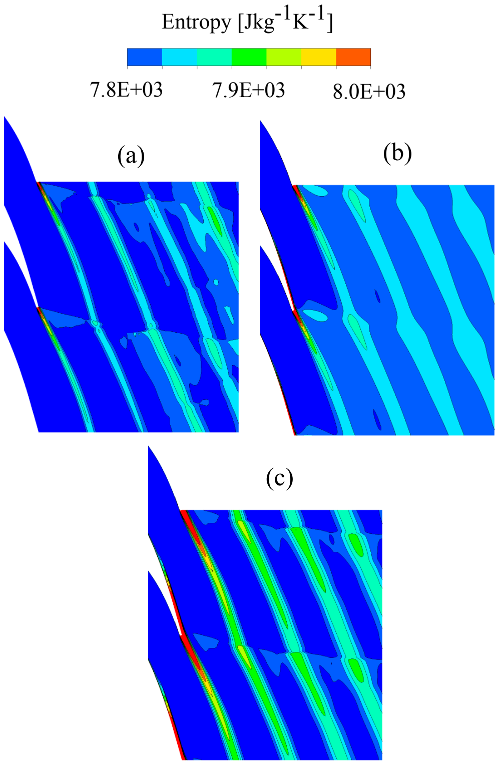

Figure 5.26: Contours of entropy predicted by (a) the inviscid model, (b) the Sk-ε model, and (c) the MSk-ε model.

where all of the utilised flow parameters were the 'mixed-out' values at a plane far downstream of the cascade, i.e. the traverse plane. Originally, White et al. (1996) divided the Markov energy loss coefficient into three components :

(i) Shockwave plus wetness loss: calculated from the mass-averaged values across a section of the traverse plane, excluding the wake regions.

(ii) Viscous loss: calculated by subtracting the shock wave and wetness loss from the mass-averaged loss across the entire pitch on the traverse plane.

(iii) Mixing loss: calculated by subtracting the total mass-averaged loss on the traverse plane from the fully mixed-out loss.

Figure 5.27 compares the predicted and the measured losses for all of the selected cases. In the cases L1 and H3, it can be observed that the Sk-ε model underpredicted the viscous loss. The reason of this discrepancy is that the intensity of the $\mathrm{S_p}$ for the Sk-ε model is relatively lower (Figure 5.20). After the model modification, the MSk-ε model predicted a higher strength of the $\mathrm{S_p}$ compered to the Sk-ε model. Further, the $\mathrm{S_p}$ merges with the

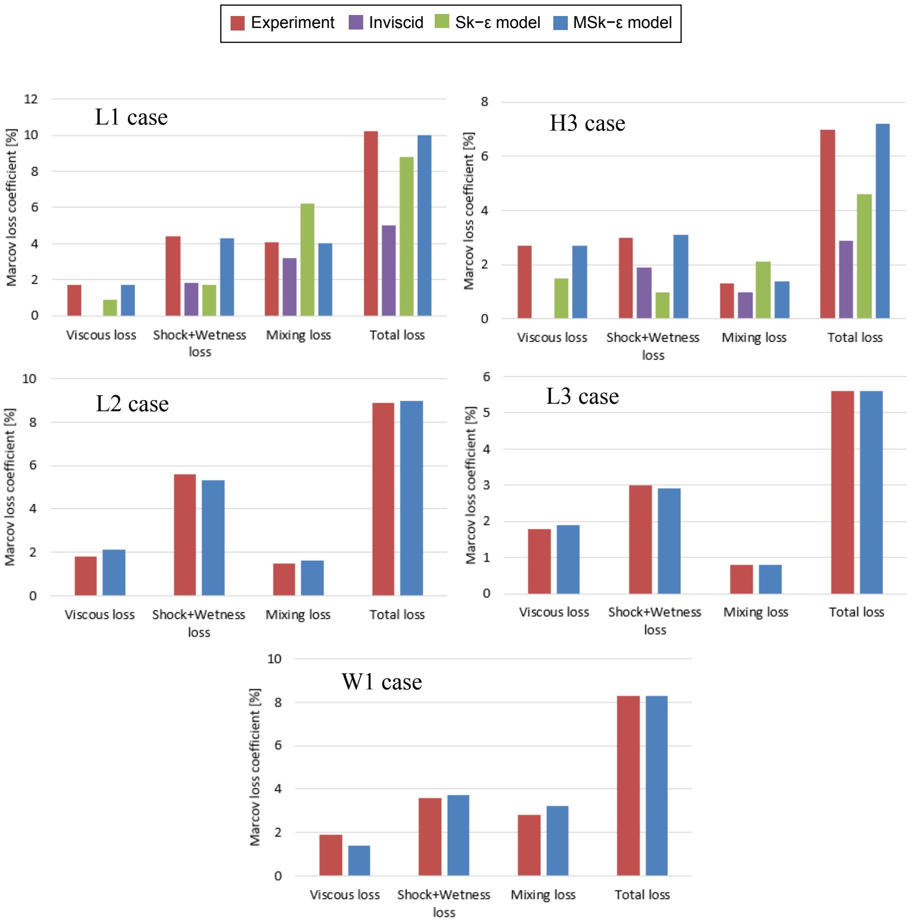

Figure 5.27: Markov loss coefficients predicted by the inviscid, the Sk-ε and the MSk-ε models compared with the experiments of White et al. (1996).

S_c, thickening the suction side boundary layer on the suction side of the adjacent blade, which increases the viscous loss. Therefore, the MSk-ε model yields a higher viscous loss and estimates good agreement with the experimental values for both cases. The inviscid and the Sk-ε models calculated a notably smaller value of the shock plus wetness loss for both cases L1 and H3. In contrast, the predicted magnitude of the shock plus wetness loss for the MSk-ε model corresponded very well with the measured data. Among the selected test cases, the mixing loss for the L1 case was higher than for the other test cases because case L1 was performed with the highest exit Mach number, and the magnitude of mixing loss increases with high Mach numbers. Moreover, the combined action of shock waves, expansion waves, and viscous forces causes a gradual transition from the nonuniform flow condition on the trailing edge plane to uniform conditions far downstream, which generates mixing loss. Results show that the inviscid calculation estimated lower the mixing loss compared to both turbulence models due to a lack of the boundary layer effect, which decreased the viscous forces. The Sk-ε model overpredicted the mixing loss for both cases. The increment resulted in a mixing loss measure for the Sk-ε model, which can be explained by the larger value of the turbulent viscosity produced by the higher entropy generation particularly in the mid-passage downstream of the stator (light blue in Figure 5.26). The MSk-ε model accurately estimated the mixing loss for cases L1 and H3. The total loss, which is the sum of the viscous loss, shock plus wetness loss, and mixing loss, is calculated as well. It is observed that the inviscid calculation failed to estimate the total loss for both cases, while the Sk-ε model yielded some variation in the measured losses. The MSk-ε model predicted accurate loss trends. Further, the performance of the MSk-ε model is analysed by calculating losses for other test cases i.e. L2, L3 and W1. The results show that the MSk-ε model evaluated losses accurately.

Furthermore, Figure 5.28 compares the predicted Markov loss coefficients for the SST k-ω and the MSST k-ω models with the values measured for the selected cases of White et al. (1996). For the case L1, the MSST k-ω model yielded a larger value of viscous loss than the SST k-ω model due to the higher intensity of the shock profile. The SST k-ω model underestimated the viscous loss, the shock plus wetness loss and the mixing loss. In the MSST k-ω model, the rate of entropy generation is considerable in the blade wake, and consequently, the magnitude of mixing loss is relatively higher than the measured data for all selected cases. Also, the MSST k-ω model predicted the wetness loss correctly and determined good agreement with the experiment for all cases. Overall, the calculated magnitude of the total loss for the MSST k-ω model corresponds well with the measured values. Based on the presented analysis, it can be concluded that both the MSk-ε and the MSST k-ω turbulence models predicted accurate condensation phenomena in nozzles and in turbine cascade. Therefore, the MSk-ε and the MSST k-ω turbulence models are recommended for wet-steam flow modelling.

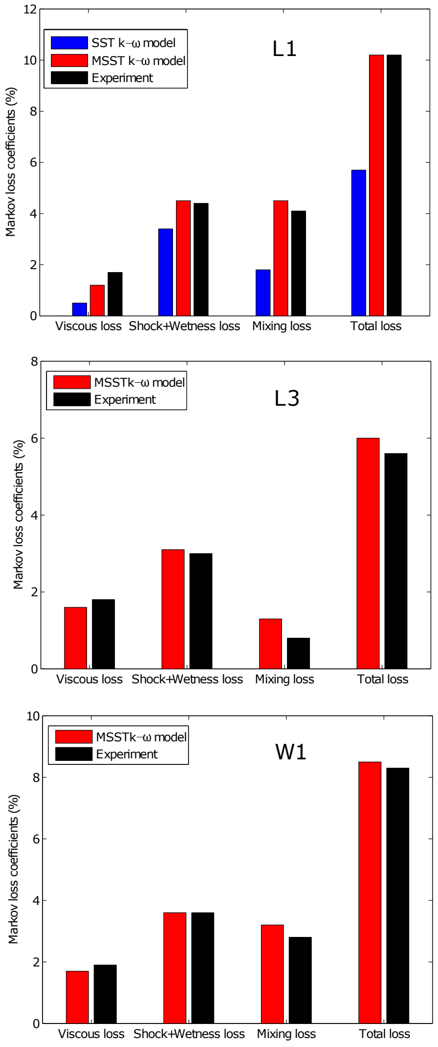

Figure 5.28: Markov loss coefficients predicted by the SST k-ω and the MSST k-ω models compared with the experiments of White et al. (1996).

5.3 Influence of trailing edge geometry on condensing steam flows

5.3.1 Effect on condensation properties

It is a fact that the condensing process is quite sensitive to the variation of the local flow field as well as to boundary conditions and particularly to some flow phenomena which affect the nucleation process, for example the viscous boundary layer and shock wave. Moreover, the LP turbine blade profiles, including their shape and thickness, may have some influence on the condensing phenomena in the LP turbine and on boundary layers. Literature in the field includes studies on the aerodynamics of LP turbine blades. However, few researchers have reported analyses on the sensitivity of the trailing edge geometry to condensation phenomena in the LP turbine. It is obvious that the shapes and the size of the trailing edge of the turbine blades have a strong influence on the pressure fields within the blade passage. Nevertheless, the formation of the liquid phase is quite sensitive to the local rate of change of the pressure fields. Therefore, it could be anticipated that the trailing edge shapes would have a significant impact on droplet growth rates and other key parameters of condensing flow.

The influence of trailing edge geometries on the non-equilibrium homogeneously condensing steam flow in an LP turbine is interesting. Therefore, in the present work the influence of trailing edge geometries was also studied using ANSYS FLUENT. The MSST k-ω turbulence model was utilised for modelling the flow turbulence. For this purpose, three distinct shapes of the trailing edge of the stationary cascade of turbine blades of White et al. (1996) were considered and their corresponding effects on condensation phenomena were examined. Three trailing edge geometries: (i) the conic trailing edge (CTE), (ii) the semicircular trailing edge (RTE), and (iii) the square trailing edge (STE) were examined (Figure 5.29). In their original experiments, White et al. (1996) used the sharp trailing edge profile.

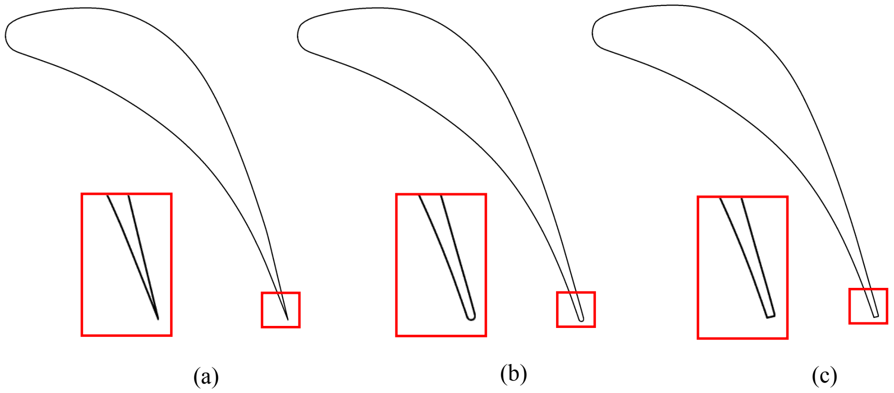
(a) (b) (c)

Figure 5.29: The stator blade trailing edge profiles: conic trailing edge (left), semicircular trailing edge (middle) and square trailing edge (right).

In the RTE profile, the pressure side and the suction side blade surfaces at the trailing edge were merged with a semicircular curve which includes a circle radius of 0.8045 mm. The STE profile was approximated from the RTE profile. To generate the STE profile, the circle of the RTE profile was cut at its centre in the axial direction with a 15° angle. The blade chord in the STE profile is lesser approximately 0.74% than the RTE profile blade chord. The CTE profile was shaped by joining the suction surface and pressure surface, where the angle between both the surfaces was about 8°. However, this angle was generated by tapering the suction surface. The suction surface of the blade was only tapered from 0.716 to 1 if the total distance of the blade suction surface was between 0 and 1, 0 indicating the leading edge and 1 indicating the trailing edge while the pressure surface was unchanged. Therefore, the original throat area of the passage was unaffected for the CTE profile. Due to suction surface blade tapering in the CTE profile, the blade chord was reduced approximately 1.23% than the RTE profile blade chord. Around the leading and trailing edges of the stator blade, a sufficiently fine grid was generated to resolve the boundary layers. Grid generation, grid density and simulation set-up are described further in Publication IV.

The L1 case of White et al. (1996) was selected for this study. The experimental conditions of the L1 test are specified in Table 5.1. First of all, the predicted pressure distributions around the blade surfaces were compared for all cases together with the experimental data (see Publication IV). However, the pressure surface was unchanged in all cases, and therefore, the static pressure distribution of the pressure side of the blade is almost the same for all shapes. Also, it could be observed that the location of the pressure rise at the suction surface for all cases was unaffected due to the trailing edge shapes. Small discrepancies have been observed on the suction side near the trailing edge between the selected trailing edge shapes. Especially the STE shape yielded a marginally lesser diffusion in the rear part of the blade.

Figure 5.30 shows the contours of the static pressure predicted by the CTE, the RTE, and the STE profiles. It can be seen that the pressure distribution along the channel and specially, downstream of the passage is affected by the trailing edge shapes. In the CTE profile, the pressure distribution is influenced near the rear part of the suction surface due to tapering. However, expansion was the highest in the RTE profile, notably at the end of the pressure side (tiny region in blue). Therefore, the subcooling level could be higher in the RTE case than in the other cases, which influences the nucleation rate. Figure 5.31 displays the Mach number contours predicted by the CTE, the RTE, and the STE profiles. The CTE profile estimated the higher Mach number than the other profiles, likely due to the higher pressure drop near to the trailing edge of suction surface.

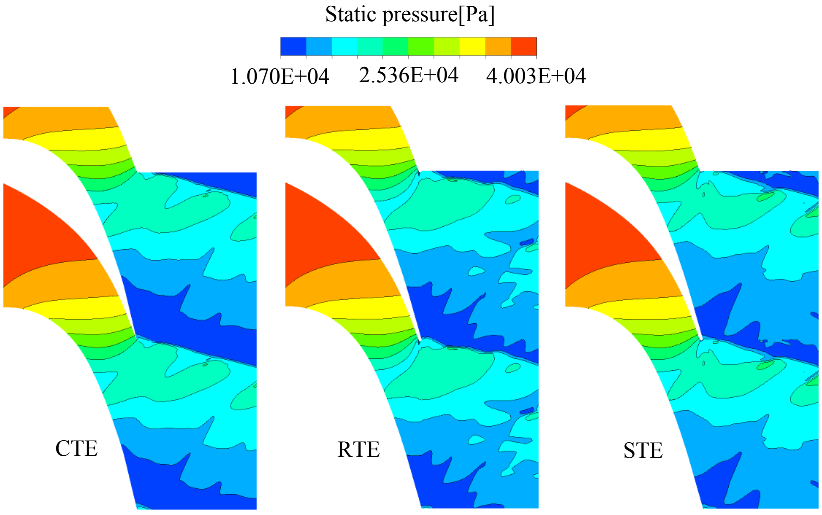

Figure 5.30: Comparison of the static pressure contours predicted by selected trailing edge shape cases.

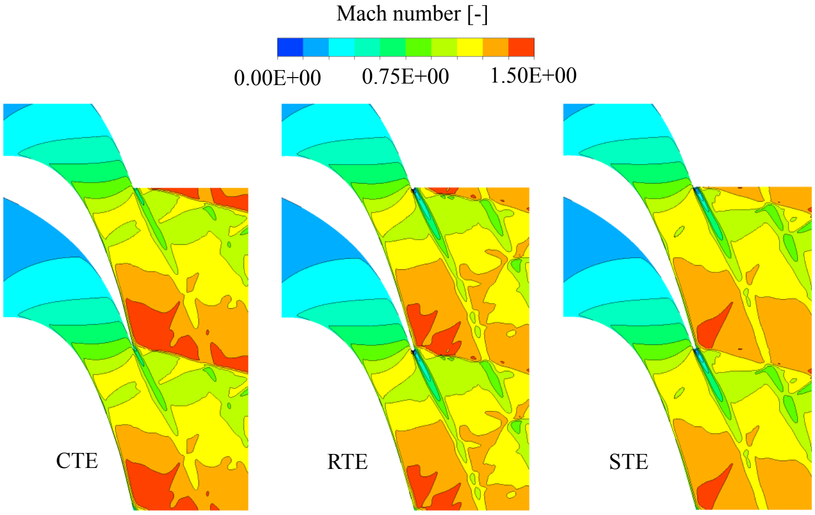

Figure 5.31: Comparison of the Mach number contours predicted by selected trailing edge shape cases.

The condensation process is quite sensitive to the local pressure distribution and expansion rate. The rapid condensation zone appears downstream of the throat. In condensing steam flows, the nucleation rate is mostly high near the suction surface and at the trailing edge of the pressure surface. This results from rapid acceleration and consequent high

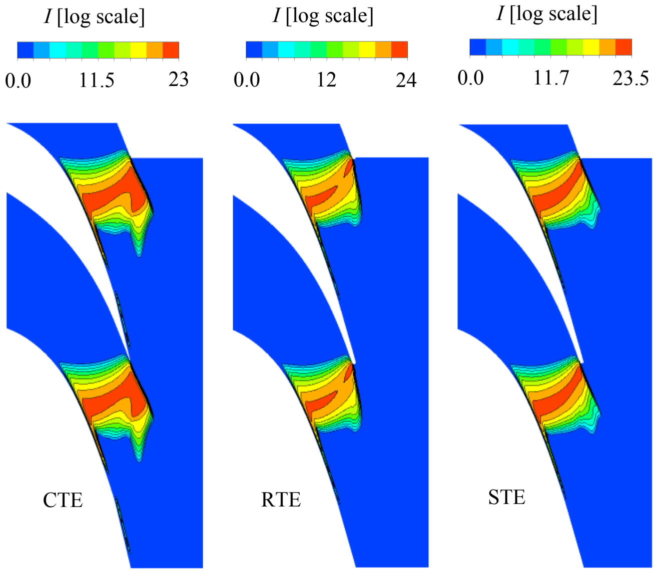

Figure 5.32: Comparison of the nucleation rate contours predicted by selected trailing edge shape cases.

subcooling. Figure 5.32 represents the contours of the nucleation rate predicted by the CTE, the RTE, and the STE profiles. It can be observed that the nucleation rate is lower and the nucleation region is longer in the mid-pitch region of the blade passage for all cases. The highest nucleation rate was observed in the case of RTE because of the highest expansion, while the lowest nucleation rate resulted in the case of CTE. Moreover, the nucleation zone was extended further to the blade wake region for the CTE case due to the suction surface tapering because the flow area near the rear part of the trailing edge for the CTE profile was enlarged. Furthermore, it is a fact that the distinct pressure and velocity distribution around the blade trailing edge instigates a variation in the droplet number distribution. However, the number of droplet is relatively larger in the wake region of the blade compared to the mainstream. This is due to the rapid deflection of steam at the pressure surface near the trailing edge where the nucleation rate reaches its peak value. The influence of the trailing edge shape on the droplet number per unit volume is presented and discussed in Publication IV.

The predicted contours of the average droplet radius for all cases are compared and displayed in Figure 5.33. When lower nucleation occurs, the droplet growth rate is dominant and the droplets are relatively larger. Therefore, the CTE estimated a larger droplet radius compared to other cases. However, the RTE profile yielded a relatively smaller droplet radius owing to the higher number of droplets. Moreover, the trailing shapes may also influence the shock wave structure generated at the trailing edge and its angles. Therefore, the influence of the trailing edge shapes on the shock wave profiles was studied.

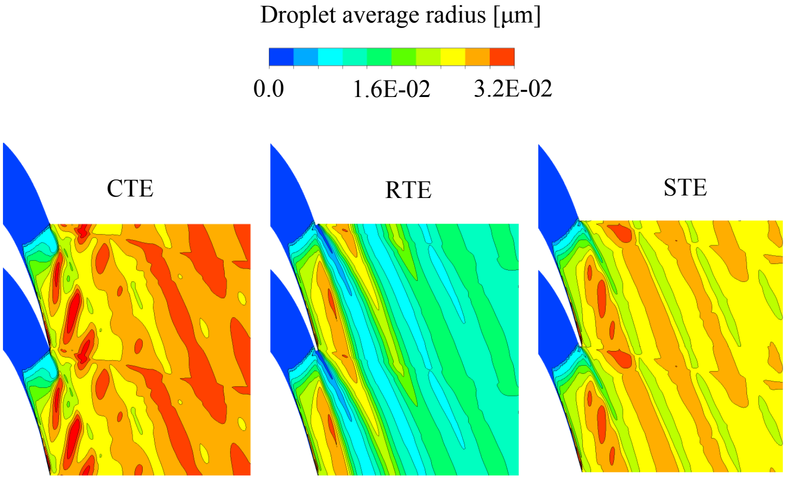

Figure 5.33: Comparison of the droplet average radius contours predicted by selected trailing edge shape cases.

Figure 5.34(a) presents the Schlieren image of the L1 case of White et al. (1996). As discussed before, the abbreviations $\mathrm{S_c}$, $\mathrm{S_p}$, and $\mathrm{S_s}$ describe the condensation shock, pressure side shock, and suction side shock, respectively. It can be seen that the predicted shock-wave profiles of the CTE, the RTE, and the STE have some variations. The intensity of $\mathrm{S_p}$ in the CTE profile was marginally lower than in other profiles, while the RTE profile yielded the maximum strength of $\mathrm{S_p}$. $\mathrm{S_p}$ merges with $\mathrm{S_c}$ and thickens the suction side boundary layer on the suction side of the adjacent blade. Some reflections have been observed for the CTE and the RTE cases that interact with the $\mathrm{S_s}$. However, these reflections did not result from the outlet boundary but were produced somewhere downstream. It appears that the wake hits the reflected shock wave which generated this disturbance. It was rather difficult to find accurate information about the corresponding angles between the shock waves. However, the angle of $\mathrm{S_s}$ to the blade wake was estimated for all profiles: $\theta_{\mathrm{CTE}} \approx 48°$, $\theta_{\mathrm{RTE}} \approx 52°$, and $\theta_{\mathrm{STE}} \approx 58°$. Here, the subscripts indicate the respective profiles of the trailing edge shape. Additional results are presented in Publication IV.

Further, the influence of trailing edge shapes on condensing steam flow was studied by comparing the flow parameters more downstream of the blade passage. Figure 5.35 shows the pitchwise distribution of the static pressure, wetness fraction, and normalised entropy at the traverse position estimated with different trailing edge shapes together with the data measured by White et al. (1996). It is interesting to observe that the steep location was changed because of the static pressure and wetness fraction from $75\,\mathrm{mm}$ to $85\,\mathrm{mm}$ due to the interaction of the shock wave $\mathrm{S_s}$ on the traverse plane for all cases. The spotted variation in the steep location for each case due to dissimilarity in the shock wave angles has previously been discussed. The wetness fraction is lower and the wake flow passes the traverse plane. This is the results of the increment in flow temperature due to mixing. For

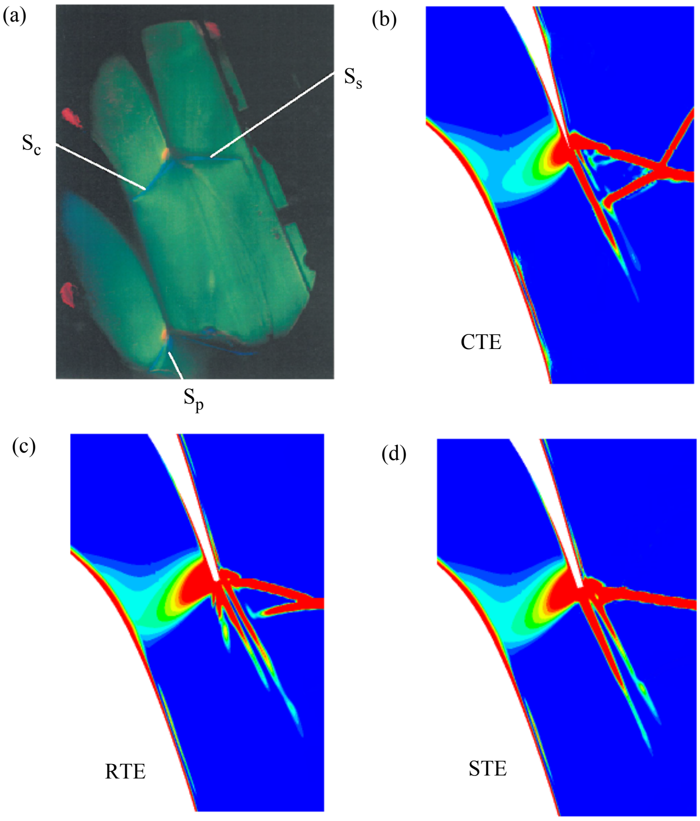

Figure 5.34: (a) Schlieren graph of the L1 case of White et al. (1996) compared with predicted density gradients of the (b) CTE (c) RTE, and (d) STE cases.

non-dimensional entropy, some discrepancies were noticed between the predicted results of different trailing edge shapes, especially in the blade wake region. The CTE profile estimated a relatively lower value of non-dimensional entropy than the RTE and STE profiles.

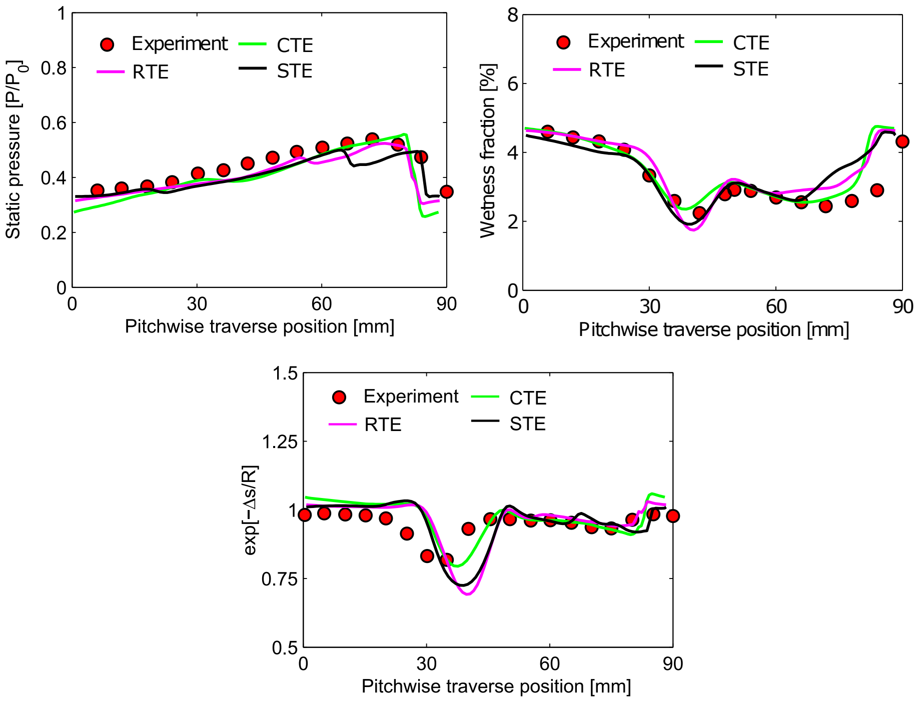

Figure 5.35: Predicted results of the static pressure, wetness fraction, and non-dimensional entropy compared with the experiments of White et al. (1996).

5.3.2 Loss analysis

The influence of trailing edge shapes on losses was studied. However, before discussing losses, the effect of trailing edge shapes on the local entropy generation rates should be assessed. In fact, the trailing edge shape and its thickness are the key parameters which directly influence entropy generation and flow mixing in the wake region of the blade passage. Turbulence plays a dominant role in the wake region as well. The effect of the trailing edge shape on the turbulent kinetic energy is presented in Publication IV. Results show that only the STE profile predicted the maximum turbulent kinetic energy due to a relatively strong wake region. Figure 5.36 shows the contours of entropy generation. It can be observed that the STE profile yielded the maximum entropy generation due to higher viscous dissipation. The CTE profile predicted the lowest entropy production due to a lack of blade wake.

Furthermore, the Markov energy loss coefficient based on the entropy increase has been calculated and compared with the measured data for all cases in Figure 5.37. The loss

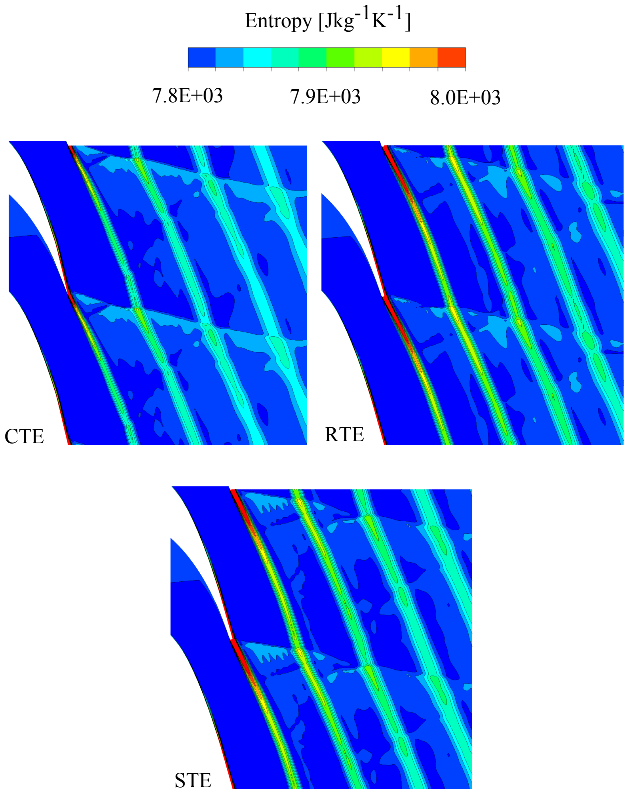

Figure 5.36: Predicted contours of entropy for the CTE, RTE, and STE cases.

estimation was based on the given definition in White et al. (1996), which was described previously in section 5.2.2.4. For the loss analysis, both the L1 and H3 cases were simulated with the CTE, RTE and STE profiles, where H3 was the high inlet superheat case were ΔT_{01}= 26.0 K.

In the case of viscous loss, the RTE profile estimated the highest value for both L1 and H3 cases. As discussed before, the pressure side shock wave merges with the condensation shock wave and thickens the suction side boundary layer on the corresponding suction side of the adjacent blade which increases the viscous loss. The intensity of the pressure side shock wave for the RTE profile was relatively higher than in other cases. This is the reason for the higher viscous loss prediction in the RTE case. The CTE profile yielded a lower value of shock plus wetness loss than the other cases. However, the shock plus wetness losses estimated by the RTE and STE profiles for the L1 and H3 cases were almost in the same range. In the experiments of White et al. (1996), the L1 and H3 cases were studied with $\mathrm{M}_{2\mathrm{s}}$ = 1.24 and 1.10, respectively. The mixing loss of the L1 case was much higher than that of the H3 case. For both cases, the mixing loss linearly increased from the CTE case over the RTE case to STE case. However, mixing loss is associated

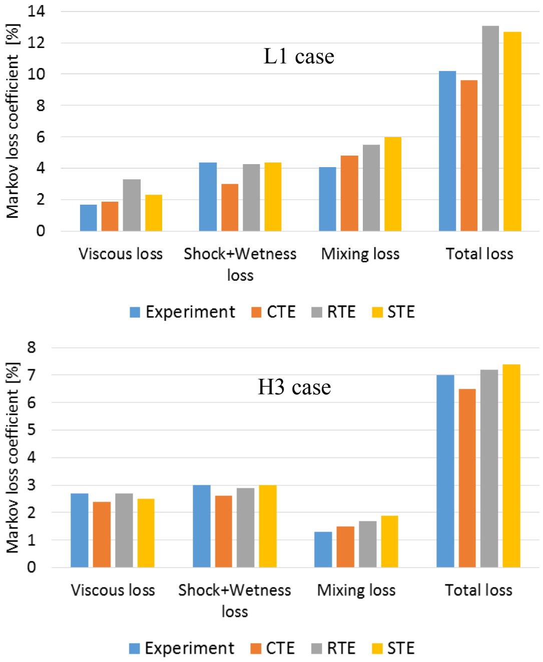

Figure 5.37: Predicted Markov loss coefficients for the CTE, RTE, and STE cases compared with the experiments of White et al. (1996).

with the wake and entropy generation. Therefore, the STE profile estimated the highest mixing loss for L1 and H3 due to a stronger wake than that of the other profiles. Overall, the total losses predicted for L1 and H3 with the CTE profile were relatively smaller than with the other cases.

5.4 Influence of unsteadiness on condensing steam flows

It is a fact that the flow in an LP turbine is strongly three-dimensional due to the arrangement of the stator and rotor blade rows. The stator-rotor interaction vigorously influences the flow phenomena in the LP turbine. Also, the wakes of the upstream blades entered the succeeding blades increase the flow mixing. Due to wake-chopping and strong mixing, the flow temperature fluctuates in the rotor passage. The temperature fluctuations induce variation at the subcooling level, nucleation and subsequently the droplet number and droplet sizes in the corresponding regions. However, the influence resulting from the flow fluctuations would not be achieved by steady calculations. In this work, both steady and unsteady simulations have been performed to analyse the influence of unsteadiness on condensing steam flows. For this purpose, a 3D stator-rotor stage was modelled with the ANSYS CFX solver. Details on the computational domain and boundary conditions are listed in section 4.1.3.

Figure 5.38 shows the turbulent viscosity contours at the mid span of the blades predicted with steady and unsteady simulation in which the unsteady contour represents an instantaneous profile of the mid-period of one pitch transition of the rotor rotation. All of the presented contours for unsteady simulation in this section are instantaneous. As explained before, a steady state simulation was conducted with a mixing plane between the rotating and stationary blades, while the unsteady simulations were carried out with a sliding mesh. It can be seen in the unsteady simulation result that the wakes coming

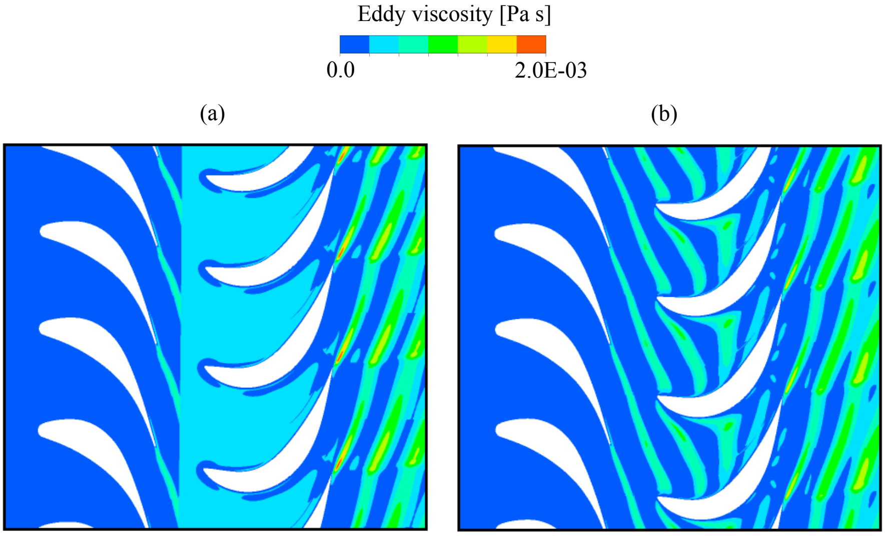

(a) (b)

Figure 5.38: Contours of the turbulent viscosity predicted by (a) steady state and (b) unsteady (at 16850 timestep) simulations. The contours represent the plane at a 50% span.

from the upstream interact with the downstream rotor blade row, and wake-chopping is clearly visible. The stator wakes approach and are split in two parts from the leading edge of the rotor blade. Both wakes travel through the rotor passage and subsequently merge with the downstream flow of the rotor. However, the steady state simulations were unable to capture these wake-chopping phenomena. Due to the mixing plane assumption in the steady state simulation, almost uniform turbulent eddy viscosity patterns were observed at the rotor inlet.

Further, to examine the influence of unsteadiness on condensing steam flow, the pressure and temperature of the flow were recorded throughout the simulation at specified locations, i.e. MP1 and MP2. Figure 5.39 displays the recorded history of flow variables and the data recording locations. It can be seen that the temperature and pressure oscillate only slightly, i.e. less than 1 K in temperature and 270 Pa in pressure at MP1. However, the oscillations in pressure and temperature at MP2 were higher, about 4800 pascal and 35 K, respectively. It is obvious that the oscillation frequency in the rotor downstream is higher due to rotational motion, wake-chopping and flow mixing.

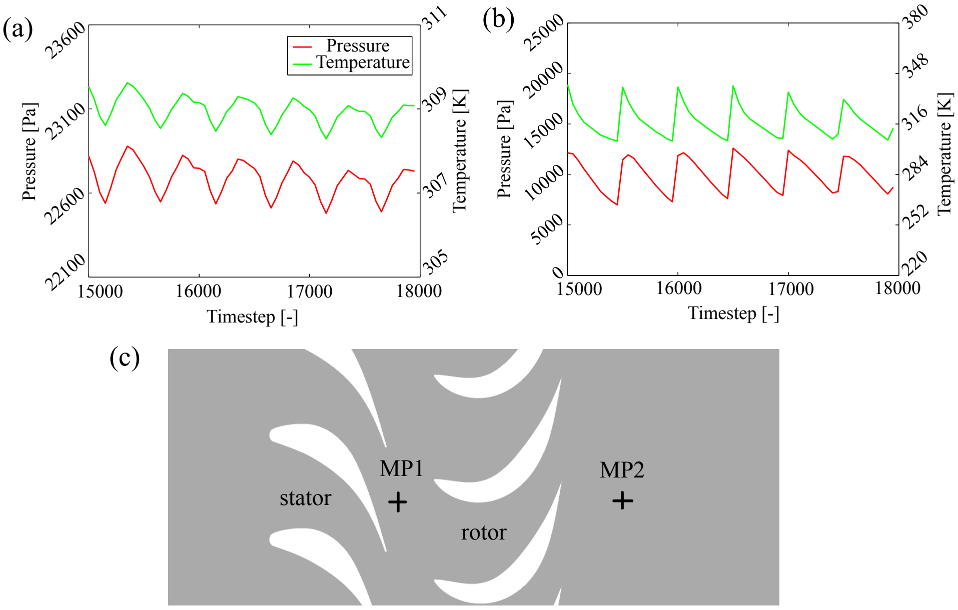

Figure 5.39: The pressure and temperature fluctuations during unsteady calculations recorded at locations (a) MP1 and (b) MP2.(c) The data recording locations in the computational domain. The points MP1 and MP2 are located at a 7.5% blade chord distance from the trailing edge of the stator and a 37% blade chord distance from the trailing edge of the rotor at 50% span, respectively.

Figure 5.40 displays the temperature profiles for the steady and unsteady calculations at a 90% span of the rotor. It can be observed that upstream wakes enter the corresponding rotor blade passage in the unsteady calculation and therefore, the temperature in that region is spread out. These upstream wakes interact in such a way to the condensation shock which subsequently influences the rotor wake flows. However, due to a lack of wake-chopping in the steady state simulation, the temperature fluctuation in the rotor blade passage and also downstream is rather different than in the unsteady simulations.

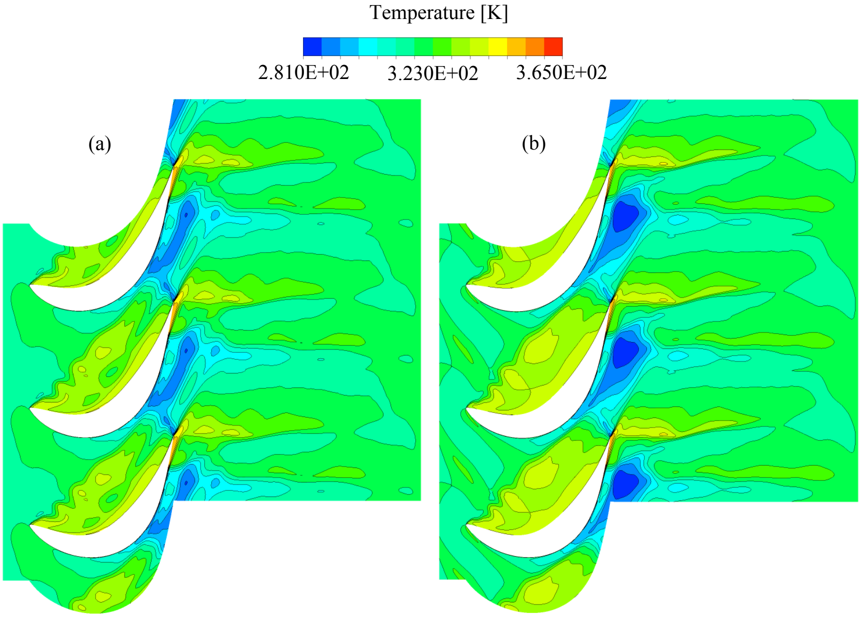

Figure 5.40: Contours of the temperature distribution predicted by (a) steady state and (b) unsteady (at 16850 timestep) simulations at a 90% span of the rotor.

Further, the subcooling and nucleation rate contours predicted by the steady state and unsteady calculations are presented in Figures 5.41 and 5.42, respectively. The figures exhibit that the critical conditions for wetness formation have been met for the stator within the throat region where the flow becomes transonic. The level of subcooling was reduced from the hub to the shroud surfaces for the stator, while for the rotor blade passage the level of subcooling was increased from the hub to the shroud surfaces. The maximum subcooling level reached up to 36 K at a 10% span in the stator. However, some differences in

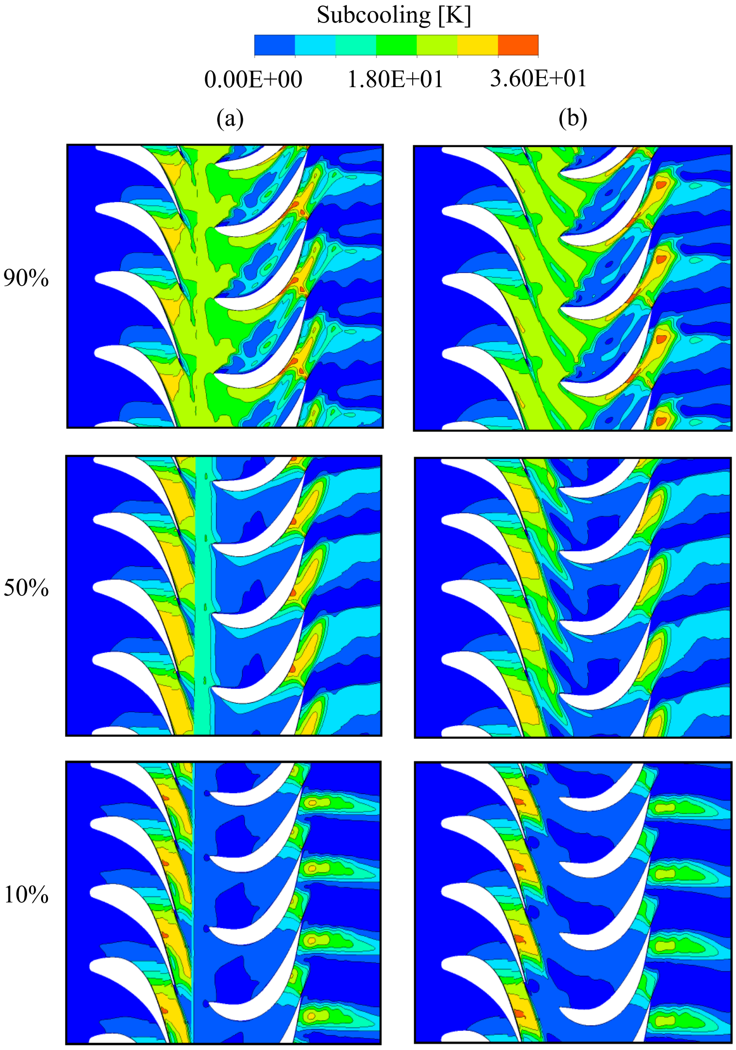

Figure 5.41: Contours of the subcooling predicted by (a) steady state and (b) unsteady (at 16850 timestep) simulations in different spanwise positions.

the subcooling profiles have been observed between the steady and unsteady calculations. In the steady state case, the subcooling was higher than in the unsteady case, particularly in rotor passages at a 50% and a 90% span. The steady state simulation was performed with a mixing plane, which mixed out the flow in the circumferential direction. Hence, the subcooling level at a 90% span was more uniformly distributed at the rotor inlet in the steady case than in the unsteady case.

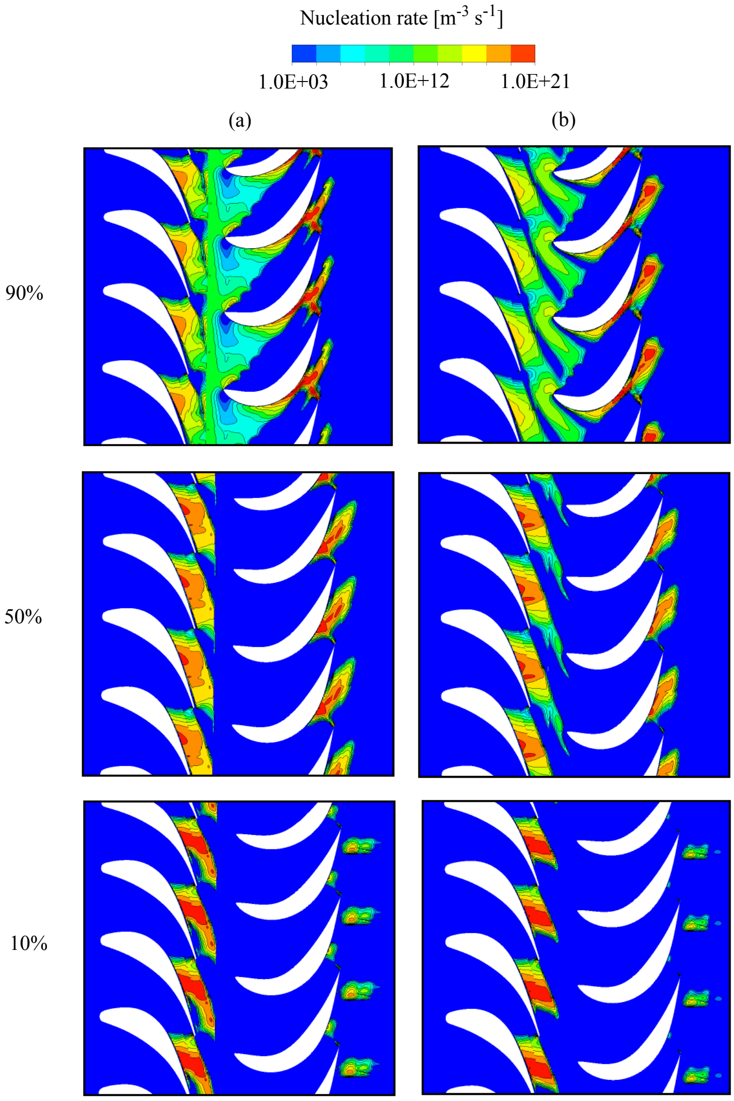

Figure 5.42: Contours of the nucleation rate predicted by (a) steady state and (b) unsteady (at 16850 timestep) simulations in different spanwise positions.

As in the unsteady simulation, the wake flow from the stator blades is slower and warmer than the main flow field. These wakes immediately interact with the rotor blade passage in the region of nucleation. The nucleation process is quite sensitive to temperature variation. Correspondingly, the upcoming stator wakes influence the nucleation process in the succeeding rotor blade passage. For all selected planes, the unsteady calculation predicted a slightly wider nucleation region in the stator compared to the steady calculation, particularly at 50% and 90% spans. Moreover, due to wake-chopping in the unsteady case, the Wilson point was slightly moved to the flow downstream by reducing the level of subcooling and the nucleation rate. However, the level of subcooling was not strong enough to achieve thermal equilibrium, and therefore, the secondary nucleation zone was appeared in the rotor passage for all selected radial planes. The intensity of secondary nucleation increased from the hub to the shroud surface for both cases. The maximum secondary nucleation rate was observed at a 90% span. However, the steady calculation yielded stronger and wider secondary nucleation in the rotor blade compared to the unsteady calculation.

The instantaneous contours of the nucleation rates, the droplet average radius and the wetness fraction estimated at different time steps of the unsteady simulation at a 50% radial height are displayed in Figures 5.43, 5.44 and 5.45, respectively. The listed time steps correspond to one pitch transition (T). It can be seen that the small oscillations have taken place in the nucleation region in both the stator and rotor passages. These variations result from temperature fluctuations as shown in Figure 5.39. Similarly, some fluctuations are observed in both the droplet radius and the wetness fraction fields during one pitch transition.

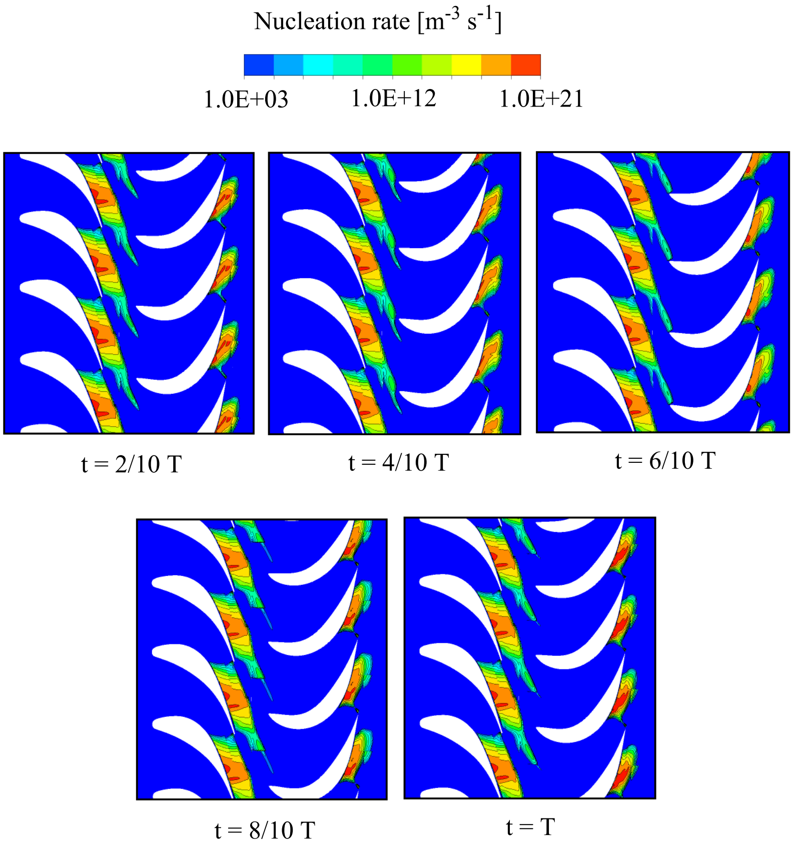

t = 2/10 T

t = 4/10 T

t = 6/10 T

t = 8/10 T

t = T

Figure 5.43: Contours of the nucleation rate predicted by unsteady simulations at a 50% span.

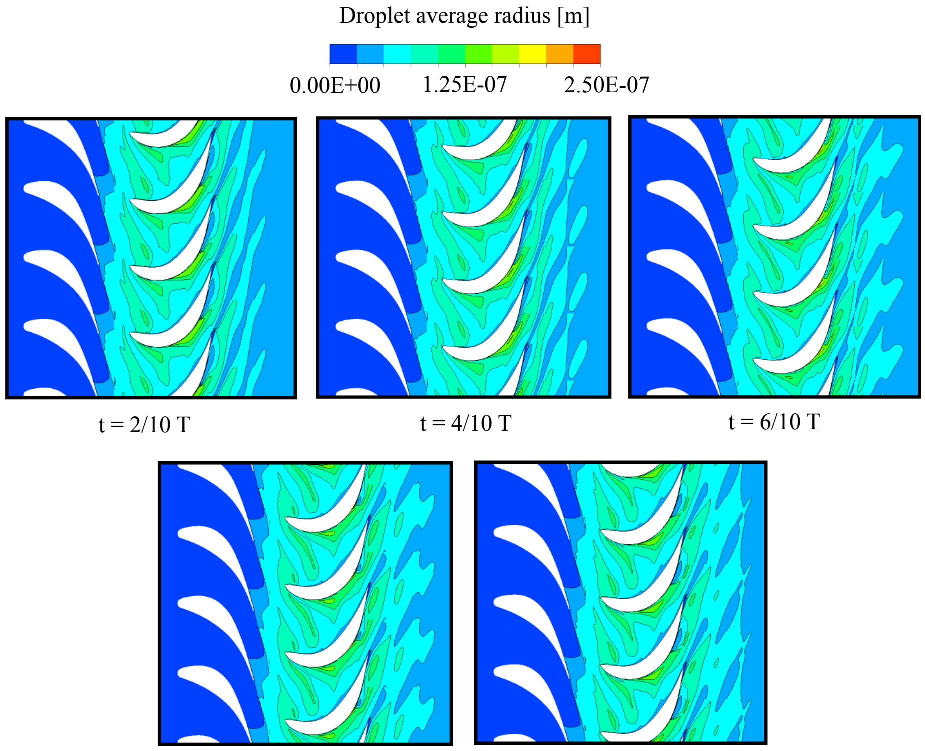

t = 2/10 T

t = 4/10 T

t = 6/10 T

t = 8/10 T

t = T

Figure 5.44: Contours of the droplet average radius predicted by unsteady simulations at a 50% span.

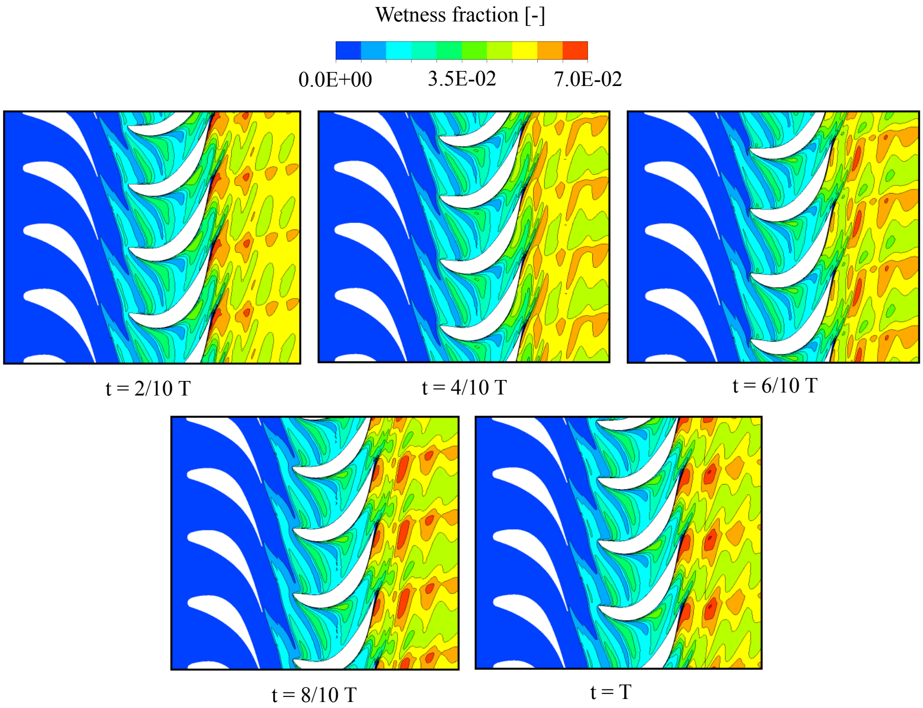

Figure 5.45: Contours of the wetness fraction predicted by unsteady simulations at a 50% span.

Further, the predicted droplet average radius contours for both cases are compared in Figure 5.46. It can be seen that the steady state simulation yielded a larger droplet average radius than the unsteady case for all of the planes. In the unsteady simulations, the variation in subcooling and nucleation affected the liquid droplet sizes. In the steady case, the droplet average radius was larger at the rotor inlet and at the mid-passage of the rotor blades than in the unsteady case. However, far downstream of the rotor blades, the steady state case yielded marginally larger droplet sizes than the unsteady case.

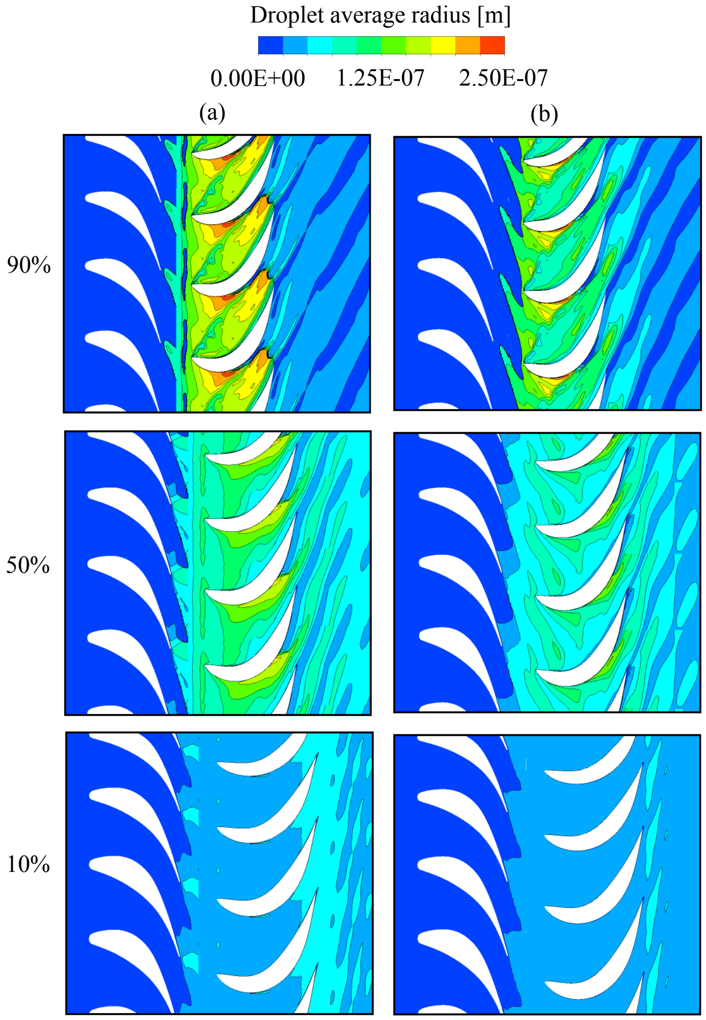

Figure 5.46: Contours of the droplet average radius predicted by (a) steady state and (b) unsteady (at 16850 timestep) simulations in different spanwise positions.

Figure 5.47 displays the contours of the wetness fraction predicted by the steady and unsteady cases. The wetness fraction increased from the hub to the shroud surfaces. Relatively greater wetness was observed downstream of the rotor. The maximum value of the wetness fraction reached up to 7%. It can be seen that the steady state calculation estimated a relatively greater wetness fraction due to the fixed Wilson point. In the unsteady calculations, due to the alteration of the Wilson point and a relatively higher temperature, the wetness fraction decreased particularly at 50% and 90% spanwise planes.

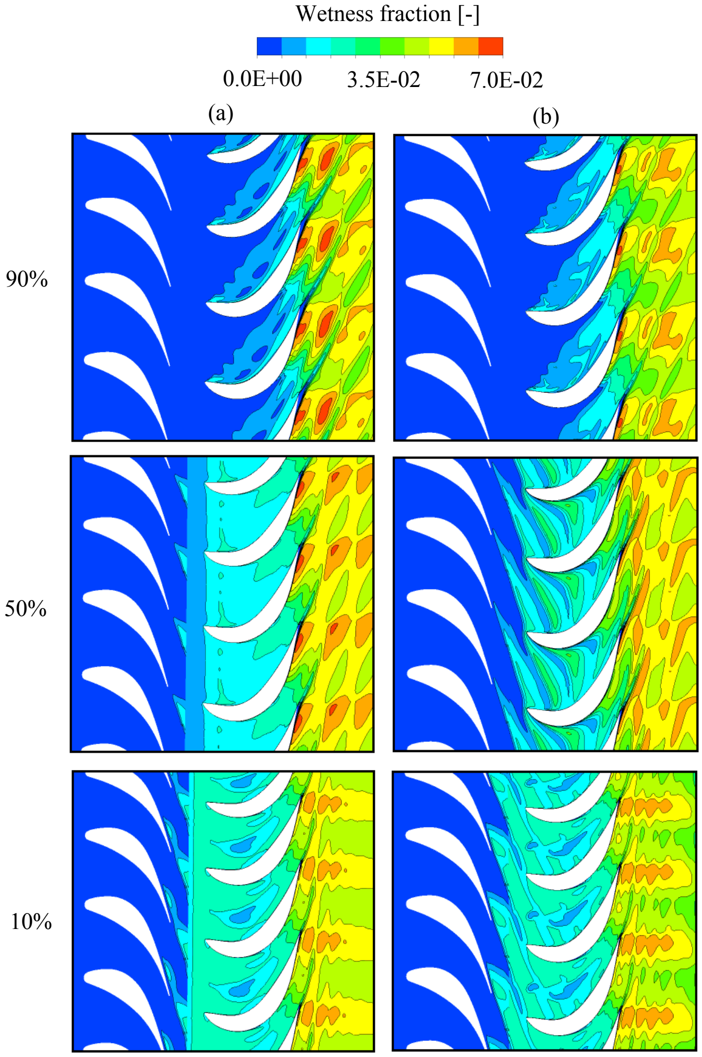

Figure 5.47: Contours of the wetness fraction predicted by (a) steady state and (b) unsteady (at 16850 timestep) simulations in different spanwise positions.

Furthermore, the predicted pressure and temperature trends along the normalised streamwise distance in the stator and rotor domains are presented in Figure 5.48 for steady state and unsteady calculations. These data were extracted from a 50% spanwise plane. The unsteady results were obtained by applying time-averaging of a corresponding one pitch transition. It can be observed that both cases yielded a similar pressure distribution near the stator exit, while small variation occurs after a 0.4 normalised streamwise distance in the rotor domain. Some differences in temperature trends between the steady and unsteady calculations were noticed downstream of the stator. In the rotor domain, the temperature is relatively higher in the unsteady case than in the steady one. However, the differences between the cases may be due to flow unsteadiness. The temperature distribution in the rotor domain was influenced by wakes from the stator and their interaction with the corresponding rotor blades, which increased the flow mixing in the blade passages. Therefore, the temperature value is relatively higher for the unsteady simulation compared to the steady simulation.

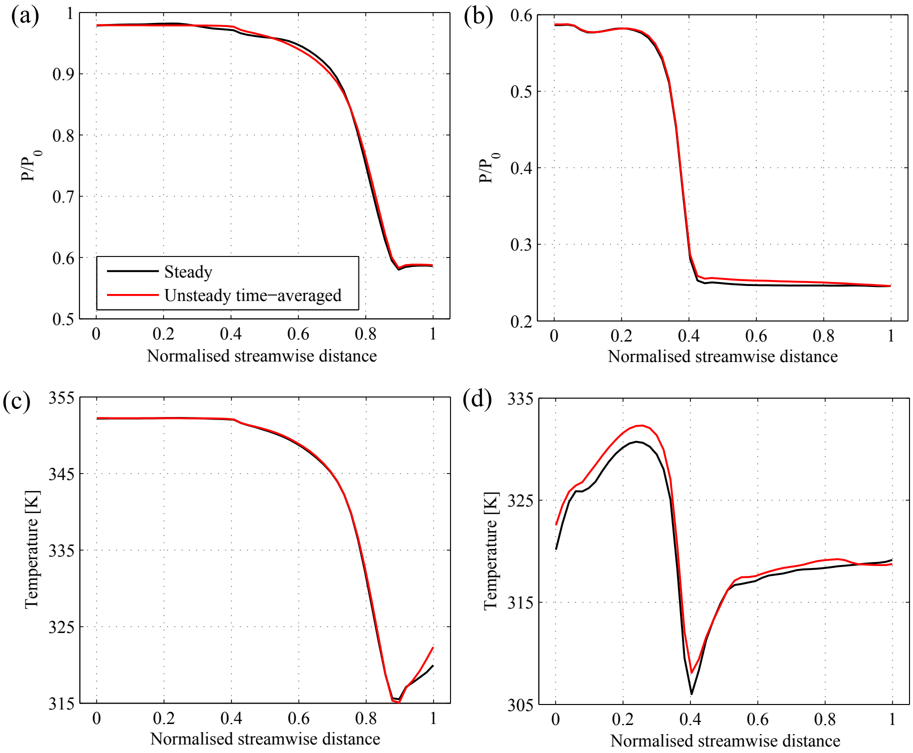

Figure 5.48: The pressure distribution (a) in stator domain, and (b) in rotor domain, and the temperature distribution (c) in stator domain, and (d) in rotor domain.

The comparison between the spanwise distribution of temperature at the stator exit and downstream of the rotor domain is presented in Figure 5.49. Here, the stator exit (stator domain outlet) is located roughly a 20% axial chord length from the stator trailing edge in the axial direction. In the case of the rotor, the selected downstream location is roughly a 25% axial chord length from the rotor trailing edge in the axial direction. The temperature in the unsteady calculations is time-averaged and corresponds to a one pitch transition. The flow condition in the stator passage was transonic near the hub and became subsonic at the shroud surface. Therefore, the flow accelerates more near the hub surface, and subsequently, the subcooling level and nucleation rate are higher in this region. Consequently, the flow temperature is rather high due to released latent heat via condensation. This is the reason for the higher temperature downstream of the stator from the shroud to the hub surface for both cases. However, some variation has been observed between the steady and unsteady temperature profiles. The unsteady case estimated a higher temperature than the steady case particularly from the mid-span to the hub surface. The average increment was 4 K. The temperature for the unsteady case is higher from the mid-span to the hub surface downstream of the rotor. This increment could be due to stator wakes which enlarged the nucleation region and consequently increased the flow temperature.

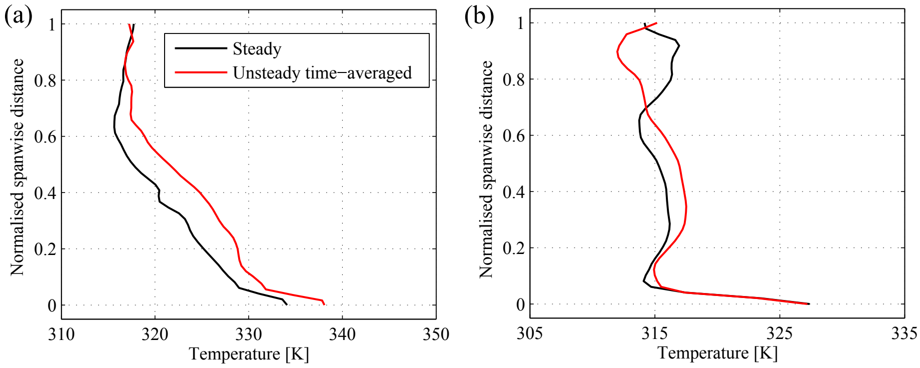

Figure 5.49: The temperature distribution at a normalised spanwise distance at (a) the stator exit and (b) rotor downstream.

Further, the predicted circumferential average droplet number, droplet average radius, wetness fraction and entropy generation at the stator exit and outlet (rotor domain outlet) are presented in Figures 5.50 and 5.51, respectively, at a spanwise distance. At the stator exit, near the hub, the unsteady case yielded a higher number of droplets due to notable nucleation, which influenced the droplet radius and wetness fraction. Therefore, the droplet radius is smaller and the wetness fraction is larger. Nevertheless, the steady simulation predicted slightly higher wetness from the mid-span to the shroud surface than the unsteady case. Further at the hub, because of the higher droplet number, the unsteady case estimated greater latent heat that increased entropy generation compared to the steady case (Figure 5.50(d)). At the rotor outlet, the unsteady case predicted a higher number of droplets than the steady case, and therefore, the droplet average radius is smaller. Subsequently, some variation has been identified in the wetness fraction and entropy generation between the steady and unsteady calculations.

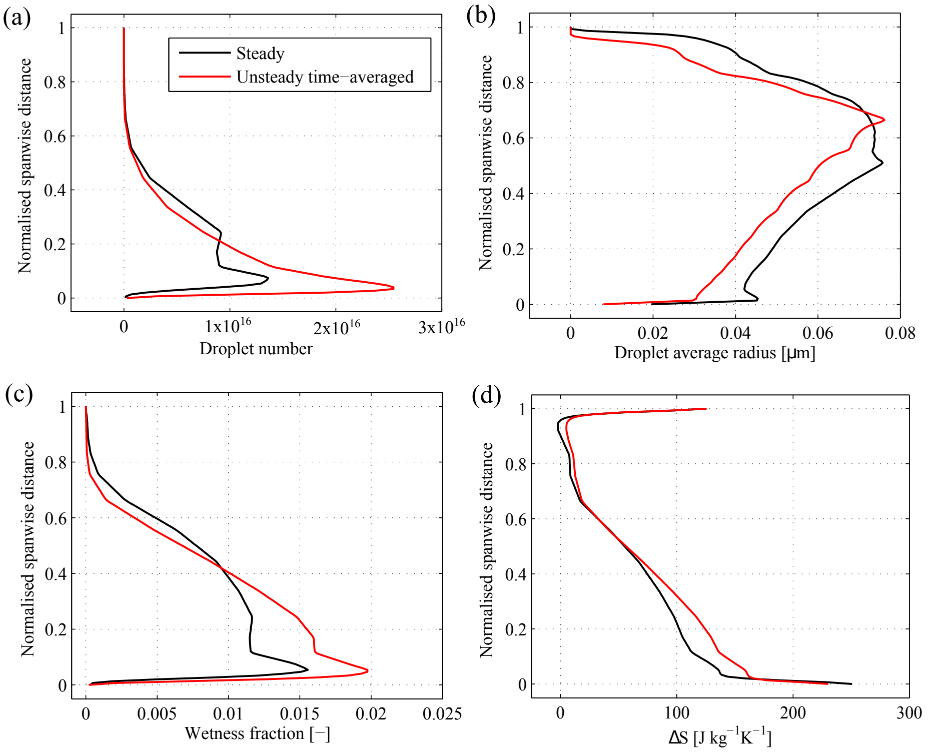

Figure 5.50: The predicted results of the (a) droplet number, (b) droplet radius, (c) wetness fraction, and (d) entropy at the stator exit.

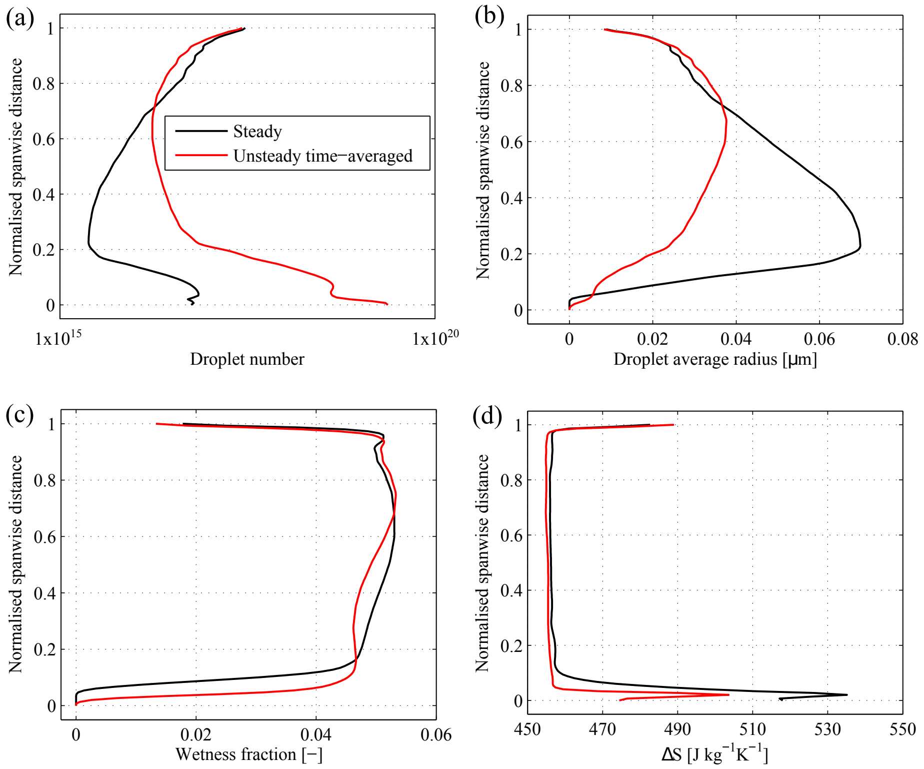

Figure 5.51: The predicted results of the (a) droplet number, (b) droplet radius, (c) wetness fraction, and (d) entropy at the outlet.

The simulations of 3D unsteady non-equilibrium wet-steam flow are quite sensitive and complex due to the rapid deflection and expansion of flow field. Therefore, these simulations require a very fine time resolution for convergence and enough time to achieve a periodic solution of flow. In the presented unsteady calculation, the time step was set such that the passing of one pitch transition of the rotor needed 500 steps. To fulfill the periodic flow condition, many blade pitch transitions were simulated, which required about 18000 time steps. Accordingly, extensive CPU power and storage were essential in modelling this unsteady case. The presented simulations required approximately 1440 hours with 24 CPUs for 18000 time steps in a cluster. In order to compare the computational expensiveness between steady and unsteady cases, 100 numerical iterations were performed with 16 CPUs, and the analysis shows that the unsteady simulation took 40 min. more than the steady state simulation.

5.5 Influence of turbulence modelling on 3D condensing steam flows

Due to the alternative arrangements of stator-rotor blade rows, the flow phenomena of an LP turbine are highly turbulent. Hence, the accurate computational prediction of LP turbine flows requires the turbulence to be modelled accurately. In this section, the influence of turbulence modelling on the 3D stator-rotor stage is discussed. Further, the effect of the freestream turbulence intensity on condensing flow and loss analysis are presented as well. In ANSYS CFX, the SST k-ω turbulence model was modified and its performance was analysed. Due to computational expensiveness of unsteady simulations, the presented results in this section was conducted with steady state simulations only. Firstly, the performance of the MSST k-ω turbulence model was examined with nozzle A from the experimental test case of Moore et al. (1973) and test cases of Moses and Stein (1978). Also, the L1 case of steam turbine stator cascade of White et al. (1996) was modelled. In the case of the Moses and Stein (1978) nozzle, Case 203 was selected, and the boundary conditions were P_{01} = 35800 Pa and T_{01} = 368.3 K.

Figure 5.52 shows a comparison between the predicted results of the MSST k-ω model and the measured data. It can be seen that the predicted pressure distributions and the location and magnitude of the condensation shock are quite accurate for both nozzles. Furthermore, the agreement between the predicted and the measured mean droplet radius size at the specified exit location is reasonably good for the nozzle case of Moore et al. (1973). However, some variation has been observed in the nozzle case of the Moses and Stein (1978).

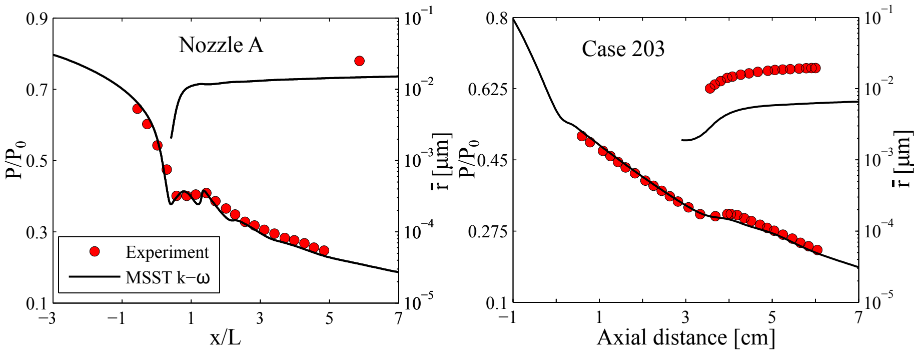

Figure 5.52: Pressure and mean droplet radius distributions along the nozzle centreline compared with the experiments by Moore et al. (1973) (left) and Moses and Stein (1978) (right).

A comparison between the predicted results of the MSST k-ω model and the measured data for the L1 case of White et al. (1996) is shown in Figure 5.53. It can be observed that the MSST k-ω model yielded correct trends of pressure distribution on blade surfaces. It also estimated the correct location and intensity of the condensation disturbance on

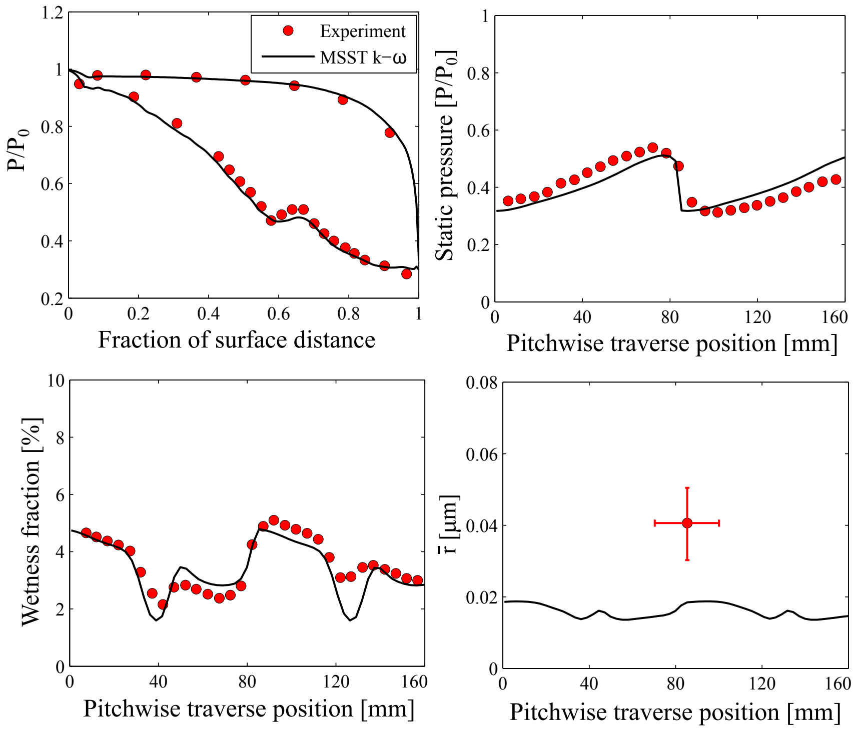

Figure 5.53: The comparison between the predicted results of the MSST k-ω model and the data measured by White et al. (1996) for the L1 case.

the suction side. The predicted trends of static pressure and the wetness fraction on the traverse plane are in good agreement with the experiments. However, some discrepancies have been noticed in the prediction of the mean droplet radius.

5.5.1 Effect on flow properties

It is worthwhile to examine the effect of model modification on turbulence properties which is responsible for governing the turbulent cascade process of eddy deformation, stretching and subsequent dissipation. Therefore, the significance of turbulence modelling in terms of turbulence properties is assessed first. The contours of turbulent kinetic energy predicted by the SST k-ω and the MSST k-ω models are compared in Figure 5.54. The maximum turbulent kinetic energy was generated in the wake of blades. The MSST k-ω model estimated lower turbulent kinetic energy than the SST k-ω model, particularly in the wake and downstream of the rotor blade. This is due to the viscosity modification and the effects of the added source terms, which increase the viscous dissipation considerably. Additionally, the rotor blade generated with the high curvature, and therefore, the flow deflection is higher at the leading edge of the pressure side of the rotor blade. Consequently, a separation bubble has been observed at the rotor pressure side on 90% of the span surface (Figure 5.55) which increases the turbulent kinetic energy in the mid passage of the rotor. The MSST k-ω model estimated comparatively higher turbulent kinetic energy in the mid passage of the rotor.

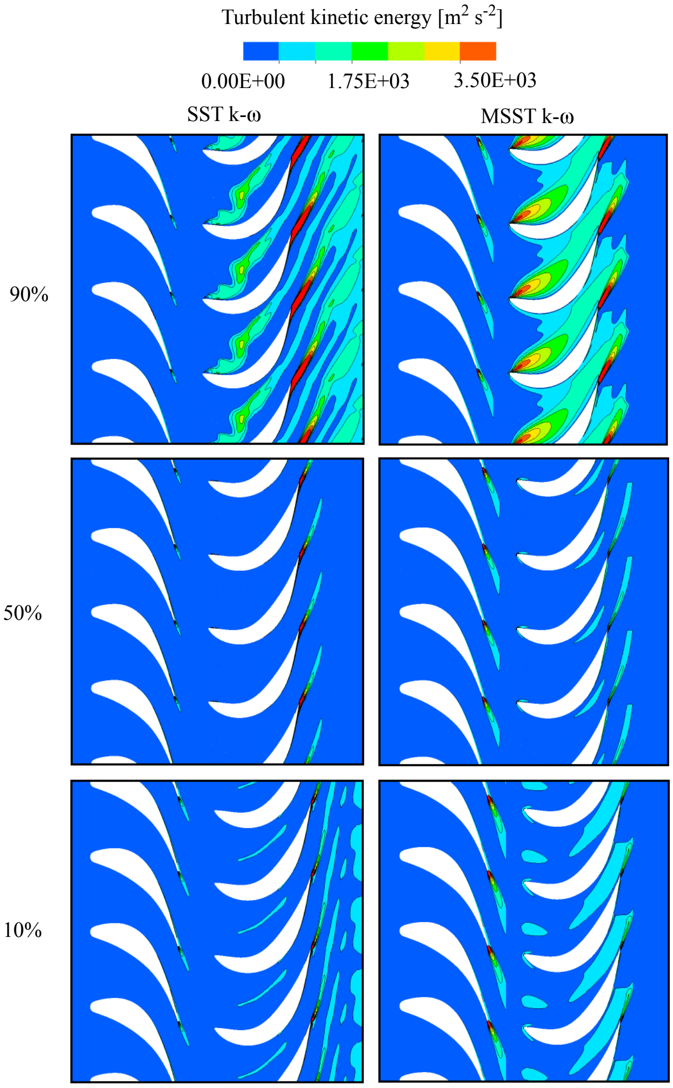

Figure 5.54: Contours of the turbulent kinetic energy predicted by the SST k-ω and the MSST k-ω turbulence models in different spanwise positions.

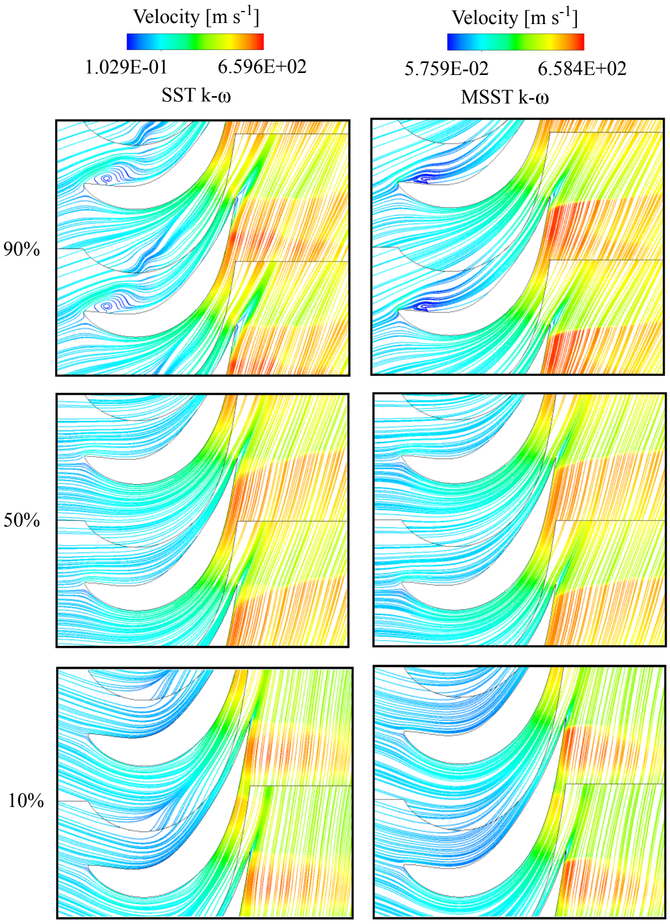

Figure 5.55: Contours of the streamlines predicted by the SST k-ω and the MSST k-ω turbulence models in different spanwise positions.

Figures 5.56 and 5.57 present the predicted circumferential averaged profiles of specific turbulence dissipation rates and turbulent viscosities at the stator exit and outlet for both models. It can be seen that the specific turbulence dissipation rate is notably high near the hub surface at the stator exit. At the outlet, the rate of specific turbulence dissipation is significantly higher at the hub and shroud surfaces due to the turbulent cascade process. The MSST k-ω model estimated a higher specific turbulence dissipation rate at both planes than the SST k-ω model. Further, the MSST k-ω model estimated higher turbulent viscosity than the SST k-ω model. This results from the addition of the production to dissipation ratio into the modified viscosity. Particularly, the turbulent viscosity is at its maximum near the hub and shroud surfaces at the outlet. Further, the influence of turbulence modelling on turbulence property, i.e. turbulence intensity is discussed in

Publication V.

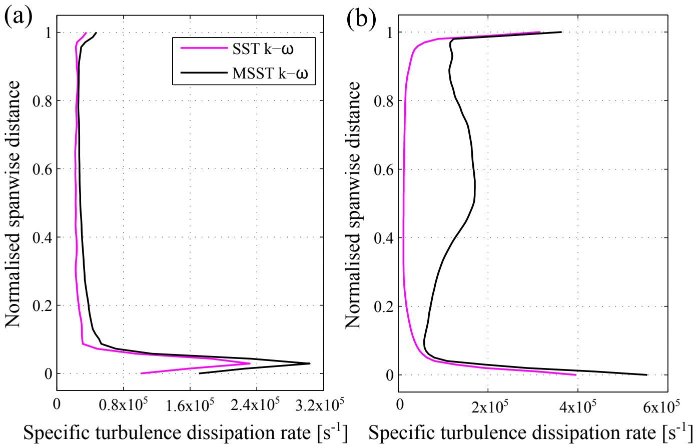

Figure 5.56: The predicted profiles of the specific turbulence dissipation rate by the SST k-ω and the MSST k-ω turbulence models at a normalised spanwise distance (a) at the stator exit and (b) outlet.

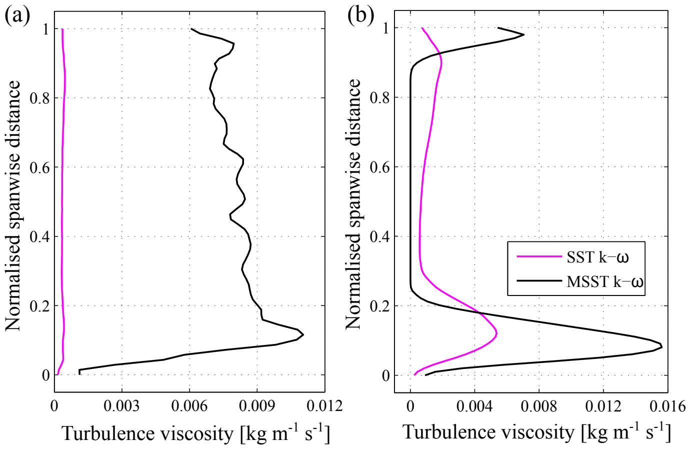

Figure 5.57: The predicted profiles of the turbulent viscosity by the SST k-ω and the MSST k-ω turbulence models at a normalised spanwise distance (a) at the stator exit and (b) outlet.

Further, Figures 5.58, 5.59 and 5.60 display the contours of the Mach number, temperature and pressure, respectively, for both models. It is a fact that the expansion rates at the stator and rotor blades, especially in the spanwise direction, are distinct from each other. As the process of liquid embryo generation ends, the released latent heat increases the pressure of the vapour phase. From the contours of the Mach number, pressure and temperature, it can be seen that the condensation shock is weakened from the hub to the shroud surfaces in the stator blade, while in the rotor, it became stronger from the hub to the shroud surfaces. After the model modification, some variation has been noted in the Mach number contours particularly near the hub and the shroud surfaces.

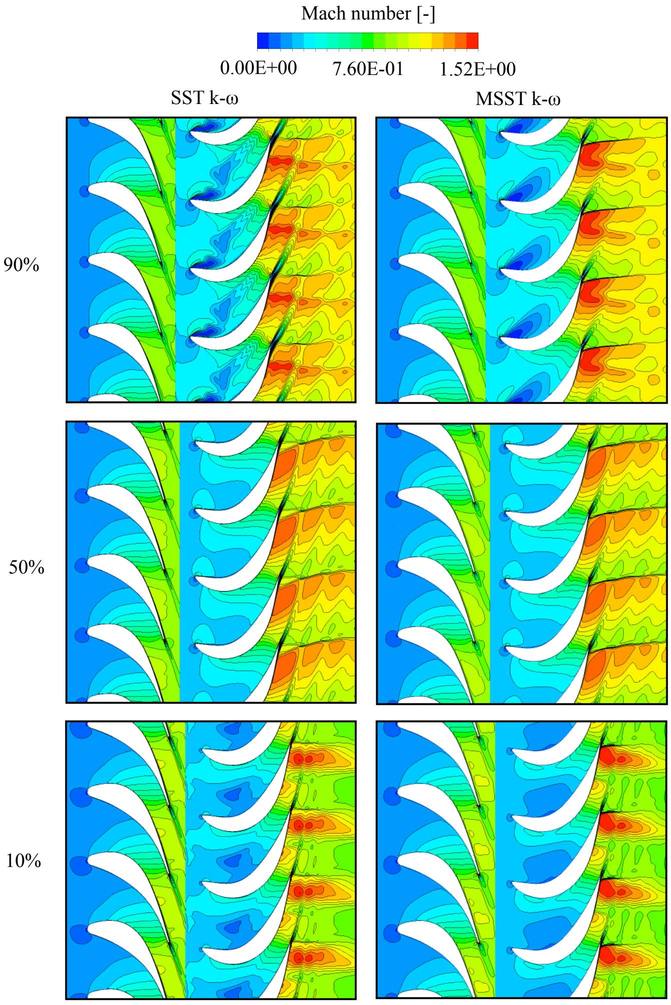

Figure 5.58: Contours of the Mach number predicted by the SST k-ω and the MSST k-ω turbulence models in different spanwise positions.

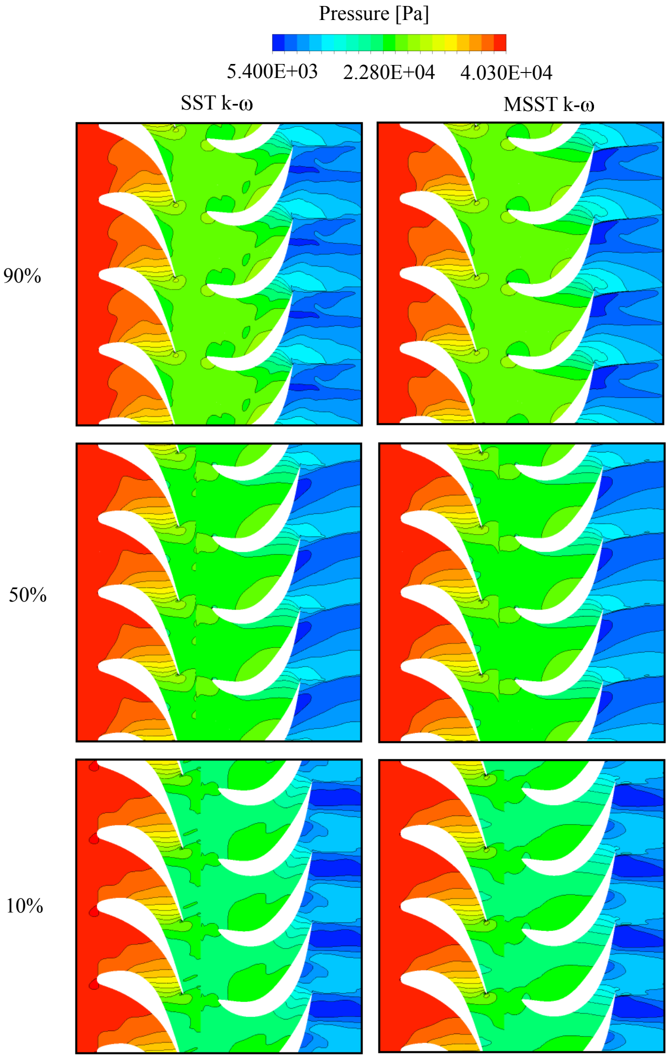

Figure 5.59: Contours of the pressure predicted by the SST k-ω and the MSST k-ω turbulence models in different spanwise positions.

As discussed previously, the rate of viscous dissipation was higher for the MSST k-ω model. Consequently, the Reynolds stresses were lower due to lesser eddy viscosity. Therefore, the shear effect was minor, which influenced the flow parameters. Thus, the flow expansion in the MSST k-ω model was different compared to the SST k-ω model (see Publication V). It is apparent that the MSST k-ω model predicted the suction side shock to be more intense than the SST k-ω model due to the higher entropy generation from the viscous dissipation at the trailing edge. Some differences have been noted in

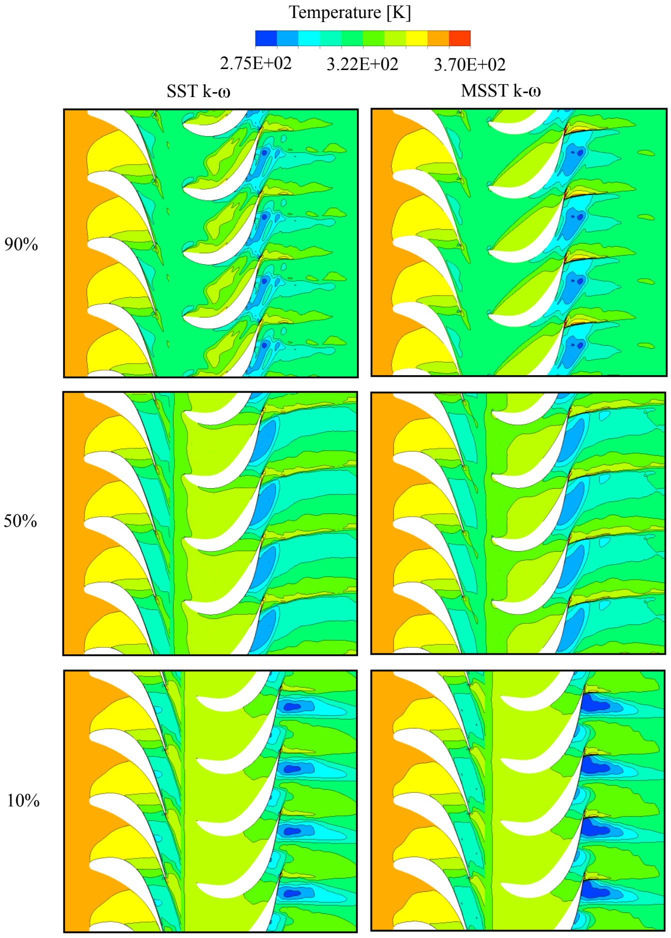

Figure 5.60: Contours of the temperature predicted by the SST k-ω and the MSST k-ω turbulence models in different spanwise positions.

the temperature distribution for all planes between both models, particularly at the throat region and downstream of it, around the trailing edge and in the wake regions of the rotor blade. In the MSST k-ω model, the increased viscous dissipation influenced the temperature distribution via the energy source, which affected the heat transfer rates. Therefore, the temperature level is higher for the MSST k-ω model than for the SST k-ω model in the rotor blade wakes.

The contours of subcooling and the nucleation rate for both models are presented in Figures 5.61 and 5.62, respectively. The MSST k-ω model estimated a higher subcooling level than the SST k-ω model. As discussed before, the nucleation phenomena and droplet growth processes are quite sensitive to local pressure and temperature distributions and the expansion rate. It can be seen that the intensity of nucleation is weaker from the hub to the shroud surfaces of the stator and the nucleation region at a 90% span is more uniformly distributed at the rotor inlet for both models. However, the nucleation is zeroed downstream of the interface at a 10% and a 50% span due to the mixing plane.

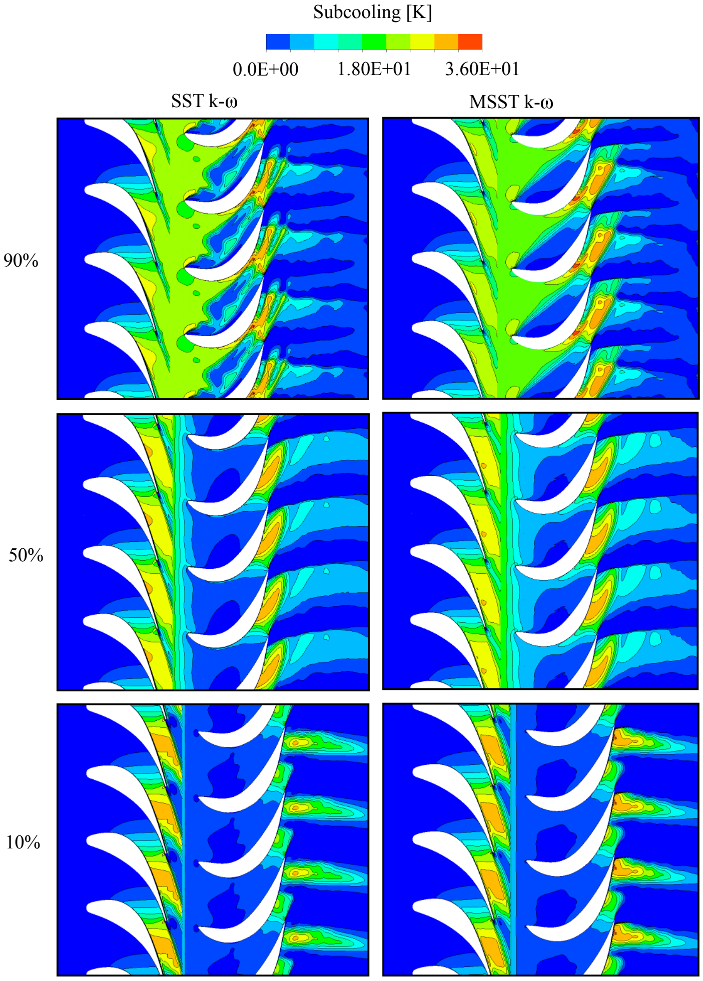

Figure 5.61: Contours of the subcooling predicted by the SST k-ω and the MSST k-ω turbulence models in different spanwise positions.

The MSST k-ω model yielded a wider nucleation region than the SST k-ω model. More-

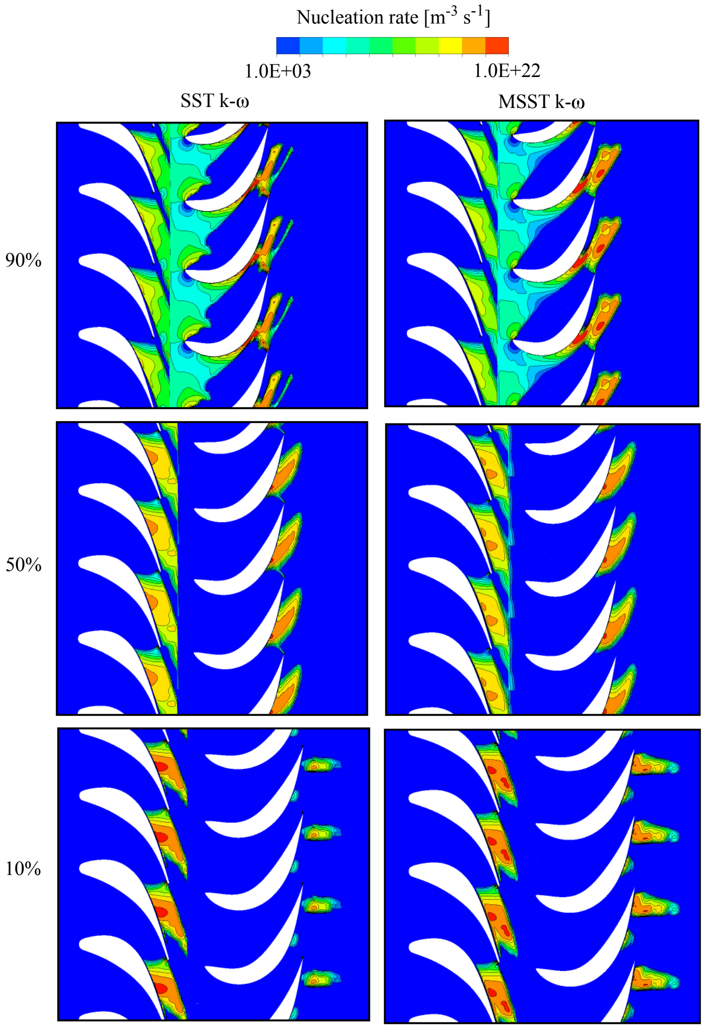

Figure 5.62: Contours of the nucleation rate predicted by the SST k-ω and the MSST k-ω turbulence models in different spanwise positions.

over, the expansion process is extended slightly downstream due to the turbulent viscosity modification and the source term addition. Therefore, the nucleation region for the MSST k-ω model has been shifted downstream. The secondary nucleation zone appeared in the rotor passage for all radial planes in both models. The intensity of secondary nucleation decreased from the shroud to the hub surfaces in both models. However, the secondary nucleation region was larger with the MSST k-ω model than the SST k-ω model.

Figure 5.63 displays the predicted profiles of the droplet number for both models. The present data are extracted at the stator exit and outlet in different spanwise positions. A large number of droplets can be observed near the hub surface of the stator exit due to a notable nucleation rate. However, at the mid-span and near the shroud surface, the total droplet number is reduced. It is noted that the model modification influenced the droplet number prediction at all locations. At the domain outlet, a large number of droplet is observed near both the hub and shroud surfaces. For all spanwise positions, the MSST k-ω model estimated a lower number of droplets compared to the SST k-ω model.

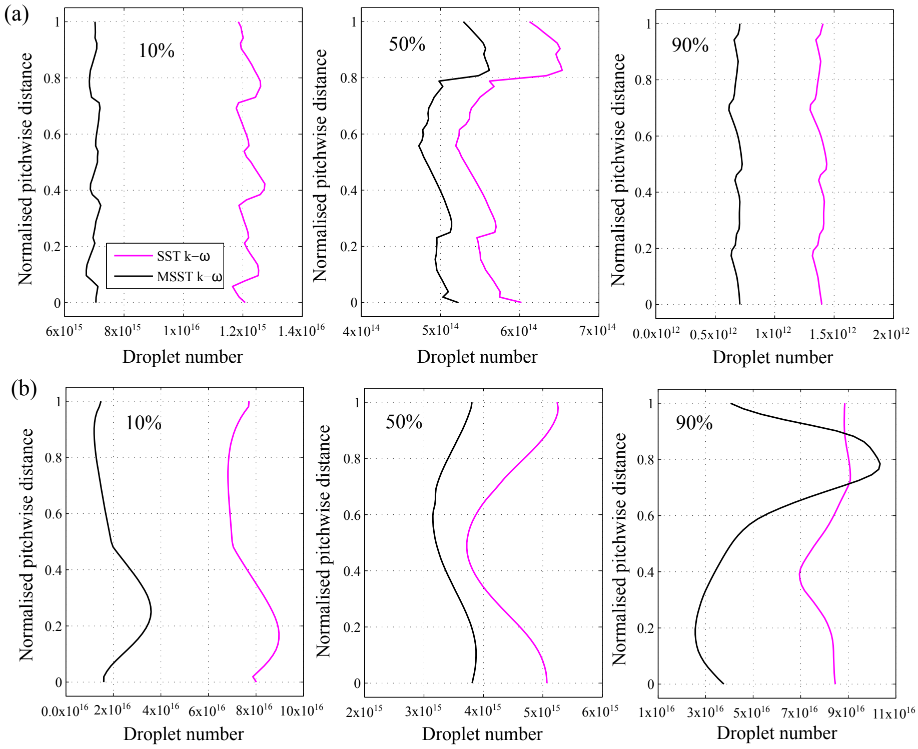

Figure 5.63: The droplet numbers predicted with the SST k-ω and the MSST k-ω turbulence models (a) at the stator exit and (b) outlet.

Further, the predicted contours of the droplet average radius for both models at spanwise surfaces are displayed in Figure 5.64. It can be seen that the droplet average radius is lower near the hub surface due to a large number of droplets, while near the shroud surface, the droplet average radius is higher for both cases. Results show that the turbulence model modification affected the droplet size prediction as well. It can be observed that the growth rate is delayed in the MSST k-ω model due to a wider nucleation region. Subsequently, the number of droplets estimated by the MSST k-ω model is lower compared to the SST k-ω model (Figure 5.63). Therefore, the MSST k-ω model yielded a larger droplet average radius than the SST k-ω model for all spanwise planes.

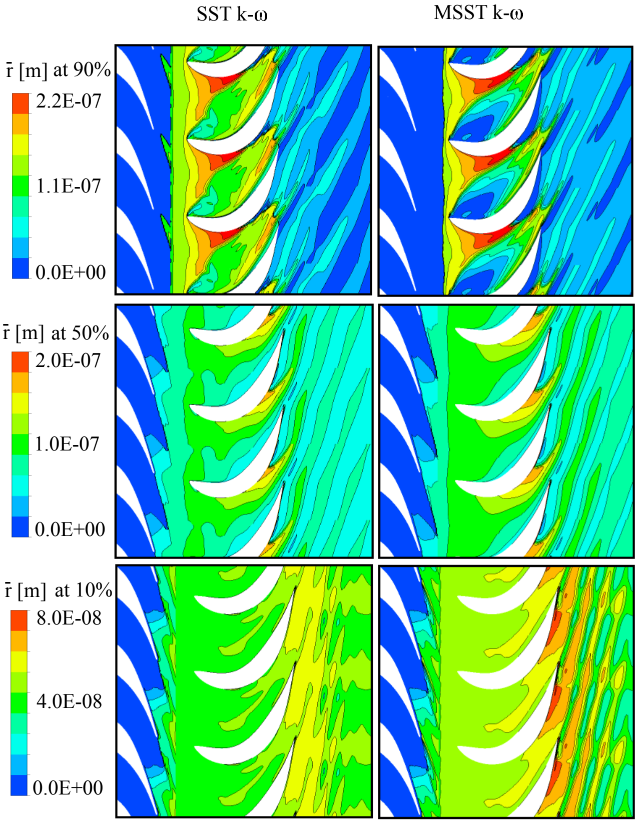

Figure 5.64: Contours of the droplet average radius predicted by the SST k-ω and the MSST k-ω turbulence models in different spanwise positions.

The contours of the wetness fraction are displayed in Figure 5.65. The wetness fraction is higher at the mid-span of the blade, and maximum wetness is observed downstream of the rotor. It can be seen that the SST k-ω model yielded a larger wetness fraction than the MSST k-ω model. However, the maximum wetness fraction was predicted by the MSST k-ω model at a 90% span of the rotor blade, particularly in the separation bubble region of the pressure side and at the suction surface near the trailing edge. Around the separation bubble region, the mass generation rate was considerably high, which increased the wetness fraction. In contrast, at suction surface near the trailing edge, the wetness level was higher due to strong nucleation, which produced more droplets, and subsequently, the wetness fraction increased. Moreover, in the blade wakes, the wetness fraction was lower, and this is the region where flow mixing is significant. Hence, the temperature is higher, which reduces the wetness fraction.

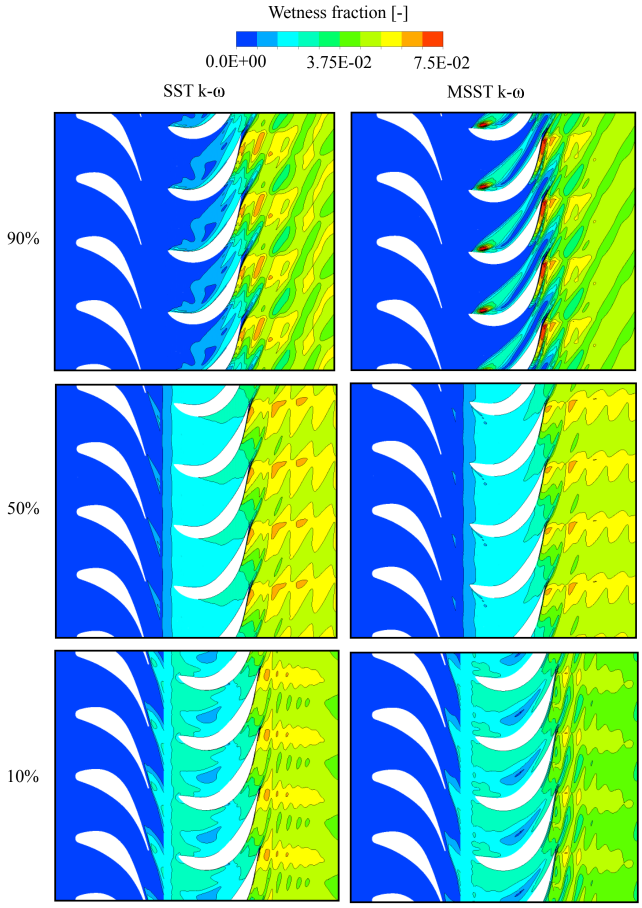

Figure 5.65: Contours of the wetness fraction predicted by the SST k-ω and the MSST k-ω turbulence models in different spanwise positions.

5.5.2 Effect of turbulence level on condensation

Furthermore, the influence of the freestream turbulence intensity on condensing steam flow at the 3D stator-rotor stage was also analysed in this work. For this purpose, two different values of freestream turbulence intensity, i.e. $\chi = 0.05$ and 0.1, were considered. Figure 5.66 displays the turbulence intensity profile plotted at a normalised streamwise distance at the mid-span, where 0 and 1 indicate the inlet and the outlet of the domain, respectively. It can be seen that the turbulence level is decreased from the inlet to the stator exit. However, before the stator exit, i.e. at a 0.5 streamwise distance, the turbulence level increases due to flow mixing. At the rotor inlet, the turbulence intensity increases and the maximum level of turbulence intensity is noted in the rotor passage. Around the streamwise distance of 0.725 which indicates the region of secondary nucleation in rotor blade, the small increment has been observed in turbulence intensity. However, in the rotor domain, there is hardly any difference between the different inlet intensities.

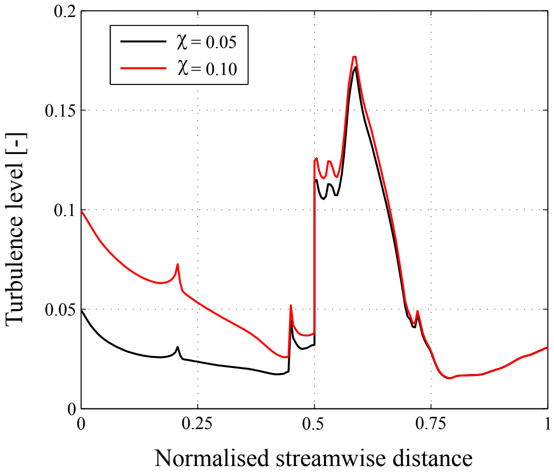

Figure 5.66: The predicted results of the streamwise distribution of turbulent intensity at the mid-span.

Figures 5.67 and 5.68 show the pitchwise distribution of the droplet number and droplet average radius at different spanwise distances, respectively. For all of the spanwise positions, the number of droplets decreased more in the case of $\chi = 0.10$ than $\chi = 0.05$. Also, if the number of liquid droplets is lower, then the growth rate is higher. Thus, the droplet average radius is larger for $\chi = 0.10$ case. Moreover, the droplet average radius was larger downstream of the mid-passage of the rotor blade because of the lower expansion rate. As the blade wakes are hotter due to considerable flow mixing, the droplet growth rate decreases in these regions. This could be the explanation for the periodic patterns in the droplet number and droplet size distribution in the pitchwise position.

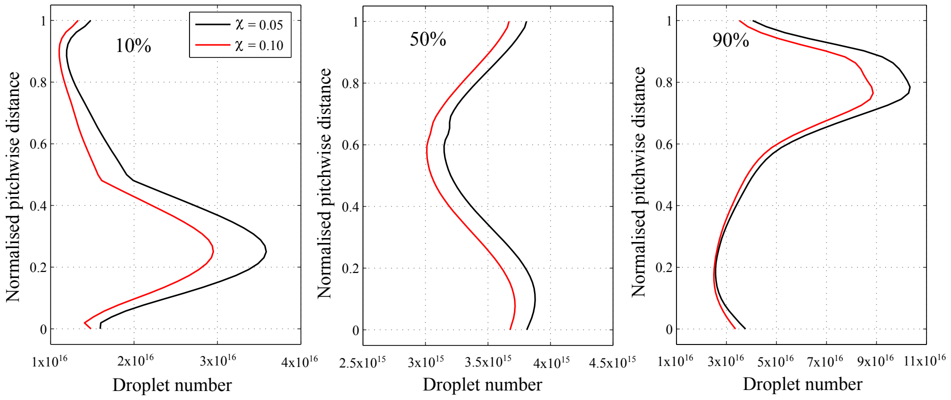

Figure 5.67: The predicted results of the pitchwise distribution of the droplet number at the outlet.

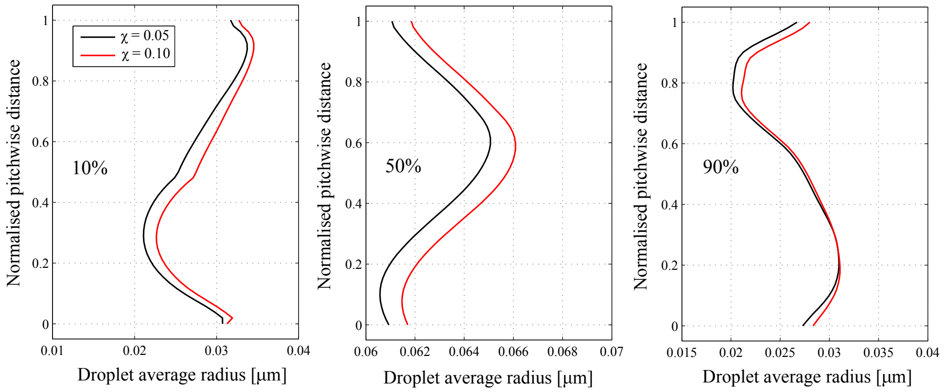

Figure 5.68: The predicted results of the pitchwise distribution of the droplet average radius at the outlet.

The circumferential average wetness fraction was calculated for both $\chi = 0.05$ and 0.1 at different spanwise distances and displayed in Figure 5.69. The data were averaged about a 25% axial chord length from the rotor trailing edge in the axial direction. It can be observed that the decrement resulted in the wetness fraction as the flow freestream turbulence intensity increased.

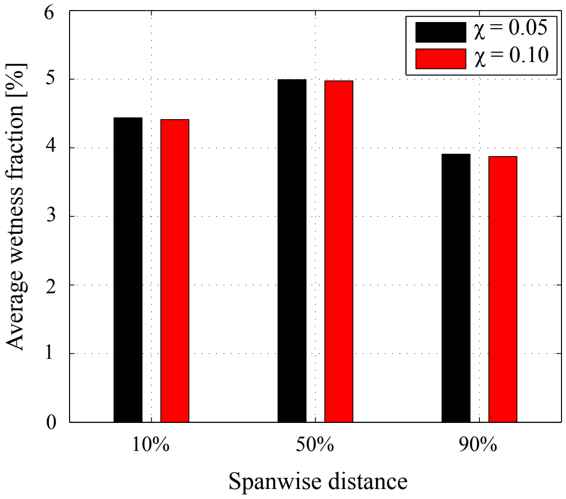

Figure 5.69: The predicted results of the average wetness fraction estimated in different spanwise distances.

5.5.3 Loss analysis

In this section, loss information was presented for both models. Firstly, the predicted contours of entropy generation for both models on different spanwise planes are compared in Figure 5.70.

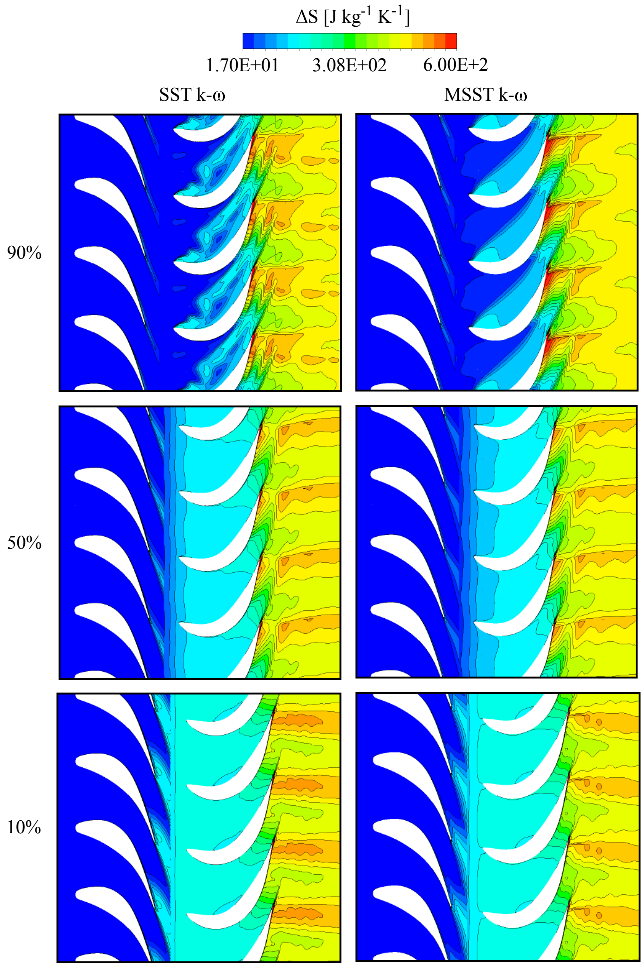

Figure 5.70: Contours of the entropy rise predicted by the SST k-ω and the MSST k-ω turbulence models in different spanwise positions.

It can be seen that the maximum rate of entropy generation is observed at the suction surface of the blades. Further, in the case of the stator, the entropy generation is lower at the 90% span surface than other surfaces due to the absence of droplet growth. In contrast, at the 90% span surface of the rotor, the production of entropy is raised because of the very strong secondary flow effect of the rotor. However, the rate of entropy generation at the rotor is notably high compared to the stator due to the rapid release of latent heat by the droplets, flow separation and secondary flow effect. The SST k-ω model yielded higher entropy generation than the MSST k-ω model, particularly in the blade wake region for the 10% and 50% span surfaces. In contrast, the MSST k-ω model predicted higher entropy near to the trailing edge of the rotor at the 90% span surface likely due to the higher turbulent dissipation in that region.

Further, a comparison of entropy generation along the normalised spanwise distance between both models is displayed in Figure 5.71. In the case of the stator exit, the rate of entropy generation is higher at the hub surface due to the larger droplet number, and it is gradually decreases towards the shroud surface, whereas at the outlet, the entropy generation is higher at both the hub and shroud surfaces. At the hub surface of both planes, the MSST k-ω model yielded lesser entropy generation than the SST k-ω model, while at the shroud surface, the MSST k-ω model estimated slightly higher entropy production because of higher turbulent dissipation.

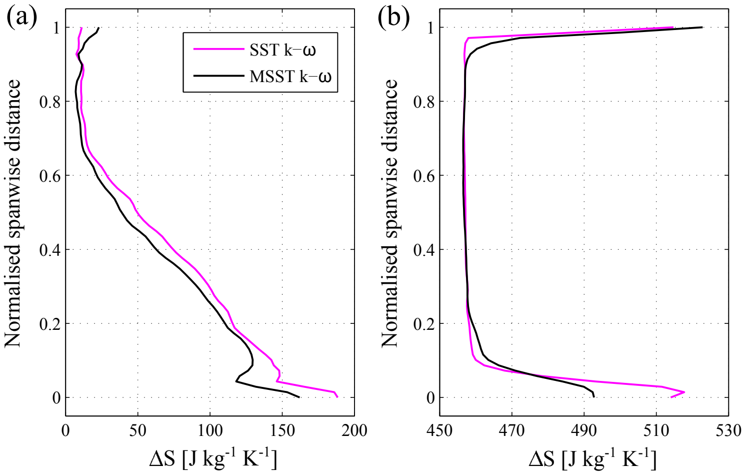

Figure 5.71: The predicted results of the entropy generation by the SST k-ω and the MSST k-ω turbulence models (a) at the stator exit and (b) outlet.

The loss coefficient was divided into two components: (i) shockwave plus wetness loss, and (ii) viscous loss. The same definitions for loss calculation were used by White et al. (1996). For the Markov loss coefficient estimation, all the parameters were calculated by the circumferential average in different span along the traverse plane. The traverse plane is located about a 25% axial chord length from the rotor trailing edge in the axial direction. Figure 5.72 shows the calculated loss information. It can be observed that the SST k-ω model estimated a higher viscous loss compared to the MSST k-ω model for the 10% and 50% span surfaces because of a large amount of entropy production in the blade wake of the rotor (Figure 5.70). Moreover, the viscous loss at the 90% span with the MSST k-ω model is higher than with the SST k-ω model due to significant viscous dissipation at the edges of the separation region immediately near/behind the trailing edge of the rotor. The MSST k-ω turbulence model yielded a smaller wetness fraction due to higher viscous dissipation. Therefore, the MSST k-ω model yielded a lower shock plus wetness loss compared to the the SST k-ω model for all span surfaces.

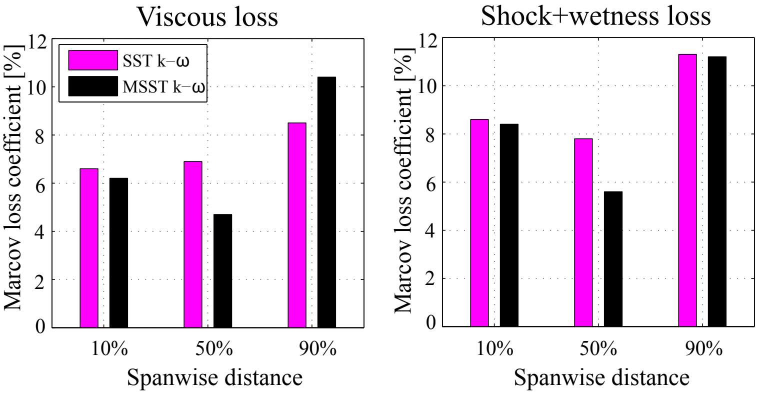

Figure 5.72: The predicted Markov loss coefficients by the SST k-ω and the MSST k-ω turbulence models.

Furthermore, the influence of the freestream inlet turbulence intensity on the loss generation was studied. For this purpose, the viscous loss and shockwave plus wetness loss was calculated for both cases and displayed in Figure 5.73. In the case of viscous loss, marginal variation was observed between both cases of freestream turbulent intensity. Due to the decreased wetness fraction, the shock plus wetness loss is slightly lower for all spanwise distances when $\chi = 0.10$.

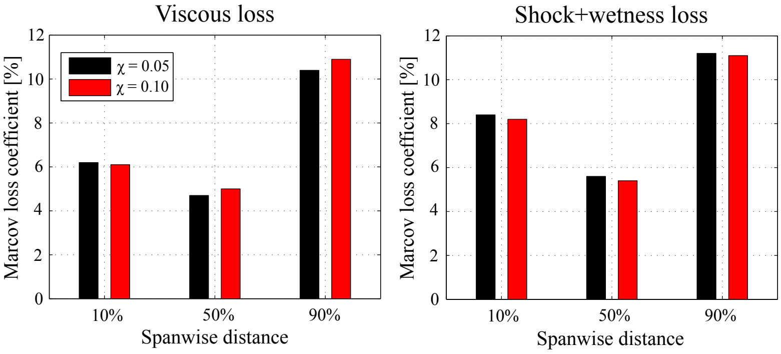

Figure 5.73: The predicted Markov loss coefficients with different freestream inlet turbulence intensities.

6 Conclusions

As steam turbines play a key role in global power generation, it is important for turbine manufacturers and the scientific community to analyse flow phenomena and corresponding losses in steam turbines through experiments or numerical simulations. Especially, research on low pressure (LP) steam turbine stages is currently in demand. During flow expansion in the final stages of an LP steam turbine, the steam crosses the saturation line, and therefore, the last few stages operate in a two-phase flow region which results in thermodynamic and aerodynamic losses as well as erosion in the stationary and rotating parts. To enhance the complicated physics involved in condensing steam flows, numerous experimental, theoretical, and numerical studies have been performed. Several researchers have carried out comprehensive experimental studies on condensing steam flows with nozzles and single or multi-stage stator/rotor turbine cascades. However, there are few experimental facilities available for condensing flow measurements, and the precise measurement of these non-equilibrium flows is very challenging. During the past few decades, computational fluid dynamics (CFD) has become an increasingly applicable, essential, and extensively adopted approach for the assessment and optimisation for turbomachinery flow investigations. Due to the tremendous improvement in computational power and the advancement of numerical techniques to determine the flow governing equations, the numerical study of condensing steam flows is the most suitable and feasible option.

The principle aim of this work was to improve existing knowledge and understanding of condensing steam flow and the loss mechanisms involved by using a numerical modelling approach. In this work, the Eulerian-Eulerian approach was adopted. The assumptions are made based on submicron condensed liquid droplets. Interactions between droplets were omitted, and the velocity slip between the liquid droplets and the vapour was neglected. Two commercial CFD codes, i.e. ANSYS FLUENT and ANSYS CFX, were used to solve the mixture of vapour and liquid phases by Reynolds-averaged Navier-Stokes (RANS) equations. The condensation phenomena were modelled on the basis of the classical nucleation theory.

To fulfill the goal of this research work, different flow domains, including 2D convergent-divergent (CD) nozzles, a stator turbine cascade and the 3D stator-rotor stage, were analysed. The achieved CFD results of this study were assessed and discussed based on the experimental data of condensing steam flow available in open literature. The CFD data concerning the losses due to irreversible heat and mass transfer throughout the condensation process were analysed in LP steam turbine flows. For this purpose, the Markov energy loss coefficient based on entropy generation was calculated. The loss coefficient was divided into three components: shockwave plus wetness loss, viscous loss, and mixing loss.

Firstly, a grid sensitivity analysis of CFD results was carried out by choosing different grid densities for selected computational models. Also, a grid convergence index (GCI) algorithm was adopted to assess the influence of grid refinement on condensation modelling. The GCI analysis indicated that the successive grid refinements decreased the numerical discretisation error. The presented study illustrates that the condensation modelling is sensitive to grid refinements. Therefore, it can be concluded that adequate grid size is required to obtain accurate trends of condensation phenomena in LP turbine flows.

An accurate prediction of nucleation and droplet growth phenomena in condensing steam flows requires the correct estimation of flow thermodynamic properties like temperature, pressure, and density particularly in the superheated region, at the saturated vapour line and in the wet-steam region. In fact, the steam flow in the meta-stable region could not be modelled accurately with the ideal-gas assumption. Therefore, steam properties must be estimated accurately to model non-equilibrium condensing steam flow expansion precisely. To analyse the influence of real gas modelling on condensing steam flows, local equation of state (EOS) for real gas and other steam properties were formulated and their performance was examined using the Young (1988) EOS. In wet-steam flow, following the Wilson point, liquid droplets generate and the flow converts to a mixture of vapour and tiny liquid droplets. Subsequently, the droplets grow by conveying latent heat to the carrier vapour phase. The addition of heat to the vapour phase increases the overall flow temperature and pressure. The results revealed that a slight variation in steam properties influenced the flow expansion. Subsequently, the rate of formation of liquid droplet embryos and their growth process were affected. It can be concluded that accurate steam properties are crucial in modelling condensing steam flow correctly.

The condensing flows in an LP steam turbine involve complex flow phenomena such as flow transition from a laminar to a highly turbulent regime, flow separation, secondary flow mixing and heat transfer, and turbulence is involved in all these phenomena. Also, turbulence has a significant role in mass, momentum, and heat transfer processes, especially in boundary layers on the surface walls where the alternation of flow variables is crucial. Consequently, turbulence may also have some influence on shock wave generation and its corresponding interaction with the condensation process. Moreover, to estimate absolute losses in steam turbine flows accurately, turbulence must be modelled precisely. Therefore, in this work, the role of turbulence modelling in the condensation process and its corresponding influence on loss generation was examined considering various computational domains. Firstly, the performance of various RANS-based turbulence models in wet-steam flow modelling was investigated. The results demonstrated that the estimation of condensation parameters is sensitive enough to the turbulence model selection. Therefore, an appropriate turbulence model is required for the precise modelling of the turbulence cascade process in non-equilibrium condensing flows of an LP turbine.

Further, the standard k-ε (Sk-ε) model and the shear stress transport k-ω (SST k-ω) model were modified by adding source terms. These source terms introduce the modulation of turbulence kinetic energy and its dissipation rate/specific dissipation rate via liquid droplets to the corresponding transport equations of both models. Also, the turbulent viscosity definition was altered by multiplying the production to dissipation ratio. The modified Sk-ε (MSk-ε) model and modified SST k-ω (MSST k-ω) model were applied to CD nozzles, the stationary cascade of turbine blades and a 3D stator-rotor stage of an LP steam turbine. The presented analysis of the influence of turbulence modelling on condensing steam flow shows that the inclusion of source terms in turbulence models and the subsequent modification of the turbulent viscosity definition induced considerable viscous dissipation. The notable viscous dissipation affected the temperature through energy sources, which impacted the heat transfer rates in the non-equilibrium condensation process. The performance of the MSk-ε model was analysed with CD nozzles and the results indicated that the MSk-ε model yielded good agreement with the experiments. In the case of the 2D turbine cascade, the reported results demonstrated that the Sk-ε and the SST k-ω models were inaccurate in predicting condensation phenomena. After the turbulence model modifications, the MSk-ε and the MSST k-ω models affected the flow expansion, and therefore, the subcooling level and the nucleation rate increased. As a result, the number of liquid droplets increased, which reduced the droplet size. The results showed that the MSk-ε and the MSST k-ω models predicted the location and intensity of condensation disturbance accurately. The loss analysis demonstrated that after model modification, both models correctly estimated the viscous loss, shock plus wetness loss, mixing loss, and total loss. Substantial improvements in the prediction accuracy were noticed for the modified turbulence models compared to the original models. For further analysis, a single stage of the 3D stator-rotor was modelled. However, the considered computational model was not that of a real turbine geometry. The stator vane was adopted from the stator cascade of White et al. (1996), while the rotor blade was designed for 25% of the reaction at the mid-span. The results of the 3D stator-rotor stage indicated that the processes of nucleation and droplet growth were influenced by the model modification. The MSST k-ω model yielded a higher subcooling level due to higher flow expansion. Eventually, the nucleation region grew and the growth process was delayed with the MSST k-ω model. It was exhibited that the increased viscous dissipation via model modification reduced the wetness fraction to some extent. The presented loss assessment indicated that after model modification, the shock plus wetness loss reduced compared to the SST k-ω model. Also the viscous loss estimation was affected by the MSST k-ω model, and its value was decreased except near shroud surface of the rotor. Based on the presented qualitative and quantitative analysis, it can be concluded that the modified turbulence models correspond well with the reference data of the experiments and are able to mimic essential trends of the condensation process in LP steam turbine flows.

The influence of freestream turbulence intensity on the condensation process was also investigated considering CD nozzles, a stator turbine cascade and the 3D stator-rotor stage. The results revealed that the flow expansion was higher when the inlet turbulence level was low. Subsequently, the nucleation and droplet growth processes were affected. The wetness level declined with higher freestream inlet turbulence intensity. Thus, the condensation phenomena are rather sensitive to the level of turbulence at the entrance of the flow passage. The studies presented in this thesis revealed that the correct computational modelling of wet-steam flow in an LP steam turbine requires the turbulence to be accurately modelled. Based on the reported analysis, it is recommended that the MSk-ε and the MSST k-ω turbulence models to be utilized for condensing steam flow modelling.

The sizes and shapes of trailing edges of turbine blades are very important because they have a strong influence on the pressure fields within the blade passage, and consequently, they play a pivotal role in the nucleation and growth processes, and other key parameters of LP turbine flows. Therefore, an attempt was made to investigate the influence of the trailing edge shape on condensing steam flow in the stationary cascade of turbine blades. For this purpose, conic, semicircular and square trailing edges were modelled. The trailing edge shapes influenced the pressure distribution, nucleation rate, wetness level, shock wave structure generated at the trailing edge and its corresponding angles, and flow angle. The results indicated that the semicircular trailing edge yielded the smallest droplet sizes compared to other cases. In blade wakes, the turbulent kinetic energy of the flow is relatively high and will eventually dissipate due to viscous effects, and consequently, the local entropy generation rate is notable there. Due to a strong wake region, the square trailing edge predicted the maximum entropy generation. The shock plus wetness loss and mixing loss were relatively higher for the square trailing edge.

The alternative arrangements of stator and rotor blade rows introduce an inherent unsteadiness in an LP turbine. Moreover, the interactions of the solid wall surfaces are vigorous due to limited flow space. The wake-chopping phenomenon could have some influence on the flow parameters. Therefore, the analysis of unsteadiness, particularly an unsteady wake segmentation and its corresponding influence on the non-equilibrium condensation, is significant. For this purpose, steady and unsteady simulations were performed with a 3D stator-rotor stage. The results revealed that the flow unsteadiness influences the Wilson point, and therefore, the nucleation rate was affected. The unsteady calculation predicted a wider nucleation region, which impacted the droplet distribution and size. The unsteady simulations yielded a relatively smaller wetness fraction than the steady state simulation.

7 Future suggestions

The research that was conducted for this thesis has highlighted various issues of importance in the precise modelling of condensing steam flows of an LP turbine. The results of this work point to various interesting directions for future work. Below are some areas that would merit further study:

- **Effect of the turbulent and the inlet boundary layer on condensing steam flows**: The proper analysis of turbulent boundary layer flow and its separation in the final stages of an LP turbine would be important for turbine design. It would be advisable to study the turbulent boundary layer in condensing steam flows because it would have an impact on the flow expansion that influenced the liquid droplet size and distributions, and the shock structure. Further, the inlet flow boundary layer is an important parameter which influences the secondary losses that effect on the heat transfer distribution on the suction surface and endwall of 3D turbine flow field. Therefore, it would be worthwhile to examine the effect of the inlet boundary layer on 3D wet-steam flows in an LP turbine.
- **Effect of turbulent modelling on multi-stage steam turbines**: The flow regime in multi-stage steam turbines is highly turbulent owing to the alternative arrangements of the stator-rotor blade rows and their relative motion. Moreover, the condensation taking place in at least the last three stages of LP turbine. The analysis presented in this thesis was only limited to a single 3D stator-rotor stage which is not the real steam turbine stage. Therefore, it would be interesting to investigate the effect of turbulent modelling with real multi-stage steam turbine geometry and its corresponding influence on loss mechanism.
- **Suitable turbulence model for the last stages of an LP turbine**: The last stages of an LP turbine operate at relatively high levels of the free stream turbulence flow field. This is due to the upstream stages of the LP turbine which may already experience large separations. Therefore, the proper modelling of boundary layers, as well as free stream turbulence in the last few stages of the LP turbine would be important. This requires a suitable turbulence model which could satisfy this need.
- **Role of turbulent modelling in heterogeneous wet-steam flows**: During the steam expansion, the existing chemical impurities in steam lead to heterogeneous nucleation, which would have some influence on flow expansion, nucleation and growth processes. However, the present work concentrated only on homogeneous condensation modelling. It would be relevant to examine the effect of turbulent modelling on heterogeneous condensing steam flows.
- **Modelling of two-way turbulence coupling between vapour and liquid droplets**: The vapour phase influences liquid droplets via aerodynamic drag and turbulence transfer. Further, the liquid droplets reduce momentum and turbulent kinetic energy in the vapour phase. However, the simulations of the current work were only limited to the indirect influence of liquid droplets on vapour phase turbulence. It would be

important to analyse the influence of two-way turbulence coupling on condensing steam flow, particularly in the last few stages of an LP turbine where liquid droplets are relatively larger.

- **Effect of wake-chopping on loss mechanisms**: It is a fact that the LP turbine flow fields are highly complex, random and unsteady. The proper analysis of flow phenomena such as wake-chopping is essential in order to design wet-steam stages of the LP turbine. Particularly, a study regarding the influence of wake segmentation on losses which are generated due to non-equilibrium condensation would be significant.
- **Influence of the trailing edge shape on fully 3D LP turbine flows**: The analysis presented in this thesis concerning the effect of the trailing edge geometry on condensing steam flows demonstrated that the formation of liquid embryos, their growth process and loss generation were affected due to trailing edge shapes. However, the analysis in this thesis was only limited to 2D flows. Therefore, it would be useful to enhance the analysis of the influence of trailing edge shapes with fully 3D LP turbine blade profiles.

References

Adam, S. (1996). *Numerische und experimentelle Untersuchung instationärer Düsenströmungen mit Energiezufuhr durch homogene Kondensation*. PhD thesis, Fakultät für Maschinenbau, Universität Karlsruhe (TH).

ANSYS Inc. (2014a). *ANSYS CFX Solver Modeling Guide*. Release 14.0, Canonsburg, Pennsylvania.

ANSYS Inc. (2014b). *ANSYS CFX Theory Guide*. Release 14.0, Canonsburg, Pennsylvania.

Avetissian, A. R., Philippov, G. A., and Zaichik, L. I. (2005). The effect of turbulence on spontaneously condensing wet-steam flow. *Nucl. Eng. Des.*, Vol. 235:1215–1223.

Avetissian, A. R., Philippov, G. A., and Zaichik, L. I. (2008). Effects of turbulence and inlet moisture on two-phase spontaneously condensing flows in transonic nozzles. *Int. J. Heat Mass Transfer*, Vol. 51:4195–4203.

Bakhtar, F., Ebrahimi, M., and Bamkole, B. (1995a). On the performance of a cascade of turbine rotor tip section blading in nucleating steam, part 2: wake traverses. *Proc. Inst. Mech. Eng. Part C: J. Mech. Eng. Sci.*, Vol. 209:169–177.

Bakhtar, F., Ebrahimi, M., and Webb, R. (1995b). On the performance of a cascade of turbine rotor tip section blading in nucleating steam, part 1: surface pressure distributions. *Proc. Inst. Mech. Eng. Part C: J. Mech. Eng. Sci.*, Vol. 209:115–124.

Bakhtar, F. and Heaton, A. V. (2005). Effects of wake chopping on droplet sizes in steam turbines. *Proc. IMechE, Part C: J. Mech. Engrg. Science*, Vol. 219:1357–1367.

Bakhtar, F. and Piran, M. (1979). Thermodynamic properties of supercooled steam. *Int. J. Heat & Fluid Flow*, Vol. 1 (2):53–62.

Bakhtar, F., Ryley, D., Tubman, K., and Young, J. (1975). Nucleation studies in flowing high pressure steam. *Inst. Mech. Eng.*, Vol. 189:427–436.

Bakhtar, F. and Tochai, M. T. M. (1980). An investigation of two-dimensional flows of nucleating and wet steam by the time-marching method. *Int. J. Heat Fluid Flow*, Vol. 2:5–18.

Bakhtar, F. and Yousif, F. H. (1974). The behaviour of wet steam after disruption by a shock wave. In *Inst. Chem. Engrs. Symposium on Multi-Phase Flow Systems. Univ. of Strathclyde*.

Bakhtar, F. and Zidi, K. (1989). Nucleation phenomena in flowing high-pressure steam: experimental results. *Proc. Inst. Mech. Eng.*, Vol. 203:195–200.

Bakhtar, F. and Zidi, K. (1990). Nucleation phenomena in flowing high-pressure steam, part, 2: theoretical analysis. *Proc. Inst. Mech. Eng.*, Vol. 204:233–242.

Bakker, A. (2012). Lecture series of computational fluid dynamics course.

Band, W. (1939). Dissociation treatment of condensation of water vapour. *J. Chem. Phys.*, Vol.7:324.

Barschdorff, D. (1971). Verlauf der Zustandsgrossen und gasdynamische Zusammenhaenge der spontanen Kondensation reinen Wasserdampfes in Lavalduesen. *Forsch, Ingenieurwes*, Vol. 37:146–157.

Barschdorff, D. and Filippov, G. (1970). Analysis of special conditions of the work of laval nozzles with local heat supply. *Heat Tranfer - Soviet Research*, Vol. 2:76–87.

Baumann, K. (1921). Some recent developments in large steam turbine practice. *J. Inst. Elec. Engrs.*, Vol. 111:435.

Becker, R. and Doring, W. (1935). Kinetische behandlung der keimbildung in ubersettigten dampfen. *Ann. d. Phys.*, Vol. 24:719–752.

Beloded, V. V., Kirichewskij, G. A., and Nuzhnyj, V. M. (1989). Condensation coefficient of metastable water. *J. Aerosol Sci.*, Vol. 20:1047–1050.

Bijl, A. (1938). *Discontinuities in the Energy and Specific Heats*. PhD thesis, University of Leiden, Germany.

Binnie, A. M. and Green, J. R. (1943). An electrical detector of condensation in high velocity steam. *Proc. Roy. SOCA.*, Vol. 181:134.

Binnie, A. M. and Woods, M. W. (1938). The pressure distribution in a convergent–divergent steam nozzle. *Proc. Inst. Mech. Eng.*, Vol. 138:229–266.

Blander, M. and Katz, J. L. (1972). The thermodynamics of cluster formation in nucleation theory. *J. Stat. Phys.*, Vol. 4:55–59.

Blythe, P. and Shih, C. (1976). Condensation shocks in nozzle flows. *J. Fluid Mech.*, Vol. 76:593–621.

Buckley, J. R. (2003). *A Study of Heterogeneous Nucleation and Electrostatic Charge in Steam Flows*. PhD thesis, The University of Birmingham.

Cai, X., Niu, F., Li, J., Su, M., Ning, T., and Song, Y. (2010a). Investigation of wet steam flow in a 300 mw direct air-cooling steam turbine. part 2: flow field and windage. *Proc. Inst. Mech. Engnrs., Part A J. Power and Energy*, Vol. 224:129–137.

Cai, X., Niu, F., Ning, T., Wu, G., and Song, Y. (2009). An investigation of wet steam flow in a 300 mw direct air-cooling steam turbine. part 1: measurement principles, probe, and wetness. *Proc. Inst. Mech. Engnrs., Part A J. Power and Energy*, Vol. 223:625–634.

Cai, X., Niu, F., Ning, T., Wu, G., and Song, Y. (2010b). An investigation of wet steam flow in a 300 mw direct air-cooling steam turbine. part 3: heterogeneous/homogeneous condensation. *Proc. Inst. Mech. Engnrs., Part A J. Power and Energy*, Vol. 224:583–589.

Callender, H. L. (1915). On the steady flow of steam through a nozzle or throttle. *Proc. Inst. Mech. Engrs.*, pages 53–77.

Campbell, B. and Bakhtar, F. (1970). Condensation phenomena in high speed flow of steam. *Proc. Instn. Mech. Engrs.*, Vol. 185:395–404.

Celik, I. (1993). Numerical uncertainty in fluid flow calculations: Needs for future research. *ASME. J. Fluids Eng.*, Vol. 115 (2):194–195.

Celik, I. B., Ghia, U., Roache, P. J., Freitas, C. J., Coleman, H., and Raad, P. E. (2008). Procedure for estimation and reporting of discretization error in cfd applications. *J. Fluids Eng.*, Vol. 130 (7), 078001:1–4.

Chandler, K., White, A. J., and Young, J. B. (2013). Non-equilibrium wet-steam calculations of unsteady low-pressure turbine flows. *Proc. IMechE, Part A: J Power and Energy*, Vol. 228:143–152.

Courtney, W. G. (1961). Remarks on homogeneous nucleation. *J. Chem. Phys.*, Vol. 35:2249.

Delale, C., Lamanna, G., and Dongen, M. (2001). On stability of stationary shock waves in nozzle flows with homogeneous condensation. *Phys. Fluids*, Vol. 13:2706–2719.

Delale, C. F., Schnerr, G. H., and Zierep, J. (1993a). Asymptotic solution of transonic nozzle flows with homogeneous condensation. I. subcritical flows. *Phys. Fluids A*, Vol. 5:2969–2981.

Delale, C. F., Schnerr, G. H., and Zierep, J. (1993b). Asymptotic solution of transonic nozzle flows with homogeneous condensation. II. supercritical flows. *Phys. Fluids A*, Vol. 5:2982–2995.

Denton, J. D. (1975). A time marching method for two and three-dimensional blade to blade flows. Technical report, ARC R. & M. No. 3775.

Denton, J. D. (1983). An improved time-marching method for turbomachinery flow calculation. *J. Eng. Power*, Vol. 105 (3):514–521.

Denton, J. D. (1993). The 1993 igti scholar lecture: Loss mechanisms in turbomachines. *ASME J. Turbomachinery*, 115 (4):621–656.

Dunning, W. J. (1969). *General and Theoretical Introduction*. Nucleation (A.C. Zettlemoyer, ed.), Marcel Dekker, New York, pp. 1-67.

Dykas, S., Majkut, M., Strozik, M., and Smolka, K. (2015). Experimental study of condensing steam flow in nozzles and linear blade cascade. *Int. J. Heat Mass Transfer*, Vol. 80:50–57.

Dykas, S. and Wróblewski, W. (2011). Single- and two-fluid models for steam condensing flow modeling. *Int. J. Multiphase Flow*, Vol. 37 (9):1245–1253.

Dykas, S. and Wróblewski, W. (2013). Two-fluid model for prediction of wet steam transonic flow. *Int. J. Heat Mass Transfer*, Vol. 60:88–94.

Eberle, T., Schatz, M., Starzmann, J., Grübel, M., and Casey, M. (2013). Experimental study of the effects of temperature variation on droplet size and wetness fraction in a low pressure model steam turbine. *Proc. Inst. Mech. Eng., Part A J. Power and Energy*, Vol. 228:97–106.

Eckert, E. R. G. and Drake, R. M. (1972). *Analysis of Heat and Mass Transfer*. McGraw-Hill Co.

Farkas, L. (1927). Keimbildungsgeschwindigkeit in Übersättigten und dämpfen. *Z. Phys. Chem.*, Vol. 125:236–242.

Filippov, G. A., Povarov, O. A., and Priahin, V. V. (1973). The investigation and analysis of wet steam turbines. Technical report, Energiya, Moscow.

Ford, I. J. (1997). Nucleation theorems, the statistical mechanics of molecular clusters and a revision of classical nucleation theory. *Phys. Rev. E*, Vol. 56:5615–5629.

Frenkel, J. (1946). *Kinetic Theory of Liquids*. Oxford University Press, New York.

Gatski, T. B. and Speziale, C. G. (1993). On explicit algebraic stress models for complex turbulent flows. *J. Fluid Mech.*, Vol. 254:59–78.

Gerber, A. (2002). Two-phase eulerian/lagrangian model for nucleating steam flow. *ASME J. Fluids Eng.*, Vol. 124:465–475.

Gerber, A. G. and Kermani, M. J. (2004). A pressure based Eulerian-Eulerian multiphase model for non-equilibrium condensation in transonic steam flow. *Int. J. Heat Mass Transfer*, Vol. 44:2217–2231.

Gerber, A. G. and Knill, K. J. (1999). Nonequilibrium phase change in steam undergoing rapid expansion: Solution method including viscous effects. In *Proc. 33rd National Heat Transfer Conference, Albuquerque, New Mexico*.

Gerber, A. G. and Mousavi, A. (2006). Application of quadrature method of moments to the polydispersed droplet spectrum in transonic steam flows with primary and secondary nucleation. *Applied Mathematical Modelling*, Vol. 31:1518–1533.

Gerber, A. G. and Mousavi, A. (2007). Representing polydispersed droplet behavior in nucleating steam flow. *J. Fluids Eng*, Vol. 129:1404–1414.

Gibbs, J. (1906). *Scientific Papers*. Vol. 1. Longmans Green, London.

Gibbs, J. W. (1888). On the equilibrium of heterogeneous surfaces. In *Collected Papers (Thermodynamics), Longmans, London,.*

Girshick, S. L. and Chiu, C. P. (1990). Kinetic nucleation theory: A new expression for the rate of homogeneous nucleation from an ideal supersaturated vapor. *J. Chem. Phys.*, Vol. 93:1273–1277.

Grübel, M., Starzmann, J., Schatz, M., Eberle, T., Vogt, D. M., and Sieverding, F. (2014). Two-phase flow modeling and measurements in low-pressure turbines: Part 1 — numerical validation of wet steam models and turbine modeling. *J. Eng. Gas Turbines Power*, Vol. 137(4):042602–042602–11.

Guha, A. (1994). A unified theory of aerodynamic and condensation shock waves in vapor-droplet flows with or without a carrier gas. *Phys. Fluids*, Vol. 6:1893–1913.

Guha, A. (1995). *Two-phase Flows with Phase Transition*. In VKI Lecture Series 1995-06, von Karman Institute for Fluid Dynamics, Belgium, 1-110.

Guha, A. (1998). Computation, analysis and theory of two-phase flows. *The Aeronautical Journal*, Vol. 102:71–82.

Guha, A. and Young, J. B. (1991). Time marching prediction of unsteady condensation phenomena due to supercritical heat addition. In *Turbomachinery : Latest Developments in a Changing Scene, London IMechE, C423/057, 167-173.*

Guha, A. and Young, J. B. (1994). The effects of flow unsteadyness on the homogeneous nucleation of water droplets in steam turbines. *Phil. Trans. Royal Soc., Series A*, Vol. 349:445–472.

Gyarmathy, G. (1962). *Grundlagen einer Theorie der Naßdampfturbine*. PhD thesis, ETH Zürich.

Gyarmathy, G. (1963). On the rate of growth of small liquid drop in a supersaturated atmosphere. *Z. Angew. Math. Phys.*, Vol. 14:280.

Gyarmathy, G. (1976). *Condensation in flowing steam*. A von Karman Institute Book on Two-Phase Steam Flow in Turbines and Separators, Hemisphere, London, pp. 127-189.

Gyarmathy, G. (1982). The spherical droplet in gaseous carrier streams: Review and synthesis. *Multiphase Science and Technology*, Vol. 1:99–279.

Gyarmathy, G. (2005). Nucleation of steam in high-pressure nozzle experiments. In *Proc. of 6th European Conference on Turbomachinery, Lille, France, March 7-11, 458-469.*

Gyarmathy, G. and Lesch, F. (1969). Fog droplet observations in a laval nozzle and in an experimental turbine. *Proc. Inst. Mech. Eng.*, Vol. 184:29.

Gyarmathy, G. and Meyer, H. (1965). Spontane kondensation. *V.D.I. Forschungsheft*, page 508.

Hagen, D. E., Schmitt, J., Trueblood, M., Carstens, J., White, D. R., and Alofs, D. J. (1989). Condensation coefficient measurement for water in the umr cloud simulation chamber. *J. Atmos. Sci.*, Vol. 132:144301–1–144301–22.

Halama, J., Benkhaldoun, F., and Fořt, J. (2011). Flux schemes based finite volume method for internal transonic flow with condensation. *Int. J. Numer. Meth. Fluids*, Vol. 65 (8):953–968.

Halama, J. and Fořt, J. (2012). Transonic flow of wet steam: some remarks on numerical simulation. In *Baumann Centenary Conference, BCC-2012-08, University of Cambridge, UK, September 10-11.*

Helmholtz, R. (1886). Untersuchungen über dämpfe und nebel, besonders über solche von lösungen. *Ann. d. Phys.*, Vol. 27:508.

Helmholtz, R. (1887). *Ann. d. Phys.*, Vol. 32:1.

Hertz, H. (1882). *Ann. Phys.*, Vol. 17:177.

Hill, P. G. (1966). Condensation of water vapour during supersonic expansion in nozzles. *J. Fluid Mech.*, Vol. 25 (3):593–620.

Hill, P. G., Witting, H., and Demetri, E. P. (1963). Condensation of metal vapours during rapid expansions. *Trans. ASME, J. Heat Transfer*, Vol. 85:303–317.

IEA (2015). World energy outlook 2015. *OECD Publishing, Paris*, ISBN: 9789264243668 (PDF):1–600.

Ishizaka, K., Ikohagi, T., and Daiguji, D. (1995). A high-resolution numerical method for transonic nonequilibrium condensation flows through a steam turbine cascade. In *Proc. of 6th International Symposium on Computational Fluid Dynamics, 479-484.*

Jonas, O. (1995). Condensation in steam turbines new theory and data. In *Joint Power Generation Conference. Vol. 2. American Society of Mechanical Engineers.*

Kantrowitz, A. (1951). Nucleation in very rapid vapour expansions. *J. Chem. Phys.*, Vol. 19:1097–1100.

Kaschiev, D. (1969). Solution of the non-steady state problem in nucleation kinetics. *Surface Science*, Vol. 14:209–220.

Kirkwood, J. G. and Buff, E. P. (1949). The statistical mechanical theory of surface tension. *J. Chem. Phys.*, Vol. 17:338.

Knudsen, M. (1915). *Ann. Phys.*, Vol. 47:697.

Konorski, A. (1966). *Pr. Inst. Maszyn Przeplywowych (in Polish)*, Vol. 29-31:27–30.

Kosolapov, Y. S. and Liberson, A. S. (1997). An implicit relaxation method for computation of three dimensional steady flows of spontaneously condensing steam. *Computational Mathematics and Mathematical Physics*, Vol. 37:739–747.

Laplace, P. (1806). *Traite de Mechanique Celeste*. Vol. 4. Coucier, Paris.

Launder, B. E. and Spalding, D. B. (1974). The numerical computation of turbulent flows. *Comput. Methods Appl. Mech. Eng.*, Vol. 3:269–289.

Liberson, A. S. and McCloskey, T. H. (1999). A unified cfd based approach to a variety of condensation processess in low pressure steam turbines. In *Proc. of Third International VGB/EPRI Conference, Freiburg*.

Lothe, J. and Pound, G. M. (1962). Reconsiderations of nucleation theory. *J. Chem. Phys.*, Vol. 36:2080–2085.

Lumley, J. L. (1980). The second-order models of turbulent flows. In *Prediction Methods for Turbulent Flows, Hemisphere, New York*.

Marek, R. and Straub, J. (2001). Analysis of the evaporation coefficient and the condensation coefficient of water. *Int. J. Heat Mass Transfer.*, Vol. 44:39–53.

Martin, H. M. (1918). A new theory of the steam turbine. *Engineering*, Vol. 106:1–3, 53–55, 107–108, 161–162, 189–191, 245–246.

McDonald, J. E. (1962). Homogeneous nucleation of vapour condensation. I - thermodynamic aspects. *Am. J. Physics*, Vol. 30:870–877.

McDonald, J. E. (1963). Homogeneous nucleation of vapour condensation. II - kinetic aspects. *Am. J. Physics*, Vol. 31:31–41.

Menter, F. R. (1994). Two-equation eddy-viscosity turbulence models for engineering applications. *AIAA Journal*, Vol. 32 (8):1598–1605.

Miyake, S., Sasao, Y., Yamamoto, S., Tabata, S., Miyawaki, T., and Ohyama, H. (2012). Simulation of unsteady 3D wet-steam flows through three-stage stator-rotor blade rows with equilibrium and non-equilibrium condensations. In *Proc. of ASME Turbo Expo, GT2012-68828, Copenhagen, Denmark, June 11-15, 1-9*.

Moheban, M. and Young, J. B. (1984). A time marching method for the calculation of blade-blade non-equilibrium wet steam flows in turbine cascades. In *Inst. Mech. Engrs., Conf. on Comp. Methods inTurbomach., C76/84, 89*.

Montomoli, F., Carnevale, M., D'Ammaro, A., Massini, M., and Salvadori, S. (2015). Limitations in turbomachinery cfd. In *Uncertainty Quantification in Computational Fluid Dynamics and Aircraft Engines*, SpringerBriefs in Applied Sciences and Technology, pages 21–32. Springer International Publishing.

Moore, M. J. and Sieverding, C. H., editors (1976). *Two-Phase Steam Flow in Turbines and Separators*. Hemisphere Publishing Corporation.

Moore, M. J., Walters, P. T., Crane, R. I., and Davidson, B. J. (1973). Predicting the fog drop size in wet steam turbines. In *Wet Steam 4 Conference, Institute of Mechanical Engineers (UK), University of Warwick, paper C37/73*.

Morita, A., Sugiyama, M., Kameda, H., Koda, S., and Hanson, D. R. (2004). Mass accommodation coefficient of water: Molecular dynamics simulation and revised analysis of droplet train/flow reactor experiment. *J. Phys. Chem. B*, Vol. 108:9111–9120.

Moses, C. A. and Stein, G. D. (1978). On the growth of steam droplets formed in a Laval nozzle using both static pressure and light scattering measurements. *J. Fluids Eng.*, Vol. 100:311–322.

Mozurkewich, M. (1986). Aerosol growth and the condensation coefficientfor water: A review. *Aerosol Sci. Technol.*, Vol. 5:223–236.

Mundinger, G. (1994). *Numerische Simulation instationärer Lavaldüsenströmungen mit Energiezufuhr durch homogene Kondensation*. PhD thesis, Dissertation, Fakultät für Maschinenbau, Universität Karlsruhe (TH).

Oriani, R. A. and Sundquist, B. E. (1963). Emendations to nucleation theory and the homogeneous nucleation of water from vapour. *J. Chem. Phys.*, Vol. 38:2082–2089.

Oswatitsch, K. L. (1942). Condensation phenomena in supersonic nozzles. (rtp translation no. 1905). *Z. Angew. Math. Mech.*, Vol. 22 (1):1–14.

Pathak, H., Mullick, K., Tanimura, S., and Wyslouzil, B. E. (2013). Nonisothermal droplet growth in the free molecular regime. *Aerosol Science and Technology*, Vol. 47:310–1324,.

Piran, M. (1975). *Thermodynamic Properties of Supercooled Steam*. PhD thesis, Ph.D. Thesis, University of Birmingham.

Plummer, P. L. M. and Hale, B. N. (1972). Molecular model for pre-nucleation water clusters. *J. Chem. Phys.*, Vol. 56 (9):4329–4334.

Puzyrewski, R. (1969). *Pr.Inst. Maszyn Przeplywowych (in Polish)*, Vol. 47.

Reiss, H. (1970). Treatment of droplike clusters by means of the classical phase integral in nucleation theory. *J. Stat. Physics*, Vol. 2:83–104.

Rettaliata, T. (1936). Undercolling in steam nozzles. *Trans. A.S.M.E.*, Vol. 58:599.

Reynolds, W. C. (1979). *Thermodynamic properties in SI: Graphs, Tables, and Computational Equations for 40 Substances*. Department of mechanical Engineering, Stanford University.

Richardson, L. F. and Gaunt, J. A. (1927). The deferred approach to the limit. *Philos. Trans. Roy. Soc. London. Ser. A.*, Vol. 226:299–361.

Rideal, E. K. (1925). The influence of thin surface films on the evaporation of water. *J. Phys. Chem.*, Vol. 29:1585–1588.

Roache, P. J. (1994). Perspective: A method for uniform reporting of grid refinement studies. *J. Fluids Eng.*, Vol. 116:405–413.

Roache, P. J. (1997). Quantification of uncertainty in computational fluid dynamics. *Annual Review of Fluid Mechanics*, Vol. 29:123–160.

Roache, P. J. (1998). Verification of codes and calculations. *AIAA Journal*, Vol. 36 (5):696–702.

Roe, P. L. (1986). Characteristic based schemes for the Euler equations. *Annual Review of Fluid Mechanics*, Vol. 18:337–365.

Saltanov, G. and Tkalenko, R. (1975). Investigation of transonic unsteady-state flow in the presence of phase transformations. *Zh. Prikl. Mek. i Tek. Fiz. (UdSSR)*, Vol. 6:42–48.

Schatz, M. and Eberle, T. (2013). Experimental study of steam wetness in a model steam turbine rig: presentation of results and comparison with computation fluid dynamics data. *Proc. Inst. Mech. Eng., Part A J. Power and Energy*, Vol. 228:129–142.

Schatz, M., Eberle, T., Grübel, M., Starzmann, J., Vogt, D. M., and Sürken, N. (2014). Two-phase flow modeling and measurements in low-pressure turbines: Part 2 — turbine wetness measurement and comparison to cfd-predictions. *J. Eng. Gas Turbines Power*, Vol. 137(4):042603–042603–9.

Schnerr, G. H. (1989). Two-dimensional transonic flow with energy supplied by homogeneous condensation: Onset condition and two-dimensional structure of steady laval nozzle flow. *Experiments in Fluids*, Vol. 7:145–156.

Schnerr, G. H. (2005). Unsteadiness in condensing flow: dynamics of internal flows with phase transition and application to turbomachinery. *J. Mech. Eng. Sci.*, Vol. 219:1369–1410.

Schnerr, G. H., Adam, S., and Mundinger, G. (1994). New modes of periodic shock formation in compressible two-phase flows. In *In IUTAM Symp. on Waves in Liquid/Gas and Liquid/Vapor Two-Phase Systems, (ed. S. Morioka & L. van Wijngaarden), 377-386, Kluwer*.

Senoo, S. and Shikano, Y. (2002). Two dimensional analysis for non-equilibrium homogeneously condensing flows through steam turbine cascade. *JSME International Journal, Series B: Fluids and Thermal Engineering*, Vol. 45 (4):865–871.

Senoo, S. and White, A. J. (2006). Numerical simulations of unsteady wet steam flows with non-equilibrium condensation in the nozzle and the steam turbine. In *Proc. ASME-FEDSM2006, FEDSM-2006-98202, Maimi, Florida, USA, July 17-20, 757-767.*

Senoo, S. and White, A. J. (2012). Non-equilibrium unsteady wet-steam condensation modelling: computations in a steam turbine cascade and a nozzle. In *Baumann Centenary Conference, BCC-2012-07, University of Cambridge, UK, September 10-11.*

Simpson, D. A. and White, A. J. (2005). Viscous and unsteadyflow calculations of condensing steam in nozzles. *Int. J. Heat and Fluid Flow*, Vol. 26 (1):71–79.

Skillings, S., Walters, P., and Moore, M. (1987). A study of supercritical heat addition as potential loss mechanism in condensing steam turbines. In *Int. Mech. Engrs., Intl. Conf. on Turbomachinery, Cambridge, C259/87, 125-134.*

Skillings, S. A. and Jackson, R. (1987). A robust time-marching solver for onedimensional nucleating steam flows. *Int. J. Heat Fluid Flow*, Vol. 8:139–144.

Speziale, C. G. (1987). On nonlinear k–l and k–e models of turbulence. *J. Fluid Mech.*, Vol. 178:459–475.

Starzmann, J., Casey, M., and Mayer, J. (2012). Unsteady numerical study of wet steam flow in a low pressure steam turbine. *High Perform Comput in Sci Eng*, Vol. 11:437–450.

Starzmann, J., Casey, M. V., and Mayer, J. F. (2013a). *Water Droplet Flow Paths and Droplet Deposition in Low Pressure Steam Turbines*, chapter IV, pages pp. 351–365. Springer Berlin Heidelberg.

Starzmann, J., Kaluza, P., Casey, M. V., and Sieverding, F. (2013b). On kinematic relaxation and deposition of water droplets in the last stages of low pressure steam turbines. In *Proc. of ASME Turbo Expo, San Antonio, Texas, USA, June 3-7, 1-12.*

Starzmann, J., Schatz, M., Casey, M. V., Mayer, J. F., and Sieverding, F. (2011). Modelling and validation of wet steam flow in a low pressure steam turbine. In *Proc. ASME Turbo Expo, GT2011-45, Vancouver, Canada, June 6-10, 1-12.*

Stodola, A. (1915). Undercooling of steam in nozzles. *Engineering*, pages 643–646.

Thomson, W. (1870). On the equilibrium of vapour at a curved surface of a liquid. *Proc. Royal Society*, Vol. 7:63–68.

Tsuruta, T. and Nagayama, G. (2004). Molecular dynamics studies on the condensation coefficient of water. *J. Phys. Chem. B*, Vol. 108:1736–1743.

Volmer, M. and Weber, A. (1926). Keimbildung in ubersettigten gebilden. *Z. Phys. Chem.*, Vol. 119:227–301.

Vukalovich, M. P. (1958). *Thermodynamic Properties of Water and Steam.* Mashgis, Moscow.

Wagner, W. and Kruse, A. (1998). *The Industrial Standard IAPWS-IF97: Properties of Water and Steam.* Springer, Berlin.

Walters, P. T. (1973). Optical measurement of water droplets in wet steam flows. In *Instn. Mech. Engnrs Conf. Proceedings, London, C32/73.*

Walters, P. T. and Skingley, P. C. (1979). An optical instrument for measuring the wetness fraction and droplet size of wet steam flows in l.p. turbines. In *Proceedings of Design Conference on Steam Turbines for the 1980's, London, C141/79.*

Wegener, P. P. (1966). *Gas dynamics of expansion flows with condensation and homogeneous nucleation of water vapour, Nonequilibrium Flows, Part 1.* Marcel Dekker, New York.

White, A. (2000). Numerical investigation of condensing steam flow in boundary layers. *Int. J. Heat and Fluid Flow*, Vol. 21:727–734.

White, A. (2003). A comparison of modeling methods for polydispersed wet-steam flow. *Int. J. Numer. Meth. Eng.*, Vol. 57:819–834.

White, A. J. and Hounslow, M. J. (2000). Modelling droplet size distributions in polydispersed wet-steam flows. *Int. J. Heat Mass Transfer*, Vol. 43:1873–1884.

White, A. J. and Young, J. B. (1993). Time-marching method for the prediction of two-dimensional unsteady flows of condensing steam. *AIAA J. Propulsion and Power*, Vol. 9 (4):579–587.

White, A. J., Young, J. B., and Walters, P. T. (1996). Experimental validation of condensing flow theory for a stationary cascade of steam turbine blade. *Philos. Trans. Roy. Soc. London.*, Vol. A 354:59–88.

Wilson, C. T. R. (1897). Condensation of water vapour in the presence of dust-free air and other gases. *Phil. Trans. Royal Society (London).*, Vol. 189:265–307.

Winkler, G. and Schnerr, G. H. (2001). Nucleating unsteady flows in low pressure steam turbine stages. In *Proc. 4th European Conf. on Turbomachinery, Fluid Dynamics and Thermodynamics, Firenze, Italy, 793-802.*

Wróblewski, W., Dykas, S., Gardzilewicz, A., and Kolovratnik, M. (2009a). Numerical and experimental investigations of steam condensation in lp part of a large power turbine. *J. Fluids Eng.*, Vo1. 131.

Wróblewski, W., Dykas, S., and Gepert, A. (2009b). Steam condensing flow in turbine channels. *Int. J. Multiphase Flow*, Vol. 35 (6):498–506.

Yamamoto, S., Sasao, Y., Kato, H., Satsuki, H., Ooyama, H., and Ishizaka, K. (2010). Numerical and experimental investigation of unsteady 3-d wet-steam flows through two-stage stator-rotor cascade channels. In *Proc. ASME Turbo Expo, GT2010-22796, Glasgow, UK, June 14-18, 1-9*.

Yamamoto, S., Sasao, Y., Sano, K., Satsuki, H., Ishizaka, K., and Ooyama, H. (2007a). Parallel computation of condensate flows through 2-d and 3-d multistage turbine cascades. In *Proc. International Gas Turbine Congress, Tokyo*.

Yamamoto, S., Sasao, Y., Sato, S., and Sano, K. (2007b). Parallel-implicit computation of three-dimensional multistage stator-rotor cascade flows with condensation. In *Proc. 18th AIAA Computational Fluid Dynamics Conference, AIAA 2007-4460, Miami, Florida, USA, June*.

Yellot, J. L. (1934). Supersaturated steam. *Trans. ASME*, Vol. 56:411–430.

Yellott, J. I. and Holland, C. K. (1937). The condensation of flowing steam - condensation in deverging nozzles. *Engineering*, Vol. 143:647–703.

Yeoh, C. C. and Young, J. B. (1984). Non-equilibrium throughflow analysis of low pressure wet steam turbines. *J. Eng. Gas Turbines Power*, Vol. 106:716–724.

Young, J. and Guha, A. (1991). Normal shock-wave structure in two-phase vapour-droplet flows. *J. Fluid Mech.*, Vol. 228:243–274.

Young, J. B. (1973). *Nucleation in High Pressure Steam and Flow in Turbines*. PhD thesis, University of Birmingham.

Young, J. B. (1982). The spontaneous condensation of steam in supersonic nozzles. *Physico Chemical Hydrodynamics*, Vol. 3:57–82.

Young, J. B. (1988). An equation of state for steam for turbomachinery and other flow calculations. *J. of Eng. for Gas Turbines and Power*, Vol. 110:1–7.

Young, J. B. (1992). Two-Dimensional nonequilibrium wet steam calculations for nozzles and turbine cascades. *ASME J. Turbomachinery*, Vol. 114:569–579.

Young, J. B. (1993). The condensation and evaporation of liquid droplets at arbitrary knudsen number in the presence of an inert gas. *Int. J. Heat Mass Transfer*, Vol. 36:2941–2956.

Yousif, A. H., Al-Dabagh, A. M., and Al-Zuhairy, R. C. (2013). Non-equilibrium spontaneous condensation in transonic steam flow. *Int. J Therm Sci*, Vol. 68:32–41.

Zaichik, L., Simonin, O., and Alipchenkov, V. (2003). Two statistical models for predicting collision rates of inertial particles in homogeneous isotropic turbulence. *Phys. Fluids*, Vol. 15:2995–3005.

Zeldovich, J. (1942). Theory of the formation of a new phase. *J. Expl. Theoret. Physics*, Vol. 12:525.

Publication I

Patel, Y., Patel, G., and Turunen-Saaresti, T. (2013).
The effect of turbulence and real gas models on the two phase spontaneously condensing flows in nozzle.

Reprinted with permission from
Proceedings of ASME Turbo Expo 2013:
Turbine Technical Conference and Exposition.
Vol. 5B, pp. 1-8.
© ASME, 2013

Proceedings of ASME Turbo Expo 2013: Turbine Technical Conference and Exposition
GT2013
June 3-7, 2013, San Antonio, Texas, USA

GT2013-94778

THE EFFECT OF TURBULENCE AND REAL GAS MODELS ON THE TWO PHASE SPONTANEOUSLY CONDENSING FLOWS IN NOZZLE

Yogini Patel*
Fluid Dynamics Laboratory
Institute of Energy Technology
Lappeenranta University of Technology
Lappeenranta, Finland
Email: yogini.patel@lut.fi

Giteshkumar Patel
Fluid Dynamics Laboratory
Institute of Energy Technology
Lappeenranta University of Technology
Lappeenranta, Finland
Email: giteshkumar.patel@lut.fi

Teemu Turunen-Saaresti
Fluid Dynamics Laboratory
Institute of Energy Technology
Lappeenranta University of Technology
Lappeenranta, Finland
Email: teemu.turunen-saaresti@lut.fi

ABSTRACT

The aim of the paper is to analyse the effect of turbulence and real gas models on the process of spontaneous condensation in converging diverging (CD) nozzle by using commercial Computational Fluid Dynamics (CFD) code. The calculations were based on the 2-D compressible Navier-Stokes (NS) equations coupled with two-equation turbulence model, and the non-equilibrium spontaneous condensing steam flow was solved on the basis of the classical nucleation theory. The results were validated to the available experimental data.

Nomenclature

C_p	specific heat at constant pressure $(J/kg \cdot K)$
C_v	specific heat at constant volume $(J/kg \cdot K)$
$C_{1\varepsilon}, C_{2\varepsilon}$	model constants
h	specific enthalpy(J/kg)
s	entropy (J/K)
K_t	thermal conductivity $(W/m \cdot K)$
I	nucleation rate $(1/m^3 \cdot s)$
r	radius (m)
K_b	Boltzmann's constant (J/K)
R	gas constant $(J/kg \cdot K)$
M_m	molecular mass (kg)
S	supersaturation
k	turbulent kinetic energy (m^2/s^2)
Q	evaporation coefficient
V	volume (m^3)
P	pressure(Pa)
T	temperature (K)

Greek Letters

ρ	density (kg/m^3)
μ	dynamic viscosity $(kg/m \cdot s)$
Γ	mass generation rate $(kg/m^3 \cdot s)$
η	number of droplets $(1/m^3)$
ε	turbulent dissipation rate $(m^2 s^{-3})$
β	liquid phase mass fraction
σ	liquid surface tension (N/m)
χ	turbulent intensity
γ	ratio of the specific heats of the vapor
Π	production of turbulence energy

Subscript

m	mixture
l	liquid phase
v	vapor phase
d	droplet
sat	saturation
i, j, k	tensor notation

---

*Corresponding author

Copyright © 2013 by ASME

1 INTRODUCTION

Two phase wet-steam flows occur in environmental context and industrial applications, such as liquid spray combustion, aerosols formulation and condensation in steam turbines. During the expansion of steam in the last stages of low-pressure (LP) turbines, the superheated steam crosses the critical phase change boundary and starts to supercool. Steam nucleates and fine liquid droplets formulate. In steam flows, the spontaneous condensation appears in the absence of foreign nuclei. The presence of liquid phase reduces the efficiency of the steam turbine. Moreover, it yields erosion in the turbine components. Therefore, an accurate prediction of the loss mechanism due to condensation in steam turbines is very important.

Comprehensive studies have been made by numerous researchers both experimentally and numerically to enhance the knowledge about the complicate physics of steam condensing flows in nozzles and turbines. Experimental work with the homogeneous condensation in nozzles and turbine cascades has been performed by many authors. Moore et al. conducted measurements of the pressure distribution in nozzles by varying the throat height and divergence angle and used the light scattering data to infer droplet sizes [1]. Moses et al. made experiments on the steam condensation in a Laval nozzle over a variety of starting conditions where the homogeneous nucleation and growth of the liquid phase were documented with both the static pressure and the laser light scattering [2]. Moreover, Barschdorff did experiments on the pressure distribution in arc nozzle flows [3]. Gyarmathy conducted experiments on Laval nozzles designed for various expansion rates and inlet stagnation states, and the study emphasized the Wilson lines and the fog structure in high-pressure saturated/subcooled steam flows [4]. White et al. performed a detailed experimental study of condensing steam flow in a stationary cascade of turbine blades operating transonically [5]. The numerical modeling of both homogeneous and heterogeneous condensation has been ongoing for several decades. Unsteady 2-D and 3-D transonic flows of moist air have been modeled [6]. Numerical studies have been presented using both steady and unsteady 2-D calculation for spontaneously nucleating flow of steam in CD nozzles [7]. Also the modeling of spontaneous condensation in a transonic steam flow in the 2-D rotor tip section of a stage turbine has been performed [8]. Moreover, recently unsteady 3-D wet steam flows through three stage stator rotar blades have been investigated numerically [9]. Some studies have emphasized on the development of numerical techniques for solving the condensing steam flow [10][11]. There are many works where the authors have ignored the effect of turbulence on the condensing steam flow. However, the turbulence has a significant effect on the processes of mass, momentum, and heat transfer in the boundary layers on the walls, and it can play an important role in the forming of condensation shocks [12]. The effect of turbulence on the steam condensing flow has been studied by Avetissian et al. by applying the moment method and the $\delta-$approximation method to determine the droplet size spectrum [12][13]. Avetissian et al. simulated the 2-D flat and the round shape nozzles, where the studies emphasized on the effect of the inlet moisture and turbulence level. Also the accurate calculation of the steam properties near to the saturation line required the real gas model. For steam properties calculation, many authors have considered various real gas models. For example Gerber et al. and Yang et al. used the thermodynamic database of Vukalovich [14][15], Simpson et al. adopted the steam properties of Young [7], etc. Nikkhani et al. utilized the equations of IAPWS-IF97 (International Association of Properties of Water and Steam) for modeling the thermodynamics properties of water and steam in numerical simulations [16]. Moreover, some studies have been conducted with their own real gas models in condensing steam flows [17][18]. The authors have carried out the numerical modeling of the transonic steam flow with both homogeneous and/or heterogeneous condensation [17]. The accuracy assessment of the single-fluid method and two-fluid method models has been emphasized by modeling wet steam flow in nozzle [18].

The aim of this work is to analyze the effect of turbulence parameters such as the coefficient of turbulent viscosity and the degree of turbulence on the spontaneous condensing steam flow. The present work is also extended to implement the local real gas equation of state (EOS) and other thermodynamical properties which are accurate and computationally less expensive. The numerical results are validated with the experiments of nozzle A in Moore et al. [1].

2 MATHEMATICAL MODEL

The results presented in this paper were obtained by means of the ANSYS Fluent 13.0 CFD code. The Eulerian-Eulerian approach has been adopted for modeling the condensing steam flow. The two-phase water-vapor mixture is modeled using the conservation-type 2-D compressible NS equations which are coupled with the two-equation turbulence model. Additionally, two transport equations for the liquid mass-fraction (β) and the number of liquid droplets per unit volume (η) are included.

2.1 Governing equations

The mixture of water and vapor is governed by the compressible NS equations which can be written in the integral Cartesian form:

$$\frac{\partial W}{\partial Q}\frac{\partial}{\partial t}\int_V Q dV + \oint M dA = \int_V N dV. \tag{1}$$

Copyright © 2013 by ASME

In Eq. (1), $Q = [p, u, v, w, T]^T$ represents the mixture quantities of water and vapor phases. The Jacobian $\partial W/\partial Q$ and M are:

$$\frac{\partial W}{\partial Q} = \begin{bmatrix} \rho_p & 0 & 0 & 0 & \rho_T \\ \rho_p u & \rho & 0 & 0 & \rho_T u \\ \rho_p v & 0 & \rho & 0 & \rho_T v \\ \rho_p w & 0 & 0 & \rho & \rho_T w \\ \rho_p H - \delta & \rho u & \rho v & \rho w & \rho_T H + \rho C_p \end{bmatrix}$$

$$M = \begin{bmatrix} \rho v \\ \rho v u + p\hat{i} - \tau_{xi} \\ \rho v v + p\hat{j} - \tau_{yi} \\ \rho v w + p\hat{k} - \tau_{zi} \\ \rho v E + p v - \tau_{ij} v_j - q \end{bmatrix}$$

where in Eq. (1), N contains all the source terms, such as body forces and energy sources, and ρ_p and ρ_T are the density variations with respect to pressure and temperature, respectively. The formulation of the conservation equations is based on the mixture properties of water and vapor phases which are determined from the following correlations:

$$\begin{aligned} h_m &= h_l\beta + (1-\beta)h_v, \\ s_m &= s_l\beta + (1-\beta)s_v, \\ C_{p_m} &= C_{p_l}\beta + (1-\beta)C_{p_v}, \\ C_{vm} &= C_{vl}\beta + (1-\beta)C_{vv}, \\ \mu_m &= \mu_l\beta + (1-\beta)\mu_v, \\ Kt_m &= Kt_l\beta + (1-\beta)Kt_v. \end{aligned} \tag{2}$$

The condensed liquid phase mass fraction is governed as:

$$\frac{\partial \rho\beta}{\partial t} + \nabla\cdot(\rho\vec{v}\beta) = \Gamma, \tag{3}$$

where Γ displays the mass generation rate per unit volume due to condensation and evaporation. The number density of the water droplets per unit volume is calculated from:

$$\frac{\partial \rho\eta}{\partial t} + \nabla\cdot(\rho\vec{v}\eta) = \Gamma I, \tag{4}$$

where I is the nucleation rate and η displays the number of droplets per unit volume which is calculated from the average droplet volume V_d, β, and density ratio of liquid to vapor as follow:

$$\eta = \frac{\beta}{(1-\beta)V_d(\rho_l/\rho_v)}. \tag{5}$$

The average droplet volume is determined as:

$$V_d = \frac{4}{3}\pi\bar{r}_d^3, \tag{6}$$

where r_d is the liquid droplet radius. In order to solve water-vapor mixture flow, some assumptions have been made: there are no interactions between water droplets, the slip velocity between the water droplets and the vapor surrounding them is negligible, the liquid phase consists of droplets whose radii are in the order of $1\mu m$ or less. Therefore, it is assumed that the volume of the condensed liquid phase is negligible.

2.2 Nucleation and droplet growth model

For modeling nucleation rate during spontaneous condensation, several theories have been proposed by many researchers. In the present work, the classical homogeneous nucleation theory defined by Frenkel [19] has been employed as follows:

$$I = \frac{q_c}{(1+\theta)}\left(\frac{\rho_v^2}{\rho_l}\right)\sqrt{\frac{2\sigma}{M_m^3\pi}}\,e^{-\left(\frac{4\pi r_*^2\sigma}{3K_bT}\right)}. \tag{7}$$

The theory determines the liquid phase formation in the form of droplets from a supersaturated phase in the absence of impurities or foreign particles. In Eq. (7), q_c, M_m, σ, ρ_l, and K_b are the evaporation coefficient, molecule mass, surface tension of the liquid phase, liquid density at temperature T, and the Boltzmann constant, respectively. The non-isothermal correction coefficient, θ, is represented as [20]:

$$\theta = \frac{2(\gamma-1)}{\gamma+1}\left(\frac{h_{l_v}}{RT}\right)\left(\frac{h_{l_v}}{RT} - 0.5\right), \tag{8}$$

where γ is the ratio of specific heat capacities and h_{l_v} displays the specific enthalpy of evaporation at pressure p. In the classical homogeneous nucleation theory, the mass generation rate Γ during the spontaneous condensation process is accounted by the addition of mass increase owing to nucleation and due to growth/demise of liquid droplets. Γ is written as [21]:

$$\Gamma = \frac{4}{3}\pi\rho_l I r_*^3 + 4\pi\rho_l\eta\bar{r}^2\frac{\partial\bar{r}}{\partial t}, \tag{9}$$

Copyright © 2013 by ASME

where $\bar{r}$ is the average radius of the liquid droplet which is calculated based on the critical droplet size and the droplets growth and r_* is the Kelvin-Helmholtz critical droplet radius. If the radius of droplet is larger than r_*, it will grow, otherwise the droplet evaporates [20]. The critical droplet radius is determined as follow:

$$r_* = \frac{2\sigma}{\rho_l RT\,lnS}, \tag{10}$$

where S is the super saturation ratio defined by the ratio of vapor pressure to the equilibrium saturation pressure as [20]:

$$S = \frac{P}{P_{sat}(T)}. \tag{11}$$

In the steam condensation process, there are two mechanisms involved. The first one is related to the mass transfer from the vapor phase to the droplets, and the other is the transfer of heat from the created droplets to the vapor in the form of latent heat [21]. Eq. (7) defines only the quantity of the droplets at a location in the vapor phase, and the droplets growth rate can be derived on the basis of heat transfer conditions surrounding the droplet [22]. The droplets growth equation can be written as [22]:

$$\frac{\partial \bar{r}}{\partial t} = \frac{P}{h_{lv}\rho_l\sqrt{2\pi RT}}\frac{\gamma+1}{2\gamma}C_p(T_0-T), \tag{12}$$

where T_0 is the droplet temperature.

2.3 Turbulence modelling

The turbulence is simulated on the basis of the standard $k-\varepsilon$ (SKE) two-equation turbulence model. As mentioned before, the liquid droplets occupy little volume in the flow. For this reason, it is assumed that there is no direct influence of the droplets on the flow turbulence but the effect of droplets through the velocity field introduced to the turbulence models. Therefore, to capture the important features of the turbulent flow, the turbulence equations are solved for the mixture of vapor and water phase. The equations of turbulence energy and its dissipation rate are presented as:

$$\frac{\partial}{\partial t}(\rho_m k) + \nabla\cdot(\rho_m \vec{v}_m k) = \nabla\cdot\left(\frac{\mu_{t,m}}{\sigma_k}\nabla k\right) + G_{k,m} - \rho_m\varepsilon, \tag{13}$$

$$\frac{\partial}{\partial t}(\rho_m \varepsilon) + \nabla\cdot(\rho_m \vec{v}_m \varepsilon) = \nabla\cdot\left(\frac{\mu_{t,m}}{\sigma_\varepsilon}\nabla \varepsilon\right) + \frac{\varepsilon}{k}(C_{1\varepsilon}G_{k,m} - C_{2\varepsilon}\rho_m\varepsilon), \tag{14}$$

where ρ_m and $\vec{v}_m$ are the mixture density and velocity, respectively. The mixture turbulent viscosity, $\mu_{t,m}$, is calculated from:

$$\mu_{t,m} = \rho_m C_\mu \frac{k^2}{\varepsilon}. \tag{15}$$

The term $G_{k,m}$ in Eq. (13) denotes the production rate of turbulence energy as:

$$G_{k,m} = \mu_{t,m}\frac{\partial v_{mi}}{\partial x_j}. \tag{16}$$

The model constants in Eqs. (13) - (15) are considered as follows: σ_k= 1.0, σ_ε = 1.3, $C_{1\varepsilon}$ = 1.44, $C_{2\varepsilon}$ = 1.92, and C_μ = 0.09 [23]. In this work, some modifications have been made to the turbulent viscosity term of the standard $k-\varepsilon$ turbulence model, to study the effect of turbulence on steam condensing flow. The modification of the turbulent viscosity term increases the turbulent kinetic energy and the Reynolds stresses of the two-phase flow mixture. Thus, the flow receives more oscillations. The turbulent viscosity coefficient is calculated by means of an expansion procedure for resolving implicit algebraic equations for Reynolds stress tensor in terms of mean velocity gradients [24][25]. In their work, Avetissian et al. added source terms to the standard $k-\varepsilon$ turbulence model in order to calculate the modulation of the turbulence energy due to additional dissipation by droplets [12]. In contrast to the less simple expression as in Eq. (15), the modified term of turbulent viscosity is adopted from Avetissian et al. as [12]:

$$\mu_{t,m} = \frac{\rho_m C_\mu}{1+(\Pi/\varepsilon-1)/C_1}\frac{k^2}{\varepsilon}. \tag{17}$$

In Eq. (17), the constant C_1 is the Rotta return-to-isentropy approximation of the pressure-strain correlation. The turbulent viscosity formulations in Eq. (15) and Eq. (17) are similar when the constant C_1 approaches to infinity. This Rotta constant plays the major role in the stability of turbulent flow [26]. In the present work, the effect of the modified standard $k-\varepsilon$ (MSKE) turbulence model has been studied in the context of turbulent viscosity on the condensing steam flow.

2.3 Equation of state

One of the intensions of this work is to calculate the correct steam properties by using the simple form of the local real gas model. In this work, the steam properties have been calculated by real gas EOS from Young's [27] and the author's own formulations. The author's EOS for real gas is given as:

$$P_v = RT_v(\rho_v A(T_v) + B(T_v)\rho_v^2), \tag{18}$$

Copyright © 2013 by ASME

where P_v, T_v, and ρ_v are the pressure, temperature, and density of the vapor phase, respectively, and R is the gas constant. The virial coefficients A and B are defined as a 2nd degree polynomial as:

$$A(T_v) = a_0 + a_1 T + a_2 T^2,$$

$$B(T_v) = b_0 + b_1 T + b_2 T^2.$$

These coefficients are approximated by regression analysis, and they are based on IAPWS-IF97 steam table. The other thermodynamical properties of vapor phase like the heat capacities C_{p_v} and C_{vv}, specific enthalpy h_v, specific entropy S_v, dynamic viscosity μ_v and thermal conductivity K_{tv} are in the form of polynomials of temperature and density. The author's real gas EOS and other steam properties formulations are applicable on the limited range of pressure from 1 to 70 kPa, and over a temperature range of 273.15 to 500 K. ρ_v, h_v, μ_v, and K_{tv} have less than 0.03% averaged error with IAPWS-IF97 steam table while the averaged error of S_v, C_{p_v}, and C_{vv} is less than 0.2%. The water properties under the conditions close to the saturation line must be calculated accurately. These properties, such as the liquid density ρ_l, σ, specific heat C_{p_l}, dynamic viscosity μ_l, and thermal conductivity K_{tl}, were obtained from [22][28][29].

3 RESULTS AND DISCUSSIONS

In the present work, the phase conservation equations of liquid and vapor phases were solved using a conservative finite-volume integration over a control volume. The spatial discretization was solved with second-order upwind schemes. The geometry of a CD nozzle was employed corresponding to the experiments of nozzle A in Moore et al. [1]. All the calculations were based on the inlet total pressure of 25 kPa and the total temperature of 354.6 K. This work emphasizes the effect of modified turbulence viscosity and real gas models on the condensing steam flow by implementing the models into the commercial CFD code utilizing user defined subroutines.

A grid-sensitivity analysis was conducted to ensure a sufficient degree of grid independence of the results. Three grids were made by increasing the resolution from Grid A (18,000 cells) over Grid B (36,000 cells) to Grid C (40,000 cells). The pressure and wetness fraction along the nozzle centerline obtained by three different grids are shown in Fig. 1. It is clear that there is no significant effect of grid refinement from Grid A to Grid C. Therefore, all the further results presented are obtained with Grid B.

Fig. 2 represents the numerical results of pressure distributions along the nozzle centerline corresponding to the experiments in the absence of initial wetness at the nozzle inlet. Both models, the SKE and the MSKE, yield nice trends in the experiments. However, the SKE predicted a high peak in the condensation shock region and fluctuated pressure profiles in the downstream of the nozzle. The MSKE computed a similar trend with the experiments and a more stable pressure drop profile. Fig. 3 demonstrates the distributions of wetness fraction along the nozzle centerline with the SKE and the MSKE models. It is clear that the SKE model predicted higher wetness fraction compared to the MSKE. Both models underestimate the average droplet radii as shown in Fig. 4. In the case of the MSKE, the average droplet radii are bigger than in the SKE model.

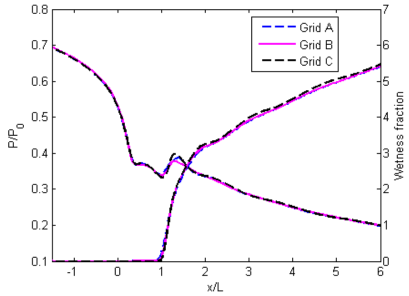

Figure 1. Pressure and wetness fraction along the nozzle centerline with standard $k-\varepsilon$ model (SKE).

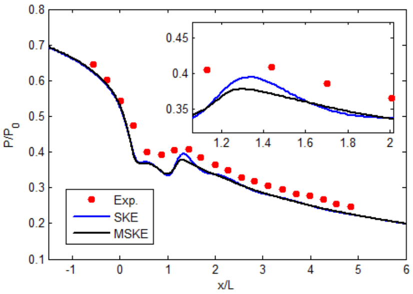

Figure 2. Pressure distributions along the nozzle centerline: experiments (Moore et al., 1973 [1]); standard $k-\varepsilon$ model (SKE); modified $k-\varepsilon$ model (MSKE).

In the present work, the computations were conducted with the MSKE at various inlet turbulence intensities (i.e., $\chi = 0.05$, 0.1, and 0.2). Fig. 5 represents the distributions of pressure along the nozzle centerline with various inlet flow turbulence levels. It is clear that the SKE predicted a high peak compared to the

Copyright © 2013 by ASME

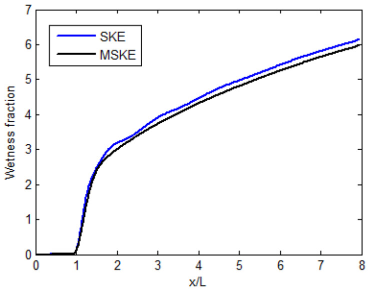

Figure 3. Wetness fraction along the nozzle centerline: standard $k-\varepsilon$ model (SKE); modified $k-\varepsilon$ model (MSKE).

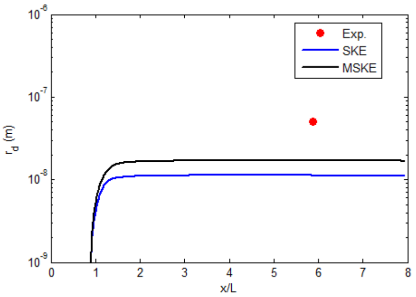

Figure 4. Average droplet radius distribution along the nozzle centerline: experiments (Moore et al., 1973 [1]); standard $k-\varepsilon$ model (SKE); modified $k-\varepsilon$ model (MSKE).

MSKE. The condensation shock spreads out at high-level inlet turbulence with the MSKE model while there is no significant variation in the condensation shock in the SKE with various inlet turbulence levels. This spread out happens due to the high value of the turbulent viscosity in the near-axis region of the nozzle. Fig. 6 demonstrates that the MSKE predicted high turbulent viscosity with high-level inlet turbulence. The SKE yields an almost constant value of turbulent viscosity along the nozzle axis. However, there is some numerical oscillation near the $x/L = 0$ region in the case of MSKE with $\chi = 0.05$ and 0.1. It is clear that the variation of the turbulent viscosity depends on the turbulence level in the condensation shock region which is demonstrated in Fig. 5. The turbulence intensity profiles are represented in Fig. 7 with various inlet turbulence levels. It demonstrates that the MSKE calculates a higher turbulence level in the downstream of nozzle while the SKE predicts a low level of turbulence.

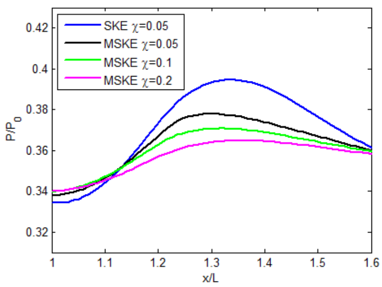

Figure 5. Pressure distributions along the nozzle centerline: SKE; MSKE with $\chi = 0.05$; MSKE with $\chi = 0.1$; MSKE with $\chi = 0.2$.

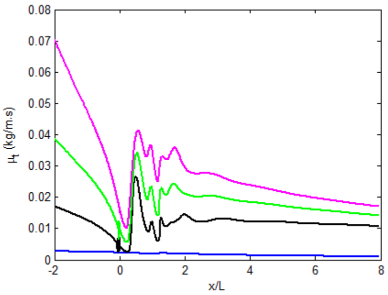

Figure 6. Turbulent viscosity along the nozzle centerline: SKE; MSKE with $\chi = 0.05$; MSKE with $\chi = 0.1$; MSKE with $\chi = 0.2$.

Fig. 8 represents the pressure drop and Mach number along the nozzle centerline without condensation produced by Young's and the author's real gas model. Fig. 9 shows the results of pressure distribution along the nozzle centerline with condensation. It is clear that the author's formulations give relatively better predictions of the condensation shock. Also the author's real gas EOS predicted good pressure drop profile with the experiments compared to Young's EOS. In order to check the computational expensiveness of both Young's and the author's real gas models, 10 numerical iterations were performed, and this analysis shows that both the models utilized 13 and 15 seconds, respectively, on the single CPU. It reveals that the author's real gas model is computationally affordable.

Copyright © 2013 by ASME

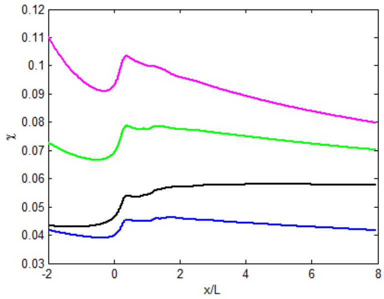

Figure 7. Turbulent intensity along the nozzle centerline: SKE; MSKE with $\chi = 0.05$; MSKE with $\chi = 0.1$; MSKE with $\chi = 0.2$.

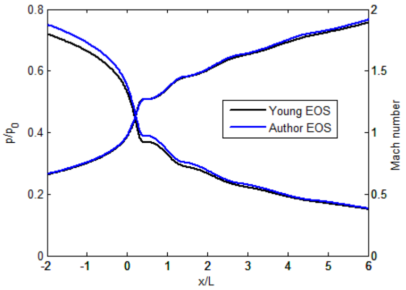

Figure 8. Pressure and Mach number distribution along the nozzle centerline with dry steam: Young's EOS [27]; Author's own EOS.

4 CONCLUSIONS

The Eulerian-Eulerian approach has been adopted for modeling the spontaneous condensing steam flow in a supersonic nozzle. The effects of turbulence and real gas model have been discussed. Based on the CFD calculations, we have obtained the following conclusions:

(i) The standard k-ε turbulence model overestimates the peak level of the condensation shock while the modified standard k-ε turbulence model yields better trends with experimental data,

(ii) The wetness prediction by the standard k-ε turbulence model is slightly higher than by the modified standard k-ε turbulence model,

(iii) The modified standard k-ε turbulence model simulated higher average droplet radii compared to the standard k-ε turbulence model,

(iv) The condensation shock spread out due to high-level turbulence,

(v) The author's real gas formulations are able to predict an accurate steam condensing flow in a CD nozzle,

(vi) The effect of steam property calculations is more sensitive to the condensing flow compared to the turbulence effect.

The presented results motivate the authors to enhance this research to a more deep level regarding steam properties and turbulence effects on the steam condensing flows. This work will be continued in future with the aim to predict the condensing flow both in nozzles and a 3D turbine cascade.

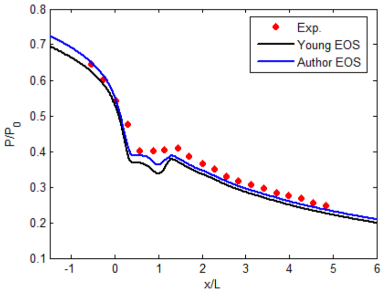

Figure 9. Pressure distributions along the nozzle centerline: experiments (Moore et al., 1973 [1]); Young's EOS [27]; Author's own EOS.

ACKNOWLEDGEMENTS

The authors would like to acknowledge the financial support from the graduate school of CFD, Finland and Academy of Finland.

REFERENCES

[1] Moore, M.J., Walters, P.T., Crane, R.I., Davidson, B.J., 1973, "Predicting the fog drop size in wet steam turbines", Wet Steam 4 Conference, Institute of Mechanical Engineers (UK), University of Warwick, paper C37/73

[2] Moses, C.A., Stein, G.D., 1978, "On the growth of steam droplets formed in a Laval nozzle using both static pressure and light scattering measurements", J. Fluids Eng., Vol. 100, pp. 311-322

[3] Barschdorff, D., 1971, "Verlauf der Zustandsgrossen und gasdynamische Zusammenhaenge der spontanen Kondensation reinen Wasserdampfes in Lavalduesen", Forsch, Ingenieurwes, Vol. 37, pp. 146-157

Copyright © 2013 by ASME

[4] Gyarmathy, G., 2005, ”Nucleation of steam in high-pressure nozzle experiments”, In: Proc. of 6th European Conference on Turbomachinery, Lille, France, pp. 458-469

[5] White, A.J., Young, J.B., Walters, P.T., 1996, ”Experimental validation of condensing flow theory for a stationary cascade of steam turbine blade”, Philos. Trans. Roy. Soc. Lond. Vol. A 354, pp. 5988

[6] Schnerr, G.H., 2005, ”Unsteadiness in condensing flow: dynamics of internal flows with phase transition and application to turbomachinery”, J. Mech. Eng. Sci. Vol. 219, pp. 1369-1410

[7] Simpson, D.A., White, A.J., 2005, ”Viscous and unsteadyflow calculations of condensing steam in nozzles”, Int. J. Heat and Fluid Flow, Vol. 26(1), pp. 71-79

[8] Sun, L., Zheng, Q., Liu, S., 2007, ”2D-simulation of wet steam flow in a steam turbine with spontaneous condensation”, Journal of Marine Science and Application, vol. 6(2), pp. 59-63

[9] Miyake, S., Sasao, Y., Yamamoto, S., Tabata, S., Miyawaki, T., Ohyama, H., 2012, ”Simulation of unsteady 3D wet-steam flows through three-stage stator-rotor blade rows with equilibrium and nonequilibrium condensations”, Proc. of ASME Turbo Expo, GT2012-68828, Copenhagen, Denmark

[10] Halama, J., Benkhaldoun, F., Fort, J., 2010, ”Flux schemes based finite volume method for internal transonic flow with condensation”, Int. J. Numer. Meth. Fluids, Wiley InterScience, doi:10.1002/fld.2223

[11] Halama, J., Fořt, J., 2012, ”Transonic flow of wet steam: some remarks on numerical simulation”,Proc. Baumann Centenary Conference, BCC-2012-08, Cambridge

[12] Avetissian, A.R., Alipchenkov, V.M., Zaichik, L.I., 2003, ”The effect of turbulence on the flow of spontaneously condensing moist steam in laval nozzles”, High Temp., Vol. 41, pp. 57-61

[13] Avetissian, A.R., Philippov, G.A., Zaichik, L.I., 2008, ”Effects of turbulence and inlet moisture on two-phase spontaneously condensing flows in transonic nozzles”, Int. J. Heat Mass Transfer, Vol. 51, pp. 4195-4203

[14] Gerber, A.G., Kermani, M.J., 2004, ”A pressure based Eulerian-Eulerian multi-phase model for non-equilibrium condensation in transonic steam flow”, Int. J. Heat Mass Transfer, Vol. 44, pp. 2217-2231

[15] Yang, Y., Shen, S., 2009, ”Numerical simulation on non-equilibrium spontaneous condensation in supersonic steam flow”, Int. Commu. Heat and Mass Transfer, Vol. 36, pp. 902-907

[16] Nikkhani, B., Shams, M., Ziabasharhagh, M., 2010, ” A numerical study of two-phase transonic steam flow through converging-divergence nozzles with different rates of expansion”, Korean J. Chem. Eng., Vol. 27(6), pp. 1646-1653

[17] Wrblewski, W., Dykas, S., Gepert, A., 2009a. ”Steam condensing flow in turbine channels”, Int. J. Multiphase Flow, Vol. 35(6), pp. 498-506

[18] Dykas, S., Wrblewski, W., 2011, ”Single- and two-fluid models for steam condensing flow modeling”, Int. J. Multiphase Flow, Vol. 37(9), pp. 1245-1253

[19] Frenkel, J., 1946, ”Kinetic Theory of Liquids”, Oxford University Press, New York

[20] Young, J. B., 1992, ”Two-Dimensional nonequilibrium wet steam calculations for nozzles and turbine cascades”, ASME J. Turbomach., Vol. 114, pp. 569-579

[21] Ishizaka, K., Ikohagi, T., Daiguji D., 1995, ”A high-resolution numerical method for transonic nonequilibrium condensation flows through a steam turbine cascade”,Proc. of 6th International Symposium on Computational Fluid Dynamics, pp. 479-484

[22] Young, J. B., 1982, ”The spontaneous condensation of steam in supersonic nozzles”, Physico Chemical Hydrodynamics, Vol. 3, pp. 57-82

[23] Launder, B.E., Spalding, D.B., 1974, ”The numerical computation of turbulent flows”, Comput. Methods Appl. Mech. Eng., Vol. 3, pp. 269-289

[24] Gatski, T.B., Speziale, C.G., 1993, ”On explicit algebraic stress models for complex turbulent flows”, J. Fluid Mech., Vol. 254, pp. 59-78

[25] Speziale, C.G., 1987, ”On nonlinear kl and ke models of turbulence”, J. Fluid Mech., Vol. 178, pp. 459-475

[26] Lumley, J.L., 1980, ”The second-order models of turbulent flows, in: Prediction Methods for Turbulent Flows”, Hemisphere, New York

[27] Young, J. B., 1988, ”An equation of state for steam for turbomachinery and other flow calculations”, Journal of Engineering for Gas Turbines and Power, Vol. 110, pp. 17

[28] Reynolds, W. C., 1979, ”Thermodynamic properties in SI: Graphs, Tables, and Computational Equations for 40 Substances”, Department of mechanical Engineering, Stanford University

[29] Eckert, E. R. G., Drake, R. M., 1972, ”Analysis of Heat and Mass Transfer”, McGraw-Hill Co.

Copyright © 2013 by ASME

Publication II

Patel, Y., Turunen-Saaresti, T., Patel, G., and Grönman, A. (2014).
Numerical investigation of turbulence modelling on condensing steam flows in turbine cascade.

Reprinted with permission from
Proceedings of ASME Turbo Expo 2014:
Turbine Technical Conference and Exposition.
Vol. 1B, pp. 1-14.
© ASME, 2014

Proceedings of ASME Turbo Expo 2014: Turbine Technical Conference and Exposition
GT2014
June 16 – 20, 2014, Düsseldorf, Germany

GT2014-26307

NUMERICAL INVESTIGATION OF TURBULENCE MODELLING ON CONDENSING STEAM FLOWS IN TURBINE CASCADE

Yogini Patel[*]
Fluid Dynamics Laboratory, LUT Energy
School of Technology
Lappeenranta University of Technology
Lappeenranta, Finland
Email: yogini.patel@lut.fi

Teemu Turunen-Saaresti
Fluid Dynamics Laboratory, LUT Energy
School of Technology
Lappeenranta University of Technology
Lappeenranta, Finland
Email: teemu.turunen-saaresti@lut.fi

Giteshkumar Patel
Fluid Dynamics Laboratory, LUT Energy
School of Technology
Lappeenranta University of Technology
Lappeenranta, Finland
Email: giteshkumar.patel@lut.fi

Aki Grönman
Fluid Dynamics Laboratory, LUT Energy
School of Technology
Lappeenranta University of Technology
Lappeenranta, Finland
Email: Aki-Pekka.Gronman@lut.fi

ABSTRACT

Understanding the condensation process at the low-pressure (LP) turbine is important because condensation introduces extra losses, and erosion caused by the droplets wear turbine blades. The paper presents an investigation of the turbulence modelling on the non-equilibrium homogeneous condensing steam flow in a stationary turbine cascade employing 2D compressible Navier-Stokes (NS) equations. The classical nucleation theory is utilized to model the condensation phenomena. The performance of various turbulence models (i.e., the Spalart-Allmaras, the k-ω, the k-ε, the RNG k-ε, the Realizable k-ε, and the SST k-ω) in condensing steam flows is discussed. The SST k-ω model is modified and implemented into a commercial computational fluid dynamics (CFD) code. Substantial improvements in the prediction accuracy are observed when compared with the original SST k-ω model. Overall, the modified model is in excellent agreement with the measurements in all studied test cases of the turbine cascade. The qualitative and quantitative analysis illustrates the importance of turbulence modeling in wet-steam flows.

Nomenclature

C_p	specific heat at constant pressure $(J/kg \cdot K)$
C_v	specific heat at constant volume $(J/kg \cdot K)$
E	total energy (J/kg)
h	specific enthalpy(J/kg)
I	nucleation rate $(1/m^3 \cdot s)$
k	turbulent kinetic energy (m^2/s^2)
K_t	thermal conductivity $(W/m \cdot K)$
M	liquid mass (kg)
P	pressure(Pa)
r	radius (m)
R	gas constant $(J/kg \cdot K)$
s	entropy $(J/kg \cdot K)$
t	time (s)

---

[*] Corresponding author

Copyright © 2014 by ASME

T	temperature (K)
u, v	velocity component (m/s)
$\mathbf{v}$	flow velocity (m/s)
V	volume (m^3)

Greek Letters

ρ	density (kg/m^3)
μ	dynamic viscosity ($kg/m \cdot s$)
β	liquid phase mass fraction
ω	specific dissipation rate ($1/s$)
η	number of liquid droplets per unit volume($1/m^3$)
σ	liquid surface tension (N/m)
γ	ratio of the specific heats of the vapor

Subscript

d	droplet
m	mixture
l	liquid phase
v	vapour phase
t	turbulence
i, j	space coordinate
$\hat{i}, \hat{j}$	tensor notation
x, y	direction
$0, 1, 2$	total, inlet, outlet condition of cascade

1 INTRODUCTION

The steam turbine remains one of the key components for the efficient production of power. Worldwide much importance has been given to the research of low-pressure (LP) turbine stages because of their relatively low efficiency. The expansion process causes the superheated dry steam to first subcool and then nucleate to form a two phase mixture of saturated vapor and fine liquid droplets. The presence of the liquid phase reduces the efficiency of the steam turbine. Moreover, it yields erosion in the turbine components. Therefore, an accurate prediction of the loss mechanism due to condensation in steam turbines is very important.

Wet steam flow has been studied both experimentally and numerically for several years. Experiments of a 1D flow in a nozzle were pioneered by Stodola [1], Binnie et al. [2], and later refined by many authors for example Barschdorff [3], Moore et al. [4], Moses and Stein [5], and Skilling et al. [6]. Later, 2D turbine blade cascades were studied experimentally by Bakhtar et al. [7, 8] and White et al. [9]. They organized significant experimental work for non-equilibrium condensing steam flow in turbine cascades, in which they provided a large set of measurement data for various parameters.

Along with experimental studies, comprehensive studies have also been done numerically by numerous researchers on various aspects of the condensing steam flow. Initially, condensation in wet-steam flows has been numerically investigated with a 1D flow in Laval nozzles for example by Barschdorff [3], Moore et al. [4], and Bakhtar and Zidi [10]. Since the real flow behaviour in steam turbines is considerably complex, later on studies were dedicated to the 2D flow in turbine blade cascades (see White and Young [11], and Bakhtar et al. [12]), in which the numerical approach was based on the inviscid time-marching scheme with a Lagrangian tracking module included to track the particle motion explicitly. Moreover, Gerber [13] developed a numerical model based on the Eulerian-Lagrangian approach to simulate two-phase wet-steam flows. The validation of this approach has been examined with the test cases of the convergent-divergent (CD) nozzle and turbine cascade, as well. However, this approach encounters difficulties with particle tracking and is also computationally expensive for 3D unsteady applications. Some works, for example by Gerber and Kermani [14], and Senoo and Shikano [15], presented an Eulerian-Eulerian multi-phase method for condensing steam flows. Also, Simpson and White [16] presented numerical calculations for the two-phase wet-steam flow using a Jameson-style finite volume method with an unstructured and adaptive triangular mesh. Additionally, Gerber and Mousavi [17] utilized the Quadrature Method of Moments (QMOM) technique for the representation of polydispersed droplet distributions in the condensing steam flow.

Some numerical works, for example by Senoo and Shikano [18], Halama et al. [19], and Halama and Fořt [20], have been devoted to the development of numerical techniques for solving the condensing steam flow. Studies have also been done to develop in-house CFD codes for modeling the non-equilibrium condensing steam flow both homogeneously and/or heterogeneously, for example by Wróblewski et al. [21], Dykas and Wróblewski [22], and Dykas and Wróblewski [23]. Their in-house codes have been validated applying both the single-fluid and two-fluid approaches in nozzles and in turbine cascades. Moreover, numerical work concerning wet-steam flows through two-stage stator rotor cascade channels in a LP steam turbine assuming non-equilibrium and equilibrium condensations was conducted by Yamamoto et al. [24] and Yamamoto et al. [25]. Recently, unsteady 3D wet-steam flows through three stage axial turbine have been investigated numerically by Miyake et al. [26]. Starzmann et al. [27] performed numerical investigations of the wet-steam flow with a three stage LP steam turbine test rig, in which the effect of different theoretical models for nucleation and droplet growth were examined. Moreover, the effect of droplet size on the deposition characteristics of the last stage stator blade and also the effect of inter-phase friction on flow field have been presented by Starzmann et al. [28].

Although numerous studies have been conducted with the condensing flows both in nozzles and in turbine cascades, the role of turbulence on wet-steam flows has not been widely investigated. Traditionally, two-phase transonic flows in nozzles and in turbine blade cascades are modelled in an approximation that ignores the effects of viscosity, thermal conductivity, and turbulence (e.g. Skillings and Jackson [29], Delale et al. [30], White and Young [11], Avetissian et al. [31], Bakhtar et al. [32], and Schnerr [33]). The turbulence plays an important role on the processes of mass, momentum, and heat transfer in boundary layers on the surface walls, as well as on the possible deposition of condensed liquid droplets. Turbulence may have some direct/indirect influence on shock waves generation under the conditions of supercooled steam flow [34]. However, published work on the influence of viscous effect and effect of turbulence on the condensing steam flow is rather sparse. For example, White [35] presented numerical method based on simple stream function technique for the prediction of condensing steam flow in converging-diverging nozzle to analyse the influence of viscous effect on condensation within compressible boundary layers. Avetissian et al. [34, 36] investigated the influence of inlet flow turbulence level and wetness on the two-phase spontaneously condensing flow in nozzles using the moment method and the Delta-approximation method to determine the droplet size spectrum. Moreover, the effect of turbulence parameters (i.e., the coefficient of turbulent viscosity and turbulence level) and real gas models in condensing steam flow in convergent-divergent nozzle have been reported by Patel et al. [37].

From this background, the aim of this paper is to investigate the influence of turbulence modelling on the non-equilibrium homogeneous condensing steam flow in a turbine cascade adopting the Eulerian-Eulerian approach in a commercial computational fluid dynamics (CFD) code. The performance of various turbulence models to wet-steam flow modeling have been presented. Additionally, a modified two-equation turbulence model is presented. The effect of turbulence modelling on the turbine cascade losses is also discussed. The calculated results have been analyzed together with experimental data available in the literature.

2 MATHEMATICAL MODEL

In the present work, an Eulerian-Eulerian approach is adopted by means of ANSYS Fluent 14.0 CFD code. The two-phase vapour-liquid mixture is modeled using 2D compressible Navier-Stokes (NS) equations. Additionally, two transport equations for the liquid phase mass fraction β, and the number of liquid droplets per unit volume η, are solved.

2.1 Governing equations

The set of governing equations of mass, momentum, and energy conservation for the mixture of vapour and liquid phases can be expressed in integral Cartesian form for an arbitrary V with differential surface area dA as below

$$\frac{\partial \mathrm{W}}{\partial \mathrm{Q}} \frac{\partial}{\partial t} \int_V \mathrm{Q}\, dV + \oint \mathrm{M}\, d\mathrm{A} = \int_V \mathrm{N}\, dV, \tag{1}$$

where vectors W, Q, and M are defined as follow, respectively,

$$\begin{pmatrix} \rho \\ \rho u \\ \rho v \\ \rho E \end{pmatrix}, \quad \begin{pmatrix} P \\ u \\ v \\ T \end{pmatrix}, \quad \begin{pmatrix} \rho \mathbf{v} \\ \rho \mathbf{v} u + P\hat{i} - \tau_{xi} \\ \rho \mathbf{v} v + P\hat{j} - \tau_{yi} \\ \rho \mathbf{v} E + P\mathbf{v} - \tau_{ij}\mathbf{v}_j - q \end{pmatrix}.$$

Here, τ and q represent the viscous stress tensor and the heat flux, respectively. In Eq. (1), N contains the source terms such as body forces and energy sources. The formulation of conservation equations is based on the mixture properties of vapour and liquid phases which are determined from the following correlation

$$\phi_m = \phi_l \beta + (1-\beta)\phi_v, \tag{2}$$

where the expression ϕ denotes h, s, C_p, C_v, μ, and K_t. The condensed liquid phase mass fraction and the estimation of the number of droplets per unit volume are calculated from the following transport equations, respectively,

$$\frac{\partial \rho\beta}{\partial t} + \nabla \cdot (\rho \vec{v} \beta) = \Gamma, \tag{3}$$

$$\frac{\partial \rho\eta}{\partial t} + \nabla \cdot (\rho \vec{v} \eta) = \rho I, \tag{4}$$

where Γ displays the mass generation rate per unit volume due to condensation and evapouration, and I is the nucleation rate. In the present work, it is assumed that the interactions between liquid droplets are omitted and the slip velocity between the droplets and the vapour surrounding them is negligible. Since the droplet sizes are sufficiently small (1 µm or less), it is assumed that the volume of the condensed liquid droplets is negligible.

2.2 Nucleation and droplet growth model

In this study, the homogeneous condensation phenomenon is modeled on the basis of the classical nucleation theory of Frenkel [38]. In the classical homogeneous nucleation theory, mass generation rate is calculated by the addition of mass increase owing to nucleation and due to growth/demise of liquid droplets which is obtained from Ishizaka et al. [39], and it can be written as

$$\Gamma = \frac{4}{3}\pi \rho_l I r_*^3 + 4\pi \rho_l \eta \bar{r}^2 \frac{\partial \bar{r}}{\partial t}, \tag{5}$$

where $\bar{r}$ is calculated based on the critical droplet size and the droplets growth. If the droplet radius is larger than r_*, it will

Copyright © 2014 by ASME

grow; otherwise the droplet evaporates [40]. Here r_* represents the Kelvin-Helmholtz critical droplet radius. The droplet growth is calculated from the proposed formula of Hill [41], which can be defined as

$$\frac{\partial \bar{r}}{\partial t} = \frac{P}{h_{lv}\rho_l\sqrt{2\pi RT}} \frac{\gamma+1}{2\gamma} C_p (T_d - T), \tag{6}$$

where T_d is the droplet temperature. More details pertaining to the droplet temperature calculation have been presented in Young [42].

2.3 Turbulence models

The liquid droplets are of sub-micron size occupying little volume in the flow, and on this basis, it is assumed that there is not any direct influence of the droplets on the flow turbulence. However, there is an indirect influence through the velocity field introduced to the turbulence models. Therefore, to capture the important features of the turbulent flow, the turbulence equations are solved for the mixture of vapor and liquid phases. The turbulence in the vapour phase does have an influence on the dispersion of the droplets. In the present work, various turbulence models such as the Spalart-Allmaras, the Standard k-ε, the RNG k-ε, the Realizable k-ε, the Standard k-ω, and the shear-stress transport (SST) k-ω are applied to simulate the condensing steam flow. Among all these turbulence models, the SST k-ω model is selected and modified for further investigation of the turbulence effect on condensing steam flows. The equations of turbulence kinetic energy k, and its specific dissipation rate ω, for the mixture of vapour and liquid phases are presented as follows, respectively,

$$\begin{aligned} \frac{\partial}{\partial t}(\rho k) + \nabla \cdot (\rho \vec{v}_m k) = \nabla \cdot \left(\left(\mu + \frac{\mu_{t,m}}{\sigma_k} \right) \nabla k \right) \\ + G_{k,m} - Y_k + S_k, \end{aligned} \tag{7}$$

$$\begin{aligned} \frac{\partial}{\partial t}(\rho \omega) + \nabla \cdot (\rho \vec{v}_m \omega) = \nabla \cdot \left(\left(\mu + \frac{\mu_{t,m}}{\sigma_\omega} \right) \nabla \omega \right) \\ + G_{\omega,m} - Y_\omega + D_\omega + S_\omega. \end{aligned} \tag{8}$$

Here, $G_{k,m}$ and $G_{\omega,m}$ represent the generation of turbulence kinetic energy and its specific dissipation rate due to mean velocity gradients, respectively. Y_k and Y_ω denote the dissipation of k and ω due to turbulence, respectively. D_ω is the cross-diffusion term. S_k and S_ω are the source terms. The original form of the mixture turbulent viscosity $\mu_{t,m}$, is defined as

$$\mu_{t,m} = \frac{\rho k}{\omega} \frac{1}{max\left[\frac{1}{\alpha^*}, \frac{S_1 F_2}{\alpha_1 \omega}\right]}, \tag{9}$$

where S_1 is the strain rate magnitude. Additional details pertaining to the closure coefficients, model constants, and auxiliary relations can be found from Menter [43].

In this work, modifications have been made in the turbulent viscosity term of the SST k-ω turbulence model, and also the source terms are included in both of the turbulence equations (based on the work of Avetissian et al. [34,36]). The added source terms to the k and ω equations determine the modulation of turbulence energy due to additional dissipation by liquid droplets. The turbulent viscosity formulation is modified by means of an expansion procedure for resolving implicit algebraic equations for Reynolds stress tensor in terms of mean velocity gradients [44,45]. In contrast to the original expression of turbulent viscosity (i.e., Eq. (9)), this expansion yields the modified term of turbulent viscosity as below

$$\mu_{t,m} = \frac{\rho k}{\omega} \frac{1}{max\left[\frac{1}{\alpha^*} \frac{S_1 F_2}{\alpha_1 \omega}\right]} \frac{C_1}{C_1 + \left[\frac{G_{k,m}}{\omega \beta^* k} - 1\right]}, \tag{10}$$

where β^* is the model constant and C_1 is the constant value of the Rotta return-to-isentropy approximation of the pressure-strain correlation [46], which is 1.1. The source term of the turbulence kinetic energy equation S_k, is defined as

$$S_k = \frac{4M}{\tau_p}(1 - f_u)k, \tag{11}$$

where M is the liquid mass per unit volume and τ_p is the droplet response time which is calculated as

$$\tau_p = C_2 \frac{2r^2 \rho_l}{9\mu_{t,m}}. \tag{12}$$

In Eq. (11), f_u is the coefficient of droplet response to the fluid velocity fluctuations which is estimated from Zaichik et al. [47] as

$$f_u = \frac{2\left(\frac{\tau_p}{T_L}\right) + \left(\frac{\tau_T}{T_L}\right)^2}{2\left(\frac{\tau_p}{T_L}\right) + 2\left(\frac{\tau_p}{T_L}\right)^2 + \left(\frac{\tau_T}{T_L}\right)^2}. \tag{13}$$

Here, T_L is the Lagrangian integral timescale and τ_T is the Taylor time microscale, which can be written as

$$T_L = C_3^{\frac{1}{2}} \left(\frac{1}{\omega \beta^*}\right), \tag{14}$$

Copyright © 2014 by ASME

$$\tau_T = \left(\frac{2Re_\lambda}{15^{\frac{1}{2}}a_0}\right)^{\frac{1}{2}} \left(\frac{\mu_t}{\rho\omega\beta^* k}\right)^{\frac{1}{2}}, \tag{15}$$

where Re_λ is determined as

$$Re_\lambda = \left(\frac{20k\rho}{3\omega\beta^*\mu_{t,m}}\right)^{\frac{1}{2}}. \tag{16}$$

The source term of the dissipation equation S_ω, is proportional to S_k, which can be written as

$$S_\omega = C_4\omega\beta^* S_k. \tag{17}$$

The values of constants C_2, C_3 and C_4 are 1.0, 0.09 and 1.92, respectively which are adjusted by trial and error method.

2.4 Equation of state

In modeling the non-equilibrium flows, supercooled thermodynamic properties are crucial because nucleation and droplet growth rate are quite sensitive to such properties. In the present work, the vapour properties are estimated from the real gas formulations of Young [48]. The equation of state for the vapour phase utilizes a virial form with temperature and density as the independent variables, and can be written as

$$P_v = \rho_v R T_v (1 + B\rho_v + C\rho_v^2). \tag{18}$$

Virial coefficients B and C are defined by the empirical functions of temperature. Additional details pertaining to the virial coefficients formulation, the constants values, and the applicability range of the formulations have been described by Young [48]. Moreover, along with the vapour properties, the liquid properties under the conditions close to the saturation line must be calculated accurately. The properties such as ρ_l, σ, C_{pl}, μ_l, and K_{tl} are obtained from Young [42], Reynolds [49], and Eckert and Drake [50].

3 NUMERICAL METHODOLOGY

In this study, all the numerical calculations have been performed with steady state 2D Reynolds Averaged Navier Stokes equations. The above mentioned turbulence model has been implemented into a commercial CFD code. The mixture of liquid and vapour phases conservation equations are discretized using conservative finite-volume integration over a control volume with a multi-grid method. Second order upwind scheme is employed for the spatial discretization. The simulations presented in this work are converged to normalized RMS residuals of the order of 10^{-4} or lower.

4 RESULTS AND DISCUSSIONS

The turbine cascade experimental data of White et al. [9] have been used for the validation purpose. The turbine blade profile was the fifth stage stator blade from the six-stage LP cylinder of a 660 MW steam turbine. In this study, three test cases have been chosen to investigate the effect of turbulence modelling on wet steam flow. The selected cases are varied by different exit isentropic Mach numbers and accordingly different pressure ratios P_{01}/P_2. Details of the experimental conditions of the selected test cases are listed in Table 1. Cases L1 and L3 are the low inlet superheat tests with the superheating of $\Delta T_{01} = 4.5$ K and 7.5 K, respectively, while case W1 is performed with the inlet wetness which was estimated to be approximately 1.6%. All the numerical calculations have been performed with 0.02 turbulence level at the inlet.

Firstly, the mesh-independence study is performed to investigate the influence of grid refinement on the solution. The quadrilateral structured and non-uniform grids have been generated for the computational domain as shown in Figure 1. Near the leading and trailing edges, fine mesh has been used to resolve the boundary layer. Three numerical grids are constructed, in which the number of grid elements has been increased from Grid A over Grid B to Grid C. For the resolution of the boundary layer, the mesh close to the wall is refined to achieve $y^+ < 1$ for all grids. More details about grid quality are listed in Table 2. For all the grids, the grid skewness is around 0.45 excepted near trailing edge of the blade which is acceptable value for CFD calculations. Figure 2 represents the pressure distribution of the blade surface obtained by different grids. It can be seen that there are some variations in the predicted results from Grid A to Grid B, particularly in the condensation shock and near to the trailing edge, while Grid B and Grid C calculated relatively similar trends. Based on the result above, Grid B is selected for the further investigation of turbine cascade cases.

In this work, various turbulence models have been tested in order to find the appropriate model to simulate wet-steam flow in the turbine cascade. Figure 3 and 4 show the contours of wetness and nucleation rate predicted by the selected turbulence models for the L1 case. It depicts that the Spalart-Allmaras, the RNG k-ε, the Realizable k-ε, and the SST k-ω turbulence models calculated similar profiles of wetness fraction, while the k-ω and the k-ε models yielded lower wetness fractions near the trailing edge. Moreover, the k-ω and the k-ε models estimated a larger nucleation zone compared to the other models. Figure 5 compares the calculated pressure distributions by different turbulence models with the measured data. It can be seen that all the models yielded relatively good agreements with the measurements of the pressure side, while there is some discrepancy for the suction side pressure prediction. It is noted that the k-ω and the k-ε turbulence models failed to capture the condensation shock, while other models estimated it more downstream compared to the experiments.

Table 1. Experimental conditions for the turbine cascade cases of White et al. [9].

	Upstream Stagnation Conditions			Downstream Conditions	
Test No.	Pressure P_{01} [Pa]	Temperature T_{01} [K]	Superheat ΔT_{01} [K]	Mean static pressure P_2 [Pa]	Isentropic Mach No. M_{2s}
L1	40300	354.0	4.5	16300	1.24
L3	41700	357.5	7.5	20600	1.08
W1	41900	350.0	wet ($\sim$ 1.6%)	17800	1.20

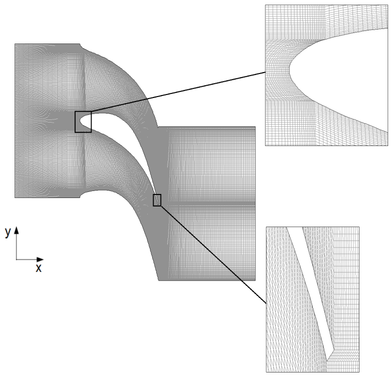

Figure 1. Computational grid (Grid B).

Based on the presented turbulence models performance, the SST k-ω turbulence model has been selected for further investigation. The SST k-ω model is modified including the turbulent viscosity (i.e., Eq. (10)) and source terms (i.e., Eq. (11) and Eq. (17)).

Figure 6 presents the turbulent viscosity contours predicted by the SST k-ω and the modified SST k-ω (MSST k-ω) turbulence models. It can be seen that the MSST k-ω model yielded a higher value of turbulent viscosity compared to the SST k-ω model in the wake region of stator blades. The increment in turbulent viscosity resulted from the model modification. The added source terms to the turbulence models are activated after second phase generation which includes additional turbulent kinetic energy and its dissipation to the flow. Also, the Reynolds stresses are dependent on the turbulent viscosity, which plays an important role in the flow governing equations. Therefore, the model modification has some influence on the flow parameters (e.g., flow velocity, and density) calculation. Consequently, the turbulence model modification has directly/indirectly an impact on the condensation phenomena. Predicted profiles of the wetness fraction and nucleation rate by the MSST k-ω model are displayed in Figure 7. It shows that both the parameters are affected due to turbulence model modification. The MSST k-ω model estimated slightly more wetness than the SST k-ω model (see Figure 3(f)). The condensation initiates on the suction surface near the point of impingement of the shock wave, and the pressure increases here due to latent heat release in this case. The figure shows that the MSST k-ω model predicted a relatively small region of nucleation near to the throat area compared to the SST k-ω model (see Figure 4(f)). Additionally, the magnitude of the liquid droplet radius is increased after the model modification as presented in Figure 8. This qualitative analysis illustrates the influence of the turbulence model modification on the condensation phenomena.

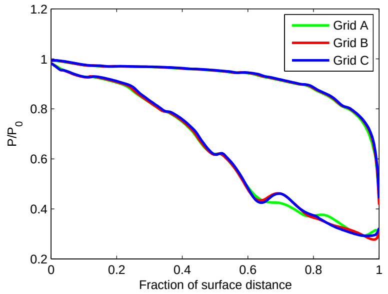

Figure 2. Blade surface pressure distribution predicted by three different grids using the SST k-ω turbulence model.

To establish more shade light on the effect of turbulence modelling on condensation phenomena, predicted results of wetness fraction, nucleation rate and droplet radius especially near the blade surfaces and in the main flow field are presented in Figure 9. Figure shows that the condensation parameters are affected by the inviscid calculation and the turbulence models. It

Copyright © 2014 by ASME

Table 2. Details of grids.

Grid	Cells	Skewness Min.-Max.	Orthogonal quality Min.-Max.	Aspect ratio Min.-Max.
A	30792	0.0005-0.8	0.24-1	1-5
B	83640	0.0001-0.75	0.23-1	1-7
C	123480	0.0-0.75	0.20-1	1-38

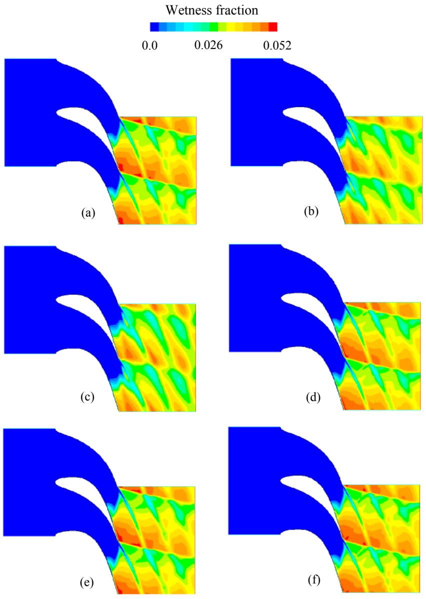

Figure 3. Wetness contours predicted by (a) the Spalart-Allmaras, (b) the k-ω, (c) the k-ε, (d) the RNG k-ε, (e) the Realizable k-ε, and (f) the SST k-ω turbulence models.

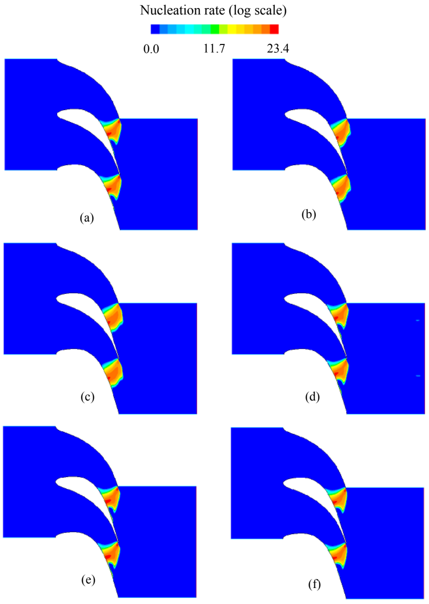

Figure 4. Nucleation rate contours predicted by (a) the Spalart-Allmaras, (b) the k-ω, (c) the k-ε, (d) the RNG k-ε, (e) the Realizable k-ε, and (f) the SST k-ω turbulence models.

can be seen that the MSST k-ω model predicted lower wetness fraction near the blade surfaces than the SST k-ω model. Also, the model modification affected on the nucleation rate and mean droplet radius prediction as well. The averaged wetness fractions predicted by the inviscid calculation, the SST k-ω model and the MSST k-ω model at downstream of the cascade at different location are presented in Figure 10. It can be seen that averaged wetness fraction is decreased as move to the downstream of cascade. Moreover, the inviscid flow predicted higher wetness fraction compared to the SST k-ω model and the MSST k-ω model.

The predicted results of the pressure distribution along the blade surface are compared with the measured data of White et al. [9] for cases L1, L3, and W1 as shown in Figure 11. The result of L1 case shows overall good agreement between predicted and measurement of the pressure side of the blade. The MSST k-ω model estimated accurate location and also peak of the condensation shock on the suction side compared to the inviscid flow and the SST k-ω model while the SST k-ω model estimated good agreement with the gradient of pressure rise on the surface side.

Copyright © 2014 by ASME

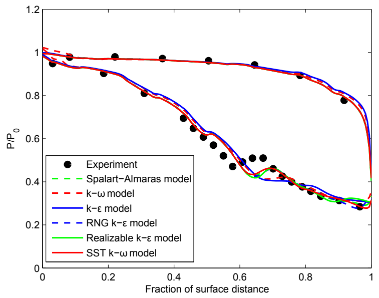

Figure 5. Blade surface pressure distribution predicted by various turbulence models and comparison with the experimental data of White et al. [9].

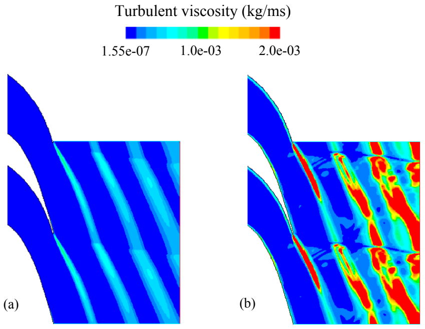

Figure 6. Turbulent viscosity contours predicted by (a) the SST k-ω and (b) the MSST k-ω turbulence models for the L1 case.

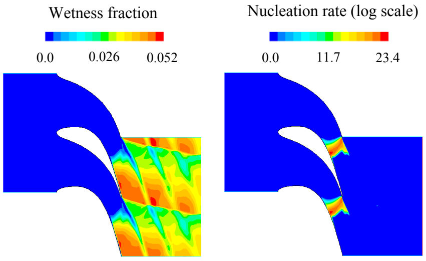

Figure 7. Wetness fraction and nucleation rate contours predicted by the MSST k-ω turbulence model for the L1 case.

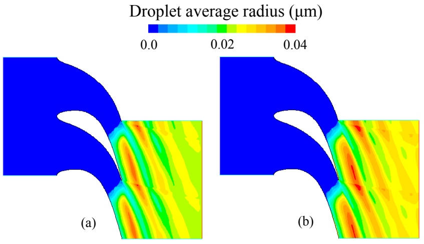

Figure 8. Droplet average radius contours predicted by (a) the SST k-ω and (b) the MSST k-ω turbulence models for the L1 case.

The MSST k-ω model calculated very good agreement with the measured data of L3 and W1 cases as well. In addition, White et al. [9] provided experimental data of the liquid droplet size at a specific location at exit. Therefore, it is possible to compare the predicted and the experimental results of liquid droplet size. However, experimental data is not available for case W1. Figure 12 represents the pitchwise distribution of the mean droplet radius at the one quarter of axial chord length away from the trailing edge. The droplet radius distribution across the passage is mostly dependent on the total number of droplets created during the nucleation process which is influenced by the distinct expansion rates along the blade passage and also due to the interaction between trailing edge shock waves and the nucleation zone. Furthermore, it is noted that the mean droplet radius predicted by the MSST k-ω model is relatively higher than the inviscid flow calculation and the SST k-ω model, particularly in main flow region of downstream the trailing edges, due to the lower expansion rate for the L1 case, while near the suction surface, nucleation occurs in the very rapid expansion region which resulted a large number of tiny droplets. Consequently, the mean droplet radius is decreased in this region compared to the downstream of mid-pitch region. Results show that the calculated mean droplet radius by the MSST k-ω model agrees very well with the measured data for cases L1 and L3. The predicted results of the static pressure, wetness fraction, and entropy by the inviscid calculation, the SST k-ω model and the MSST k-ω model for the L1 case are compared with the experimental data for pitchwise variations at the traverse plane. Figure 13(a) shows good agreement between the predicted results (the inviscid calculation and the MSST k-ω model) and the measured data of static pressure. The prediction of the wetness fraction is shown in Figure 13(b). The figure illustrates that the result of MSST k-ω model is quite accurate with

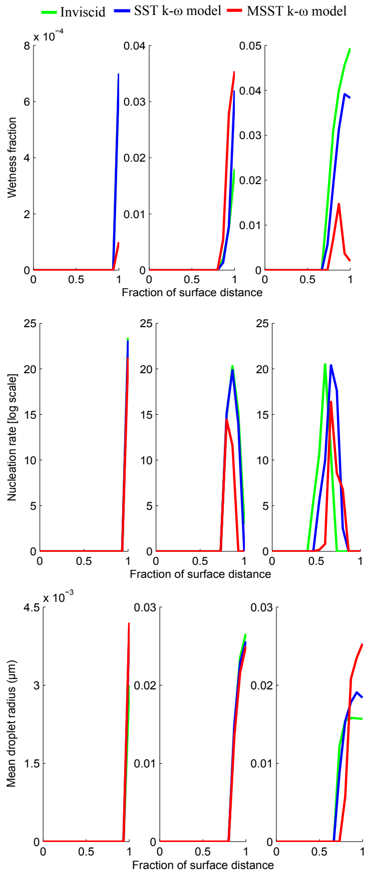

Figure 9. Predicted results of the wetness fraction, nucleation rate and mean droplet radius at near pressure side (left side), main flow field (middle), and near suction side (right side) for the L1 case.

the experimental data in the first passage; afterward some discrepancy has been observed. The wetness fraction is decreased near the middle of the passage due to the intersection of a shock wave with the traverse plane. Figure 13(c) represents the comparison between the predicted and experimental data of pitchwise variations of the entropy. The non-dimensional entropy is calculated as $\exp(-\Delta s/R)$, where Δs is the increment in a specific entropy above the cascade inlet value. It can be seen that the MSST k-ω model yielded good trend of entropy distribution with the measured data than the inviscid and the SST k-ω model.

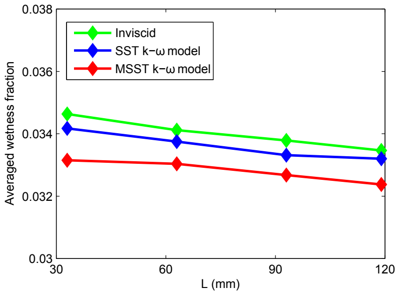

Figure 10. Predicted results of the averaged wetness fraction at downstream of the cascade for the L1 case. L is the distance from the trailing edge of the blade.

Figures 14 and 15 show the comparison between calculated Schlieren profiles and experimental Schlieren images for the L1 and L3 cases, respectively. The experimental Schlieren photographs used in this work have been taken from Senoo et a1. [51], and they are reproduced images of the original experimental photographs of White et al. [9]. The notations S_c, S_p, and S_s in the experimental photos display the condensation shock, pressure side shock, and suction side shock, respectively. In the experimental images, the red colour indicates the maximum rate of expansion, while the green colour demonstrates a very small value of compression. The grey colour scale is employed for the predicted profiles. The experimental Schlieren image of the L1 case presents that the curved S_c wave does not reflect from the suction surface. On the other hand, the aerodynamic shock interacts and merges with the condensation shock across the central blade passage. The inviscid calculation, the SST k-ω model and the MSST k-ω model yielded relatively correct locations of the shock waves. It depicts that the predicted curvature of shockwave by the inviscid calculation and the SST k-ω model is weak compared to the MSST k-ω model. However, in general CFD predicted relatively low intensity of the shock profile than the experimental photograph. The L3 case consists of a lower exit Mach number than the L1 case, and it has higher inlet superheating. Therefore, the shock profile of the L3 case has been changed. Figure 15 (b) shows that the entire condensation shock configuration is moved to the downstream. Moreover, the pressure surface shock wave is much weaker than in the L1 case. Good agreement has been captured between the predicted results

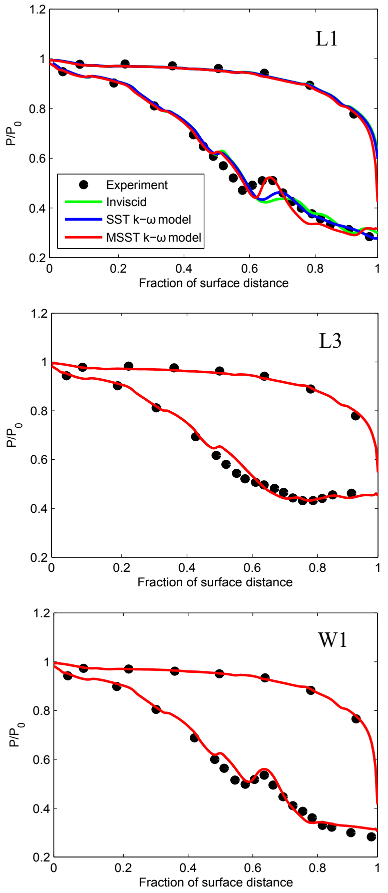

Figure 11. Predicted results of blade surface pressure distribution and compared with the experimental data of White et al. [9].

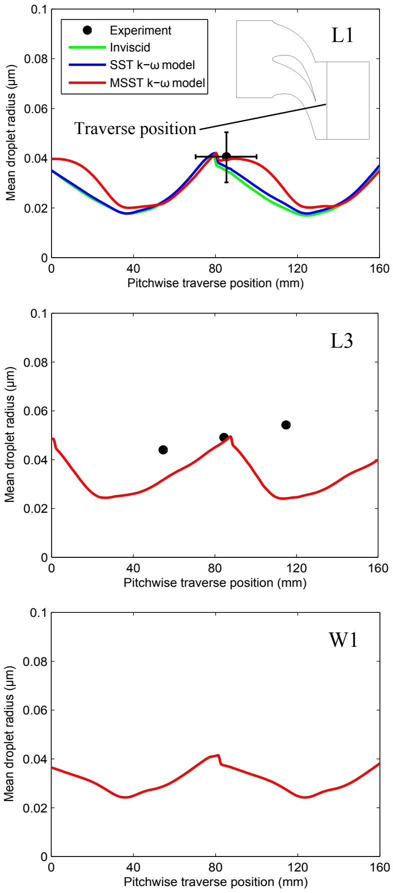

Figure 12. Predicted results of mean droplet radius and compared with the experimental data of White et al. [9].

of the MSST k-ω model and the experimental images.

Moreover, White et al. [9] yielded information about the losses which occur due to the irreversible heat and mass transfer during the condensation process. Therefore, it is possible to investigate the effect of turbulence model modification on the loss mechanism. The cascade loss coefficients are calculated in the conventional way based on the entropy increase which is known as the Markov energy loss coefficient. It can be defined as

$$\zeta = \frac{T_2 . \Delta s}{0.5 v_2^2}. \tag{19}$$

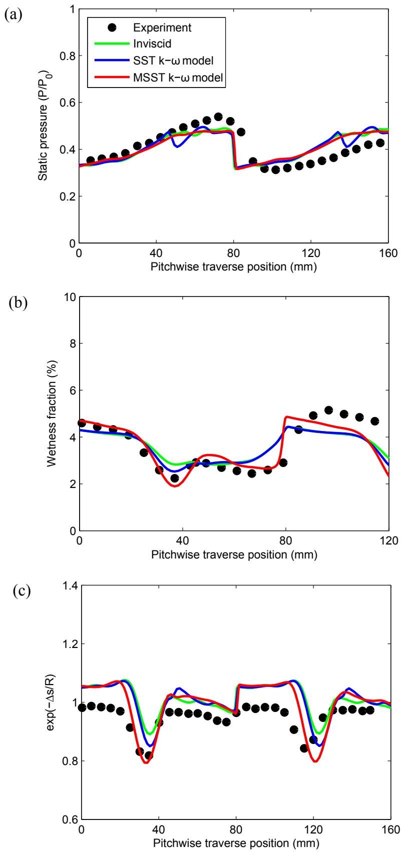

Figure 13. Predicted results of (a) static pressure, (b) wetness fraction, and (c) non-dimensional entropy and comparison with the experimental data of White et al. [9] for the L1 case.

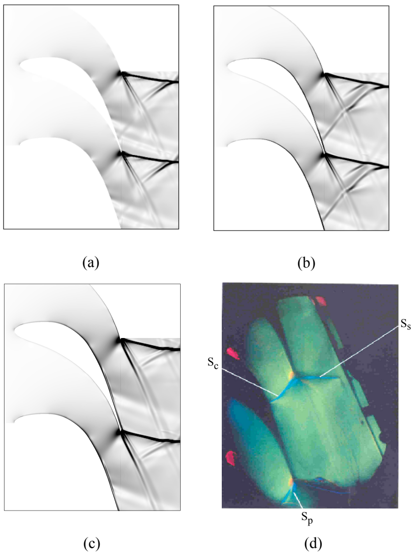

Figure 14. Schlieren graph predicted by (a) inviscid (b) the SST k-ω turbulence model (c) the MSST k-ω turbulence model compared with (d) the experiment of White et al. [9] for the L1 case.

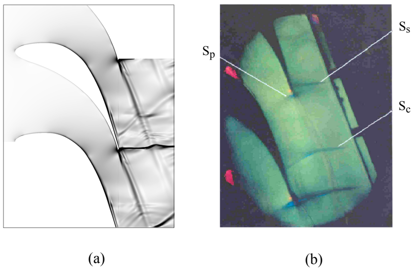

Figure 15. Schlieren graphs predicted by (a) the MSST k-ω turbulence model compared with (b) the experiment of White et al. [9] for the L3 case.

In the calculation of the Markov energy loss coefficient, it is assumed that all the quantities are 'mixed-out' values referring to a plane far downstream of the cascade. The Markov loss coefficients have been divided in three components as below [9]

1. Shockwave plus wetness loss was calculated from the mass-averaged values across a section of the traverse plane excluding the wake regions.
2. Viscous loss was calculated by subtracting the shock wave and wetness loss from the mass-averaged loss across the entire pitch at the traverse plane.

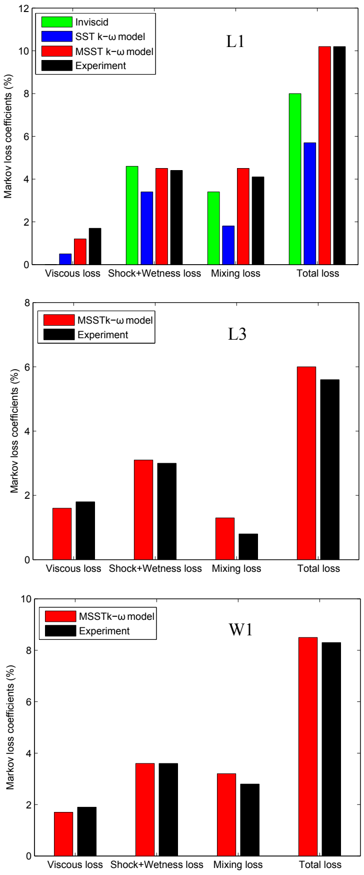

Figure 16. Predicted Marcov loss coefficients compared with the experiments of White et al. [9].

3. Mixing loss was calculated by subtracting the total mass-averaged loss at the traverse plane from the fully mixed-out loss.

The predicted values of viscous loss, shock plus wetness loss, mixing loss, and the total loss are compared with the measured data of White et al. [9]. Figure 16 shows the comparison between predicted and measured losses for the L1, L3 and W1 cases. From the L1 case, it can be seen that the SST *k*-ω model failed to predict the correct magnitude of losses. Particularly, it underestimated the viscous loss and mixing loss more than 50% compared to the measured data while the inviscid calculation predicted very good value of the wetness loss. The MSST *k*-ω model predicted the wetness loss correctly for all studied cases. However, the calculated values of viscous loss and mixing loss are slightly lower and higher than experimental data, respectively. It can be seen that the MSST *k*-ω model is able to calculate the total loss correctly.

The presented results show that the MSST *k*-ω model predicted good agreement with the experimental data for all studied cases, and it simulated the crucial trends of condensing flow in turbine cascade.

5 CONCLUSIONS

In this study, the influence of the turbulence modelling on the condensing steam flow in a stationary turbine cascade has been discussed. The two-phase vapour-liquid mixture has been modeled adopting the Eulerian-Eulerian approach using 2D compressible NS equations.

First, the grid independence study was conducted, and the results indicated that the sufficient grid density is essential to resolve the flow details. Additionally, the performance of various turbulence models has been compared in order to determine the appropriate model to predict the wet-steam flow in the turbine cascade. The analysis shows that the *k*-ε and the *k*-ω turbulence models failed to capture the condensation shock, while other turbulence models were relatively poor in predicting the location of the condensation shock compared to the experiments.

To improve the accuracy of the modeling, the turbulent viscosity and source terms of the SST *k*-ω model were modified. The qualitative analysis of calculated results indicated that the turbulence model modification has an influence on the wet-steam flow prediction. The MSST *k*-ω model was validated with three experimental cases of the turbine cascade. The results indicated that the MSST *k*-ω model is in very good agreement with the experimental data of blade surface static pressure distribution and liquid droplet size. Also the pitchwise distribution of calculated parameters (i.e., static pressure, wetness fraction, and normalized entropy) at downstream by the MSST *k*-ω model were in good correspondence with the measurements.

The cascade loss coefficients have been calculated from the numerical simulations. It can be concluded that the SST *k*-ω model underpredicted all the losses. The MSST *k*-ω model predicted the wetness loss accurately, while the viscous loss and mixing loss were near to the measured losses.

Based on this study, it can be concluded that the prediction of steam condensing flow in turbine cascade has been influenced

Copyright © 2014 by ASME

by turbulence modelling. Therefore, the proper modeling of turbulence is essential to understand the loss mechanism in it. Further work will concentrate on the investigation of the turbulence effect and loss mechanism in the nozzle and stator-rotor turbine cascade flow.

ACKNOWLEDGEMENTS

The authors would like to acknowledge the Finnish Graduate School in Computational Fluid Dynamics and Academy of Finland for the financial support.

REFERENCES

[1] Stodola, A., 1905. *Steam Turbines: with an Appendix on Gas Turbines and the Future of Heat Engines*. New York. pp. 52-85 (Chapters 16-24, translated from second German edition).

[2] Binnie, A. M., and Woods, M. W., 1938. "The pressure distribution in a convergent-divergent steam nozzle". *Proc. Inst. Mech. Eng.,* **Vol. 138**, pp. 229–266.

[3] Barschdorff, D., 1971. "Verlauf der Zustandsgrossen und gasdynamische Zusammenhaenge der spontanen Kondensation reinen Wasserdampfes in Lavalduesen". *Forsch, Ingenieurwes,* **Vol. 37**, pp. 146–157.

[4] Moore, M. J., Walters, P. T., Crane, R. I., and Davidson, B. J., 1973. "Predicting the fog drop size in wet steam turbines". In Wet Steam 4 Conference, Institute of Mechanical Engineers (UK), University of Warwick, paper C37/73.

[5] Moses, C. A., and Stein, G. D., 1978. "On the growth of steam droplets formed in a Laval nozzle using both static pressure and light scattering measurements". *J. Fluids Eng.,* **Vol. 100**, pp. 311–322.

[6] Skillings, S., Walters, P., and Moore, M., 1987. "A study of supercritical heat addition as potential loss mechanism in condensing steam turbines". In Int. Mech. Eng. Conf., Vol. C259/87, pp. 125-134.

[7] Bakhtar, F., Ebrahimi, M., and Bamkole, B., 1995. "On the performance of a cascade of turbine rotor tip section blading in nucleating steam, part 2: wake traverses". *Proc. Inst. Mech. Eng. Part C: J. Mech. Eng. Sci.,* **Vol. 209**, pp. 169–177.

[8] Bakhtar, F., Ebrahimi, M., and Webb, R., 1995. "On the performance of a cascade of turbine rotor tip section blading in nucleating steam, part 1: surface pressure distributions". *Proc. Inst. Mech. Eng. Part C: J. Mech. Eng. Sci.,* **Vol. 209**, pp. 115–124.

[9] White, A. J., Young, J. B., and Walters, P. T., 1996. "Experimental validation of condensing flow theory for a stationary cascade of steam turbine blade". *Philos. Trans. Roy. Soc. Lond.,* **Vol. A 354**, pp. 59–88.

[10] Bakhtar, F., and Zidi, K., 1990. "Nucleation phenomena in flowing high-pressure steam, part, 2: theoretical analysis". *Proc. Inst. Mech. Eng.,* **Vol. 204**, pp. 233–242.

[11] White, A. J., and Young, J. B., 1993. "Time-marching method for the prediction of two-dimensional unsteady flows of condensing steam". *AIAA J. Propulsion and Power,* **Vol. 9** (**4**), pp. 579–587.

[12] Bakhtar, F., Mahpeykar, M. R., and Abbas, K. K., 1995. "An investigation of nucleating flows of steam in a cascade of turbine blading-theoretical treatment". *ASME J. Fluids Eng.,* **Vol. 117**, pp. 138–144.

[13] Gerber, A., 2002. "Two-phase eulerian/lagrangian model for nucleating steam flow". *ASME J. Fluids Eng.,* **Vol. 124**, pp. 465–475.

[14] Gerber, A. G., and Kermani, M. J., 2004. "A pressure based Eulerian-Eulerian multi-phase model for non-equilibrium condensation in transonic steam flow". *Int. J. Heat Mass Transfer,* **Vol. 44**, pp. 2217–2231.

[15] Senoo, S., and Shikano, Y., 2002. "Non-equilibrium homogeneously condensing flow analyses as design tools for steam turbines". In ASME FEDSM'02, Montreal, July 14-18, FEDSM2002-31191.

[16] Simpson, D. A., and White, A. J., 2005. "Viscous and unsteadyflow calculations of condensing steam in nozzles". *Int. J. Heat and Fluid Flow,* **Vol. 26** (**1**), pp. 71–79.

[17] Gerber, A. G., and Mousavi, A., 2006. "Application quadrature method of moments to the polydispersed droplet spectrum in transonic steam flows with primary and secondary nucleation". *J. Appl. Math. Modeling,* **Vol. 31**, pp. 1518–1533.

[18] Senoo, S., and Shikano, Y., 2002. "Two-dimensional analysis for non-equilibrium homogeneously condensing flows through steam turbine cascade". *JSME International Journal, Series B,* **Vol. 45** (**4**), pp. 865–871.

[19] Halama, J., Benkhaldoun, F., and Fořt, J., 2011. "Flux schemes based finite volume method for internal transonic flow with condensation". *Int. J. Numer. Meth. Fluids,* **Vol. 65** (**8**), pp. 953–968.

[20] Halama, J., and Fořt, J., 2012. "Transonic flow of wet steam: some remarks on numerical simulation". In Baumann Centenary Conference, BCC-2012-08, University of Cambridge, UK, September 10-11.

[21] Wróblewski, W., Dykas, S., and Gepert, A., 2009. "Steam condensing flow in turbine channels". *Int. J. Multiphase Flow,* **Vol. 35** (**6**), pp. 498–506.

[22] Dykas, S., and Wróblewski, W., 2011. "Single- and two-fluid models for steam condensing flow modeling". *Int. J. Multiphase Flow,* **Vol. 37** (**9**), pp. 1245–1253.

[23] Dykas, S., and Wróblewski, W., 2013. "Two-fluid model for prediction of wet steam transonic flow". *Int. J. Heat Mass Transfer,* **Vol. 60**, pp. 88–94.

[24] Yamamoto, S., Sasao, Y., Sato, S., and Sano, K., 2007. "Parallel-implicit computation of three-dimensional mul-

Copyright © 2014 by ASME

tistage stator-rotor cascade flows with condensation". In Proc. 18th AIAA Computational Fluid Dynamics Conference, AIAA 2007-4460, Miami, FL, June 25-28.

[25] Yamamoto, S., Sasao, Y., Kato, H., Satsuki, H., Ooyama, H., and Ishizaka, K., 2010. "Numerical and experimental investigation of unsteady 3-D wet-steam flows through two-stage stator-rotor cascade channels". In Proc. ASME Turbo Expo, GT2010-22796, Glasgow, UK, June 14-18, pp. 1-9.

[26] Miyake, S., Yamamoto, S., Sasao, Y., Momma, K., Miyawaki, T., and Ooyama, H., 2013. "Unsteady flow effect on nonequilibrium condensation in 3-D low pressure steam turbine stages". In Proc. ASME Turbo Expo, GT2013-94832, San Antonio, Texas, USA, June 3-7, pp. 1-9.

[27] Starzmann, J., Schatz, M., Casey, M. V., Mayer, J. F., and Sieverding, F., 2011. "Modelling and validation of wet steam flow in a low pressure steam turbine". In Proc. ASME Turbo Expo, GT2011-45, Vancouver, Canada, June 6-10, pp. 1-12.

[28] Starzmann, J., Kaluza, P., Casey, M. V., and Sieverding, F., 2013. "On kinematic relaxation and deposition of water droplets in the last stages of low pressure steam turbines". In Proc. ASME Turbo Expo, GT2013-95179, San Antonio, Texas, USA, June 3-7, pp. 1-12.

[29] Skillings, S. A., and Jackson, R., 1987. "A robust time-marching solver for onedimensional nucleating steam flows". *Int. J. Heat Fluid Flow,* **Vol. 8**, pp. 139–144.

[30] Delale, C. F., Schnerr, G. H., and Zierep, J., 1993. "Asymptotic solution of transonic nozzle flows with homogeneous condensation. I. subcritical flows". *Phys. Fluids A,* **Vol. 5**, pp. 2969–2981.

[31] Avetissian, A. R., Alipchenkov, V. M., and Zaichik, L. I., 2002. "Simulation of a flow of spontaneously condensing moist steam in laval nozzles". *High Temp.,* **Vol. 40**, pp. 872–880.

[32] Bakhtar, F., White, A. J., and Mashmoushy, H., 2005. "Theoretical treatments of two-dimensional two-phase flows of steam and comparison with cascade measurements". *J. Mech. Eng. Sci.,* **Vol. 219**, pp. 1335–1355.

[33] Schnerr, G. H., 2005. "Unsteadiness in condensing flow: dynamics of internal flows with phase transition and application to turbomachinery". *J. Mech. Eng. Sci.,* **Vol. 219**, pp. 1369–1410.

[34] Avetissian, A. R., Philippov, G. A., and Zaichik, L. I., 2008. "Effects of turbulence and inlet moisture on two-phase spontaneously condensing flows in transonic nozzles". *Int. J. Heat Mass Transfer,* **Vol. 51**, pp. 4195–4203.

[35] White, A., 2000. "Numerical investigation of condensing steam flow in boundary layers". *Int. J. Heat and Fluid Flow,* **Vol. 21**, pp. 727–734.

[36] Avetissian, A. R., Philippov, G. A., and Zaichik, L. I., 2005. "The effect of turbulence on spontaneously condensing wet-steam flow". *Nucl. Eng. Des.,* **Vol. 235**, pp. 1215–1223.

[37] Patel, Y., Patel, G., and Turunen-Saaresti, T., 2013. "The effect of turbulence and real gas models on the two phase spontaneously condensing flows in nozzle". In Proc. ASME Turbo Expo, GT2013-94778, San Antonio, USA, June 3-7, pp. 1-8.

[38] Frenkel, J., 1946. *Kinetic Theory of Liquids*. Oxford University Press, New York.

[39] Ishizaka, K., Ikohagi, T., and Daiguji, D., 1995. "A high-resolution numerical method for transonic nonequilibrium condensation flows through a steam turbine cascade". In Proc. 6th International Symposium on Computational Fluid Dynamics, pp. 479-484.

[40] Young, J. B., 1992. "Two-Dimensional nonequilibrium wet steam calculations for nozzles and turbine cascades". *ASME J. Turbomachinery,* **Vol. 114**, pp. 569–579.

[41] Hill, P. G., 1966. "Condensation of water vapour during supersonic expansion in nozzles". *J. Fluid Mech.,* **Vol. 25**, pp. 593–620.

[42] Young, J. B., 1982. "The spontaneous condensation of steam in supersonic nozzles". *Physico Chemical Hydrodynamics,* **Vol. 3**, pp. 57–82.

[43] Menter, F. R., 1994. "Two-equation eddy-viscosity turbulence models for engineering applications". *AIAA Journal,* **Vol. 32 (8)**, pp. 1598–1605.

[44] Speziale, C. G., 1987. "On nonlinear k-l and k-ε models of turbulence". *J. Fluid Mech.,* **Vol. 178**, pp. 459–475.

[45] Gatski, T. B., and Speziale, C. G., 1993. "On explicit algebraic stress models for complex turbulent flows". *J. Fluid Mech.,* **Vol. 254**, pp. 59–78.

[46] Lumley, J. L., 1980. "The second-order models of turbulent flows". In Prediction Methods for Turbulent Flows, Hemisphere, New York.

[47] Zaichik, L., Simonin, O., and Alipchenkov, V., 2003. "Two statistical models for predicting collision rates of inertial particles in homogeneous isotropic turbulence". *Phys. Fluids,* **Vol. 15**, pp. 2995–3005.

[48] Young, J. B., 1988. "An equation of state for steam for turbomachinery and other flow calculations". *J. Eng. Gas Turbines Power,* **Vol. 110**, pp. 1–7.

[49] Reynolds, W. C., 1979. *Thermodynamic properties in SI: Graphs, Tables, and Computational Equations for 40 Substances*. Department of mechanical Engineering, Stanford University.

[50] Eckert, E. R. G., and Drake, R. M., 1972. *Analysis of Heat and Mass Transfer*. McGraw-Hill Co.

[51] Senoo, S., and White, A. J., 2012. "Non-equilibrium unsteady wet-steam condensation modelling: computations for a steam turbine cascade and a nozzle". In Baumann Centenary Conference, BCC-2012-07, University of Cambridge, UK, September 10-11.

Publication III

Patel, Y., Patel G., and Turunen-Saaresti, T. (2015).
Influence of turbulence modelling on non-equilibrium condensing flows in nozzle and turbine cascade.

Reprinted with permission from
International Journal of Heat and Mass Transfer.
Vol. 88, pp. 165-180.
© Elsevier, 2015

International Journal of Heat and Mass Transfer 88 (2015) 165–180

Contents lists available at ScienceDirect

International Journal of Heat and Mass Transfer

journal homepage: www.elsevier.com/locate/ijhmt

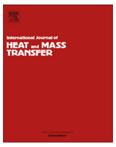

Influence of turbulence modelling on non-equilibrium condensing flows in nozzle and turbine cascade

Yogini Patel *, Giteshkumar Patel, Teemu Turunen-Saaresti

Fluid Dynamics Laboratory, LUT Energy, School of Technology, Lappeenranta University of Technology, PO Box 20, FIN-53851 Lappeenranta, Finland

ARTICLE INFO

Article history:
Received 17 December 2014
Received in revised form 23 April 2015
Accepted 23 April 2015
Available online 14 May 2015

Keywords:
CFD
Condensation
Steam
Turbulence modelling
Loss coefficient

ABSTRACT

The accurate analysis of a condensing flow plays an important role in the development of high-efficiency steam turbines. This paper presents an investigation of turbulence modelling influence on non-equilibrium condensing steam flows in a Laval nozzle and in a stationary cascade of turbine blades using a commercial computational fluid dynamics (CFD) code. The calculations were conducted by employing 2D compressible Reynolds-averaged Navier–Stokes (RANS) equations coupled with a two equation turbulence model. The condensation phenomena were modelled on the basis of the classical nucleation theory. The standard k–ε turbulence model was modified, and the modifications were implemented in the CFD code. The influence of inlet flow turbulence on condensing process was discussed. The impact of turbulence modelling on wet-steam flow was examined based on the experimental data available in the literature. The cascade loss coefficients were calculated numerically as well. The presented study of losses that occur due to the irreversible heat and mass transfer during the condensation process emphasised the importance of turbulence modelling for wet-steam flows in turbines. The paper demonstrates that the accurate computational prediction of condensing steam flow requires the turbulence to be modelled accurately.

© 2015 Elsevier Ltd. All rights reserved.

1. Introduction

Two-phase wet-steam flows consisting of tiny liquid droplets have a fundamental importance in both scientific contexts and in industrial applications, such as the combustion of liquid droplets, meteorological processes, the formations of contrails from aircraft exhausts, chemical engineering applications, and condensation of steam in turbines. Particular attention has been given to wet-steam flow research in turbines to take into account the thermodynamical and mechanical losses, blade erosion, and the influence of the condensation process on blade aerodynamics. With a large role played by steam turbines in the area of power generation, any progress in understanding the condensation and loss mechanisms might lead to improved designs of steam turbines, and, as a result, yield handsome economic dividends. Therefore, detailed analysis of condensing steam flow, either by experiments or with numerical simulations, has great importance.

The condensing steam flow in nozzles and in turbines has been widely studied experimentally, theoretically, and numerically since the work of Stodola [1] in order to enhance knowledge about the complicated physics involved. Comprehensive experimental works have been organised for condensing flow in the nozzle by numerous researchers, that is, Barschdorff [2], Moore et al. [3], Bakhtar et al. [4], Moses and Stein [5], Skillings et al. [6], Bakhtar and Zidi [7,8], Gyarmathy [9]. The experimental work for condensing steam flows in turbine cascades has been performed as well. For example, Bakhtar et al. [10,11] and White et al. [12]conducted experiments of non-equilibrium condensing steam flow in turbine cascades, in which they provided a large set of measurement data for various parameters.

Many numerical studies over the past several decades have been directed toward modelling condensing steam flow utilising various approaches, where the vapour phase is always treated by the Eulerian method and the liquid phase is solved by the Lagrangian/Eulerian method. Much of the modelling work was initially performed on convergent–divergent (CD) nozzles with simplified one-dimensional flow, considering both the inviscid and turbulence conditions. Later on, studies were dedicated to two-dimensional flows in turbine cascades, with more sophisticated numerical models utilised to handle the additional dimension. For example, in the studies of Bakhtar and Tochai [13], Young [14,15], White and Young [16], Bakhtar et al. [17], White et al. [12], the most often used numerical approach was the

---

* Corresponding author. Tel.: +358 40 765 2489.
E-mail addresses: yogini.patel@lut.fi (Y. Patel), giteshkumar.patel@lut.fi (G. Patel), teemu.turunen-saaresti@lut.fi (T. Turunen-Saaresti).

http://dx.doi.org/10.1016/j.ijheatmasstransfer.2015.04.069
0017-9310/© 2015 Elsevier Ltd. All rights reserved.

Nomenclature

Latin alphabet

C_p	specific heat at constant pressure	J kg^{-1} K^{-1}
C_v	specific heat at constant volume	J kg^{-1} K^{-1}
h	specific enthalpy	J kg^{-1}
H	total enthalpy	J kg^{-1}
I	nucleation rate	m^{-3} s^{-1}
k	turbulent kinetic energy	m^2 s^{-2}
K_t	thermal conductivity	W m^{-1} K^{-1}
M	liquid mass	kg
M_m	molecular mass	kg mol^{-1}
P	pressure	Pa
r	radius	m
$\bar{r}$	average radius	m
r_*	critical radius	m
R	gas constant	J kg^{-1} K^{-1}
Re_λ	Reynolds number	
s	entropy	J kg^{-1} K^{-1}
S_1	mass source term	kg m^{-2} s^{-1}
S_2	momentum source term	kg m^{-2} s^{-2}
S_3	energy source term	W m^{-3} K^{-1}
t	time	s
T	temperature	K
u	velocity component	m s^{-1}

Greek alphabet

β	liquid phase mass fraction	
γ	specific heat ratio	
Γ	mass generation rate	kg m^{-3} s^{-1}
Γ_E	thermal diffusion coefficient	W m^{-1} K^{-1}
ε	turbulence dissipation rate	m^2 s^{-3}
η	number of liquid droplets per unit volume	m^{-3}
μ	dynamic viscosity	Pa s
μ_t	turbulent viscosity	kg m^{-1} s^{-1}
ρ	density	kg m^{-3}
σ	liquid surface tension	N m^{-1}
τ	viscous stress tensor	Pa
τ_p	droplet response time	s
χ	turbulence intensity	

Subscripts

d	droplet
m, l, v	mixture, liquid phase, vapour phase
i, j	cartesian tensor notation
x	cartesian coordinate
$0, 1, 2$	total, inlet, outlet condition of cascade

inviscid time-marching scheme of Denton [18] for turbomachinery flows.

An Eulerian–Lagrangian approach for two-phase steam flow was adopted by Gerber [19] to conduct numerical simulations of low-pressure (LP) CD nozzle and turbine cascade. He utilised the k–ε turbulence model by assuming oneway coupling between the gas phase turbulence and dispersed droplets. Later on, Gerber and Kermani [20] presented an Eulerian–Eulerian multi-phase method for non-equilibrium condensation in nozzles. Moreover, Senoo and White [21,22] utilised a coupled numerical approach, considering the two-phase flow as a mixture, to simulate inviscid wet-steam flow in LP steam turbine stator cascade and in Laval nozzle. Wróblewski et al. [23], Dykas and Wróblewski [24,25] have developed in-house CFD codes for modelling non-equilibrium wet-steam flow. They validated their code using the single-fluid and two-fluid approaches coupled with both one-equation and two-equation turbulence models as well. Moreover, numerical work concerning wet-steam flows through multistage stator rotor cascade channels in a low-pressure steam turbine were performed by Yamamoto et al. [26–28], Starzmann et al. [29], Miyake et al. [30], who solved flow turbulence using the SST k–ω turbulence model.

Turbine flows include a variety of complex flow phenomena, including laminar-to-turbulent transition, flow separation, secondary flow mixing, rotor–stator interaction, and heat transfer. A common thread among all of these phenomena is turbulence. The turbulence plays an important role in the processes of mass, momentum, and heat transfer in boundary layers on the surface walls, especially on the possible deposition of condensed liquid droplets. Turbulence may have some direct/indirect influence on shock wave generation under the conditions of subcooled steam flow [31]. Additionally, the accurate prediction of absolute losses requires the turbulence to be modelled accurately [32,33].

However, published work on the influence of turbulence on the condensing steam flow is rather sparse. White [34] presented a numerical method based on a simple stream function technique for the prediction of condensing steam flow in a CD nozzle to analyse the influence of the viscous effect on condensation within compressible boundary layers. Moreover, Simpson and White [35] conducted a numerical study performing viscous calculations for a steady flow condition with CD nozzle using the standard k–ε turbulence model, and they concluded that the growth of the boundary layer has a significant impact on the predicted pressure distributions and droplet sizes. Additionally, Avetissian et al. [36] investigated the influence of the turbulence level and inlet wetness on the process of spontaneous condensation in Laval nozzles, utilising the moment method and the Delta-approximation method to determine the droplet size spectrum. They concluded that the effect of both high-level turbulence and inlet wetness causes the shock of spontaneous condensation to disappear. Later on, the effect of turbulence was investigated by Avetissian et al. [31]. Their study emphasised the steady and unsteady spontaneously condensing transonic turbulent flows in 2D flat nozzles and round shape nozzle dealing with and without initial moisture at the nozzle inlet. Additionally, the influence of turbulence parameters and real gas models in condensing steam flow in a CD nozzle has been studied by Patel et al. [37]. The performance of various turbulence models for the wet-steam flow has been studied by Patel et al. [38]. In the work of Patel et al. [38], the SST k–ω model was modified to predict steam condensing flow and losses in turbine cascade. It was concluded that the prediction of steam condensing flow in turbine cascade is influenced by turbulence.

The aim of this work is to investigate the influence of turbulence modelling on the process of spontaneously condensing flow in a nozzle and turbine blade cascade using the Eulerian–Eulerian approach. The significance of turbulence modelling on the loss mechanism is discussed, as well. The achieved numerical results are analysed with the available experimental data.

2. Governing equations

2.1. Conservation equations

All results presented in this paper were obtained by means of ANSYS Fluent 14.0 CFD code. The mixture of vapour and liquid phases was governed by Reynolds-averaged Navier–Stokes

(RANS) equations, which were coupled with the two-equation turbulence model. The conservation of mass, momentum, and energy equations for a compressible flow are expressed as follows,

$$\frac{\partial \rho}{\partial t} + \frac{\partial}{\partial x_i}(\rho u_i) = S_1, \tag{1}$$

$$\frac{\partial}{\partial t}(\rho u_i) + \frac{\partial}{\partial x_j}(\rho u_i u_j) = -\frac{\partial P}{\partial x_i} + \frac{\partial \tau_{ij}}{\partial x_j} + S_2, \tag{2}$$

$$\frac{\partial}{\partial t}(\rho H) + \frac{\partial}{\partial x_j}(\rho u_j H) = \frac{\partial P}{\partial t} + \frac{\partial}{\partial x_j}\left(\Gamma_E \frac{\partial T}{\partial x_j}\right) + \frac{\partial}{\partial x_j}(u_i \tau_{ij}) + S_3, \tag{3}$$

In Eq. (1), the source term S_1 represents the mass transfer due to the condensation process or evaporation on the already existing droplet. The term S_2 in Eq. (2) is the momentum source term, which includes the momentum exchange between the liquid droplets and the surrounding vapour, and the smaller terms from the gradient of the Reynolds stress tensor. In Eq. (3), the source term S_3 includes the interphase heat transfer.

The formulation of conservation equations was based on the mixture properties of the vapour and liquid phases, which can be calculated from the following mixing law

$$\phi_m = \phi_l \beta + (1 - \beta)\phi_v. \tag{4}$$

Here, ϕ represents h, s, C_p, C_v, μ, and K_t. Additionally, two transport equations for the liquid-phase mass-fraction, β, and the number of liquid droplets per unit volume, η, were calculated and can be expressed as

$$\frac{\partial \rho \beta}{\partial t} + \frac{\partial}{\partial x_i}(\rho u_i \beta) = \Gamma, \tag{5}$$

$$\frac{\partial \rho \eta}{\partial t} + \frac{\partial}{\partial x_i}(\rho u_i \eta) = \rho I, \tag{6}$$

respectively, where Γ is the mass generation rate per unit volume due to condensation and evaporation, and I is the nucleation rate. Some assumptions have been made concerning solving the vapour–liquid mixture flow. The condensed liquid phase consists of droplets whose radii are on the order of 1 µm or less. Therefore, it was assumed that the volume of the condensed liquid phase was negligible. Moreover, the interactions between droplets were omitted, and the slip velocity between the liquid droplets and the vapour surrounding them was negligible.

2.2. Nucleation and droplet growth model

The phase change phenomenon regarding the condensing steam flow involves two main processes: nucleation and droplet growth. The rate of formation of liquid droplet embryos due to the homogeneous condensation per unit mass of the mixture was obtained from the classical theory of non-isothermal homogeneous condensation given by Frenkel [39] as

$$I = \frac{q_c}{(1+\theta)} \left(\frac{\rho_v^2}{\rho_l}\right) \sqrt{\frac{2\sigma}{M_m^3 \pi}}\, e^{-\left(\frac{4\pi r_*^2 \sigma}{3K_b T}\right)}. \tag{7}$$

In Eq. (7), q_c denotes the condensation coefficient, which was assumed to be unity; K_b is Boltzmann's constant; and θ is non-isothermal correction coefficient. In the classical homogeneous nucleation theory, the mass generation rate per unit volume, Γ was estimated by the addition of mass increase owing to nucleation and due to the growth/demise of liquid droplets. The mass generation rate per unit volume Γ was obtained from Ishizaka et al. [40], and can be expressed as

$$\Gamma = \frac{4}{3}\pi \rho_l I r_*^3 + 4\pi \rho_l \eta \bar{r}^2 \frac{\partial \bar{r}}{\partial t}, \tag{8}$$

There are two mechanisms involved in the steam condensation process. The first one is related to the mass transfer from the vapour phase to the droplets, and the other is the transfer of heat from the created droplets to the vapour phase in the form of latent heat [40]. The droplets growth rate can be derived on the basis of heat transfer conditions surrounding the droplet [41]. The droplets growth can be defined as

$$\frac{\partial \bar{r}}{\partial t} = \frac{P}{h_{lv}\rho_l \sqrt{2\pi RT}} \frac{\gamma + 1}{2\gamma} C_p (T_d - T), \tag{9}$$

More details pertaining to the droplet temperature calculation have been presented by Young [42].

2.3. Equation of state

In the modelling of non-equilibrium flows, subcooled thermodynamic properties are crucial because nucleation and droplet growth rate are quite sensitive to such properties. In the present work, the vapour properties were estimated by the formulations of Young [43]. The equation of state for the vapour phase utilised a virial form with temperature and density as the independent variables, which can be written as

$$P = \rho_v RT(1 + B\rho_v + C\rho_v^2), \tag{10}$$

where B, and C are the second and the third virial coefficients. Along with the vapour properties, it is essential to calculate the liquid properties under the conditions close to the saturation line accurately. The properties, such as, $\rho_l, \sigma, C_{pl}, \mu_l$, and K_{tl}, were obtained from Young [42], Reynolds [44], Eckert and Drake [45].

2.4. Turbulence modelling

In an LP turbine, more than 90% of the total mass concentration of the liquid phase consists of a very large number of very fine droplets having sub-micron size [46]. Therefore, it could be assumed that there is no direct influence of the droplets on the flow turbulence, and in this study, direct influence was not investigated. However, there is an indirect influence through the velocity field introduced to the turbulence models. The turbulence in the vapour phase does have an influence on the dispersion of the liquid droplets. In the work of Patel et al. [38], various turbulence models, performance was discussed to predict the wet-steam flow in the turbine cascade. In the present work, the standard k–ε (Sk–ε) turbulence model was employed for modelling the flow turbulence. Due to the relatively small mass concentrations and sizes of droplets, the turbulence equations were solved for the mixture of the vapour and liquid phases. The equations of k and ε can be written as

$$\frac{\partial}{\partial t}(\rho k) + \frac{\partial}{\partial x_i}(\rho u_i k) = \frac{\partial}{\partial x_j}\left(\left(\mu + \frac{\mu_t}{\sigma_k}\right)\frac{\partial k}{\partial x_j}\right) + G_k + G_b - \rho\varepsilon - Y_M + S_k, \tag{11}$$

$$\frac{\partial}{\partial t}(\rho \varepsilon) + \frac{\partial}{\partial x_i}(\rho u_i \varepsilon) = \frac{\partial}{\partial x_j}\left(\left(\mu + \frac{\mu_t}{\sigma_\varepsilon}\right)\frac{\partial \varepsilon}{\partial x_j}\right) + \frac{\varepsilon}{k}(C_{1\varepsilon}G_k - C_{2\varepsilon}\rho\varepsilon + C_{1\varepsilon}C_{3\varepsilon}G_b) + S_\varepsilon, \tag{12}$$

respectively, where S_k and S_ε are the source terms, G_k and G_b represent the production of turbulence kinetic energy due to the mean velocity gradients and buoyancy, respectively, and Y_M is the contribution of the fluctuating dilatation in compressible turbulence to the overall dissipation rate. The original form of μ_t, is given by

$$\mu_t = \rho C_\mu \frac{k^2}{\varepsilon}. \tag{13}$$

The applicability of the Sk–ε turbulence model has been proven in various flow phenomena. However, there are still some limitations to its relevance: for example, flows with large velocity gradients, strong contraction or expansion, surface curvature, rotational effects such as swirl or separated flows, and transition. Therefore, the proper modelling of non-equilibrium homogeneous condensing steam flows in nozzles and turbine blade channels requires some modification to the Sk–ε model. In the present work, the Sk–ε turbulence model has been modified (based on Avetissian et al. [36,31]) by adding the modulation of turbulence kinetic energy due to liquid droplets via source terms. The effect of liquid droplets in the flow introduces an extra turbulent kinetic energy and its dissipation to the flow via the acceleration/deceleration of the droplets. Additionally, the turbulent viscosity was modified by means of an expansion procedure for resolving implicit algebraic equations for the Reynolds stress tensor in terms of mean velocity gradients [47,48]. The modified term of turbulent viscosity, including the turbulence production to dissipation ratio, is expressed as

$$\mu_t = \frac{\rho C_\mu}{1 + (G_k/\varepsilon - 1)/C_1} \frac{k^2}{\varepsilon}, \tag{14}$$

where C_1 is the Rotta return-to-isentropy approximation of the pressure-strain correlation [49]. The source term of the turbulence kinetic energy equation represents the addition of turbulent kinetic energy which includes the effect of mass generation rate and droplet response time. The source term, S_k, in Eq. (11) is defined as

$$S_k = \frac{4M}{\tau_p}(1 - f_u)k, \tag{15}$$

The response time of droplet to changes in the flow velocity or flow temperature are important in establishing non-dimensional parameters to characterise the flow, which relates to the time required for a liquid droplet to respond to a change in velocity. The droplet response time, τ_p was calculated as

$$\tau_p = \frac{2\bar{r}^2 \rho_l}{9\mu}. \tag{16}$$

In Eq. (15), f_u is the coefficient of droplet response to the fluid velocity fluctuations, which can be written as [50]

$$f_u = \frac{2\left(\frac{\tau_p}{T_L}\right) + \left(\frac{\tau_T}{T_L}\right)^2}{2\left(\frac{\tau_p}{T_L}\right) + 2\left(\frac{\tau_p}{T_L}\right)^2 + \left(\frac{\tau_T}{T_L}\right)^2}, \tag{17}$$

where T_L and τ_T are the Lagrangian integral timescale and the Taylor time microscale, respectively, which are defined as

$$T_L = C_\mu^{\frac{1}{2}} \frac{k}{\varepsilon}, \tag{18}$$

$$\tau_T = \left(\frac{2Re_\lambda}{15^{\frac{1}{2}} a_0}\right)^{\frac{1}{2}} \left(\frac{\mu}{\rho\varepsilon}\right)^{\frac{1}{2}}, \tag{19}$$

where Re_λ is determined as

$$Re_\lambda = \left(\frac{20k^2\rho}{3\varepsilon\mu}\right)^{\frac{1}{2}}. \tag{20}$$

The source term of the dissipation equation represents the modulation of turbulent dissipation via liquid droplets. The source term, S_ε, in Eq. (12) is presented as

$$S_\varepsilon = C_{2\varepsilon} \frac{\varepsilon}{k} S_k. \tag{21}$$

The model constants were considered as: $\sigma_k = 1.0$, $\sigma_\varepsilon = 1.3$, $C_{1\varepsilon} = 1.44$, $C_{2\varepsilon} = 1.92$, and $C_\mu = 0.09$ [51]. The abovementioned equations (from Eqs. (14)–(21)) have been implemented by the authors within the commercial CFD code using user defined subroutines. Furthermore, the enhanced wall treatment was utilised to improve the near-wall flow details. The enhanced wall treatment blends the linear and logarithmic laws of the wall and provides the smooth transition between the log-law and viscous sub-layer. To resolve the viscous sublayer near the wall boundaries, the y^+ value should be sufficiently smaller. Therefore, the grid density close to the wall surfaces was refined to achieve the y^+ value close to unity value for all cases.

3. Numerical details

All of the presented numerical results of nozzle and turbine stator cascade were performed with steady state RANS equations. The conservation equations of the mixture of the vapour and liquid phases were discretized applying conservative finite-volume integration over a control volume with multi-grid method. The solution methodology of flow solving algorithm was based on explicit density based couple solver. The Roe scheme of Roe [52] was used to calculating the convective fluxes. An upwind scheme was employed for the spatial discretization. The structured meshes were utilised to generate the computational grid. The results presented in this work were converged to normalised RMS residuals of the order of 10^{-4} or lower.

3.1. Grid independence study

In order to check the influence of computational grid density on the CFD results, a grid independence study was performed in nozzle and turbine cascade. Furthermore, the influence of grid refinements was conducted using the grid convergence index (GCI) method. The GCI method proposed by Celik et al. [53] was used in this work. This method is based on the Richardson extrapolation technique, in which multiple solutions to the numerical calculation are found by adjusting a parameter (grid size) and are used to extrapolate a more accurate solution [54,55]. The grid convergence was evaluated using a relative error measure of different parameters between the grids as,

$$e_a^{ij} = \left|\frac{\phi_i - \phi_j}{\phi_j}\right|, \tag{22}$$

where ϕ_i and ϕ_j are the selected parameter of ith and jth grids, respectively. An extrapolated relative error was calculated as,

$$e_{ext}^{ij} = \left|\frac{\phi_{ext}^{ij} - \phi_i}{\phi_{ext}^{ij}}\right|, \tag{23}$$

where ϕ_{ext}^{ij} is the extrapolated value, which can be calculated as,

$$\phi_{ext}^{ij} = \frac{r_{ij}^p \phi_j - \phi_i}{r_{ij}^p - 1}. \tag{24}$$

Here, r represents the grid refinement factor and p is the order of the discretization method. Further details pertaining to the GCI method can be found from Celik et al. [53]. The GCI provides a uniform measure of convergence for grid refinement studies [56]. The GCI value can be achieved as,

$$\mathrm{GCI}^{ij} = F_s \frac{e_a^{ij}}{r^p - 1}, \tag{25}$$

where F_s is the safety factor, which is 1.25. The influence of the grid density was discussed in Section 4.2.

4. Results and discussions

4.1. Results of the Barschdorff nozzle

Firstly, the influence of turbulence modelling on condensation phenomenon was examined with the Barschdorff [2] nozzle. The presented CFD results of the nozzle were carried out considering a sufficiently refined grid to obtain a grid independent solution. The grid generation in the region of condensation was fine enough to resolve the droplet formation and the droplet growth accurately. The boundary conditions corresponding to the experiments of Barschdorff [2] have been applied at the inlet: $P_0 = 78{,}390$ Pa, $T_0 = 380.55$ K. The nozzle outlet was fixed with the supersonic condition. First, the effect of the freestream turbulence intensity on the condensing steam flow was investigated. The turbulence intensity of the flow is one of the most important parameters that influence directly the flow field and flow transition, as well. Therefore, it could also be possible that the flow turbulence intensity has some impact on the condensation process. The calculations were performed with various freestream inlet turbulence intensities (i.e., $\chi = 0.02$, 0.05, 0.1, and 0.2) with the Sk–ε turbulence model. In the case of condensing steam flow, the flow is initially dry, but after reaching the Wilson point, liquid droplets are formed and a two-phase flow is generated. The liquid droplet is growing rapidly by exchanging latent heat with the surrounding subcooled vapour. Therefore, the heat addition increases the flow temperature and pressure. The flow pressure rise is called the 'condensation disturbance' [57]. Fig. 1 shows the predicted results with various freestream inlet turbulence intensities along the nozzle centreline.

It is obvious that the flow intensity is proportional to the flow turbulent kinetic energy and its dissipation rate. The higher value of turbulence intensity increases the viscous dissipation in the flow, which influences the flow expansion. It is apparent that the flow expansion has been increased in the case of lower freestream inlet turbulence intensity as presented in Fig. 1(a). Moreover, the flow turbulence intensity influenced the subcooling level, the nucleation rate, and the wetness fraction as well (Figs. 1(b)–(d)). The nucleation region was slightly expanded in the downstream, while the wetness fraction was decreased with the higher freestream inlet turbulence intensity. Furthermore, the droplet

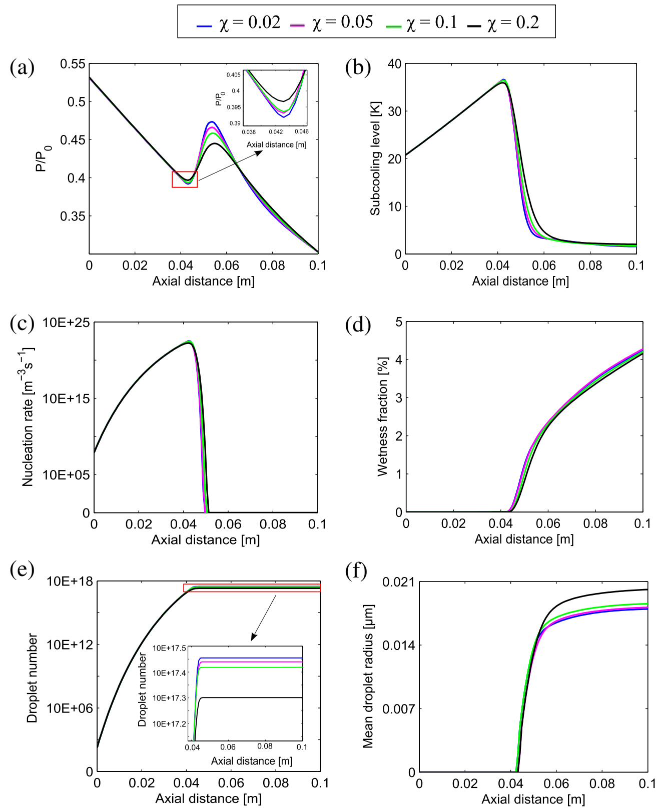

Fig. 1. Predicted results of (a) pressure, (b) subcooling level, (c) nucleation rate, (D) wetness fraction, (E) droplet number, and (F) mean droplet radius along the nozzle centreline. 0 axial distance indicates the nozzle throat.

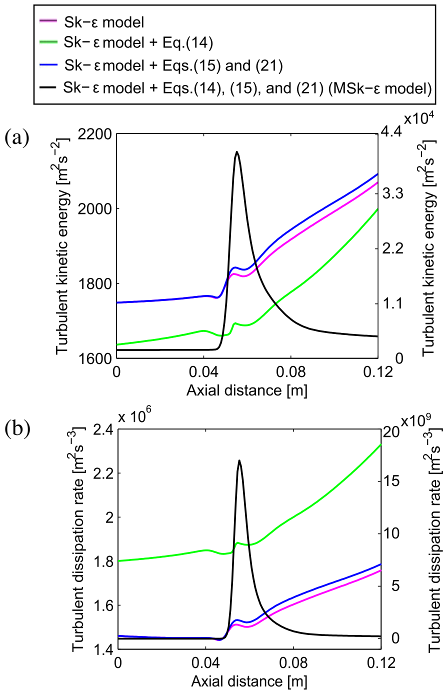

Fig. 2. Distribution of (a) the turbulent kinetic energy, and (b) the turbulent dissipation rate at nozzle centreline predicted by the Sk–ε model and other subsequent modifications with it. The right side scales of y-axis present the MSk–ε model.

number was increased, and the mean droplet radius was decreased with the lower turbulence intensity (Fig. 1(e) and (f)). Additionally, it is important to notice that the magnitude of the condensation disturbance was also influenced by the freestream turbulence intensity as presented in Fig. 1(a). As discussed above, the flow temperature and pressure increases due to the latent heat releases from the rapidly growing droplets. If the droplet number will be higher, it releases higher latent heat, which increases the peak of condensation disturbance. Therefore, the predicted peak of condensation disturbance was highest in the case of lower inlet freestream turbulence intensity.

Furthermore, the influence of turbulence modelling was analysed by a modified the Sk–ε model. Fig. 2(a) and (b) present the predicted distribution of the turbulent kinetic energy and the turbulent dissipation rate with various modification to the Sk–ε model, respectively. Fig. 2(a) shows that the steep rise for the turbulent kinetic energy was started around 0.046 m axial distance for all the models, which indicates the peak location of the nucleation rate. Moreover, the gradual increment in the turbulent kinetic energy appeared from 0.057 m axial distance for pink, green, and blue lines. This location demonstrates the condensation peak. Subsequent addition of the source terms (i.e., Eqs. (15) and (21)) to the Sk–ε model increased the turbulent kinetic and its dissipation rate. Particularly, this increment resulted after the second phase generation. However, the reduction in the turbulent kinetic energy for the Sk–ε model including the modified viscosity term (i.e. Eq. (14)) can be explained by the considerably higher dissipation rate as shown in Fig. 2(b). Moreover, it would be interesting to examine the influence of the model modification by including both: the modified viscosity term (i.e., Eq. (14)) and the source terms (i.e., Eqs. (15) and (21)) to the Sk–ε (MSk–ε) turbulence model. The black solid line indicates the predicted trends of the turbulent kinetic energy and its dissipation rate with the MSk–ε turbulence model in Fig. 2(a) and (b), respectively. It can be seen that the MSk–ε model predicted a notably higher value of the turbulent kinetic energy and its dissipation rate compared to the Sk–ε model, particularly after the throat at the downstream of the nozzle. The right side y-axis scales in Fig. 2(a) and (b) are indicated for the MSk–ε model. The trends of turbulent kinetic energy and its dissipation rate profiles predicted by the MSk–ε model and the Sk–ε model including modified viscosity term are similar before second phase generation due to modified viscosity effect. The variation observed before the droplet formation (approx. 0.046 m) in Fig. 2 is resulted only due to scale differences in y-axis. The addition of source terms to the turbulence models increased liquid mass generation rate. Therefore, the Sk–ε model including source terms and the MSk–ε model yielded higher liquid mass generation rate than the models without the source terms. However, the combined effect of source terms addition and the viscosity modification (i.e., MSk–ε model) increased turbulent kinetic energy and

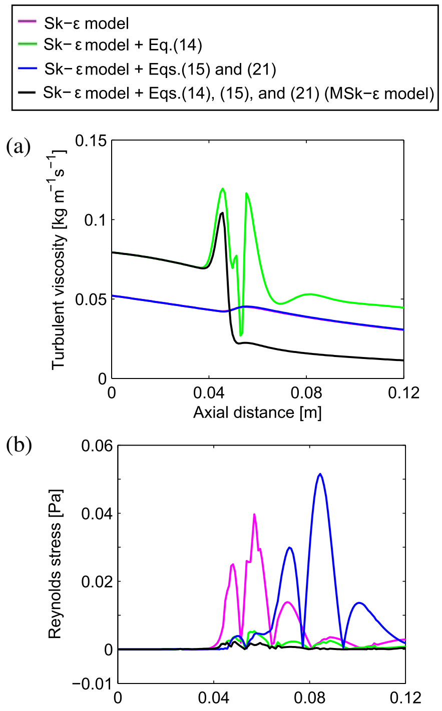

Fig. 3. Distribution of (a) the turbulent viscosity, and (b) the Reynolds stress along the nozzle centreline predicted by the Sk–ε model and other subsequent modifications with it.

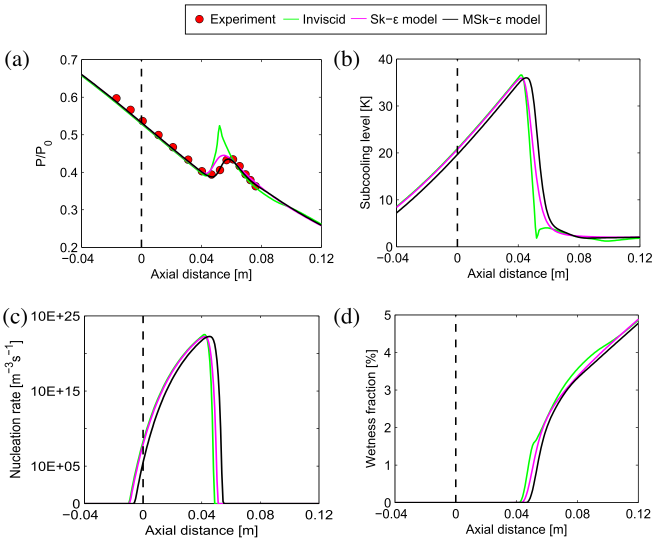

Fig. 4. Predicted profiles of (a) the pressure ratio, (b) subcooling level, (c) nucleation rate, and (d) wetness fraction along the nozzle centreline. The black vertical dashed line at $x = 0$ axial distance indicates the nozzle throat.

Table 1
Experimental conditions for the turbine cascade cases of White et al. [12].

Test No.	Upstream stagnation conditions			Downstream conditions	
	P_{01} [kPa]	T_{01} [K]	ΔT_{01} [kPa]	P_2 [kPa]	M_{2s}
L1	40.3	354.0	4.5	16.3	1.24
L2	40.9	354.0	4.0	19.4	1.11
L3	41.7	357.5	7.5	20.6	1.08
W1	41.9	350.0	wet (∼1.6%)	17.8	1.20
H3	41.4	376.0	26.0	19.4	1.10

its dissipation rate notably. The significant increment is noted from axial distance of 0.046–0.066 m in both the turbulent properties. In this region, the droplet growth rate is higher and due to that the liquid mass generation rate is increased. Consequently, both the turbulent properties are significantly higher in the case of MSk–ε model. The mass generation rate remains stable/constant due to lower droplet growth rate after the axial distance of 0.08 m. Therefore, the profiles of turbulent kinetic energy and its dissipation rate in the case of MSk–ε model are almost constant towards the downstream of nozzle.

The predicted profiles of turbulent viscosity and the Reynolds stress along the nozzle centreline with various modification to the turbulence model are presented in Fig. 3.

It can be seen that the turbulent viscosity is relatively higher for the Sk–ε model including the modified viscosity term and the MSk–ε model. This is likely due to the modified viscosity terms which contain the production to dissipation ratio. However, the Sk–ε model and the Sk–ε model with source terms were estimated to have an almost identical distribution of the turbulent viscosity. The jump was located around 0.046 m axial distance for the Sk–ε model with modified viscosity term, and the MSk–ε model indicates the location of the highest rate of the nucleation. Additionally, the increment in the turbulent viscosity demonstrates the region where the droplet growth is mainly occurring. It is clear that the droplet growth is increasing the turbulent viscosity (causing turbulence) and then bigger droplets (which are not much growing) are decreasing the turbulent viscosity (stabilizing the flow). After the nozzle throat in the downstream, the MSk–ε model yielded a comparatively lower value of the turbulent viscosity than the other models, due to higher viscous dissipation. Fig. 3(b) shows that the Sk–ε model and the Sk–ε model with source terms yielded a notably higher value of the Reynolds stress along the nozzle centreline. The Reynolds stress is calculated based on the Boussinesq approximation, in which the Reynolds stress is proportional to the turbulent viscosity and the velocity gradients. The oscillations in Reynolds stress in the cases of Sk–ε model and Sk–ε model with the source terms resulted due to relatively stronger velocity gradients compared to the MSk–ε model and the Sk–ε model with modified viscosity after the second phase generation. Furthermore, the jumps in the Reynolds stress profiles noted at 0.046 m and 0.057 m axial distances for the Sk–ε model indicate the nucleation and the condensation peak regions, respectively. However, these jumps were shifted more downstream for the Sk–ε model including source terms. In contrast, the Sk–ε model with modified viscosity term and the MSk–ε model estimated comparatively the lower value of the Reynolds stress. Furthermore, the predicted pressure distribution of the inviscid calculation, and the Sk–ε and the MSk–ε turbulence models along the nozzle centreline are compared with the experiments of [2] in Fig. 4(a). Both turbulence models yielded good agreement of pressure distribution with the experiments. However, the Sk–ε model failed to capture the right location of condensation disturbance. In the case of MSk–ε model, the increased viscous dissipation influenced on the temperature distribution via energy source, which affected the heat transfer rates. Therefore, the condensation process is extended to the downstream for the MSk–ε model. The MSk–ε model yielded an accurate profile of the pressure rise. The intensity of the condensation disturbance for the

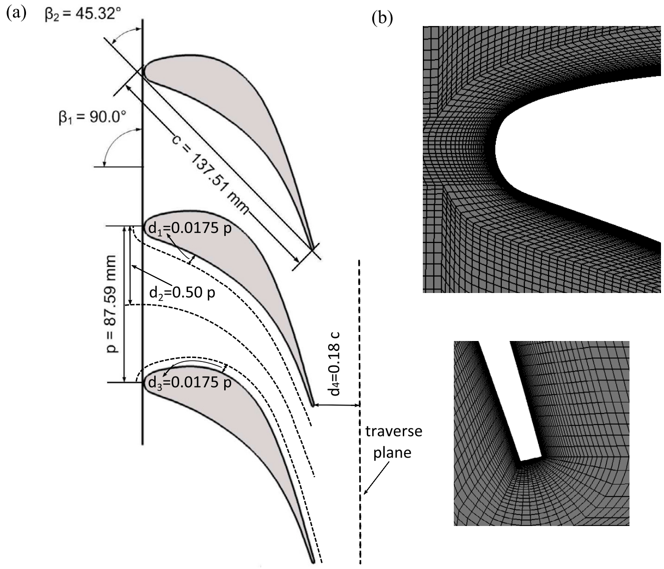

Fig. 5. (a) LP turbine stator blade geometry used for the experiments of White et al. [12], where the dotted black lines indicate the locations in which the CFD data are obtained, and (b) the computational mesh around the leading and trailing edge of the stator blade (Grid B).

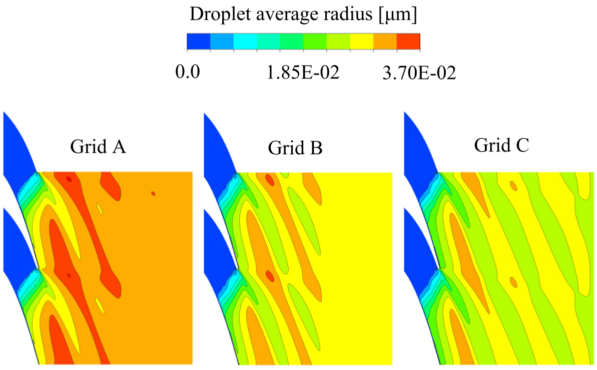

Fig. 6. Contours of the droplet average radius predicted by the Sk–ε turbulence model with various grid densities.

Table 2
Details about the grid discretization error.

Case	Parameter	e_a (%)	e_{ext} (%)	GCI (%)
Case A	Static pressure	0.14	0.25	0.32
	Velocity	0.09	0.05	0.06
	Wetness fraction	0.18	1.12	1.38
Case B	Static pressure	0.05	0.09	0.11
	Velocity	0.01	0.01	0.01
	Wetness fraction	0.17	1.03	1.30

inviscid case was almost double than other cases, in which the increment in the pressure rise was resulted due to the higher rate of latent heat released via droplets. Fig. 4(b) and (c) show that the model modification influenced on the sub-cooling level and the nucleation rate as well. The expansion process is extended to the downstream due to the turbulent viscosity modification and the source terms addition (Fig. 4(a)). Therefore, the nucleation region for the MSk–ε model has been shifted little bit towards the downstream of the nozzle. It can also be seen that the MSk–ε model predicted marginally lower wetness fraction than the inviscid calculation and the Sk–ε model.

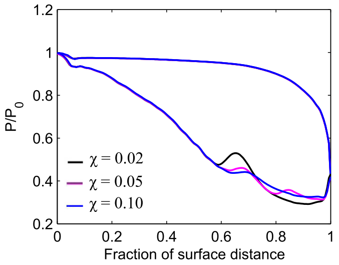

Fig. 7. Blade surface pressure distribution predicted by the MSk–ε turbulence model with various freestream turbulence intensities.

4.2. Results of stationary turbine stator cascade

The influence of turbulence modelling was investigated with the steam turbine cascade of White et al. [12]. White et al. [12] performed experiments with the turbine blade profile, which is the planar stator cascade of the fifth stage stator blade from the six-stage LP cylinder of a 660 MW steam turbine. The test cases of White et al. [12] were more associated with the flow in the steam turbine where there is an interaction between the aerodynamic effects and the condensation process itself.

In the present work, five experimental cases named with L1, L2, L3, W1, and H3 of the test series of White et al. [12] were modelled. The selected tests were varied by different exit isentropic Mach numbers and accordingly different total pressure ratios P_{01}/P_2. Cases L1, L2, and L3 were the low inlet superheat tests and Case H3 was the high inlet superheat test, while Case W1 was per-

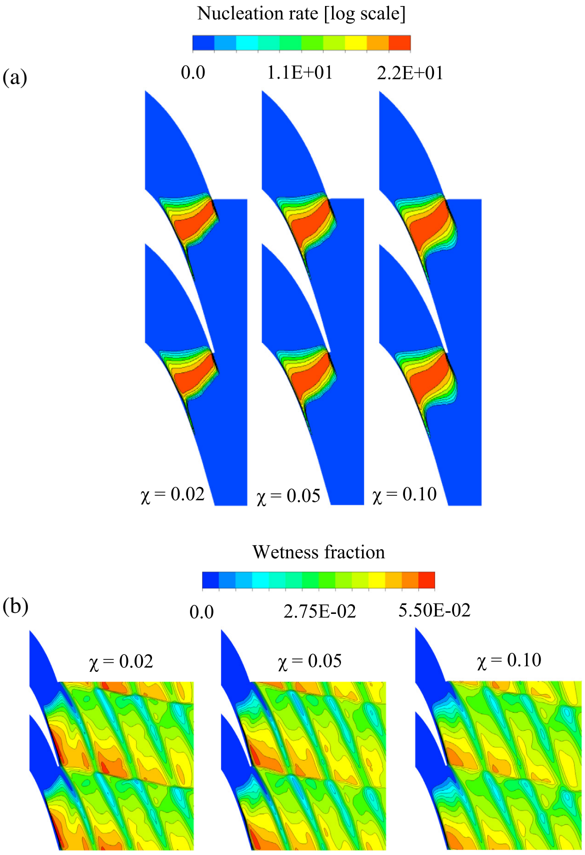

Fig. 8. Contours of (a) the nucleation rate, and (b) the wetness fraction predicted by the MSk–ε turbulence model with various freestream turbulence intensities.

formed with the inlet wetness. Details of the experimental conditions of the selected cases are listed in Table 1.

There were four stator vanes in the experiments of White et al. [12]. In this work, only two passages of the experimental facility were modelled employing a periodic boundary condition in the *y*-direction. The outlet of the computational domain was considered downstream of the traverse plane. A schematic view of the LP turbine stator blade geometry of the White et al. [12] experiments is shown in Fig. 5(a). The structured and non-uniform grid was generated for the computational domain. The O-grid around the blade surfaces was generated. A sufficiently fine grid was constructed around the leading and trailing edges of the stator to resolve the boundary layers as presented in Fig. 5(b).

For the grid independence study, three different grid sizes were used, where the number of the grid elements was increased from Grid A (40,970 cells) over Grid B (76,554 cells) to Grid C (103,582 cells). Fig. 6 presents the predicted average droplet radius with the selected grids, showing that the estimation of the droplet size is sensitive to the grid refinement from coarser to finer. Grid A predicted comparatively bigger droplet sizes than Grid B and C.

The GCI method was used to estimate the discretization error measurement. Table 2 summarises the discretization error measurement for an averaged value of the static pressure, velocity, and wetness fraction at the pitchwise traverse position which was at 50 mm downstream of the trailing edge. In Table 2, Cases A and B represent the grid refinements from Grid A to B and Grid B to C, respectively. The calculated relative error was very small for all parameters. It can be seen that the wetness fraction was more sensitive to the grid refinement than the others. Moreover, the successive grid refinements resulted in a reduction for an extrapolated relative error as well. Table 2 shows that the GCI value for the successive grid refinements (i.e., Case A to Case B) has been reduced for all three variables. The GCI values indicate that the grid refinement from Grid B to C yielded a minimal numerical error. Therefore, an intermediate grid (i.e., Grid B) was chosen for the rest of the study.

The influence of the freestream turbulence intensity on turbine cascade flow was studied with three different values of $\chi = 0.02$, 0.05, and 0.1. Fig. 7 shows the effect of the freestream turbulence intensity on the pressure distribution along the blade surfaces. It is noted that the increment in the turbulence intensity reduces the flow expansion. The reduction in the flow expansion leads to a decrease in the heat release from the droplets. Therefore, the higher freestream turbulence intensity weakens the condensation disturbance strength, and its location is extended to the downstream. The predicted contours of the nucleation rate and wetness fraction with various freestream turbulence intensities are presented in Fig. 8. It was observed that when the freestream turbulence intensity increases from $\chi = 0.02$ to 0.1, the nucleation rate occurred in a larger area. As the flow expansion rate increases, the superheated steam crosses the saturation line and becomes saturated steam. It can be seen that the lower freestream turbulence intensity predicted a relatively higher wetness fraction due to the higher expansion rate on the suction side of the blades (Fig. 8(b)).

In fluid flow problems, near wall surfaces, fluid viscosity plays a dominant role in momentum and heat transfer. Moreover, the rapid variation of flow variables occurs within the boundary layer region. The turbulent flow consists of a spectrum of different scales (eddy sizes) in which the largest eddies are of the order of the flow geometry. These structures are deformed and stretched by the fluid dynamics until they break into smaller eddies, and the process is repeated so that energy is transported to smaller and smaller structures. Finally, at small scales the kinetic energy is dissipated by the viscosity of the fluid. The whole process of transport of energy from the large scale of injection to the small dissipative scale, through the hierarchy of eddies is known as the turbulent cascade. It would be worthwhile to identify the influence of turbulence modelling near wall surfaces and in the main flow stream (at the middle of the passage). Therefore, the various flow properties were calculated near the blade surfaces and at the mid-passage. The information about these locations were displayed in Fig. 5(a). Fig. 9 shows the predicted results of turbulent kinetic energy,

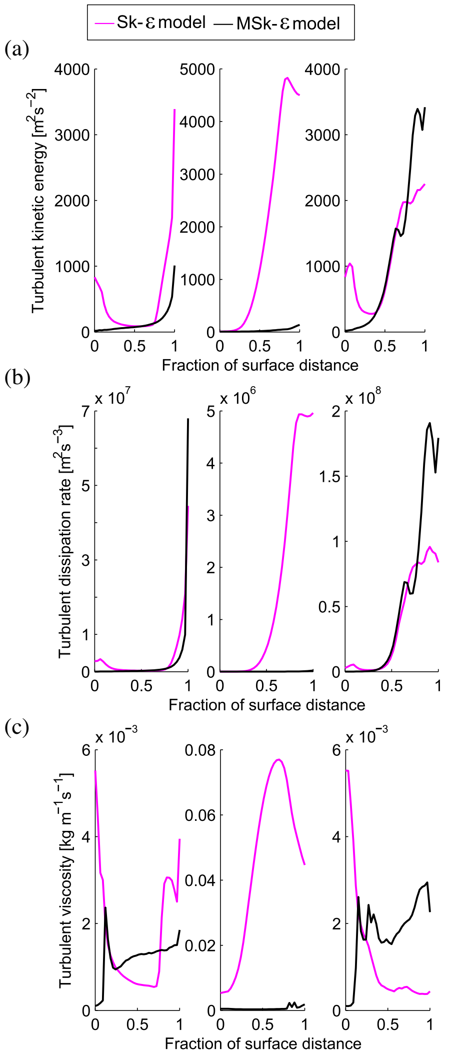

Fig. 9. Predicted results of (a) turbulent kinetic energy, (b) turbulent dissipation rate, and (c) turbulent viscosity at near pressure side (left side), mid-passage (middle), and near suction side (right side) for Case L1. Here 0 and 1 at the *x*-axis indicate the locations near the leading and trailing edges of the blade, respectively.

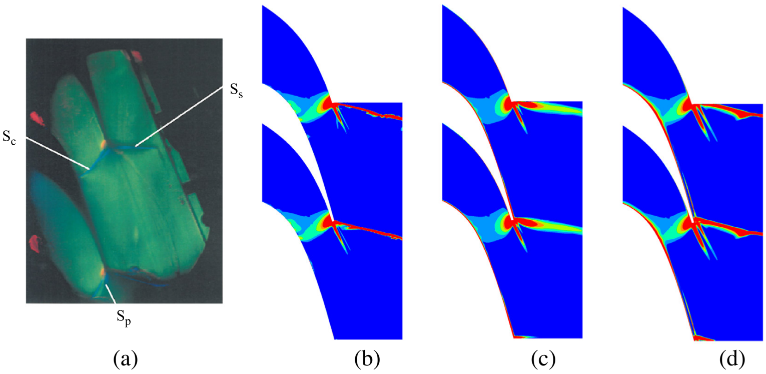

Fig. 10. (a) Reproduced image of the original experimental Schlieren graph of Case L1 of [12] compared with predicted density gradients of, (b) the inviscid, (c) the Sk–ε model, and (d) the MSk–ε model.

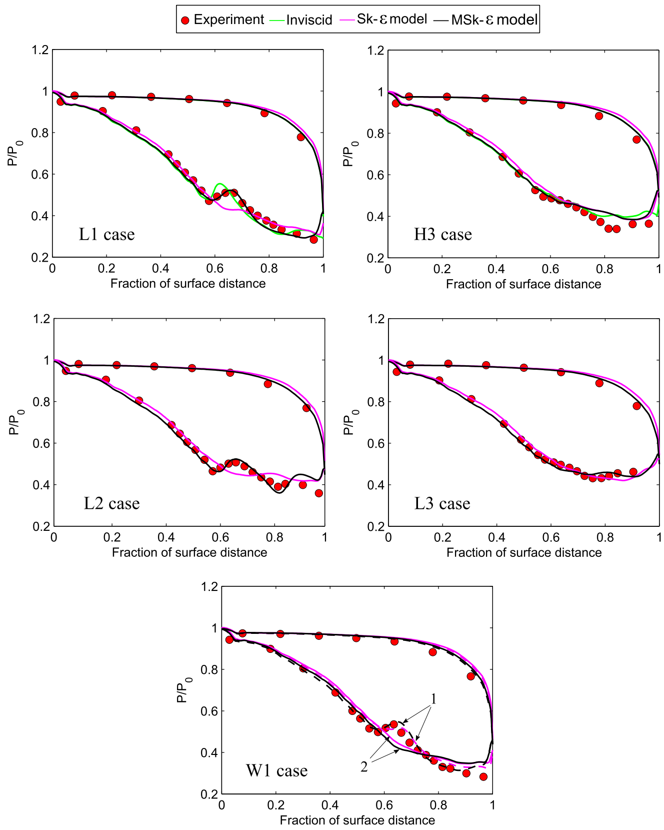

Fig. 11. Predicted results of blade surface pressure distribution and compared with the experimental data of [12]. In Case W1, the indication 1 and 2 represent the saturated inflow and the wet inflow, respectively.

turbulent dissipation rate, and turbulent viscosity near the blade surfaces and in the mid-passage. The large differences have been observed in the predicted values of turbulent kinetic energy, turbulent dissipation rate, and turbulent viscosity at the mid-passage by the Sk–ε model and the MSk–ε model. Near the pressure side, the MSk–ε model predicted lower value of turbulent kinetic energy than the Sk–ε model, likely due to the higher dissipation rate for the MSk–ε model near the pressure side. The jump locating around 0.8 fraction of the surface distance near the pressure side indicates the location of the highest rate of the nucleation. The MSk–ε model estimated a considerably higher turbulent kinetic energy and its dissipation rate compared to the Sk–ε model near the suction side, particularly after the second phase generation. This notable increment in the turbulent kinetic energy, turbulent dissipation rate, and turbulent viscosity can be explained by the viscosity modification and the added source terms effects, which increase the viscous dissipation near the suction surface.

Fig. 10 presents the Schlieren photograph and the calculated density gradient of Case L1. The experimental Schlieren photograph is the reproduced image of the original experimental photograph of White et al. [12], in which the expansion is indicated by red, orange, and yellow colours, while light blue and green colours express the small values of the compression. Moreover, the condensation shock, pressure side shock, and suction side shock are labelled with S_c, S_p, and S_s, respectively. It can be seen that the oblique shock profile is little bit curved across the central blade passage, and it is not reflected from the suction surface. Additionally, the pressure side shock interacts and merges with the condensation shock across the central blade. Figs. 10(b)–(d) show the density gradient contour for the selected models. The inviscid calculation yielded a relatively thinner profile of the S_s shock due to the absence of viscous dissipation. It is observed that the MSk–ε model predicted the S_s shock with a higher intensity than the others, likely due to the higher entropy generation resulting from the viscous dissipation at the trailing edge. The Sk–ε model failed to predict the S_c shock. In general, the shockwave patterns yielded by the MSk–ε model and the inviscid calculation match well with the experiment photograph.

Moreover, the quantitative analysis of the calculated results was performed based on the experimental data of White et al. [12]. The calculated pressure distribution on the blade surfaces with the Sk–ε model and the MSk–ε model is compared with the measured data in Fig. 11 for the selected test cases. The results of inviscid calculation are displayed only for the L1 and H3 cases. Fig. 11 shows that the yielded trends of pressure side pressure distribution by the inviscid and the turbulence models are similar. However, some variation was observed in the suction side pressure distribution. In Case L1, the MSk–ε model estimated the correct location and the intensity of the condensation disturbance on the suction side, while the inviscid calculation yielded the correct intensity of the pressure rise, but the location was moved little to the flow upstream. The predicted subcooling level in the case of Sk–ε model is lower due to lower expansion rate than the MSk–ε model. The Sk–ε model estimated less number of droplets which directly influenced on the latent heat released by droplets. Therefore, the Sk–ε model failed to capture the condensation disturbance. However, some discrepancy was observed between the calculated and the measured pressure distribution after the condensation shock on the surface side. The inlet superheat is 26 K for Case H3. Therefore, the effects of condensation were absent on the surface pressure distributions. Moreover, the measured data displays a second pressure rise close to the blade trailing edge. However, this is not observed in the calculated results. This pressure rise is not caused by the condensation phenomena; it happens due to the reflections from the upper tailboard during measurement [12]. Relatively good correspondence has been observed

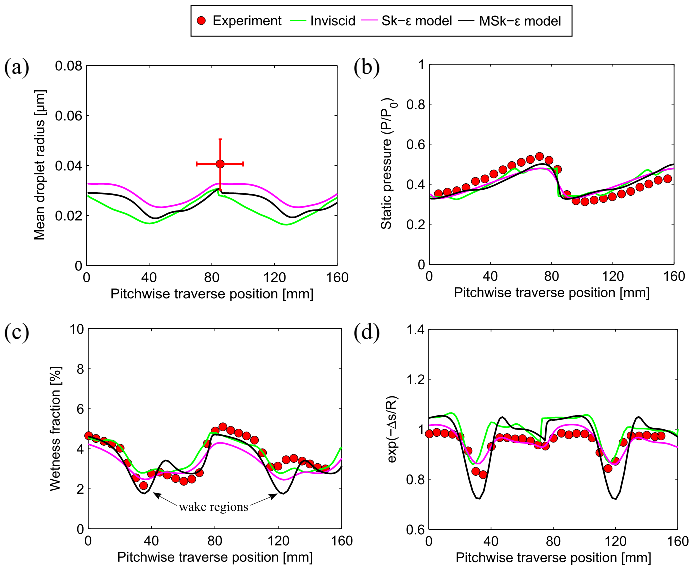

Fig. 12. Predicted results of Case L1: (a) mean droplet radius, (b) static pressure, (c) wetness fraction, and (d) non-dimensional entropy compared with the experiments of White et al. [12].

between the predicted and the measured results except near the suction surface trailing edge. Particularly, the Sk–ε and the MSk–ε models yielded similar trends near the suction surface trailing edge. Furthermore, both the turbulence models validated with the other low inlet superheat cases i.e. L2 and L3. It can be seen that the MSk–ε model yielded good results of blade surfaces' pressure distribution for both cases. In Case L2, the Sk–ε model failed to obtain the condensation disturbance. Moreover, the comparison between the predicted blade pressure profile of the Sk–ε model and the MSk–ε model including the wet inflow and the saturated inflow, and the measured data is given in Fig. 11 for Case W1. For Case W1, the inlet droplet radius ($\approx 0.5\ \mu m$) and liquid mass fraction ($\approx 1.6\%$) was assumed corresponding to the experimental values. It can be seen that the calculation with wet inflow with both the turbulence models was failed to predict the pressure rise resulted because the condensation on the primary liquid droplet was high enough preventing excessive departures from the equilibrium. Therefore, the secondary nucleation was relatively weak and remained up for a longer period [12]. It might be possible that the utilised values of inlet wetness fraction and liquid droplet size in the experiments have differed marginally from the assumed values [12]. However, the saturate inflow with the MSk–ε model is in good correspondence with the measurements. The Sk–ε model predicted the condensation disturbance with lower intensity.

In addition, White et al. [12] provided experimental data for the mean droplet size, static pressure distribution, wetness fraction, and normalised entropy at a specific location at downstream for Case L1. Therefore, it was also possible to compare the predicted and the experimental results at traverse plane. The position of traverse plane is indicated in Fig. 5(a). The predicted pitchwise distribution of the mean droplet radius, static pressure, wetness fraction, and normalised entropy at the traverse position are compared with the experimental data in Fig. 12. The variation of the droplet radius distribution across the passage is mostly dependent on the total number of droplets created during nucleation process, which is influenced by the distinct expansion rates along the blade passage and also due to the interaction between trailing edge shock waves and the nucleation zone. It can be seen that the mean droplet radius is relatively larger particularly in the downstream of mid-pitch region due to lower expansion rate. Additionally, near the suction surface, nucleation occurs in the very rapid expansion region resulting in an enormous number of tiny droplets. Therefore, in these regions (i.e., 35–45 mm and 115–125 mm), the mean droplet radius is decreased compared to the mid-pitch region. Fig. 12(a) shows that the mean droplet radius predicted by the Sk–ε model is slightly bigger, while after the model modification the mean droplet radius is reduced due to the higher droplet number. Relatively similar trends of the static pressure have been observed between the predicted and the experimental results. The wetness fraction is relatively lower between 35–45 mm and 115–125 mm at the traverse position because in these regions the trailing edge wake flows pass the traverse plane. Moreover, the flow mixing is higher in these regions, in which the temperature is comparatively higher. Therefore, the wetness fraction is relatively low in these regions. Furthermore, the cascade experiments were conducted for three passages, and therefore, it could be difficult to achieve periodicity in the downstream of the flow field. However, the CFD results yielded periodic profiles due to periodic boundary conditions. This could be the reason for some discrepancy observed between the predicted and the measured results in the second passage. Fig. 12(c) shows that the MSk–ε model yielded better correspondence with the measured wetness fraction profile than others. Fig. 12(d) shows the comparison between the calculated and the measured data of pitchwise variations in non-dimensional entropy, $\exp(-\Delta s/R)$, in which Δs is the increment in a specific entropy above the cascade inlet value. Fig. 12 shows that the Sk–ε model estimated good trends for the result of the non-dimensional entropy distribution, except in the wake region. The MSk–ε model predicted relatively higher entropy compared to the inviscid calculation and the Sk–ε model, particularly, in the wake region of the blade, likely due to the higher turbulent dissipation in that region, which increases the entropy generation.

4.3. Loss analysis

The primary goal of turbomachinery designers is to increase the performance of turbomachinery by increasing the efficiency. The reduction in the efficiency of turbomachinery is entitled as loss. The only rational measure of loss in an adiabatic machine is entropy generation [58]. The entropy generation happens due to three main processes: (i) viscous friction (either in boundary layers or in free shear layers), (ii) heat transfer, and (iii) non-equilibrium processes (occur in very rapid expansions or in shock waves) [58].

The local entropy generation rates are considerably high in the blade wakes, at the edges of separated regions and in vortices, in which, the shearing rates are relatively high. Moreover, in these regions, the flow turbulence is the leading phenomenon, which governs the heat, mass, and momentum transfer processes. Consequently, the accurate prediction of entropy generation needs accurate turbulence modelling. The predicted contours of entropy generation by the inviscid calculation, and the Sk–ε and MSk–ε models are presented in Fig. 13 for Case L1.

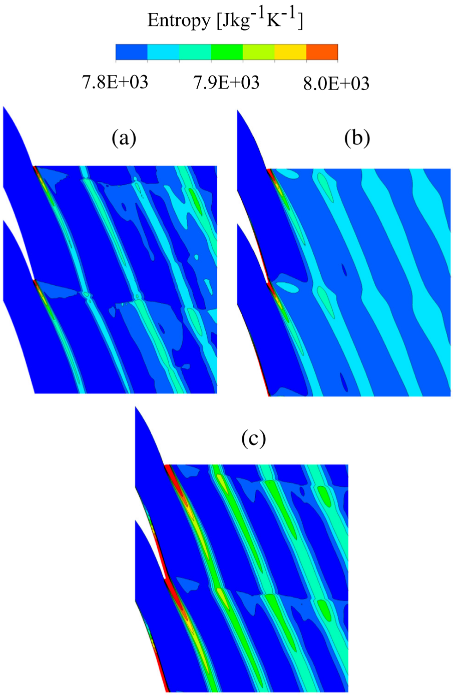

Fig. 13. Contours of entropy predicted by (a) the inviscid, (b) the Sk–ε model, and (c) the MSk–ε model.

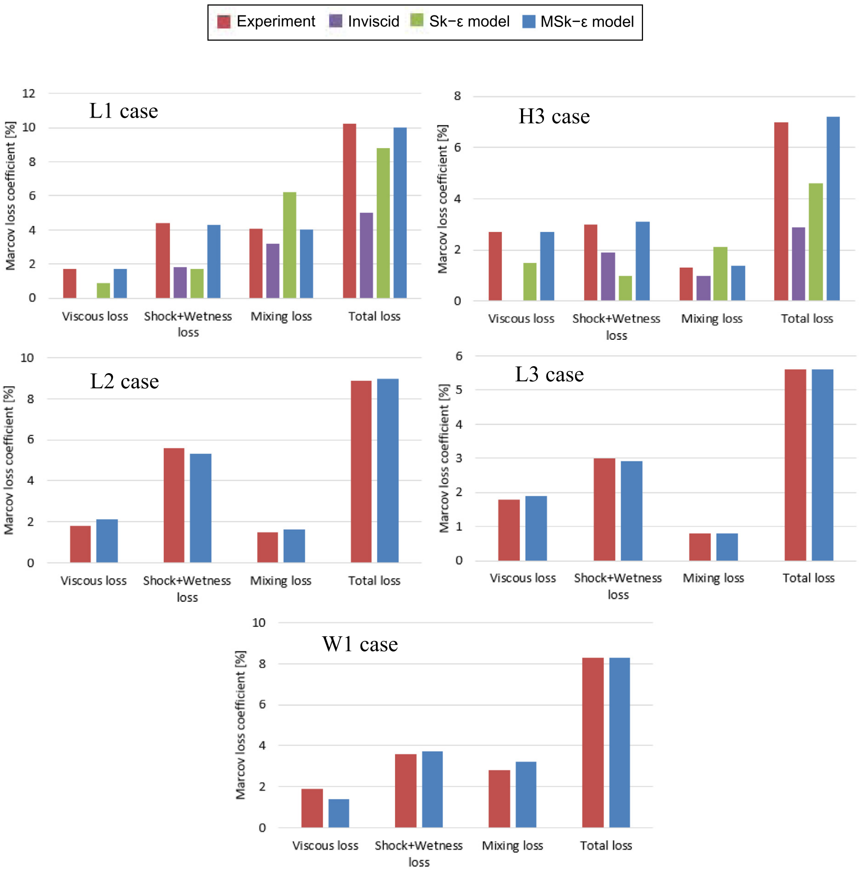

Fig. 14. Predicted Markov loss coefficients compared with the experiments of White et al. [12].

It appears that the inviscid calculation yielded relatively weak entropy generation compared to the Sk–ε and the MSk–ε models owing to the lack of the boundary layer effect in the inviscid calculation. The MSk–ε model predicted the highest entropy generation among all the cases particularly in the blade wake region. Furthermore, White et al. [12] presented information about the losses that occur due to the irreversible heat and mass transfer during the condensation process. Accordingly, it was possible to analyse the influence of turbulence modelling on the loss mechanism occurring in the condensing steam flow. In the present work, the Markov energy loss coefficient based on the entropy increase was calculated. The Markov energy loss coefficient is defined as,

$$\zeta = \frac{T_2 \cdot \Delta s}{0.5 u_2^2}. \tag{26}$$

For the loss coefficient calculation, it was assumed that all of the parameters were 'mixed-out' values to a plane far downstream of the cascade. The Markov energy loss coefficients were divided into three components [12]:

(i) Shockwave plus wetness loss was calculated from the mass-averaged values across a section of the traverse plane, excluding the wake regions.
(ii) Viscous loss was calculated by subtracting the shock wave and wetness loss from the mass-averaged loss across the entire pitch at the traverse plane.
(iii) Mixing loss was calculated by subtracting the total mass-averaged loss at the traverse plane from the fully mixed-out loss.

Fig. 14 presents the comparison between the predicted and the measured losses for all the selected cases.

It can be seen that the Sk–ε model underpredicts the viscous loss, while the MSk–ε model estimates an accurate value of the viscous loss for Cases L1 and H3. The intensity of the S_p shock wave for the MSk–ε model is comparatively higher than that of the Sk–ε model (Fig. 10). Moreover, it can be observed that the S_p shock merges with the S_c shock, thickening the suction side boundary layer onto the suction side of the adjacent blade, which increases the viscous loss. Therefore, the MSk–ε model yields higher viscous loss than the Sk–ε model.

For Cases L1 and H3, the predicted magnitude of the shock plus wetness loss for the MSk–ε model corresponds well with the experimental values. In contrast, the inviscid calculation and the Sk–ε model calculated a notably smaller value of the shock plus wetness loss. The magnitude of mixing loss increases with the high Mach numbers. Among the selected test cases, Case L1 was performed with the highest exit Mach number. Therefore, the mixing loss for the L1 case is higher than for the other test cases. Furthermore, it is known that the combined action of shock waves, expansion waves, and viscous forces causes a gradual transition from nonuniform flow condition in the trailing edge plane to uniform conditions far downstream, which induce mixing loss. The boundary layer effect was absent in the inviscid calculations, reducing the viscous forces. Therefore, the inviscid calculation estimated lower mixing loss compared to both turbulence models. As shown in Fig. 9(c), the Sk–ε model estimated fairly larger value of the turbulent viscosity than the MSk–ε model. Therefore, this could be the reason for the higher entropy generation in the mid-passage at downstream for the Sk–ε model (Fig. 13), which indicated the higher value of mixing loss. The presented values of the total loss in Fig. 14 indicate the sum of viscous loss, shock plus wetness loss, and mixing loss. It can be seen that the inviscid calculation failed to predict the total loss for both cases. Also, the Sk–ε models yielded some variation with the measured losses. The MSk–ε model estimated accurate trends of the losses occurring in the condensing flow of turbine cascade. Additionally, losses were calculated for Cases L2, L3 and W1 by the MSk–ε model. Good agreement was observed between the predicted and the measured losses.

5. Conclusions

In this work, the influence of turbulence modelling on non-equilibrium homogeneously condensing steam flow was presented, adopting the Eulerian–Eulerian approach based on compressible Reynolds-averaged Navier–Stokes equations. The standard k–ε (Sk–ε) turbulence model was modified by introducing the modulation of turbulence kinetic energy and its dissipation due to liquid droplets via source terms. Additionally, the definition of turbulent viscosity was modified by production to dissipation ratio.

In the case of laval nozzle, the presented results illustrated that the freestream turbulence intensity of the flow and the condensation disturbance magnitude were inversely proportional. Moreover, the flow turbulence intensity influenced the growth rate and droplet size. It can be concluded that the inviscid calculation and the Sk–ε turbulence model were inadequate in predicting the two-phase flow phenomena in a nozzle. After the addition of the source terms and modified turbulent viscosity into the Sk–ε turbulence model, the modified Sk–ε (MSk–ε) turbulence model predicted relatively higher viscous dissipation. The viscous dissipation changes the temperature distribution via energy source, which affects the heat transfer rates. Therefore, the nucleation process and droplet growth rate were influenced by the turbulence model modification. It can be concluded that the MSk–ε model corresponds well with the experimental results and mimics crucial trends of the condensation process of a nozzle.

The influence of turbulence modelling was further studied with the condensing steam flow in a stationary cascade of turbine blades operating under transonic conditions. Five test cases were modelled and discussed. The calculations of turbine cascade flow were conducted with different inlet freestream turbulence intensities. The predicted results demonstrated that the high freestream turbulence intensity expanded the nucleation region, and consequently the condensation disturbance disappeared. As seen qualitatively, also the wetness fraction was reduced with a higher freestream turbulence intensity.

The results of blade surface pressure distribution, liquid droplet size, variation of static pressure, wetness and normalised entropy along the traverse plane at downstream, and Schlieren photograph predicted by the inviscid calculation, the Sk–ε and the MSk–ε turbulence models were compared with the experimental data. It is demonstrated that the Sk–ε model failed to predict condensation disturbance in the turbine cascade. In the case of the MSk–ε model, the subcooling level was increased due to the higher flow expansion. As the subcooling level increases, the rate of nucleation of liquid droplets increases, affecting the droplets growth rates. The MSk–ε model yielded a higher number of droplets, which released more latent heat to the vapour phase, thus increasing the pressure rise. The presented results indicated that the MSk–ε model predicted the condensation disturbance more accurately than the inviscid calculation and the Sk–ε model. Generally, the MSk–ε model produced more promising trends for the results at the traverse plane of the downstream than the inviscid calculation and the Sk–ε model.

The cascade loss coefficients were calculated from the numerical simulations. The presented loss analysis indicated that the MSk–ε estimated an accurate value of the viscous loss, shock plus wetness loss, mixing loss, and total loss for the selected cases. Both the inviscid calculation and the Sk–ε model failed to predict shock plus wetness loss and mixing loss. The study demonstrated that the ignorance of turbulence modelling to condensing steam flow calculation may induce an incorrect estimation of the key phenomena.

The presented study shows that the prediction of condensing steam flows is influenced by turbulence modelling. Therefore, the accurate computational prediction of condensing steam flow requires the turbulence to be accurately modelled. This work will be continued in the future with the aim to investigate the influence of turbulence in 3D turbine cascade condensing flow with steady and unsteady conditions.

Acknowledgements

The authors would like to acknowledge the Finnish Graduate School in Computational Fluid Dynamics and the Academy of Finland for the financial support.

References

[1] A. Stodola, Die Dampfturbinen, 4. Edition., Springer verlag, Berlin, 1910.
[2] D. Barschdorff, Verlauf der zustandsgrossen und gasdynamische zusammenhaenge der spontanen kondensation reinen wasserdampfes in lavalduesen, Forsch. Ingenieurwes. 37 (1971) 146–157.
[3] M.J. Moore, P.T. Walters, R.I. Crane, B.J. Davidson, Predicting the fog drop size in wet steam turbines, in: Wet Steam 4 Conference, Institute of Mechanical Engineers (UK), University of Warwick, Paper C37/73, 1973.
[4] F. Bakhtar, D. Ryley, K. Tubman, J. Young, Nucleation studies in flowing high pressure steam, Inst. Mech. Eng. 189 (1975) 427–436.
[5] C.A. Moses, G.D. Stein, On the growth of steam droplets formed in a Laval nozzle using both static pressure and light scattering measurements, J. Fluids Eng. 100 (1978) 311–322.
[6] S. Skillings, P. Walters, M. Moore, A study of supercritical heat addition as potential loss mechanism in condensing steam turbines, in: Int. Mech. Engrs., Intl. Conf. on Turbomachinery, Cambridge, C259/87, 1987, pp. 125–134.
[7] F. Bakhtar, K. Zidi, Nucleation phenomena in flowing high-pressure steam: experimental results, Proc. Inst. Mech. Eng. 203 (1989) 195–200.
[8] F. Bakhtar, K. Zidi, Nucleation phenomena in flowing high-pressure steam, part 2: theoretical analysis, Proc. Inst. Mech. Eng. 204 (1990) 233–242.
[9] G. Gyarmathy, Nucleation of steam in high-pressure nozzle experiments, in: Proc. of 6th European Conference on Turbomachinery, Lille, France, March 7–11, 2005, pp. 458–469.
[10] F. Bakhtar, M. Ebrahimi, B. Bamkole, On the performance of a cascade of turbine rotor tip section blading in nucleating steam, part 2: wake traverses, Proc. Inst. Mech. Eng. Part C: J. Mech. Eng. Sci. 209 (1995) 169–177.
[11] F. Bakhtar, M. Ebrahimi, R. Webb, On the performance of a cascade of turbine rotor tip section blading in nucleating steam, part 1: surface pressure

distributions, Proc. Inst. Mech. Eng. Part C: J. Mech. Eng. Sci. 209 (1995) 115–124.

[12] A.J. White, J.B. Young, P.T. Walters, Experimental validation of condensing flow theory for a stationary cascade of steam turbine blade, Philos. Trans. R. Soc. London A 354 (1996) 59–88.

[13] F. Bakhtar, M.T.M. Tochai, An investigation of two-dimensional flows of nucleating and wet steam by the time-marching method, Int. J. Heat Fluid Flow 2 (1980) 5–18.

[14] J.B. Young, Critical conditions and the choking mass flow rate in non-equilibrium wet steam flows, ASME J. Fluids Eng. 106 (1984) 452–458.

[15] J.B. Young, Two-Dimensional nonequilibrium wet steam calculations for nozzles and turbine cascades, ASME J. Turbomach. 114 (1992) 569–579.

[16] A.J. White, J.B. Young, Time-marching method for the prediction of two-dimensional unsteady flows of condensing steam, AIAA J. Propul. Power 9 (4) (1993) 579–587.

[17] F. Bakhtar, M.R. Mahpeykar, K.K. Abbas, An investigation of nucleating flows of steam in a cascade of turbine blading-theoretical treatment, ASME J. Fluids Eng. 117 (1995) 138–144.

[18] J.D. Denton, An improved time-marching method for turbomachinery flow calculation, J. Eng. Power 105 (3) (1983) 514–521.

[19] A. Gerber, Two-phase Eulerian/lagrangian model for nucleating steam flow, ASME J. Fluids Eng. 124 (2002) 465–475.

[20] A.G. Gerber, M.J. Kermani, A pressure based Eulerian–Eulerian multi-phase model for non-equilibrium condensation in transonic steam flow, Int. J. Heat Mass Transfer 44 (2004) 2217–2231.

[21] S. Senoo, A.J. White, Numerical simulations of unsteady wet steam flows with non-equilibrium condensation in the nozzle and the steam turbine, in: Proc. ASME-FEDSM2006, FEDSM-2006-98202, Maimi, Florida, USA, July 17–20, 2006, pp. 757–767.

[22] S. Senoo, A.J. White, Non-equilibrium unsteady wet-steam condensation modelling: computations in a steam turbine cascade and a nozzle, in: Baumann Centenary Conference, BCC-2012-07, University of Cambridge, UK, September 10–11, 2012.

[23] W. Wróblewski, S. Dykas, A. Gepert, Steam condensing flow in turbine channels, Int. J. Multiphase Flow 35 (6) (2009) 498–506.

[24] S. Dykas, W. Wróblewski, Single- and two-fluid models for steam condensing flow modeling, Int. J. Multiphase Flow 37 (9) (2011) 1245–1253.

[25] S. Dykas, W. Wróblewski, Two-fluid model for prediction of wet steam transonic flow, Int. J. Heat Mass Transfer 60 (2013) 88–94.

[26] S. Yamamoto, Y. Sasao, K. Sano, H. Satsuki, K. Ishizaka, H. Ooyama, Parallel computation of condensate flows through 2-d and 3-d multistage turbine cascades, in: Proc. International Gas Turbine Congress, Tokyo, 2007.

[27] S. Yamamoto, Y. Sasao, S. Sato, K. Sano, Parallel-implicit computation of three-dimensional multistage stator-rotor cascade flows with condensation, in: Proc. 18th AIAA Computational Fluid Dynamics Conference, AIAA 2007-4460, Miami, Florida, USA, June 2007.

[28] S. Yamamoto, Y. Sasao, H. Kato, H. Satsuki, H. Ooyama, K. Ishizaka, Numerical and experimental investigation of unsteady 3-d wet-steam flows through two-stage stator-rotor cascade channels, in: Proc. ASME Turbo Expo, GT2010-22796, Glasgow, UK, June 14–18, 2010, pp. 1–9.

[29] J. Starzmann, M. Schatz, M.V. Casey, J.F. Mayer, F. Sieverding, Modelling and validation of wet steam flow in a low pressure steam turbine, in: Proc. ASME Turbo Expo, GT2011-45, Vancouver, Canada, June 6–10, 2011, pp. 1–12.

[30] S. Miyake, Y. Sasao, S. Yamamoto, S. Tabata, T. Miyawaki, H. Ohyama, Simulation of unsteady 3D wet-steam flows through three-stage stator-rotor blade rows with equilibrium and non-equilibrium condensations, in: Proc. of ASME Turbo Expo, GT2012-68828, Copenhagen, Denmark, June 11–15, 2012, pp. 1–9.

[31] A.R. Avetissian, G.A. Philippov, L.I. Zaichik, Effects of turbulence and inlet moisture on two-phase spontaneously condensing flows in transonic nozzles, Int. J. Heat Mass Transfer 51 (2008) 4195–4203.

[32] D.G. Gregory-Smith, J.A. Walsh, C.P. Graves, K.P. Fulton, Turbulence measurements and secondary flows in a turbine rotor cascade, ASME J. Turbomach. 110 (4) (1988) 479–485.

[33] G.D. MacIsaac, T.J. Praisner, S.A. Sjolander, Measurements of losses and reynolds stresses in the secondary flow downstream of a low-speed linear turbine cascade, ASME J. Turbomach. 134 (6) (2012) 1–12. 061015.

[34] A. White, Numerical investigation of condensing steam flow in boundary layers, Int. J. Heat Fluid Flow 21 (2000) 727–734.

[35] D.A. Simpson, A.J. White, Viscous and unsteadyflow calculations of condensing steam in nozzles, Int. J. Heat Fluid Flow 26 (1) (2005) 71–79.

[36] A.R. Avetissian, G.A. Philippov, L.I. Zaichik, The effect of turbulence on spontaneously condensing wet-steam flow, Nucl. Eng. Des. 235 (2005) 1215–1223.

[37] Y. Patel, G. Patel, T. Turunen-Saaresti, The effect of turbulence and real gas models on the two phase spontaneously condensing flows in nozzle, in: Proc. of ASME Turbo Expo, GT2013-94778, San Antonio, USA, June 3–7, 2013, pp. 1–7.

[38] Y. Patel, T. Turunen-Saaresti, G. Patel, A. Grönman, Numerical investigation of turbulence modelling on condensing steam flows in turbine cascade, in: Proc. of ASME Turbo Expo, GT2014-26307, Düsseldorf, Germany, June 16–20, 2014, pp. 1–14.

[39] J. Frenkel, Kinetic Theory of Liquids, Oxford University Press, New York, 1946.

[40] K. Ishizaka, T. Ikohagi, D. Daiguji, A high-resolution numerical method for transonic nonequilibrium condensation flows through a steam turbine cascade, in: Proc. of 6th International Symposium on Computational Fluid Dynamics, 1995, pp. 479–484.

[41] P.G. Hill, Condensation of water vapour during supersonic expansion in nozzles, J. Fluid Mech. 25 (3) (1966) 593–620.

[42] J.B. Young, The spontaneous condensation of steam in supersonic nozzles, Phys. Chem. Hydrodyn. 3 (1982) 57–82.

[43] J.B. Young, An equation of state for steam for turbomachinery and other flow calculations, J. Eng. Gas Turbines Power 110 (1988) 1–7.

[44] W.C. Reynolds, Thermodynamic properties, in: SI: Graphs, Tables, and Computational Equations for 40 Substances, Department of mechanical Engineering, Stanford University, 1979.

[45] E.R.G. Eckert, R.M. Drake, Analysis of Heat and Mass Transfer, McGraw-Hill Co., 1972.

[46] A. Guha, Two-phase flows with phase transition, in: VKI Lecture Series 1995-06, von Karman Institute for Fluid Dynamics, Belgium, 1995, pp. 1–110.

[47] C.G. Speziale, On nonlinear k–l and k–e models of turbulence, J. Fluid Mech. 178 (1987) 459–475.

[48] T.B. Gatski, C.G. Speziale, On explicit algebraic stress models for complex turbulent flows, J. Fluid Mech. 254 (1993) 59–78.

[49] J.L. Lumley, The second-order models of turbulent flows, in: Prediction Methods for Turbulent Flows, Hemisphere, New York, 1980.

[50] L. Zaichik, O. Simonin, V. Alipchenkov, Two statistical models for predicting collision rates of inertial particles in homogeneous isotropic turbulence, Phys. Fluids 15 (2003) 2995–3005.

[51] B.E. Launder, D.B. Spalding, The numerical computation of turbulent flows, Comput. Methods Appl. Mech. Eng. 3 (1974) 269–289.

[52] P.L. Roe, Characteristic based schemes for the Euler equations, Annu. Rev. Fluid Mech. 18 (1986) 337–365.

[53] I.B. Celik, U. Ghia, P.J. Roache, C.J. Freitas, H. Coleman, P.E. Raad, Procedure for estimation and reporting of discretization error in cfd applications, J. Fluids Eng. 130 (7) (2008) 1–4. 078001.

[54] L.F. Richardson, The approximate arithmetical solution by finite differences of physical problems involving differential equations, with an application to the stresses in a masonary dam, Philos. Trans. R. Soc. London. Ser. A 210 (1910) 307–357.

[55] L.F. Richardson, J.A. Gaunt, The deferred approach to the limit, Philos. Trans. R. Soc. London. Ser. A 226 (1927) 299–361.

[56] P.J. Roache, Perspective: a method for uniform reporting of grid refinement studies, J. Fluids Eng. 116 (1994) 405–413.

[57] P.P. Wegener, Non-equilibrium flow with condensation, Acta Mech. 21 (1–2) (1975) 65–91.

[58] J.D. Denton, The 1993 igti scholar lecture: loss mechanisms in turbomachines, ASME J. Turbomach. 115 (4) (1993) 621–656.

Publication IV

G., Patel, Y., and Turunen-Saaresti, T. (2015).
Influence of trailing edge geometry on the condensing steam flow in low-pressure steam turbine.

Reprinted with permission from
Proceedings of ASME Turbo Expo 2015:
Turbine Technical Conference and Exposition.
Vol. 8, pp. 1-11.
© ASME, 2015

Proceedings of ASME Turbo Expo 2015: Turbine Technical Conference and Exposition
GT2015
June 15 – 19, 2015, Montréal, Canada

GT2015-43189

INFLUENCE OF TRAILING EDGE GEOMETRY ON THE CONDENSING STEAM FLOW IN LOW-PRESSURE STEAM TURBINE

Giteshkumar Patel[*]
Fluid Dynamics Laboratory
School of Technology
Lappeenranta University of Technology
Lappeenranta, Finland
Email: giteshkumar.patel@lut.fi

Yogini Patel
Fluid Dynamics Laboratory
School of Technology
Lappeenranta University of Technology
Lappeenranta, Finland
Email: yogini.patel@lut.fi

Teemu Turunen-Saaresti
Fluid Dynamics Laboratory
School of Technology
Lappeenranta University of Technology
Lappeenranta, Finland
Email: teemu.turunen-saaresti@lut.fi

ABSTRACT

The paper describes the influence of trailing edge geometries on the non-equilibrium homogeneously condensing steam flow in the stationary cascade of turbine blades. The computational fluid dynamics (CFD) simulations were performed with the ANSYS Fluent CFD code using the Eulerian-Eulerian approach. The condensation phenomena were simulated on the basis of the classical nucleation theory, and the steam properties were calculated with the real gas model. Flow turbulence was solved by employing the modified version of the shear-stress transport (SST) k-ω turbulence model. For this study, three trailing edge profiles; that is, conic, semicircular and square were considered. The influence of the trailing edge shapes were discussed together with experimental data available in the literature. The presented results show that the trailing edge geometries influence on the nucleation process, the droplet size, wetness fraction, the shock waves structure generated at trailing edge and its angles, the flow angle, the entropy generation and flow mixing in the wake. The cascade loss coefficients were calculated for the low inlet superheat case and for the high inlet superheat case. The presented results demonstrated that the losses that occur due to the irreversible heat and mass transfer during the condensation process were also influenced due to the trailing edge shapes.

Nomenclature

C_p	specific heat at constant pressure (J kg^{-1} K^{-1})
h_{fg}	specific enthalpy (J kg^{-1})
H	total enthalpy(J kg^{-1})
I	nucleation rate (m^{-3} s^{-1})
k	turbulent kinetic energy (m^2 s^{-2})
M	liquid mass (kg)
P	pressure(Pa)
r	radius (m)
r_*	critical radius (m)
R	gas constant (J kg^{-1} K^{-1})
s	entropy (J kg^{-1} K^{-1})
S_1	mass source term (kg m^{-2} s^{-1})
S_2	momentum source term (kg m^{-2} s^{-2})
S_3	energy source term (W m^{-3} K^{-1})
t	time (s)
T	temperature (K)
u	velocity component (m s^{-1})
$\mathbf{v}$	flow velocity (m s^{-1})

Greek Letters

ρ	density (kg m^{-3})
β	liquid phase mass fraction
ω	specific dissipation rate (s^{-1})
η	number of liquid droplets per unit volume (m^{-3})
σ	liquid surface tension (N m^{-1})
Γ_E	thermal diffusion coefficient (W m^{-1} K^{-1})

---

[*] Corresponding author

Copyright © 2015 by ASME

Subscript

d	droplet
l	liquid phase
v	vapour phase
i,j	cartesian tensor notation
x	cartesian coordinate
$0,1,2$	total, inlet, outlet condition of cascade

1 INTRODUCTION

The efficiency of the entire power plant is largely dependent on the efficiency of the energy conversion in the turbine. Nowadays, the research on low pressure (LP) turbine stages is of special importance due to their relatively low efficiency. A marginal improvement in the LP turbine performance would produce significant economic benefits. It is essential to understand and to analyze the condensation process that occurs in the LP turbine because condensation in the LP turbine introduces thermodynamic and aerodynamic losses, as well as erosion in rotating and stationary parts. Therefore, the condensing steam flows in turbines have been widely studied for more than a century.

Comprehensive studies have been done by many researchers experimentally and theoretically to enhance the knowledge about the complicated physics of condensing steam flows. However, experimental facilities for condensing steam flows are in short supply throughout the world. Additionally, the measurements of some key parameters of these flows are very challenging, for example the droplet sizing measurements. Therefore, numerical study of condensing steam flows is necessary and feasible. Along with the experimental and theoretical studies, extensive numerical studies on condensing steam flow have also been done by numerous researchers on various aspects of it.

In the condensing steam flow, the flow is initially dry, but after reaching the Wilson point, liquid droplets are formed, and a two-phase flow is generated. The rapidly growing liquid droplets release latent heat to the surrounding vapour phase, which increases the flow temperature and pressure. The flow pressure rise is called the 'condensation disturbance' [1]. Some flow phenomena would affect the nucleation process such as viscous boundary layer and shock wave [2–5]. The condensing process is sensitive to the variation of local flow field as well as to the boundary conditions. Moreover, the blade profiles including the shape and thickness may have some influence on the condensing phenomena occurring in the LP turbine.

Many work have been done to analyze the aerodynamics of the LP turbine blades, for example Stein et al. [6] studied the impact of key geometrical features on the aerodynamic performance of transonic tip sections using CFD solvers. The geometrical features were subsonic overlap, supersonic overlap, trailing edge thickness, trailing edge wedge angle and camber distribution. Torre et al. [7] investigated the effect of airfoil thickness on the efficiency of LP turbines experimentally in a multistage turbine high-speed rig. Zhou et al. [8] presented the effects of the blade trailing edge thickness on the profile loss of ultrahigh-lift low-pressure turbine blades using experimental, numerical and analytical methods. However, the published work on the effects of the trailing edge geometry in condensing steam flows and its corresponding influence on the loss mechanism is rather sparse. For example Singh [9] investigated numerically the effects of geometrical changes on the wetness generation in the blade profile of a LP turbine rotor blade cascade of Bakhtar et al. [10]. This work concluded that the geometrical changes including blade chord length have large effects on the amount of wetness generated. Also, An et al. [11] studied the effect of blade profile modification on the nucleation zone distribution and the degree of boundary layer separation in primary nucleation stage in the wet steam flows adopting Eulerian method. They altered the blade profiles by changing the blade curvature distribution of the profile. They concluded that the nucleation rate and the flow outlet angle were influenced by the blade modification.

The shapes and the size of the trailing edge of the turbine blades have strong effects on the pressure fields within the blade passage. Additionally, since the liquid phase generation is influenced by the local rate of change of the pressure fields, it can be expected that the trailing edge shapes would have significant effects on the droplet growths and other parameters. Therefore, the aim of this work is to investigate the influence of trailing edge geometries on the non-equilibrium homogeneously condensing steam flow in the stationary cascade of turbine blades using the Eulerian-Eulerian approach. For this purpose, three different trailing edge shapes are considered. The numerical results are compared and discussed with the experimental data of White et al. [12]. Moreover, the cascade loss coefficients are calculated for all the selected cases.

2 NUMERICAL METHODOLOGY

All the results presented in this paper have been obtained by means of the ANSYS Fluent 14.5 CFD code. The CFD simulations of two-phase vapour-liquid mixture were conducted by employing 2D steady state compressible Reynolds-averaged Navier-Stokes (RANS) equations based on the Eulerian-Eulerian approach. When modeling non-equilibrium flows, the prediction of nucleation and droplet growth rate are quite sensitive to the thermodynamic properties calculations. In the present work, the estimation of real gas properties was based on Young [13] formulations, in which the equation of state for the vapour phase utilizes a virial form with temperature and density as the independent variables. More details about the virial coefficients formulation and the constants values can be found from Young [13].

Copyright © 2015 by ASME

2.1 Governing equations

The governing equations of mass, momentum, and energy conservation for the mixture of vapour and liquid phases can be written as

$$\frac{\partial \rho}{\partial t} + \frac{\partial}{\partial x_i}(\rho u_i) = S_1, \tag{1}$$

$$\frac{\partial}{\partial t}(\rho u_i) + \frac{\partial}{\partial x_j}(\rho u_i u_j) = -\frac{\partial P}{\partial x_i} + \frac{\partial \tau_{ij}}{\partial x_j} + S_2, \tag{2}$$

$$\begin{aligned}\frac{\partial}{\partial t}(\rho H) + \frac{\partial}{\partial x_j}(\rho u_j H) = \frac{\partial P}{\partial t} + \frac{\partial}{\partial x_j}\left(\Gamma_E \frac{\partial T}{\partial x_j}\right) \\ + \frac{\partial}{\partial x_j}(u_i \tau_{ij}) + S_3,\end{aligned} \tag{3}$$

where i and j are the Cartesian tensor notations. τ_{ij} represents the stress tensor components. In eq. (1), the source term S_1 represents the mass transfer due to the condensation process or evaporation on the already existing droplet. The S_2 term in eq. (2) is the momentum source term which includes the momentum exchange between the liquid droplets and the surrounding vapour, and the smaller terms from the gradient of the Reynolds stress tensor. In eq. (3), the source term S_3 includes the interphase heat transfer. Moreover, two additional transport equations were solved for the liquid phase mass fraction, and the number of liquid droplets per unit volume, which can be written as following, respectively,

$$\frac{\partial \rho \beta}{\partial t} + \frac{\partial}{\partial x_i}(\rho u_i \beta) = \Gamma, \tag{4}$$

$$\frac{\partial \rho \eta}{\partial t} + \frac{\partial}{\partial x_i}(\rho u_i \eta) = \rho I, \tag{5}$$

where Γ is the mass generation rate per unit volume due to condensation and evaporation, and I is the nucleation rate. However, the following assumptions have been considered in the CFD code concerning the vapour-liquid mixture flow modeling; (i) the slip velocity between the liquid droplets and the vapour surrounding them was negligible, (ii) the condensed liquid phase consisted of droplets whose radii were on the order of 1 μm or less, and therefore, it was assumed that the volume of the condensed liquid phase was negligible; and (iii) the interactions between droplets were omitted.

2.2 Nucleation and droplet growth model

The classical nucleation theory given by Frenkel [14] was adopted to model the homogeneous condensation phenomenon. The rate of the formation of liquid droplet embryos due to the homogeneous condensation per unit mass of the mixture was calculated as

$$I = \frac{q_c}{(1+\theta)}\left(\frac{\rho_v^2}{\rho_l}\right)\sqrt{\frac{2\sigma}{M^3\pi}}\, e^{-\left(\frac{4\pi r_*^2 \sigma}{3K_b T}\right)}, \tag{6}$$

where q_c denotes the condensation coefficient that was assumed to be unity, M is the mass of a molecule, σ is the surface tension of the liquid phase, r_* is the Kelvin-Helmholtz critical droplet radius, K_b is Boltzmann's constant, and θ is the non-isothermal correction coefficient.

The mass generation rate was obtained from Ishizaka et al. [15], and it can be written as

$$\Gamma = \frac{4}{3}\pi \rho_l I r_*^3 + 4\pi \rho_l \eta \bar{r}^2 \frac{\partial \bar{r}}{\partial t}. \tag{7}$$

The mass generation rate, Γ, was based on the sum of mass increase due to nucleation (the formation of critically sized droplets) and also due to the growth/demise of these droplets. In eq. (7), $\bar{r}$ denotes the average radius of the liquid droplet, which was calculated based on the critical droplet size and the droplets growth. If the droplet radius is larger than r_*, it will grow; otherwise the droplet evaporates [16]. The critical droplet radius was calculated as

$$r_* = \frac{2\sigma}{\rho_l RT lnS}, \tag{8}$$

where S is the super saturation ratio defined by the ratio of vapour pressure to the equilibrium saturation pressure. The droplet growth rate was estimated from the proposed formula of Hill [17], which can be defined as

$$\frac{\partial \bar{r}}{\partial t} = \frac{P}{h_{fg}\rho_l\sqrt{2\pi RT}}\frac{\gamma+1}{2\gamma}C_p(T_d - T), \tag{9}$$

where T_d is the droplet temperature. The details about droplet temperature calculation have been presented in Young [18].

2.3 Turbulence models

Previously, Patel et al. [19] presented the modified version of the shear-stress transport (SST) k-ω turbulence model of Menter [20] in which they modified the turbulent viscosity term of the

Copyright © 2015 by ASME

SST k-ω turbulence model, and also the source terms were included in both of the turbulence equations. The performance of modified SST k-ω model has been validated by Patel et al. [19] with three experimental cases of the turbine cascade of White et al. [12]. Therefore, in this study, the modified version of the SST k-ω turbulence model of Patel et al. [19] is used for modeling the flow turbulence. The equations of the turbulence kinetic energy k, and its specific dissipation rate ω for the mixture of vapour and liquid phases can be written in the following form, respectively,

$$\frac{\partial}{\partial t}(\rho k)+\frac{\partial}{\partial x_i}(\rho k u_i)=\frac{\partial}{\partial x_j}\left[\Gamma_k\frac{\partial k}{\partial x_j}\right]+\widetilde{G}_k-Y_k+S_k \qquad (10)$$

$$\begin{aligned}\frac{\partial}{\partial t}(\rho\omega)+\frac{\partial}{\partial x_i}(\rho\omega u_i)=\frac{\partial}{\partial x_j}\left[\Gamma_\omega\frac{\partial k}{\partial x_j}\right]+\widetilde{G}_\omega\\ -Y_\omega+D_\omega+S_\omega,\end{aligned} \qquad (11)$$

where Γ_k and Γ_ω are the effective diffusivities of k and ω, respectively. In eqs. (10) and (11), $\widetilde{G}_k$ and $\widetilde{G}_\omega$ represent the generation of turbulence kinetic energy and its specific dissipation rate due to the mean velocity gradients, respectively. The terms Y_k and Y_ω represent the dissipations of k and ω due to turbulence, respectively. D_ω is the cross-diffusion term. S_k and S_ω are the source terms of the equations of turbulence kinetic energy, and its specific dissipation rate, respectively. Additional details pertaining to the model modifications can be found from Patel et al. [19].

3 NUMERICAL DETAILS

In this work, the steam turbine cascade of White et al. [12] has been selected as a reference case, which is the planar stator cascade of the fifth stage stator blade from the six-stage LP cylinder of a 660 MW steam turbine. The experiments of White et al. [12] are related to the flow in steam turbines in which there is an interaction between aerodynamics effects and the condensation process itself. These phenomena are absent in steady nozzle flows. White et al. [12] have provided experimental data for various test conditions.

There were four stator vanes in the experiments of White et al. [12]. In this work, only a single passage of the experimental facility has been modeled. Originally, the sharp trailing edge profile was used in the experiments. In the present work, three trailing edge geometries were considered: (i) conic trailing edge (CTE), (ii) semicircular trailing edge (RTE), and (iii) square trailing edge (STE), in order to check the influence of the trailing-edge shapes on the condensing steam flow field (Figure 1(a)). The RTE profile has at its end a circle of radius 0.8045 mm. The STE profile was approximated from the RTE profile. To generate the STE profile, the circle of RTE profile was cut at its centre in the axial direction with a 15° angle. The CTE profile has about an 8° angle between the suction surface and pressure surface. This angle has been generated by tapering the suction surface. If the total blade suction surface distance is defined between 0 and 1, in which 0 indicates the leading edge and 1 indicates the trailing edge. Based on this, the suction surface of the blade in the case of CTE was only tapered from 0.716 to 1. Therefore, the original throat area of the passage was unchanged for the CTE profile.

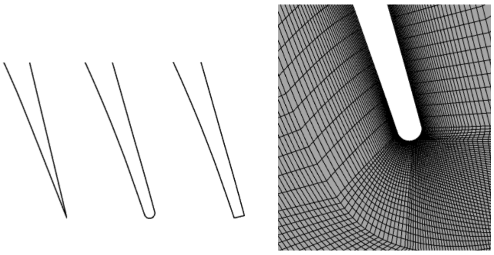
(a) (b)

Figure 1. (a) Blade trailing edge geometries: conic trailing-edge (left), semicircular trailing-edge (middle) and square trailing-edge (right) (b) grid generation around semicircular trailing-edge case.

The 2D-structured grid has been generated in the computational domain for all the cases. Moreover, the O-grid around the blade surfaces were generated as shown in Figure 1(b). Sufficiently fine grid was constructed around the leading and trailing edges of the stator to resolve the boundary layers. Moreover, the grid density close to the wall boundaries was refined to achieve smaller y^+ value. The computational grids of CTE case, RTE case, and STE case were contained around 39260, 40016, and 39875 cells. The sufficient grid density is essential to resolve the flow details [19]. In the present study, sufficiently finer grid is considered for all the cases. All the numerical calculations were performed with the steady state assumption. The conservation equations of the mixture of vapour and liquid phases were discretized applying the conservative finite-volume integration over a control volume with the multi-grid method. A second order upwind scheme was employed for the spatial discretization. The simulations presented in this work were converged to normalized RMS residuals of the order of 10^{-4} or lower.

Copyright © 2015 by ASME

4 RESULTS AND DISCUSSIONS

In the present work, the low inlet superheat experimental case named with L1 of White et al. [12] has been modeled. On the basis of the measurement data, L1 case with the inlet conditions P_{01} = 40.3 kPa, T_{01} = 354 K and outlet static pressure P_2 = 16.3 kPa were selected. The inflow angle was 0°.

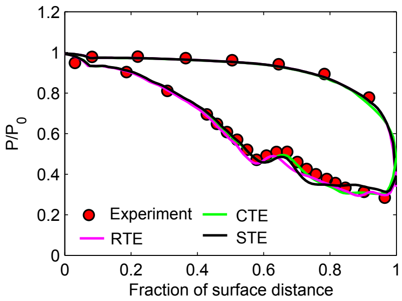

Figure 2. Blade surface pressure distribution comparison between predicted and measurements of White et al. [12].

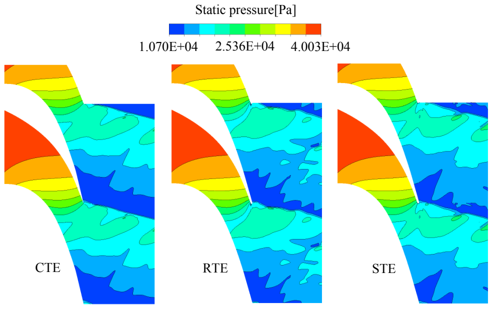

Figure 3. Predicted contours of the static pressure.

Figure 2 presents the comparison of the predicted pressure distribution around the blade surfaces with the experimental data of White et al. [12]. It shows that the static pressure distribution of the pressure side of the blade is not influenced with the trailing edge shapes. Moreover, all the cases modeled the correct location of the condensation. However, small discrepancy has been captured in the predicted pressure gradient on the suction side near the trailing edge between the selected trailing edge shapes. Particularly, the STE profile shows a slightly lower diffusion in the rear part of the blade. The predicted contours of static pressure by the CTE, the RTE, and the STE profiles are presented in Figure 3. It can be seen that the pressure distribution along the channel and in the downstream of passage is influenced with the trailing edge shapes. In the case of CTE profile the pressure distribution is influenced near the rear part of suction surface due to tapering. However, the highest expansion is observed in the cases of RTE particularly at the end of the pressure side (which is displayed with tiny region of blue colour). Therefore, the subcooling level is highest for the RTE profile which increases the nucleation rate. It has been known fact that the nucleating and growth processes are sensitive to the local pressure distribution and expansion rate [12]. The expansion rate varies in the blade passage, in which, it is relatively very low at the entrance and extremely high in the vicinity of the throat. As a consequence, the zone of rapid condensation occurs downstream of the throat, where the flow is bounded by solid surface. In condensing steam flows, the nucleation rate is especially large near the suction surface and at the trailing edge of the pressure surface. This happens due to the rapid acceleration and consequent high subcooling. Figure 4 shows the contours of the nucleation rate predicted by the CTE, the RTE, and the STE profiles. It can be seen that the nucleation rate is smaller and the nucleation region is longer in the mid-pitch region for all the cases. Moreover, in the case of CTE, the nucleation zone is extended more to the wake region of the blade. This

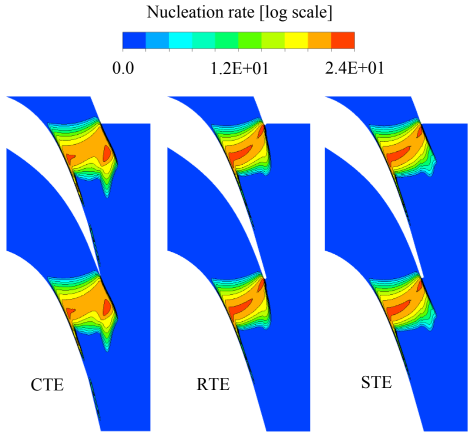

Figure 4. Predicted contours of the nucleation rate.

Copyright © 2015 by ASME

is resulted due to the suction surface tapering because the flow area near the rear part of trailing edge for the CTE profile is enlarged. The highest nucleation rate is observed in the case of RTE and the lowest nucleation rate is noted in the case of CTE. The variation in the pressure and velocity distribution near the trailing edge would induce a different droplet number distribution. The droplet number in the blade wake is higher than that in the mainstream. This happens due to the rapid deflection of steam on the pressure surface near the trailing edge where nucleation rate reaches its peak value as shown in Figure 4. Therefore, the droplet number carried into the blade wake region is greater than that in the mainstream. The distinct nucleation rates influence on the total number of droplets via distinct droplet growth rates. Therefore, the droplets number per unit volume is calculated and presented in Figure 5 for all the cases. The droplets number per unit volume is estimated at the traverse plane which is situated at the position of one fourth axial chord length away from the trailing edge in axial flow direction. It can be seen that the RTE profile predicted higher number of droplets than the other profiles due to lower growth rates. It is a fact that the droplet radius distribution across the passage is mostly dependent on the total number of droplets created during the nucleation process, which is influenced by the distinct expansion rates along the blade passage and also due to the interaction between the trailing edge shock waves and the nucleation zone. The predicted contours of the average droplet radius for all cases are presented in Figure 6. A higher nucleation rate can be related to a lower growth rate, i.e. if a large number of tiny liquid droplets nucleate, their growth will be lower. On the other side, when a lower nucleation occurs, the growth rate is predominant and larger droplets are present. Therefore, the CTE predicted higher droplet radius compared to the RTE and the STE cases. The RTE profile estimated relatively smaller droplet radius due to higher number of droplets per unit volume. Moreover, for all the cases, the droplet average radius is lower in the blade wakes. This appears because the temperature is relatively higher in the blade wakes, which prevents the droplet growth. This phenomenon yielded the cyclic patterns of the droplet sizes in the downstream of the flow.

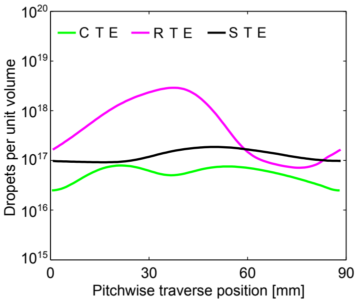

Figure 5. Predicted results of droplets per unit volume.

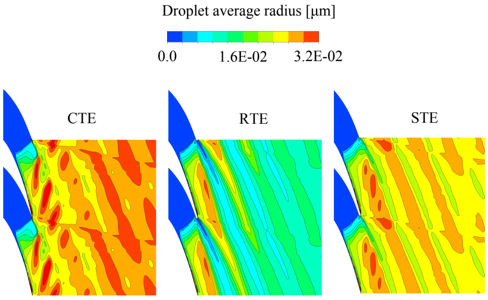

Figure 6. Predicted contours of droplet average radius.

Furthermore, the average droplet radius along the pitchwise traverse position at four different distances from the trailing edge of the blade has been compared (Figure 7). It is clear that the RTE profile has smaller sizes of droplets and the CTE profile has much larger droplet radii (nearly twice the value of the RTE profile). It is a fact that, the liquid phase generation is influenced by the local rate of change of the pressure fields. Perhaps it is worthwhile to check the influence of the trailing edge shapes on the wetness prediction. Therefore, the average wetness fractions predicted by the CTE, the RTE, and the STE profiles at downstream of the cascade were calculated and wetness trends are presented in Figure 8. It can be seen that the average wetness is decreased gradually as move to the downstream of the cascade for all cases. The average wetness fractions estimated by the CTE and the RTE are very similar. The STE profile predicted relatively higher wetness than the other profiles from the blade wake to the far downstream. However, at the outlet, marginal variation has been captured between all profiles. The explanation for the variation in the droplet sizes and the wetness fraction is associated with the rate of pressure change (expansion) in the flow field.

Figure 9(a) shows the Schlieren image of the L1 case, which is the reproduced image of the original experimental photograph of White et al. [12]. It has been adopted from Senoo and White [21]. In Figure 9(a), the condensation shock, pressure side shock, and suction side shock are marked with S_c, S_p, and S_s, respectively. The red, orange, and yellow colours indicate the expan-

Copyright © 2015 by ASME

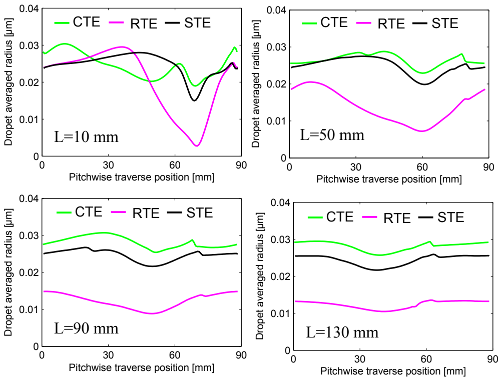

Figure 7. Predicted results of the droplet average radius at downstream of the cascade. L represents the distance from the trailing edge of the blade.

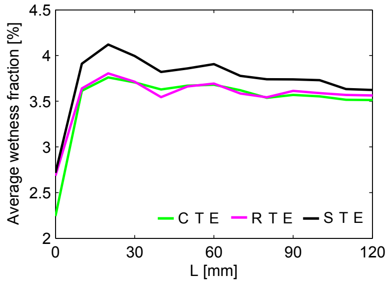

Figure 8. Predicted results of the average wetness fraction at downstream of the cascade. L is the distance from the trailing edge of the blade.

sion phenomenon, while light blue and green colours represent small values of the compression. It can be seen that the oblique shock profile is little bit curved across the central blade passage. The S_p interacts and merges with the S_c across the central blade passage. Moreover, the low base pressure is generated immediately behind the trailing edge, and the flow is expanded around the trailing edge, and then decompressed by a strong shock wave at the point where the suction and pressure side flows meet. This phenomenon is observed in all the cases of the predicted density gradient contours as well (Figure 9(b), (c), and (d)). However, the intensity of S_p predicted by the CTE profile was marginally lower than those of the RTE and the STE profiles. In the case of RTE profile, the intensity of S_p is highest than other profiles which contributes to the suction side boundary layer generation. Moreover, in the cases of CTE and RTE, some reflections have been observed that interact with the S_s. However, these reflections were not generated from the outlet boundary but they were generated somewhere from the downstream. It seems that the wake is hitting to the reflected shockwave and which causing this disturbance. It may also be possible that the trailing shapes influence the shock waves structure generated at the trailing edge and its angles. It is slightly difficult to find exact information about the angles between them. However, in this work, the angle of S_s w.r.to blade wake has been calculated for all profiles, which are $\theta_{\mathrm{CTE}} \approx 48^\circ$, $\theta_{\mathrm{RTE}} \approx 52^\circ$, and $\theta_{\mathrm{STE}} \approx 58^\circ$. Here, the indicated subscripts CTE, RTE, and STE represents the corresponding profiles that are the CTE, the RTE, and the STE, respectively.

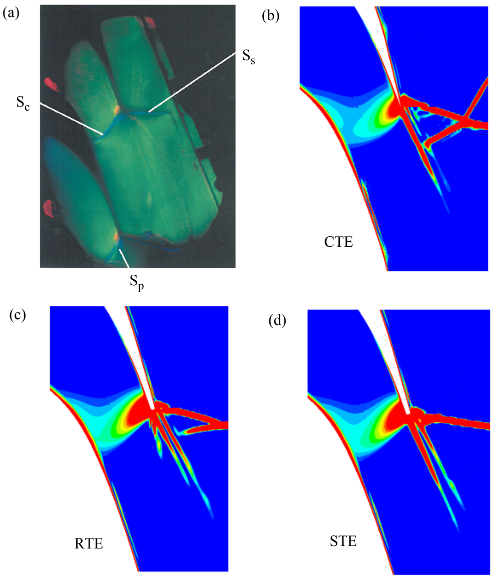

Figure 9. (a) Reproduced image of the original experimental photograph of Schlieren graph of the L1 case of White et al. [12] compared with predicted density gradients of the (b) CTE (c) RTE, and (d) STE cases.

In supersonic flow, there are some known influential phenomena for example shock waves, mixing, etc., which would

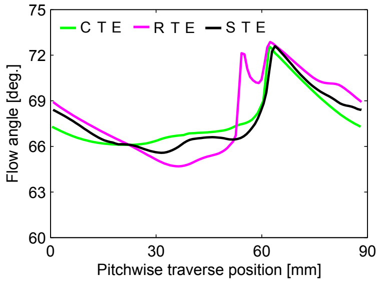

Figure 10. Predicted results of flow angle at the outlet of cascade.

have some impact on the flow angle. Therefore, the flow angle at the outlet of the cascade has been calculated and presented in Figure 10. It can be seen that the RTE profile predicted lower flow angle particularly in the wake region (i.e. between 25 mm to 40 mm at pitchwise traverse position in Figure 10), while the CTE profile yielded a higher value there. The maximum value of the flow angle in all the cases has been captured at about 70 mm at pitchwise traverse position due to shockwave interaction.

In addition, White et al. [12] provided test data of the static pressure, wetness fraction, and normalized entropy at a specific location at downstream. Therefore, it is possible to compare the predicted and the experimental results at traverse plane. The traverse plane is situated at the position of one fourth axial chord length away from the trailing edge in axial flow direction (see Figure 11 (upper most)). The predicted pitchwise distribution of the static pressure, wetness fraction, and normalized entropy at the traverse position are compared with the experimental data in Figure 11. The predicted trends are in good agreement with the experiments. However, for all profiles, the steep location has been changed in the static pressure and wetness fraction between 75 mm to 85 mm due to the interaction of the shock wave S_s at the traverse plane. Also, the variation in the steep location in each cases resulted due to dissimilarity in the shock wave angle as discussed above. The wetness fraction is relatively lower between 35 mm to 45 mm at the traverse position because in this region the trailing edge wake flow passes the traverse plane. This is the region of higher mixing. Therefore, temperature is comparatively higher, which causes a lower wetness fraction. Generally good trends of non-dimensional entropy have been captured by all trailing edge profiles with the experiments of White et al. [12]. However, some discrepancy has been observed between the predicted results, particularly in the wake region. The CTE profile has a lower value of non-dimensional entropy than the RTE and STE profiles.

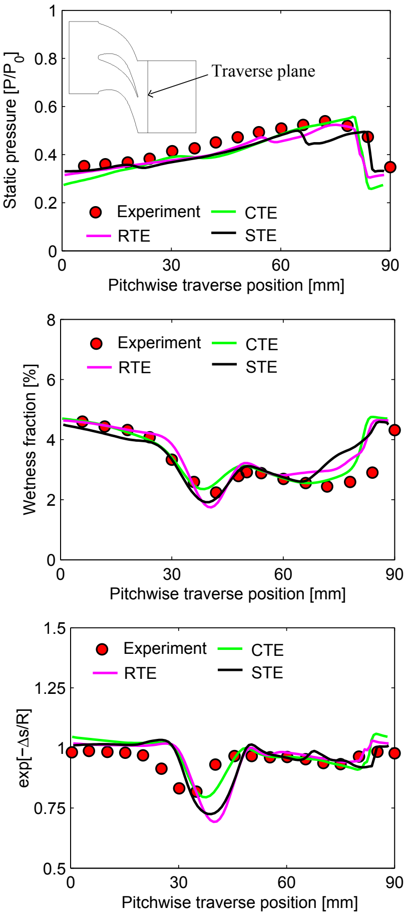

Figure 11. Predicted results of static pressure (upper), wetness fraction (middle), non-dimensional entropy (lower) compared with the experiments of White et al. [12].

The entropy generation occurs due to three main processes: (i) viscous friction (either in boundary layers or in free shear layers), (ii) heat transfer, and (iii) non-equilibrium processes (occur in very rapid expansions or in shock waves) [22]. Regarding to the entropy generation and flow mixing in the wake, the trailing edge shape is one of the main parameters. Figure 12 shows the contours of the turbulent kinetic energy predicted by the CTE, the RTE, and the STE profiles. It is a fact that the STE profile has relatively higher turbulent kinetic energy due to strong wake than the RTE profile, while the CTE profile predicted very low turbulent kinetic energy. The turbulent kinetic energy in the wake region will subsequently dissipate by viscous effects. Moreover, the flow mixing contributes to the entropy generation. Therefore, the local entropy generation rates are considerably high in the wakes, at the edges of separated regions, and in vortices, in which the shearing rates are relatively high. Figure 13 shows the predicted contours of entropy for all cases. It appears that the CTE profile predicted the lowest entropy generation compared to other cases.

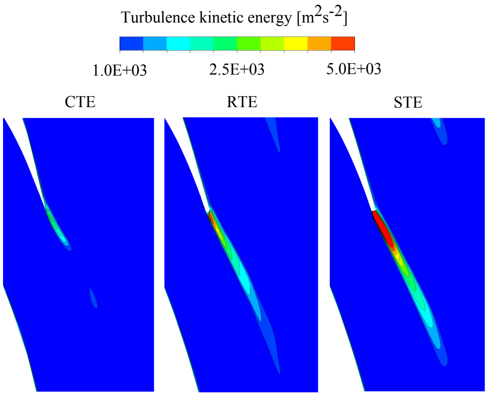

Figure 12. Predicted contours of turbulence kinetic energy.

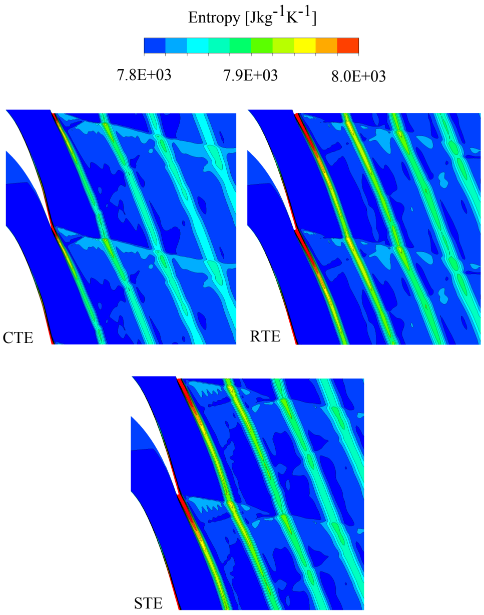

Figure 13. Predicted contours of entropy.

The prime objective of turbomachinery designers is to improve the performance by increasing the efficiency. Any cutback in the efficiency of turbomachinery caused by the flow is termed loss. One objective of this paper was to analyze the influence of trailing edge shapes on the loss mechanism of condensing steam flow. Moreover, White et al. [12] presented information about the losses that occur due to the irreversible heat and mass transfer during the condensation process. Therefore, in the present work, the Markov energy loss coefficient based on the entropy increase has been calculated. The Markov energy loss coefficient is defined as $\zeta = \frac{T_2 \cdot \Delta s}{0.5 v_2{}^2}$. White et al. [12] divided the loss coefficients into three components: (i) viscous loss, (ii) shockwave plus wetness loss, and (iii) mixing loss. Detailed information pertaining to the losses evaluation can be found from White et al. [12]. Figure 14 presents the comparison between the computed and measured Markov loss coefficients for L1 case and H3 case. The H3 case is the high inlet superheat case that has ΔT_{01} = 26.0 K. The inlet conditions of H3 case were P_{01} = 41.4 kPa and T_{01} = 376 K, while the outlet static pressure, P_2, was 19.4 kPa. The main purpose for H3 case selection was to check the influence of the trailing edge profiles on the losses.

The magnitude of mixing loss increases with high Mach numbers. Therefore, the mixing loss of the L1 case is relatively higher than the H3 case. As presented before that the S_p merges with the S_c, and it thicken the suction side boundary layer onto the suction side of the adjacent blade. Therefore, it increases the viscous losses. The intensity of S_p shock wave for the RTE profile is relatively higher than other cases. This could be the explanation of higher viscous loss prediction in the case of RTE profile. It can be seen that the CTE profile predicted low value of shock plus wetness loss than the RTE and STE profiles both for L1 and H3 cases. It is interesting to note that the magnitude of shock plus wetness losses predicted by the RTE and STE profiles for L1 and H3 cases are almost in the same range. Moreover, it is observed that the value of the mixing loss for the STE profile was higher due to stronger wake than those of the other profiles. The

Copyright © 2015 by ASME

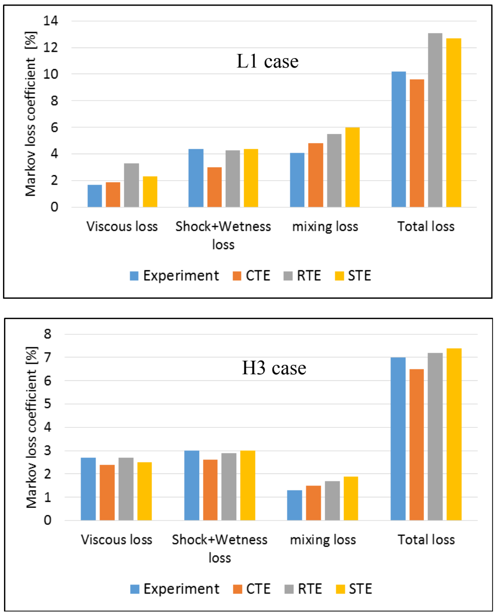

Figure 14. Predicted Markov loss coefficients compared with the experiments of White et al. [12].

explanation for the higher value of mixing loss in the STE profile is associated with the higher entropy generation in the wake region as shown in Figure 13. The CTE profile predicted relatively smaller total loss than the RTE and STE profiles for L1 and H3 cases.

5 CONCLUSIONS

This study emphasized the influence of the trailing edge geometry on the non-equilibrium homogeneously condensing steam flow in the stationary cascade of turbine blades. The experimental test cases of White et al. [12] were used as the reference. In this study, the two-phase vapour-liquid mixture was modeled adopting the Eulerian-Eulerian approach by means of ANSYS Fluent 14.5 CFD code. The condensation phenomena were simulated on the basis of the classical nucleation theory, and the steam properties were calculated by the real gas model.

Three trailing edge geometries were considered. The conic trailing edge was generated with 8° degree wedge angle by tapering the suction surface. The presented analysis exhibits that the conic trailing edge has a very different pressure gradient particularly at the suction surface near trailing edge which makes the biggest contribution to the nucleation rate. Based on the presented results, it can be conclude that the nucleation region and nucleation rate have been influenced due to the variation in trailing edge geometries. Moreover, the droplet sizes are much sensitive to the trailing edge shapes. The conic trailing edge estimated bigger droplet radius than the other cases, while semi-circular trailing edge predicted the smallest droplet sizes. The trailing shapes influenced also on the wetness fraction, on the shock waves structure generated at the trailing edge and its angles, and on the flow angle. Additionally the entropy generation and flow mixing in the wake were influenced due to the trailing edge shapes.

Based on the presented information of the losses by White et al. [12], the Markov energy loss coefficients were calculated for the low inlet superheat case and for the high inlet superheat case. It can be concluded that the cascade loss coefficients are sensitive to the trailing edge shapes. The conic trailing edge predicted lower value of total loss than other selected shapes.

Further work will concentrate on the influence of the pressure surface tapering in the case of turbine cascade flow. Also the influence of the trailing edge thickness, its size and shape in the case of stator-rotor turbine cascade flows will be studied.

ACKNOWLEDGEMENTS

The authors would like to acknowledge the Finnish Cultural Foundation and Academy of Finland for the financial support.

REFERENCES

[1] Wegener, P. P., 1975. *Non-eqnilibrium Flow with Condensation*. Acta Mech. 21 (1-2), pp. 65-91.

[2] Simpson, D. A., and White, A. J., 2005. “Viscous and unsteadyflow calculations of condensing steam in nozzles”. *Int. J. Heat and Fluid Flow,* **Vol. 26 (1)**, pp. 71–79.

[3] White, A., 2000. “Numerical investigation of condensing steam flow in boundary layers”. *Int. J. Heat and Fluid Flow,* **Vol. 21**, pp. 727–734.

[4] Winkler, G., and Schnerr, G., 2001. “Nucleating unsteady flows in low-pressure steam turbine stages”. *Proc. Instn. Mech. Eng.,* **Vol. 215 (A)**, pp. 773–781.

[5] Kermani, M., and Gerber, A., 2003. “A general formula for the evaluation of thermodynamic and aerodynamic losses in nucleating steam flow”. *Int. J. Heat Mass Transfer,* **Vol. 46 (17)**, pp. 3265–3278.

[6] Stein, A., Hofer, D. C., Filippenko, V., and Slepski, J., 2010. “Aerodynamic design of transonic tip sections”. In Proc. ASME Turbo Expo, GT2010-22165, Glasgow, UK, June 14-18, pp. 1-10.

[7] D.Torre, Vázquez, R., Armañanzas, L., Partida, F., and García-Valdecasas., G., 2012. "The effect of airfoil thickness on the efficiency of lp turbines". In Proc. of ASME Turbo Expo, GT2012-68556, Copenhagen, Denmark, June 11-15, pp. 1-10.

[8] Zhou, C., Hodson, H., and Himmel, C., 2014. "The effects of trailing edge thickness on the losses of ultrahigh lift low pressure turbine blades". *J. Turbomach.,* **Vol. 136 (8)**, pp. 081011–1–9.

[9] Singh, U., 2001. "A study of the effects of geometrical changes on wetness in low pressure steam turbine". In The 4th European Conference on Turbomachinery, Firenze, Italy, pp. 823-841.

[10] Bakhtar, F., Ebrahimi, M., and Webb, R., 1995. "On the performance of a cascade of turbine rotor tip section blading in nucleating steam, part 1: surface pressure distributions". *Proc. Inst. Mech. Eng. Part C: J. Mech. Eng. Sci.,* **Vol. 209**, pp. 115–124.

[11] An, L., Wang, Z., and Han, Z., 2009. "Numerical study and control method of interaction of nucleation and boundary layer separation in condensing flow". *Front. Energy Power Eng. China,* **Vol. 3 (3)**, pp. 254–261.

[12] White, A. J., Young, J. B., and Walters, P. T., 1996. "Experimental validation of condensing flow theory for a stationary cascade of steam turbine blade". *Philos. Trans. Roy. Soc. Lond.,* **Vol. A 354**, pp. 59–88.

[13] Young, J. B., 1988. "An equation of state for steam for turbomachinery and other flow calculations". *J. Eng. Gas Turbines Power,* **Vol. 110**, pp. 1–7.

[14] Frenkel, J., 1946. *Kinetic Theory of Liquids*. Oxford University Press, New York.

[15] Ishizaka, K., Ikohagi, T., and Daiguji, D., 1995. "A high-resolution numerical method for transonic nonequilibrium condensation flows through a steam turbine cascade". In Proc. of 6th International Symposium on Computational Fluid Dynamics, pp. 479-484.

[16] Young, J. B., 1992. "Two-Dimensional nonequilibrium wet steam calculations for nozzles and turbine cascades". *ASME J. Turbomachinery,* **Vol. 114**, pp. 569–579.

[17] Hill, P. G., 1966. "Condensation of water vapour during supersonic expansion in nozzles". *J. Fluid Mech.,* **Vol. 25**, pp. 593–620.

[18] Young, J. B., 1982. "The spontaneous condensation of steam in supersonic nozzles". *Physico Chemical Hydrodynamics,* **Vol. 3**, pp. 57–82.

[19] Patel, Y., Turunen-Saaresti, T., Patel, G., and Grönman, A., 2014. "Numerical investigation of turbulence modelling on condensing steam flows in turbine cascade". In Proc. of ASME Turbo Expo, GT2014-26307, Düsseldorf, Germany, June 16-20, pp. 1-14.

[20] Menter, F. R., 1994. "Two-equation eddy-viscosity turbulence models for engineering applications". *AIAA Journal,* **Vol. 32 (8)**, pp. 1598–1605.

[21] Senoo, S., and White, A. J., 2012. "Non-equilibrium unsteady wet-steam condensation modelling: computations in a steam turbine cascade and a nozzle". In Proc. The Cambridge Baumann Centenary Conference on Wet Steam Flows, BCC-2012-07, University of Cambridge, CD-ROM.

[22] Denton, J. B., 1993. "Loss meachanisms in turbomachines". *ASME J. Turbomachinery,* **Vol. 115**, pp. 621–650.

Copyright © 2015 by ASME

Publication V

Patel, Y., Patel, G., and Turunen-Saaresti, T. (2016).
Influence of turbulence modelling to condensing steam flow in the 3D low-pressure steam turbine stage.

Reprinted with permission from
Proceedings of ASME Turbo Expo 2016:
Turbomachinery Technical Conference and Exposition.
pp. 1-11.
© ASME, 2016

Proceedings of ASME Turbo Expo 2016: Turbomachinery Technical Conference and Exposition
GT2016
June 13 – 17, 2016, Seoul, South Korea

GT2016-57590

INFLUENCE OF TURBULENCE MODELLING TO CONDENSING STEAM FLOW IN THE 3D LOW-PRESSURE STEAM TURBINE STAGE

Yogini Patel*
Laboratory of Fluid Dynamics
School of Energy Systems
Lappeenranta University of Technology
Lappeenranta, Finland
Email: yogini.patel@lut.fi

Giteshkumar Patel
Laboratory of Fluid Dynamics
School of Energy Systems
Lappeenranta University of Technology
Lappeenranta, Finland
Email: giteshkumar.patel@lut.fi

Teemu Turunen-Saaresti
Laboratory of Fluid Dynamics
School of Energy Systems
Lappeenranta University of Technology
Lappeenranta, Finland
Email: teemu.turunen-saaresti@lut.fi

ABSTRACT

With the tremendous role played by steam turbines in power generation cycle, it is essential to understand the flow field of condensing steam flow in a steam turbine to design an energy efficient turbine because condensation at low pressure (LP) turbine introduces extra losses, and erosion in turbine blades. The turbulence has a leading role in condensing phenomena which involve a rapid change of mass, momentum and heat transfer. The paper presents the influence of turbulence modelling on non-equilibrium condensing steam flows in a LP steam turbine stage adopting CFD code. The simulations were conducted using the Eulerian-Eulerian approach, based on Reynolds-averaged Navier-Stokes equations coupled with a two equation turbulence model, which is included with nucleation and droplet growth model for the liquid phase. The SST k-ω model was modified, and the modifications were implemented in the CFD code. First, the performance of the modified model is validated with nozzles and turbine cascade cases. The effect of turbulence modelling on the wet-steam properties and the loss mechanism for the 3D stator-rotor stage is discussed. The presented results show that an accurate computational prediction of condensing steam flow requires the turbulence to be modelled accurately.

Nomenclature

h_{lv}	specific enthalpy (J kg^{-1})
H	total enthalpy(J kg^{-1})
I	nucleation rate (m^{-3} s^{-1})
M	mass generation rate (kg m^{-3} s^{-1})
M_m	droplet mass (kg)
P	pressure(Pa)
r	radius (m)
r_*	critical radius (m)
R	gas constant (J kg^{-1} K^{-1})
S_d	mass source term (kg m^{-2} s^{-1})
S_E	energy source term (W m^{-3})
$S_{F,m}$	momentum source term (kg m^{-2} s^{-2})
t	time (s)
T	temperature (K)
u	velocity component (m s^{-1})

Greek Letters

α	phase volume fraction
Γ_E	thermal diffusion coefficient (W m^{-1} K^{-1})
η	number of liquid droplets per unit volume (m^{-3})
μ	dynamic viscosity ($kg/m \cdot s$)
ρ	density (kg m^{-3})
σ	liquid surface tension (N m^{-1})
τ	viscous stress tensor (Pa)
τ_p	droplet response time (s)

---

*Corresponding author

Copyright © 2016 by ASME

Subscript

d	droplet index
i, j	cartesian tensor notation
l	liquid phase
v	vapour phase
x	cartesian coordinate
$0, 1, 2$	total, inlet, outlet conditions

1 INTRODUCTION

Today, steam turbines play an important role in the global power production. Thus, the advancement and understanding of technologies relevant to enhancing the general performance of steam turbines is important in order to meet the global electricity demand. However, due to the comparatively low efficiency of low pressure (LP) turbine stages, the research concerning LP stages is of special importance for the scientific community, steam turbine vendors and power plant owners. Particularly, in penultimate stages of LP turbine, the temperature of superheated vapour decreases due to rapid expansion and a condensation process takes place shortly after the state path crosses the vapour-saturation line. The expansion process causes the superheated dry steam to first subcool and then nucleate to form a two-phase mixture of saturated vapour and fine liquid droplets which is generally known as wet-steam. The presence of the liquid phase within the turbine causes irreversible thermodynamic losses, aerodynamic losses and mechanical losses or erosion. For more than a century, extensive studies of condensing steam flows have been executed by numerous researchers experimentally, theoretically and numerically. However, the experimental facilities for wet-steam flows are in short supply throughout the world. Additionally, the precise measuring of essential parameters (e.g., droplet size and its distribution, wetness fraction, etc) of these flows is very challenging and, therefore, the numerical simulations of the condensing steam flows are the most feasible option.

Turbine flows involve very intricate flow phenomena including flow transition, flow separation and mixing due to stator-rotor interaction, and turbulence is involved in all these phenomena. Moreover, the role of turbulence in wet-steam flows is significant in the processes of phase change, momentum and heat transport either at main flow regions or in boundary layers on the solid walls, particularly on the possible deposition of condensed liquid droplets. Consequently, it is essential to simulate turbulence in wet-steam flow precisely, as the ignorance of turbulence modelling to condensing steam flow calculation may cause an erroneous appraisal of key phenomena and eventually result in the modelling of erroneous losses.

In recent years, 3D numerical modelling of wet-steam flow across LP turbine including multistage blade rows has become feasible because of immense improvement in computational power for computational fluid dynamics (CFD) calculations. Nevertheless, in literature the work regarding 3D steady/unsteady CFD simulations is rather sparse. A few works e.g., [1] and [2], exists, in which CFD simulations on condensing steam flows through multistage stator-rotor cascade channels of a LP steam turbine with non-equilibrium and equilibrium condensations are presented. [3] presented numerical results of wet-steam flow with a three stage LP steam turbine test rig, in which the effect of different theoretical models for nucleation and droplet growth were examined. Further, the effect of droplet size on the deposition characteristics of the last stage stator blade and also the effect of inter-phase friction on flow field were studied by [4]. However, reported work concerning the influence of turbulence on the condensing steam flow at 3D turbine stage/stages is not available. Only few publications are available e.g., [5] and [6] in which authors conducted an analysis of turbulence modelling influence to wet-steam flow considering 2D nozzles and stator turbine cascade.

This work is the continuation of the previous works. In previous studies of [7], the influence of turbulence modelling to 2D nozzle and stator cascade flows was analyzed. Also, its corresponding influence on loss mechanism was presented. In the present work, the numerical investigation of turbulence modelling effect on condensation phenomena is extended to 3D stator-rotor stage. For this purpose, only steady state simulations were performed using a mixing plane as interface between stator and rotor domain by neglecting the interaction between the stator wakes and the rotor blade. The Eulerian-Eulerian approach has been used to model two-phase flow. In this work, the performance of modified shear-stress transport (SST) k-ω turbulence model is demonstrated with the SST k-ω turbulence model. The significance of turbulence modelling on the loss mechanism in 3D stator-rotor stage is discussed as well.

2 NUMERICAL METHODOLOGY

In this paper, all the presented results were obtained by means of the ANSYS CFX. The real gas properties were evaluated from the IAPWS-IF97 formulation in which the thermodynamic properties of steam in the subcooled region were calculated by means of extrapolations from the superheated region.

2.1 Governing equations

The mass conservation equations for vapour and liquid phases are written as follows, respectively,

$$\frac{\partial}{\partial t}(\rho_v \alpha_v) + \frac{\partial}{\partial x_j}(\rho_v \alpha_v u_{j_v}) = -\sum_{\mathrm{d}=1}^{\mathrm{D}} \mathrm{S_d} - \sum_{\mathrm{d}=1}^{\mathrm{D}} m^* \alpha_v \mathrm{I}_d, \qquad (1)$$

$$\frac{\partial}{\partial t}(\rho_l \alpha_l) + \frac{\partial}{\partial x_j}(\rho_l \alpha_l u_{j_l}) = \sum_{\mathrm{d}=1}^{\mathrm{D}} \mathrm{S_d} + \sum_{\mathrm{d}=1}^{\mathrm{D}} m^* \alpha_v \mathrm{I}_d. \qquad (2)$$

Here, m^* is the mass of stable nucleus. To estimate liquid phase, a separate equation was used to calculate droplet numbers which can be written as

$$\frac{\partial}{\partial t}(\rho_l \eta) + \frac{\partial}{\partial x_j}(\rho_l \eta u_{j_l}) = \rho_l \alpha_v \mathrm{I}_l. \qquad (3)$$

In an LP turbine, more than 90% of the total mass concentration of the liquid phase consists of a very large number of very fine droplets having sub-micron size [8]. However, due to the negligible drag effect of liquid droplets on vapour phase it could be considered that all the phases flow at the identical velocity field. Therefore, in this work, only one momentum equation was used. The momentum equation of vapour phase was based on the Reynolds-averaged Navier-Stokes (RANS) equations which can be written as

$$\frac{\partial}{\partial t}(\rho_v \alpha_v u_{i_v}) + \frac{\partial}{\partial x_j}(\rho_v \alpha_v u_{i_v} u_{j_v}) = -\alpha_v \frac{\partial P}{\partial x_i} + \frac{\partial}{\partial x_j}(\alpha_v \tau_{ij_v}) + \mathrm{S_{F,m}}. \qquad (4)$$

The energy conservation equation for the vapour phase was written as

$$\frac{\partial}{\partial t}(\rho_v \alpha_v H_v) + \frac{\partial}{\partial x_j}(\rho_v \alpha_v u_{j_v} H_v) = -\alpha_v \frac{\partial P}{\partial t} + \frac{\partial}{\partial x_j}\left(\alpha_v \Gamma_E \frac{\partial T_v}{\partial x_j}\right) + \frac{\partial}{\partial x_j}(\alpha_v u_{i_v} \tau_{ij_v}) + \mathrm{S_E}, \qquad (5)$$

More details pertaining to the governing equations and their source terms can be found in [9].

2.2 Nucleation and droplet growth model

The phase change phenomenon in condensing steam flow involves two main processes viz., nucleation and droplet growth. In this work, the nucleation rate was obtained from the classical theory of non-isothermal homogeneous condensation given by [10] which can be written as,

$$\mathrm{I} = \frac{q_c}{(1+\theta)}\left(\frac{\rho_v^2}{\rho_l}\right)\sqrt{\frac{2\sigma}{M_m^3 \pi}}\, e^{-\left(\frac{4\pi r_*^2 \sigma}{3K_b T}\right)}. \qquad (6)$$

Here, q_c is a condensation coefficient, K_b is the Boltzmann's constant and θ is the non-isothermal correction factor which has been adopted from [11]. The droplet growth rate equation of [12] was utilised and can be expressed as,

$$\frac{dr}{dt} = \frac{k_v}{r(1+cK_n)} \cdot \frac{(T_l - T_v)}{(h_v - h_l)\rho_l}, \qquad (7)$$

where, K_n is the Knudsen number, c is the empirical factor, which is 3.18, and k_v is the thermal conductivity. More details on droplet growth rate can be found in [9].

2.3 Turbulence models

In the present work, the SST k-ω turbulence model was employed for modelling the flow turbulence. Due to the very small sizes of droplets in the vapour phase, the direct effect of liquid droplets on the flow turbulence was not considered. However, an indirect influence exists though the velocity field introduced to the turbulence models. Particulary, the vapour phase turbulence could influence the dispersion of the liquid droplets. Due to the relatively small mass concentrations and sizes of droplets, the turbulence equations were calculated for the mixture of the vapour and liquid phases. The transport equations for the turbulent kinetic energy, k, and its specific rate of dissipation, ω, can be written as [13],

$$\frac{\partial}{\partial t}(\rho k) + \frac{\partial}{\partial x_j}(\rho u_j k) = \frac{\partial}{\partial x_j}\left[\left(\mu + \frac{\mu_t}{\sigma_k}\right)\frac{\partial k}{\partial x_j}\right] + P_k - \acute{\beta}\rho k \omega + P_{kb} + S_k, \qquad (8)$$

$$\frac{\partial}{\partial t}(\rho \omega) + \frac{\partial}{\partial x_j}(\rho u_j \omega) = \frac{\partial}{\partial x_j}\left[\left(\mu + \frac{\mu_t}{\sigma_\omega}\right)\frac{\partial \omega}{\partial x_j}\right] + \alpha \frac{\omega}{k} P_k - \beta \rho \omega^2 + P_{\omega b} + S_\omega. \qquad (9)$$

Here, P_k indicates the production rate of turbulence due to viscous forces, P_{kb} and $P_{k\omega}$ represent the buoyancy turbulence terms for k and ω equations, respectively. The model constants were considered as: $\alpha = \frac{5}{9}$, $\beta = 0.075$, $\acute{\beta} = 0.09$, $\sigma_k = 2$, and $\sigma_\omega = 2$. The turbulent viscosity, μ_t, is defined in the SST k-ω turbulence model as

$$\mu_t = \frac{a_1 \rho k}{max(a_1 \omega, SF_2)}, \qquad (10)$$

where a_1 is the model constant, S is the strain rate magnitude and F_2 is the blending functions. In this work, the SST k-ω turbulence model was modified in the manner described in the previous work of [7]. The SST k-ω turbulence model was modified

Copyright © 2016 by ASME

to include the modulation of turbulence kinetic energy due to liquid droplets via source terms (i.e., S_k and S_ω in Eqs. (8) and (9), respectively). Therefore, the added source terms introduce an extra turbulent kinetic energy and its dissipation to the flow via the acceleration/deceleration of the droplets. These modifications directly influence on turbulent viscosity and Reynolds stresses. In such a way momentum and energy transport equations will be affected. Furthermore, the definition of μ_t was modified by means of an expansion procedure for resolving implicit algebraic equations for the Reynolds stress tensor in terms of mean velocity gradients. The modified turbulent viscosity term including turbulence production to dissipation ratio can be written as

$$\mu_t = \frac{a_1 \rho k}{max(a_1 \omega, SF_2)} \frac{C1}{C1 + \left[\frac{P_k}{\omega\beta^* k - 1}\right]}, \tag{11}$$

where C_1 defines the Rotta return-to-isentropy approximation of the pressure-strain correlation. Here S_k represents the addition of turbulent kinetic energy including the effect of liquid mass generation and droplet response time which can be expressed as $S_k = \frac{4M}{\tau_p}(1 - f_u)k$, where f_u indicates the coefficient of droplet response to the fluid velocity fluctuations. The term S_ω can be written as $S_\omega = C_2 \omega \beta^* S_k$, where C_2 and β^* are the model constants. More details about model constants and corresponding closer relations of these modification are discussed in [7]. The abovementioned modifications were implemented by the authors within the CFD code using user defined subroutines.

3 COMPUTATIONAL GRID AND NUMERICAL DETAILS

To study the influence of turbulence modelling on condensing steam flow in a LP turbine, a 3D stator-rotor stage was used. The used stator vane is the stator cascade of White [14]. However, the utilised rotor blade is not that of a real turbine geometry. It was intended to be representative of 25% of reaction for rotor at mid span. The stator blade row consisted of 30 blades while the rotor blade row included 31 blades. The blade height of stator and rotor outlet was 76 mm and 126.5 mm, respectively. However, for the sake of simplicity, both blade profiles had constant radial thickness without twisting. Moreover, the domain was modelled without rotor tip clearance in order to exclude the influence of tip swirls on the flow. The flow inlet condition was set as: $P_0 = 40300$ Pa, $T_0 = 354$ K which are the similar inlet flow conditions as of [14]. Only single passage of stator and rotor was modelled employing a periodic boundary condition in the circumferential direction. An adiabatic no-slip wall boundary was defined at the blade surfaces and at the domain walls. The computational grid is displayed in Figure 1. The grid quality/density near solid boundaries is very important to precisely resolve boundary layers. Therefore, the grid distribution near the solid surfaces was fine enough to achieve sufficiently smaller y^+ value i.e $y^+_{stator} = 3.5$ and $y^+_{rotor} = 2.5$. An O-grid was generated near to the blade surfaces with boundary layers meshing. Moreover, the grid was more refined around the leading and trailing edges of the stator and rotor blades. Based on the previous experiences of the conducted grid independence study for 2D stator cascade case, an adequate grid refinement was assumed for this case. The computational grid included about 2.87 million hexahedral cells. All the simulations were based on finite-volume discretization and the solution of the RANS equations was done with a coupled solver. The advection was treated with high resolution scheme. Furthermore, flow turbulence models, volume fraction and energy equations were calculated using high resolution methodology. An automatic wall treatment was utilised, which provides an automatic switching from a low-Reynolds number formulation to a wall function treatment based on grid spacing near to the wall surfaces.

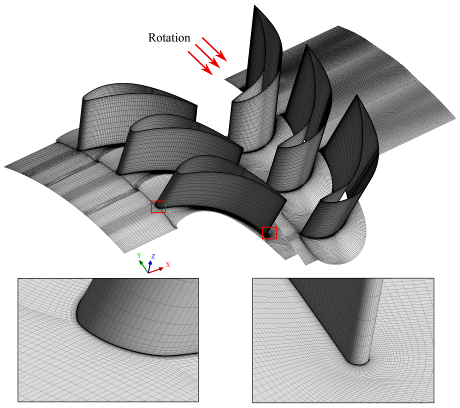

Figure 1. The computational grid.

4 RESULTS AND DISCUSSIONS

Firstly, the performance of SST k-ω and modified SST k-ω (MSST k-ω) turbulence models were examined with the nozzle cases of [15] and [16], and also with the steam turbine stator cascade case of [14]. In Figure 2, it can be seen that both models predicted accurate pressure distributions, and the location and magnitude of the condensation shock, and yielded good correspondence with the experiments for both nozzles. Furthermore, the agreement between the predicted and the measured mean droplet radius size at the specified exit location is reasonably good for the Nozzle A of [15] for both models. However, some variation has been observed for the [16] nozzle case.

Copyright © 2016 by ASME

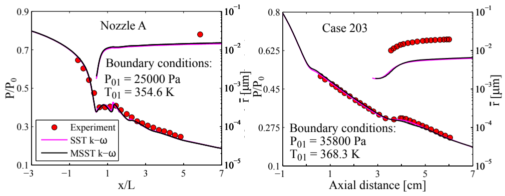

Figure 2. Comparison between the predicted and the measured data of [15] (left) and [16] (right).

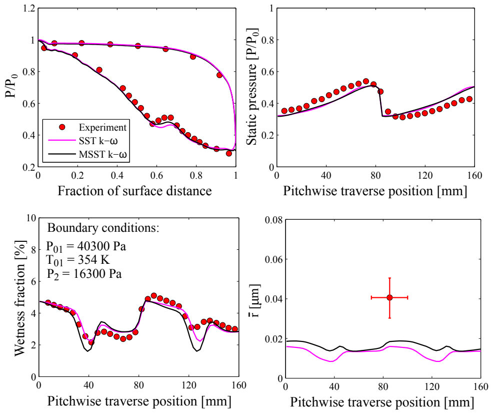

Figure 3. Comparison between the predicted and the measured data of [14] for the L1 case.

Further, the low inlet superheat experimental case named L1 of [14] has been modelled. The comparison between the predicted results of the SST k-ω model, the MSST k-ω model and the measured data is shown in Figure 3. The traverse plane is situated at the position of one fourth axial chord length from the trailing edge in axial flow direction. It can be seen that both models yielded correct trends of pressure distribution on blade surfaces. However, the MSST k-ω model estimated the correct location and intensity of the condensation disturbance on the suction side compared to the SST k-ω model. The predicted trends of static pressure and wetness fraction at traverse plane by both models are in good agreement with the experiments. Nevertheless, some discrepancy has been noted for mean droplet radius prediction.

It is fact that the flow in LP turbine has a strong three-dimensional nature due to the arrangements of stator and rotor blade rows. Moreover, the stator-rotor interaction strongly influences the flow phenomena. The wakes of stator blades enter the succeeding rotor blades, in which the flow is accelerated and rotated. Therefore, the accurate computational prediction of LP turbine flows requires the turbulence to be accurately modelled. Firstly, the influence of turbulence modelling has been analyzed with the turbulence properties. Figure 4 presents the contours of turbulence kinetic energy yielded by both models at 90% span. It is obvious that the maximum turbulent kinetic energy appears in the wake of the blades. The MSST k-ω model predicted lower turbulent kinetic energy, particularly in the wake and at the downstream of rotor blade than the SST k-ω model. This is resulted due to the viscosity modification and the effects of the added source terms, which increase the viscous dissipation considerably for the MSST k-ω model case. Moreover, the rotor blade has been generated with high curvature and therefore, the flow deflection is higher at the leading edge of the pressure side of rotor blade. Due to that a separation bubble has been observed at rotor pressure side for 90% span (Figure 5) which contributes

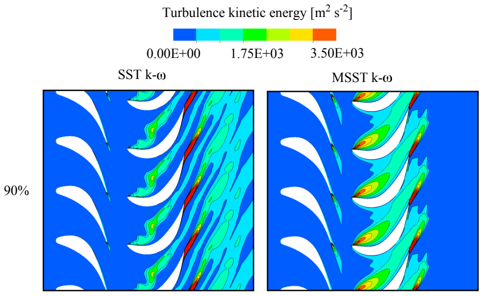

Figure 4. Predicted contours of the turbulence kinetic energy at 90% span.

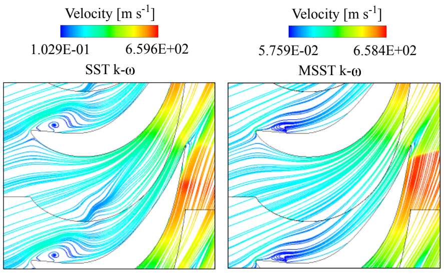

Figure 5. Predicted contours of the streamlines at 90% span.

to the turbulent kinetic energy in the mid passage of the rotor. The MSST k-ω model estimated comparatively higher turbulent kinetic energy in the mid passage of the rotor.

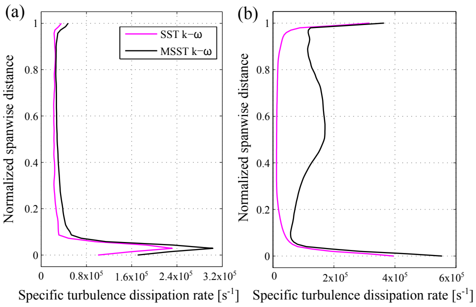

Figure 6. Predicted profiles of the specific turbulence dissipation rate at normalized spanwise distance (a) at the stator exit, and (b) outlet.

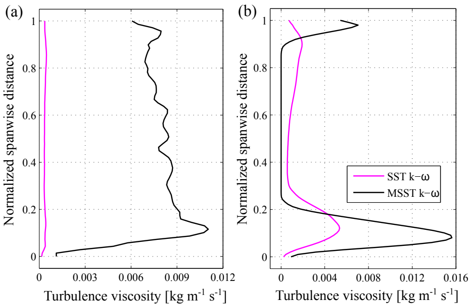

Figure 7. Predicted profiles of the turbulent viscosity at normalized spanwise distance (a) at the stator exit, and (b) outlet.

The turbomachinary flows are categorised as the wall-bounded flows in which fluid viscosity plays an important role in transport phenomena, particularly near wall surfaces. Also, the rapid variation of flow variables occurs within the boundary layer regions. These flows consist of a spectrum of different scales (eddy sizes). These structures are deformed and stretched by the fluid dynamics. These eddy structures break into smaller eddies. This phenomenon continues until the energy is transported to smaller and smaller structures. However, at the end, the kinetic energy is dissipated by the viscosity of the fluid. The whole process of transport of energy from the large scale of injection to the small dissipative scale, through the hierarchy of eddies is known as the turbulent cascade. Therefore, it is worthwhile to examine the effect of model modification on turbulence properties which are responsible for taking into account above mentioned turbulent process. The predicted circumferential average profiles of specific turbulence dissipation rate and turbulent viscosity for both the models are displayed in Figures 6 and 7. The stator exit is at the 20% axial chord distance of stator blade from the trailing edge of stator blade. It can be seen that the specific turbulence dissipation rate is notably high near the hub surface due to boundary layer effect. At outlet, the rate of specific turbulence dissipation is significantly higher at hub and shroud surfaces due to the turbulent cascade process. The MSST k-ω model yielded a higher value of specific turbulence dissipation rate at both planes than the SST k-ω model. Further, the MSST k-ω model estimated higher turbulent viscosity than the SST k-ω model. This is likely due to the modified viscosity which contains the production to dissipation ratio. Particularly, the turbulent viscosity is maximum near hub and shroud surfaces for outlet plane.

The expansion rates at stator and rotor blades, particularly at the spanwise direction, are distinct from each other. In Figure 8, the contours of vapour temperature are displayed for both models. Some variation has been observed in temperature profiles at both planes after model modification, particularly at the throat region and the downstream of it, around trailing edge and in the wake regions of rotor blade. It is obvious that the flow temperature is higher in the blade wakes due to flow mixing. In the case of MSST k-ω model, the increased viscous dissipation influenced the temperature distribution via energy source, which affected the heat transfer rates. Therefore, the temperature level is higher for the MSST k-ω model than the SST k-ω model in rotor blade wakes.

In condensing steam flow, the nucleating and growth processes are quite sensitive to local pressure distribution and expansion rate. Figure 9 shows the contours of the flow expansion rate for both models. The expansion rate varies in the blade passage, in which it is very low at the entrance and extremely high in the vicinity of the throat. As a consequence, the zone of rapid condensation occurs downstream of the throat region. As discussed previously, the rate of viscous dissipation is higher for the MSST k-ω model. Consequently, the Reynolds stresses are lower due to lesser eddy viscosity. Therefore, the shear effect is minor which influences on the flow parameters in the MSST k-ω model. Hence, the flow expansion in the MSST k-ω model is higher than the SST k-ω model.

The nucleation rate is especially large near the suction surface and at the trailing edge of the pressure surface in blade. This

Copyright © 2016 by ASME

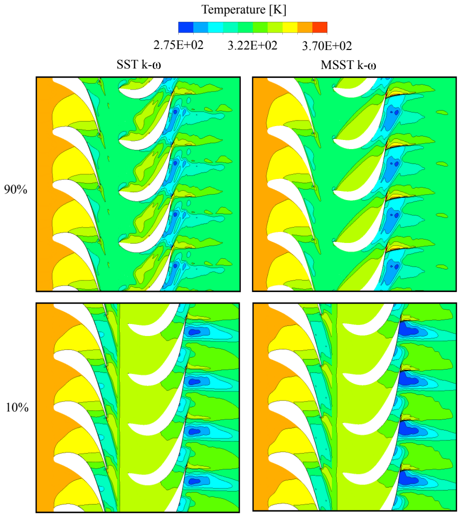

Figure 8. Predicted contours of the vapour temperature at spanwise planes.

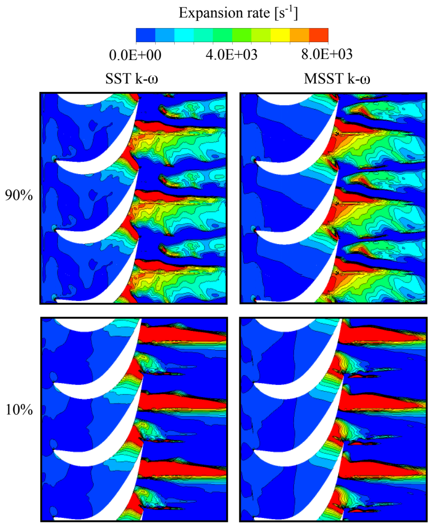

Figure 9. Predicted contours of the flow expansion rate of rotor at spanwise planes.

is caused by rapid acceleration and consequent high subcooling. The contours of subcooling and nucleation rate for both models are presented in Figures 10 and 11. The results show that the critical conditions for wetness formation have been accomplished near the hub surface for the stator within the throat region where the flow becomes transonic. The level of subcooling was reduced from the hub to the shroud surfaces for stator. While for rotor blade passage the level of subcooling was decreased from the shroud to the hub surfaces. The highest subcooling level reached was 36 K. However, some differences have been observed between the models. The MSST *k*-ω model estimated a higher subcooling level than the SST *k*-ω model. The intensity of nucleation is weaker from the hub to the shroud surfaces of stator. In addition, the nucleation region at 90% span is more uniformly distributed at rotor inlet. However, the nucleation is zeroed at the downstream of the interface at 10% and 50% span due to mixing plane assumption. The MSST *k*-ω model yielded a wider nucleation region than the SST *k*-ω model. Moreover, the expansion process is extended slightly to the downstream due to the turbulent viscosity modification and the source terms addition. Therefore, the nucleation region for the MSST *k*-ω model has been shifted slightly towards the downstream. Also, the level of subcooling was not strong enough to attain thermal equilibrium, and consequently the secondary nucleation zone appeared

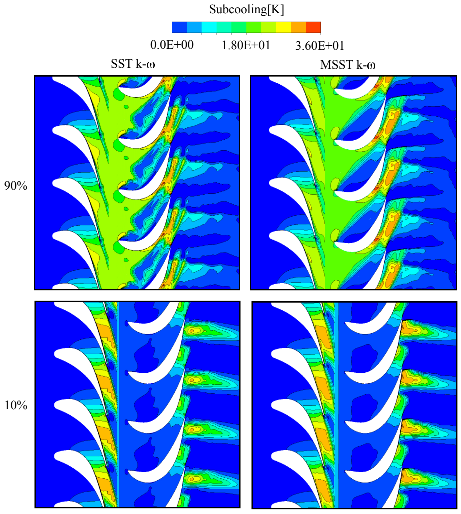

Figure 10. Predicted contours of the subcooling at spanwise planes.

Copyright © 2016 by ASME

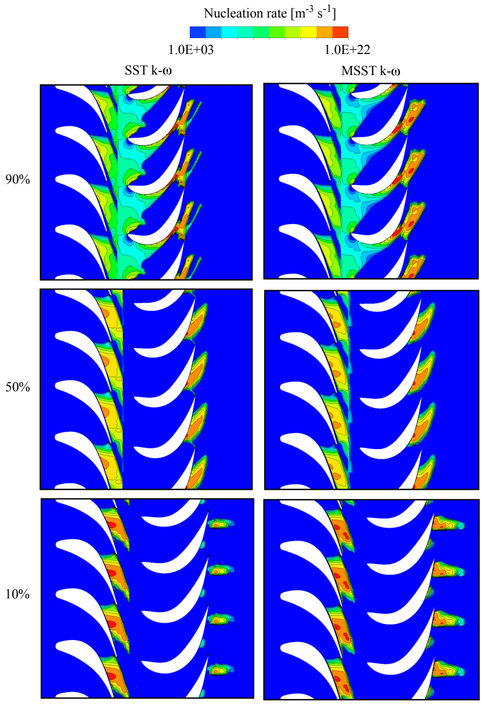

Figure 11. Predicted contours of the nucleation rate at spanwise planes.

in the rotor passage for all radial planes in both models. The intensity of secondary nucleation was decreased from the shroud to the hub surfaces of rotor for both the cases. The Wilson point fluctuates due to wake-chopping in the LP turbine flow. In the steady state calculations of this work, the secondary nucleation is stronger. This could be explained by the fixed Wilson point. The secondary nucleation region was larger for the MSST *k*-ω model than the SST *k*-ω model.

Further, the predicted contours of droplet average radius for both models at spanwise surfaces are displayed in Figure 12. If a large number of tiny liquid droplets nucleate, their growth is lower. In contrast, when a lower nucleation results, the growth rate is predominant and larger droplets are present. It can be seen that the droplet radius near the hub surface is lower due to large number of droplet. A larger droplet average radius has been observed near shroud surface. The turbulence modelling influenced the droplet sizes. The droplet radius distribution across the passage is mostly dependent on the total number of droplets created during the nucleation process, which is influenced by the distinct expansion rates along the blade passage and also the interaction between the trailing edge shock waves and the nucleation zone. It can be observed that, the growth rate is delayed in the case of MSST *k*-ω model due to larger nucleation region. Subsequently, the number of droplets estimated by the MSST *k*-ω model is lower compared to the SST *k*-ω model. Therefore, the MSST *k*-ω model yielded larger droplet average radius than the SST *k*-ω model.

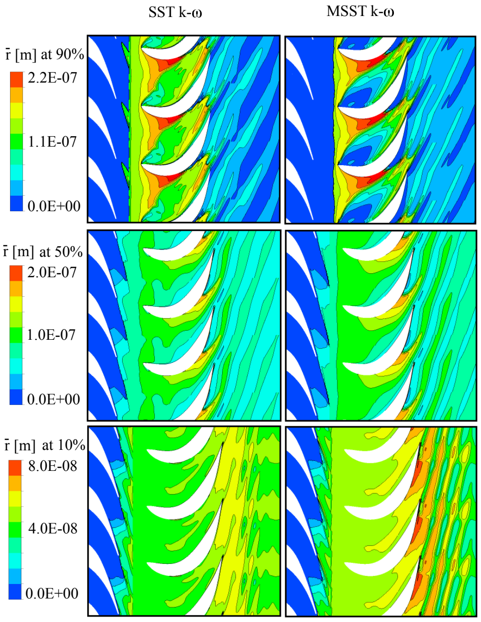

Figure 12. Predicted contours of the droplet average radius at spanwise planes.

The contours of wetness fraction are presented in Figure 13. It is clear that the level of wetness fraction increased from hub to shroud surfaces. Maximum wetness was observed in the downstream of rotor. It is clear that the SST *k*-ω model yielded higher wetness distribution than the MSST *k*-ω model. However, the MSST *k*-ω model predicted higher wetness fraction up to 7.5% at 90% span of rotor blade, particularly at separation bubble region of pressure side and at suction surface near trailing edge. Around

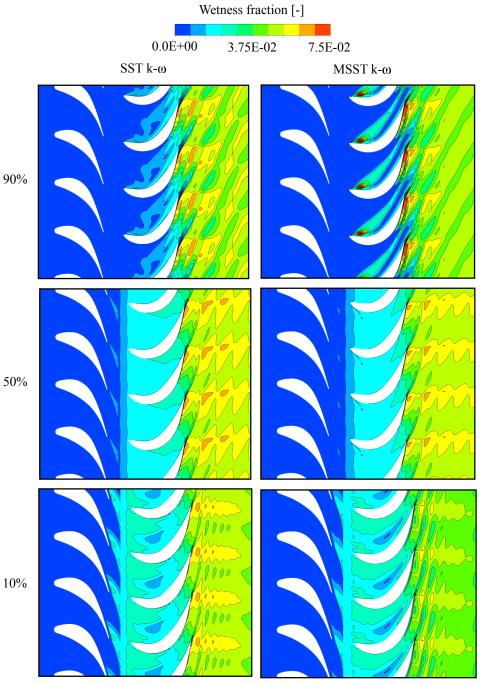

Figure 13. Predicted contours of the wetness fraction at spanwise planes.

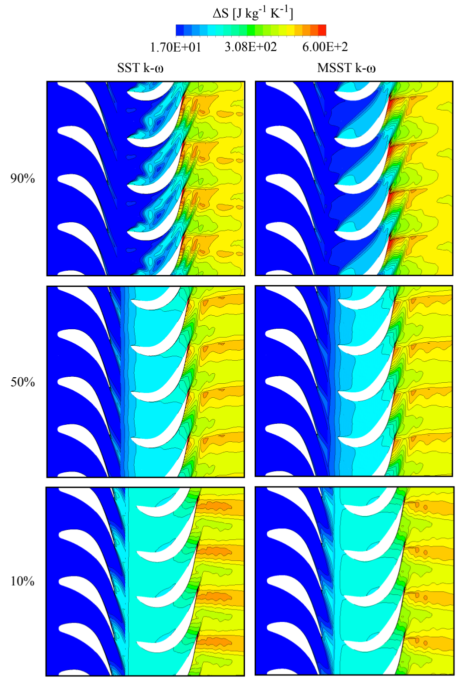

Figure 14. Predicted contours of the entropy rise at spanwise planes.

separation bubble region, the mass generation rate is considerably high which increased the wetness fraction. While at suction surface near trailing edge the wetness level is higher due to separation and secondary flow effect. Moreover, the wetness fraction is lower in the blade wakes and this is the region where flow mixing is prominent. Hence, the temperature is higher, which reduces the wetness fraction.

Figure 14 presents the predicted contours of the entropy generation for both models. Regions of steep velocity gradients such as blade wakes, edges of separated regions and vortices, in which the shear stresses are relatively high, are responsible for a large amount of entropy generation. Moreover, the flow turbulence which governs the heat, mass, and momentum transfer processes is considerably high in these regions as shown in Figure 15. It can be observed that the maximum rate of entropy is generated at the suction surface of the blade. Further, in the case of stator, the entropy generation is lower at the 90% span surface than other surfaces due to larger nucleation zone. In contrast, at the 90% span surface of the rotor, the production of entropy is raised because of very strong rotor secondary flow. However, the entropy production at the rotor is notably high compared to the stator due to the rapid release of latent heat by the droplets, flow separation and secondary flow effect. The SST k-ω model predicted a higher entropy generation compared to the MSST k-ω model particularly in the blade wake region for the 10% and 50% span surfaces, while the MSST k-ω model yielded higher entropy near to the trailing edge of rotor at the 90% span surface likely due to the higher turbulent dissipation in that region.

Further, the losses which occur due to the irreversible heat and mass transfer during the condensation process are estimated. In this work, the Markov energy loss coefficient based on the entropy increase was calculated and it can be defined as $\zeta = \frac{T_2.\Delta s}{0.5u_2^2}$, where Δs refers to the increment in a specific entropy. Here, T_2 and u_2 refer the local static temperature and relative velocity, respectively. The loss coefficient was divided into two compo-

Copyright © 2016 by ASME

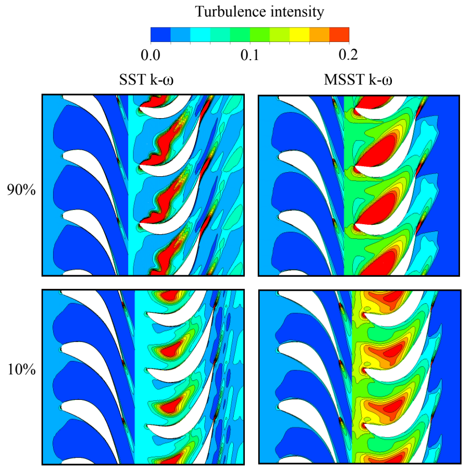

Figure 15. Predicted contours of the turbulence intensity at spanwise planes.

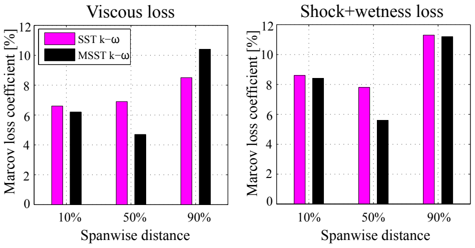

Figure 16. Predicted Markov loss coefficients.

nents: (i) shockwave plus wetness loss, which was calculated from the mass-averaged values across a section of the traverse plane excluding the wake regions, and (ii) viscous loss, which was calculated by subtracting the shockwave and wetness loss from the mass-averaged loss across the entire pitch at the traverse plane [14]. For the Markov loss coefficient estimation, all the parameters were calculated by the circumferential average at different span along the traverse plane. The traverse plane is located at the position of about 25% axial chord length from the rotor trailing edge in the axial direction. Figure 16 shows the calculated loss information. It can be seen that the SST k-ω model predicted higher viscous loss compared to the MSST k-ω model for the 10% and 50% span surfaces because of a large amount of entropy production in the blade wake of rotor (Figure 14). Moreover, it is observed that the value of viscous loss at the 90% span with the MSST k-ω was higher than with the SST k-ω model due to intense viscous dissipation at the edges of the separated region immediately behind the trailing edge of rotor. The MSST k-ω turbulence model predicted lower wetness due to higher viscous dissipation. It can be observed that the MSST k-ω model yielded lower shock plus wetness loss compared to the the SST k-ω model for all span surfaces.

5 CONCLUSIONS

The condensing steam flows at LP turbine involve rapid phase change, momentum and heat transport phenomena in which the role of turbulence is significant. Thus, the precise condensing steam flow prediction needs proper turbulence modelling. In this work, the preliminary study of the influence of turbulence modelling on non-equilibrium homogeneously condensing steam flow in 3D stator-rotor stage is discussed. For this purpose, the Eulerian-Eulerian approach based on compressible RANS equations was used. The SST k-ω turbulence model was modified by introducing the modulation of turbulence kinetic energy and its dissipation due to liquid droplets via source terms. Furthermore, the original definition of turbulent viscosity was modified by introducing production to dissipation ratio.

Firstly, the performance of MSST k-ω model was illustrated at 2D nozzles and turbine stator cascade flows. It can be concluded that the MSST k-ω model corresponded well with the test results and mimicked an accurate condensation process. The presented simulation results of a 3D stator-rotor stage case show that the inclusion of the source terms and modified turbulent viscosity at SST k-ω model caused notably higher estimates of viscous dissipation and, therefore, the increased viscous dissipation altered the temperature distribution through energy source, which impacted the heat transfer rates. Consequently, the nucleation process and droplet growth rates were influenced by the model modification. It can be seen that the MSST k-ω model yielded a higher subcooling level because of higher flow expansion. Subsequently, the nucleation region was expanded and the droplet growth rate was delayed. Therefore, the wetness fraction was decreased due to larger droplet sizes. It can be concluded that the increased viscous dissipation via model modification decreases wetness fraction.

The significance of turbulence modelling on the loss mechanism was also presented. For this purpose, the loss coefficients were estimated from the simulated results. The presented loss assessment demonstrates that after model modification the measure of shock plus wetness loss reduced. Also the viscous loss estimation was affected by the model modification and the viscous loss was decreased except near shroud surface. Based on the presented results, it is observed that the accurate computational modelling of wet-steam flow at LP turbine requires the

Copyright © 2016 by ASME

turbulence to be accurately modelled. Because an inaccurate prediction of turbulence may lead to an imprecise evaluation of the crucial phenomena of condensing flow and ultimately erroneous losses. However, this study is at an introductory stage in which the influence of unsteadiness is absent. Results show that the influence of turbulence modelling affected on wet-steam phenomena even with steady state simulations. Therefore, corresponding comparative simulations are encouraged concerning the further analysis of turbulence modelling influence to condensing steam flow at multistage LP turbine with unsteady condition.

ACKNOWLEDGEMENTS

The authors would like to acknowledge the Finnish Graduate School in Computational Fluid Dynamics and the Academy of Finland for the financial support and CSC-IT Center for Science, Finland for providing the scientific computing platform.

REFERENCES

[1] Yamamoto, S., Sasao, Y., Sato, S., and Sano, K., 2007. “Parallel-implicit computation of three-dimensional multistage stator-rotor cascade flows with condensation”. In Proc. 18th AIAA Computational Fluid Dynamics Conference, AIAA 2007-4460, Miami, Florida, USA, June.

[2] Yamamoto, S., Sasao, Y., Kato, H., Satsuki, H., Ooyama, H., and Ishizaka, K., 2010. “Numerical and experimental investigation of unsteady 3-d wet-steam flows through two-stage stator-rotor cascade channels”. In Proc. ASME Turbo Expo, GT2010-22796, Glasgow, UK, June 14-18, 1-9.

[3] Starzmann, J., Schatz, M., Casey, M. V., Mayer, J. F., and Sieverding, F., 2011. “Modelling and validation of wet steam flow in a low pressure steam turbine”. In Proc. ASME Turbo Expo, GT2011-45, Vancouver, Canada, June 6-10, 1-12.

[4] Starzmann, J., Kaluza, P., Casey, M. V., and Sieverding, F., 2013. “On kinematic relaxation and deposition of water droplets in the last stages of low pressure steam turbines”. *J. Turbomachinery,* **Vol. 136 (7)**, pp. 1–10.

[5] Avetissian, A. R., Philippov, G. A., and Zaichik, L. I., 2008. “Effects of turbulence and inlet moisture on two-phase spontaneously condensing flows in transonic nozzles”. *Int. J. Heat Mass Transfer,* **Vol. 51**, pp. 4195–4203.

[6] Patel, Y., Patel, G., and Turunen-Saaresti, T., 2015. “Influence of turbulence modelling on non-equilibrium condensing flows in nozzle and turbine cascade”. *Int. J. Heat Mass Transfer,* **Vol. 88**, pp. 165–180.

[7] Patel, Y., Turunen-Saaresti, T., Patel, G., and Grönman, A., 2014. “Numerical investigation of turbulence modelling on condensing steam flows in turbine cascade”. In Proc. of ASME Turbo Expo, GT2014-26307, Düsseldorf, Germany, June 16-20, 1-14.

[8] Guha, A., 1998. “Computation, analysis and theory of two-phase flows”. *The Aeronautical Journal,* **Vol.102**, pp. 71–82.

[9] Gerber, A. G., and Kermani, M. J., 2004. “A pressure based Eulerian-Eulerian multi-phase model for non-equilibrium condensation in transonic steam flow”. *Int. J. Heat Mass Transfer,* **Vol. 44**, pp. 2217–2231.

[10] McDonald, J. E., 1962. “Homogeneous nucleation of vapour condensation. I -thermodynamic aspects”. *Am. J. Physics,* **Vol. 30**, pp. 870–877.

[11] Kantrowitz, A., 1951. “Nucleation in very rapid vapour expansions”. *J. Chem. Phys.,* **Vol.19**, pp. 1097–1100.

[12] Gyarmathy, G., 1976. *Condensation in flowing steam*. A von Karman Institute Book on Two-Phase Steam Flow in Turbines and Separators, Hemisphere, London.

[13] Menter, F. R., 1994. “Two-equation eddy-viscosity turbulence models for engineering applications”. *AIAA Journal,* **Vol. 32 (8)**, pp. 1598–1605.

[14] White, A. J., Young, J. B., and Walters, P. T., 1996. “Experimental validation of condensing flow theory for a stationary cascade of steam turbine blade”. *Philos. Trans. Roy. Soc. London.,* **Vol. A 354**, pp. 59–88.

[15] Moore, M. J., Walters, P. T., Crane, R. I., and Davidson, B. J., 1973. “Predicting the fog drop size in wet steam turbines”. In Wet Steam 4 Conference, Institute of Mechanical Engineers (UK), University of Warwick, paper C37/73.

[16] Moses, C. A., and Stein, G. D., 1978. “On the growth of steam droplets formed in a Laval nozzle using both static pressure and light scattering measurements”. *J. Fluids Eng.,* **Vol. 100**, pp. 311–322.

Copyright © 2016 by ASME

667. VANHALA, ERNO. The role of business model in computer game development organizations. 2015. Diss.

668. SALAMPASIS, DIMITRIOS. Trust-embedded open innovation: Towards a human-centric approach in the financial industry. 2015. Diss.

669. DE SMET, DIETER. Innovation ecosystem perspectives on financial services innovation. 2015. Diss.

670. PORRAS, PÄIVI. Utilising student profiles in mathematics course arrangements. 2015. Diss.

671. SALMINEN, JUHO. The role of collective intelligence in crowdsourcing innovations. 2015. Diss.

672. ROSAS, SAILA. Co-operative acquisitions – the contextual factors and challenges for co-operatives when acquiring an investor-owned firm. 2015. Diss.

673. SINKKONEN, TIINA. Item-level life-cycle model for maintenance networks – from cost to additional value. 2015. Diss.

674. TUUNANEN, JUSSI. Modelling of changes in electricity end-use and their impacts on electricity distribution. 2015. Diss.

675. MIELONEN, KATRIINA. The effect of cationic-anionic polyelectrolyte multilayer surface treatment on inkjet ink spreading and print quality. 2015. Diss.

676. OMAJENE, JOSHUA. Underwater remote welding technology for offshore structures. 2015. Diss.

677. NUUTINEN, PASI. Power electronic converters in low-voltage direct current distribution – analysis and implementation. 2015. Diss.

678. RUSATSI, DENIS. Bayesian analysis of SEIR epidemic models. 2015. Diss.

679. STRAND, ELSI. Enhancement of ultrafiltration process by pretreatment in recovery of hemicelluloses from wood extracts. 2016. Diss.

680. TANNINEN, PANU. Press forming of paperboard – advancement of converting tools and process control. 2015. Diss.

681. VALTONEN, PETRI. Distributed energy resources in an electricity retailer’s short-term profit optimization. 2015. Diss.

682. FORSSTRÖM-TUOMINEN, HEIDI. Collectiveness within start up-teams – leading the way to initiating and managing collective pursuit of opportunities in organizational contexts. 2015. Diss.

683. MAGUYA, ALMASI. Use of airborne laser scanner data in demanding forest conditions. 2015. Diss.

684. PEIPPO, JUHA. A modified nominal stress method for fatigue assessment of steel plates with thermally cut edges. 2015. Diss.

685. MURASHKO, KIRILL. Thermal modelling of commercial lithium-ion batteries. 2016. Diss.

686. KARKKAINEN, TOMMI. Observations of acoustic emission in power semiconductors. 2016. Diss.

687. KURVINEN, EMIL. Design and simulation of high-speed rotating electrical machinery. 2016. Diss.

688. RANTAMÄKI, JUKKA. Utilization of statistical methods for management in the forest industry. 2016. Diss.

689. PANOVA, YULIA. Public-private partnership investments in dry ports – Russian logistics markets and risks. 2016. Diss.

690. BAHARUDIN, EZRAL. Real-time simulation of multibody systems with applications for working mobile vehicles. 2016. Diss.

691. MARTIKAINEN, SOILI. Development and effect analysis of the Asteri consultative auditing process – safety and security management in educational institutions. 2016. Diss.

692. TORVINEN, PEKKA. Catching up with competitiveness in emerging markets – An analysis of the role of the firm’s technology management strategies. 2016. Diss.

693. NORONTAUS, ANNUKKA. Oppisopimuskoulutus yritysten tuottamana koulutuspalveluna: tavoitteista vaikutuksiin. 2016. Diss.

694. HALMINEN, OSKARI. Multibody models for examination of touchdown bearing systems. 2016. Diss.

695. TALONPOIKA, ANNA-MARIA. Financial working capital – management and measurement. 2016. Diss.

696. INKINEN, HENRI. Intellectual capital, knowledge management practices and firm performance. 2016. Diss.

697. YANG, XIAOCHEN. Development of a welding production quality control and management system model for China. 2016. Diss.

698. LEMINEN, VILLE. Leak-proof heat sealing of press-formed paperboard trays. 2016. Diss.

699. LAAKSONEN, LAURI. Spectral retinal image processing and analysis for ophthalmology. 2016. Diss.

700. OINONEN, MINNA. Management of customer co-development in business-to-business markets. 2016. Diss.

701. ALATALO, SARA-MAARIA. Hydrothermal carbonization in the synthesis of sustainable porous carbon materials. 2016. Diss.

702. UZHEGOV, NIKITA. Design and material selection of high-speed rotating electrical machines. 2016. Diss.

703. RICHTER, CHRIS. Digital collaborations and entrepreneurship – the role of shareconomy and crowdsourcing in the era of smart city. 2016. Diss.

704. JAFARI, SHILA. Investigation of adsorption of dyes onto modified titanium dioxide. 2016. Diss.